

Estimation of Fatigue Life under Multiaxial Loading: Modelling and Experimentation

Thesis submitted to the Department of Engineering Science of the University of Oxford in partial fulfilment of the requirements for the degree of Doctor of Philosophy

by

João Vitor Sahadi Cavalheiro

Christ Church
University of Oxford

Michaelmas Term, 2019

Abstract

This doctorate research project investigates the multiaxial deformation and fatigue behaviour of two Nickel-based superalloys used in the discs of aero-engines, named Waspaloy and RR1000, under proportional and non-proportional loading conditions. For that a systematic analysis has been performed to identify and quantify the biaxiality of loading effects on fatigue life, the effects of non-proportional multiaxial loading – including additional cyclic hardening and cross-hardening – on crack initiation and fatigue life, and lastly the role of material micro-structure and crystal orientation on fatigue crack nucleation. An extensive experimental programme with uniaxial and biaxial fatigue tests with Waspaloy and non-proportional tension-torsion tests with RR1000 was carried out. It was experimentally observed that the variation of biaxiality ratio, for the same maximum principal stress, was found to cause a significant change in fatigue life and failure location for Waspaloy. Furthermore, results show that RR1000 presents no load path dependency for stress levels near the yield strength of the material. On the other hand, fatigue lives and cyclic hardening are highly dependent on the degree of non-proportionality. Lives for non-proportional tests were around three times shorter than fatigue lives for proportional tests at comparable stress levels. The experimental programme was used for calibrating and benchmarking a wide range of stress-, strain- and energy-based multiaxial fatigue damage parameters. Most of them could provide a reasonable collapse of both Waspaloy and RR1000 test data. Particularly good fatigue life predictions were obtained with stress-based criteria, especially with Walker stress and Matake's critical plane approach. Lastly, a GND-coupled crystal plasticity framework and stored energy criterion was implemented for predicting fatigue lives of RR1000. It was concluded that Wan et al.'s stored energy criterion, which combines stress, plastic

slip and GNDs density represents an excellent tool for accurately predicting fatigue lives under complex multiaxial loading conditions.

To my wife Larissa and family

Acknowledgements

First and foremost, I would like to express my profound gratitude to my supervisor Prof David Nowell who has provided me with enormous support since my application to Oxford. I truly appreciate the freedom Prof Nowell has given me to pursue my DPhil and his guidance as I endeavoured in the different aspects of my research work. His constant trust and encouragement deeply inspired me. It was a terrific privilege to have worked with him.

I also would like thank Prof David Hills who acted as my internal supervisor with the move of Prof Nowell to Imperial College. Although I did not have a work engagement with Prof Hills, he ensured my period at Oxford was as smooth as possible.

My sincere gratitude goes to Dr Robert Paynter who shared his enormous experience and kindly taught me so much on the experimental aspects of my thesis. Dr Paynter has a great contribution to the success of the optical strain measurement system developed for the uniaxial tests with Waspaloy.

I would like to thank my office colleagues, especially Dr Elsiddig Elmukashfi for his willingness to share his vast knowledge on solid mechanics. Chapter 5 of this thesis would not have been possible without his help.

I am also grateful to Prof José Alexander Araújo, Prof Lucival Malcher and Prof Edgar Mamiya for creating the possibility of my coming to Oxford.

I appreciate the Brazilian National Council of Technological and Scientific Development (CNPq) and Rolls-Royce plc for their financial support throughout my doctorate research programme. I would also like to acknowledge the use of the University of Oxford Advanced Research Computing (ARC) facility in carrying out this work and the assistance of all the staff and technicians in the Solids Mechanics group at the

University of Oxford, in particular Hisham Elamin for his kindness and support.

Last, but definitely not least, I would like to thank my parents, my grandmother and all my family in Brazil for their unconditional support and encouragement during the course of this thesis. I am especially thankful to my wife Larissa who on-boarded this journey with me and brought me clarity during the challenging moments.

Contents

1 Introduction **1**

1.1 Industrial Context 1

1.2 Gas turbine jet engines 2

1.2.1 Sources of Stresses 4

1.2.2 Materials investigated 5

1.3 Thesis outline 6

2 Background and Literature Review **8**

2.1 Physics of crack nucleation 8

2.2 Multiaxial fatigue testing 13

2.3 Non-proportional loading 15

2.4 Multiaxial fatigue modelling 17

2.4.1 Stress-based criteria 19

2.4.2 Strain-based criteria 24

2.4.3 Energy-based criteria 25

2.5 Micromechanics approach 26

3 Experimental Work **29**

3.1 Waspaloy 30

3.1.1 Biaxial Fatigue tests 32

3.1.2 Uniaxial Fatigue tests 47

3.2 RR1000 60

3.2.1 Non-proportional tension-torsion tests 62

3.3 Conclusions . . . 74
3.3.1 Conclusions for Waspaloy . . . 74
3.3.2 Conclusions for RR1000 . . . 75

4 Multiaxial Fatigue Damage Parameters 76

4.1 Overview . . . 76
4.2 Axial and torsional fatigue behaviour . . . 79
4.3 Stress-strain response modelling . . . 81
4.4 Critical plane search . . . 86
4.5 Stress-based criteria . . . 89
4.5.1 Static yield criteria . . . 89
4.5.2 Invariant-based approaches . . . 101
4.6 Critical Plane approach . . . 107
4.6.1 Stress-based criteria . . . 108
4.6.2 Strain-based criteria . . . 110
4.6.3 Energy-based criteria . . . 114
4.7 Conclusion . . . 121

5 Crystal Plasticity Modelling 123

5.1 Overview . . . 123
5.2 Crystal plasticity framework . . . 124
5.2.1 Crystal slip rule . . . 124
5.2.2 Evolution of SSD and GND densities . . . 131
5.2.3 Hardening rule . . . 134
5.2.4 Stored energy criterion . . . 134
5.3 Crystal plasticity implementation . . . 136
5.3.1 Microstructurally representative volume element model . . . 139
5.3.2 Mesh discretisation . . . 140
5.3.3 Boundary conditions and loads . . . 143
5.3.4 Model Calibration . . . 145

5.4 Results 149
5.5 Conclusions 163

6 Conclusion **165**

6.1 Summary of Thesis 165
6.2 Concluding remarks 169
6.2.1 Highlights 169
6.2.2 Experimental work 170
6.2.3 Multiaxial fatigue damage parameters 171
6.2.4 Crystal plasticity modelling of RR1000 171
6.3 Suggestions for future work 172
6.3.1 Experimental work 172
6.3.2 Multiaxial fatigue damage parameters 173
6.3.3 Crystal plasticity modelling of RR1000 173

References **174**

1 Introduction

This chapter introduces the research topic of this doctoral thesis and its industrial context. The focus of this research project was to answer two key questions: 1) Should multiaxial fatigue be taken into consideration when designing aero engines discs? 2) How load multiaxiality impacts the fatigue response of Nickel-based superalloys used for aero engine discs? In order to answer to these questions, it is necessary to first understand aero-engines discs and the load conditions under which they operate. Secondly, the fatigue phenomenon state of the art must be reviewed, together with the various techniques used to model it, considering different length scales. Lastly, a comparison of the various model formulations, assessing their performances, advantages and disadvantages, has to be performed.

1.1 Industrial Context

The safety and reliability of complex systems, such as nuclear reactors, gas turbines and aircrafts, are strongly dependent on the design of their constituent parts and on the dynamic forces acting during their operation. Cyclic loading, even for stress levels considerably below the ultimate strength of the material, facilitates movement of dislocations, which eventually form persistent slip bands at critical points. Some

of these slip bands grow to form extrusions and/or intrusions that may lead to the nucleation of micro-cracks. Finally, one of the micro-cracks dominates the fatigue process by propagating and leading to final failure [Castro & Jiang, 2016; Stephens et al., 2000].

Often, mechanical components are designed considering ideal uniaxial loading conditions, due to the simplicity and cost effectiveness of uniaxial testing and the sheer amount of experimental data available. However, engineering components and structures are commonly loaded by a combination of variable loads in multiple directions, due to their complex geometry and/or complexity of external loading. In contrast to uniaxial fatigue, the multiaxial fatigue problem involves complex stress/strain states, mean stress effects, loading history dependency and non-proportional hardening. Thus, the study of multiaxial fatigue requires experiments to properly reproduce such loading conditions and fatigue damage parameters which accurately predict multiaxial fatigue lives.

From the industrial standpoint, the use of multiaxial fatigue modelling techniques for the design of critical components represents a potential commercial advantage, as improved fatigue live prediction can reduce material waste and component failure. However, implementation can be expensive and time consuming, requiring additional processing steps. In this sense, this thesis investigates different approaches for multiaxial fatigue modelling, including extended yield criteria, multiaxial fatigue damage parameters and a crystal plasticity framework on their performance and ease of implementation in the industrial context.

1.2 Gas turbine jet engines

Turbofan engines, or bypass engines, are carefully designed to meet governmental regulations and customers' demands for greater thrust, reduced fuel consumption and lower noise levels at subsonic flights. Rolls-Royce engines, for instance, are normally

comprised of three parts: a fan located at the front of the engine, and multiple compressor and turbine stages, often referred to low (LP), intermediate (IP) and high pressure (HP) stages. Figure 1.1 illustrates an example of the Rolls-Royce three-shaft engine configuration. The measure of performance for aeroengines is based on thermal efficiency and is strongly dependent upon, and limited by, the high-temperature strength of the Nickel-based superalloys used for its hottest sections, i.e. the turbine system [Cumpsty, 2003; Reed, 2006].

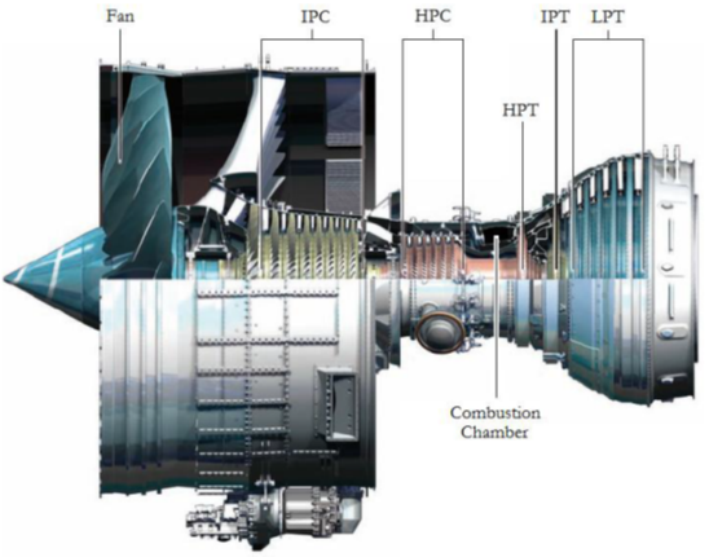


Figure 1.1 – Three-shaft aeroengine – Low, intermediate and high pressure system configuration. Adapted from Pattison [2012].

High-pressure turbine (HPT) discs, located immediately downstream of the combustion chamber, are the components experiencing the most extreme and demanding conditions. The main function of HPT discs is to position and retain the turbine blades in their correct positions in the axial and radial directions, and in doing so, transfer their circumferential loads to the high-pressure compressor system. In a typical flight cycle, the gas path in the HPT system can reach temperatures of 1500°C and spool speeds of 12,000 rpm, resulting in great thermal stresses and centrifugal loads (exerted by the spinning disc mass itself and the blades attached to the disc) [Pattison, 2012]. The magnitude and contribution of these stresses varies both geometrically across the component, and in time through the flight cycle, creating a true non-proportional

multiaxial stress state.

1.2.1 Sources of Stresses

Assuming an elastic homogeneous and isotropic material at uniform temperature, the radial and hoop stress distribution in a spinning disc of uniform thickness, representative of an actual HPT disc, can be described by Eqs. 1.1 and 1.2, respectively [Alexandrova et al., 2006; Bees, 2016].

$$\sigma_{radial} = (3+\nu)\frac{\rho\omega^2}{8}\left[r_i^2 + r_o^2 - \frac{r_i^2 r_0^2}{r^2} - r^2\right], \tag{1.1}$$

and,

$$\sigma_{hoop} = \frac{\rho\omega^2}{8}\left[(3+\nu)\left(r_i^2 + r_o^2 - \frac{r_i^2 r_0^2}{r^2}\right) - (1+3\nu)r^2\right], \tag{1.2}$$

where, ρ is the material density, ω the angular velocity, and ν the Poisson ratio. r_i and r_o represent the central hole radius and maximum outer radius, respectively. r is the radius from the disc centre line, representing the point of interest along the disc surface. Figure 1.2 illustrates the normalised distribution of radial and hoop stresses. Peak hoop stress is observed at the bore of the discs and decreases as it moves towards the rim. Radial stress, in contrast, is zero at the bore, increases rapidly to a maximum point in the diaphragm region (mid-section of the disc), and decreases after that to zero at the disc rim free surface. For the uniform thickness disc considered, hoop stress is greater than radial stress throughout the entire disc. However, it is possible to change the magnitude of radial and hoop stresses by varying disc thickness profile. Lower disc mass at the rim directly reduces peak radial stresses, while lower mass at the radial direction minimise hoop stress [Pattison, 2012]. This analysis is based on a simplified representation of actual stresses, as the disc is considered as a two-dimensional object and the effects of plasticity, creep, temperature and multiaxial loading are neglected.

For realistic analysis and calculation of stress distribution in HPT discs, computational Finite Element modelling is required due to the complex geometry.

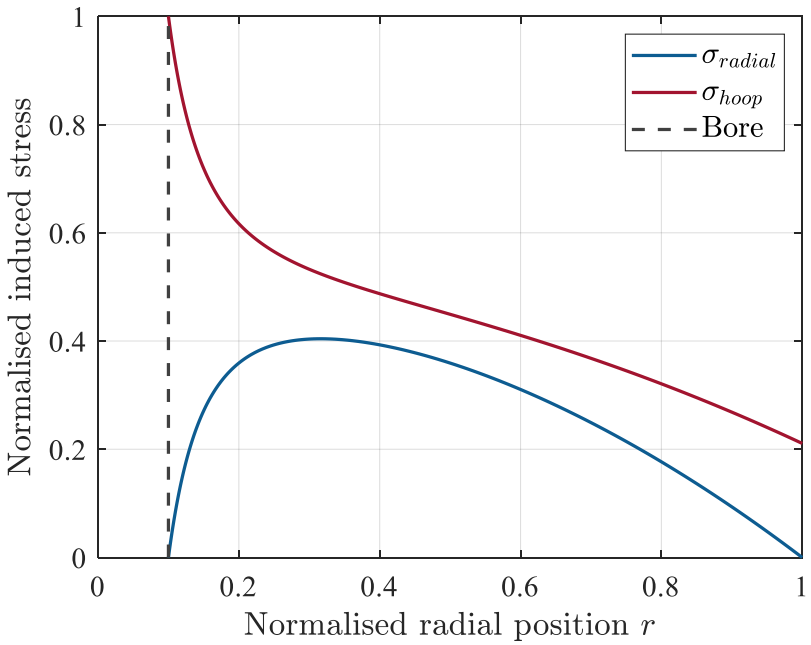


Figure 1.2 – Stress distribution in a spinning disc of uniform thickness.

1.2.2 Materials investigated

The concentration of thermal energy from the combustion process and kinetic energy in the rotating parts, represent issues for the structural integrity of the engine [Bees, 2016]. Therefore, HPT discs are typically manufactured from casting, forging or powder metallurgy processing of polycrystalline Nickel-based superalloy to mitigate the risk of failure, as such superalloys exhibit elevated creep resistance, high fatigue strength, low thermal expansion coefficient and high thermal conductivity, fundamental characteristics to sustain the extreme mechanical and thermal loads.

This doctoral research project investigates the multiaxial deformation and fatigue behaviour of two Nickel-based superalloys, named Waspaloy and RR1000, under proportional and non-proportional loading conditions. For that an extensive analysis has been performed to identify and quantify the biaxiality of loading effects on fatigue

life, the effects of non-proportional multiaxial loading - including additional cyclic hardening and cross-hardening - on crack initiation and fatigue life, and lastly the role of material micro-structure and crystal orientation on fatigue crack nucleation. The two materials represent different generations of polycrystalline superalloys. Waspaloy was developed in the 1950s and has since been widely used for hot gas turbine applications [Bloch & Soares, 2001]. RR1000, on the other hand, represents the current generation of Nickel-based superalloys developed by Rolls-Royce plc for HPT disc applications. Although the discs themselves were not investigate in this work, their operating conditions were taken into account for the preparation of the experimental programme conducted. In order to isolate load multiaxiality effects from creep effects, these two materials were tested at room temperature only. Creep effects and possible coupling between multiaxiality and creep should be studied in a future work.

1.3 Thesis outline

The overall aim of the research completed in this doctoral thesis is to determine the most suitable techniques for predicting multiaxial fatigue lives of Nickel-based superalloys in the low cycle fatigue (LCF) regime at room temperature (no creep). For that, the research investigation has been structured considering three main pieces of work: 1) Experimental work; 2) Multiaxial Fatigue Modelling; and 3) Micro-mechanical modelling of crack nucleation under multiaxial loading considering a CPFE framework.

CHAPTER 1 – Introduction: This chapter sets the background for the project, presenting the motivation for investigating multiaxial fatigue, the aerospace industrial context and a brief description of discs of the turbine section of aero-engines – and the sources of stresses. It also introduces the Nickel-based superalloys investigated and used in turbine disc applications, Waspaloy and RR1000.

CHAPTER 2 – Background and Literature Review: Chapter 2 presents the multiaxial fatigue phenomenon and the current state of the art in its investigation. The

chapter presents a thorough review of proportional and non-proportional multiaxial fatigue testing and modelling at different length scales, considering fatigue damage parameters and crystal plasticity modelling.

CHAPTER 3 – Experimental Work: Chapter 3 establishes the methodology for low cycle multiaxial fatigue testing carried out at room temperature, so that creep effects could be neglected. The initial section describes uniaxial and biaxial tests conducted under a range of loading conditions with cruciform specimens made of Waspaloy. This chapter also presents stress-controlled tension-torsion tests with RR1000 under various non-proportional loading conditions.

CHAPTER 4 – Multiaxial Fatigue Damage Parameters: This Chapter uses the experimental results from Chapter 3 to examine several stress-, strain- and energy-based multiaxial fatigue criteria and assess their ability to correlate multiaxial fatigue test data.

CHAPTER 5 – Crystal Plasticity Modelling: In this chapter the crystal plasticity framework adopted for modelling the non-proportional tension-torsion tests with RR1000 is presented. Wan et al. [2014] stored energy criterion is implemented for predicting fatigue lives and compared with the multiaxial fatigue damage parameters investigated in Chapter 4.

CHAPTER 6 – Conclusions: The last Chapter of the thesis summarises the major findings and key conclusions drawn from this research project. It recaps the experimental and numerical results, and provides recommendations on the best criteria for multiaxial fatigue life prediction and topics for future work.

2 Background and Literature Review

This chapter presents the fundamental background and literature review of this research study. This includes the damage mechanisms associated with the fatigue phenomenon, differences between proportional and non-proportional loading, and the current state of the art for multiaxial fatigue testing and modelling considering different length scales.

2.1 Physics of crack nucleation

Fatigue damage is always caused by cyclic plastic deformation, even if restricted to a microscopic scale. For instance, high-cycle fatigue crack initiation is a highly localised process induced by relatively low loads and associated with relatively long crack initiation lives. The microscopic fatigue cracking phenomenon is related to the density and arrangement of the dislocation structure and substructure of the metal. Dislocations are linear imperfections around which some of the atoms are misaligned [Callister & Rethwisch, 2010]. Typically, dislocations are introduced into a crystal either during material solidification or when the material is plastically deformed [Askeland & Wright, 2014]. According to Hull & Bacon [2011], the most useful definition of dislocations is given in terms of the Burgers circuit and Burgers vector. Considering the illustration

of a dislocation-free crystal in Fig. 2.1a, i.e. a crystal with no atom misalignment, the Burgers circuit refers to the atom-to-atom path that forms the closed loop $ABCDE$. If the same atom-to-atom sequence is followed in a crystal containing dislocations and the circuit is not closed, then the vector required to complete the circuit is called the Burgers vector [Hull & Bacon, 2011]. Fig. 2.1b illustrates the Burgers vector, in red, required to close the path $ABCDE$ due to the extra half plane of atoms.

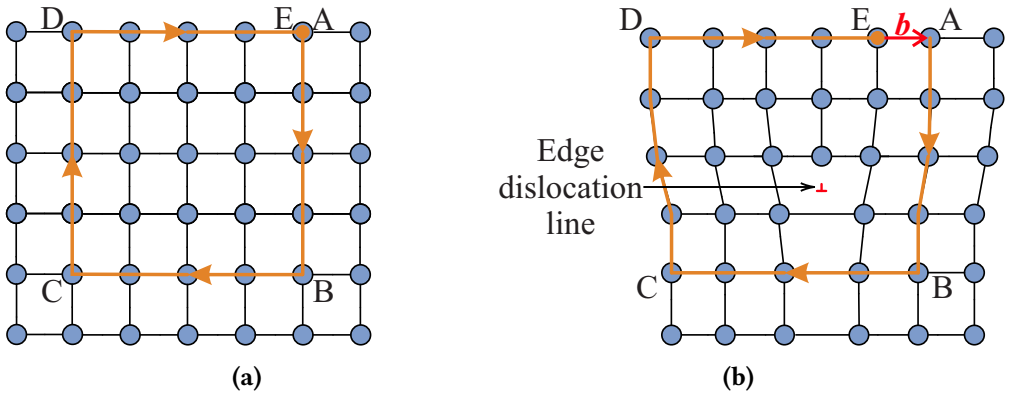


Figure 2.1 – Burgers circuit: a) closed, and b) open.

The glide of dislocations involves only very local rearrangements of atoms close to it. Each dislocation is associated with a unit of slip displacement given by the Burgers vector, $\boldsymbol{b}$ [Dunne & Petrinic, 2005]. Figure 2.2 illustrates atom positions around two types of dislocations. The first type, termed edge dislocation, is a linear defect that centres on the line that is defined along the end of the extra half-plane of atoms. For an edge dislocation, the dislocation line is perpendicular to the Burgers vector and the dislocation glide parallel to the Burgers vector. Screw dislocation is the other type of dislocations illustrated in Fig. 2.2. Their nomenclature derives from the spiral path that is traced around the dislocation line by the atomic planes of atoms. Screw dislocations are oriented parallel to the Burgers vector and glide perpendicular to it. Most commonly, materials exhibit a combination of edge and screw dislocations, referred to as mixed dislocations, where the line dislocation is oriented neither perpendicular nor parallel to the Burgers vector [Callister & Rethwisch, 2010].

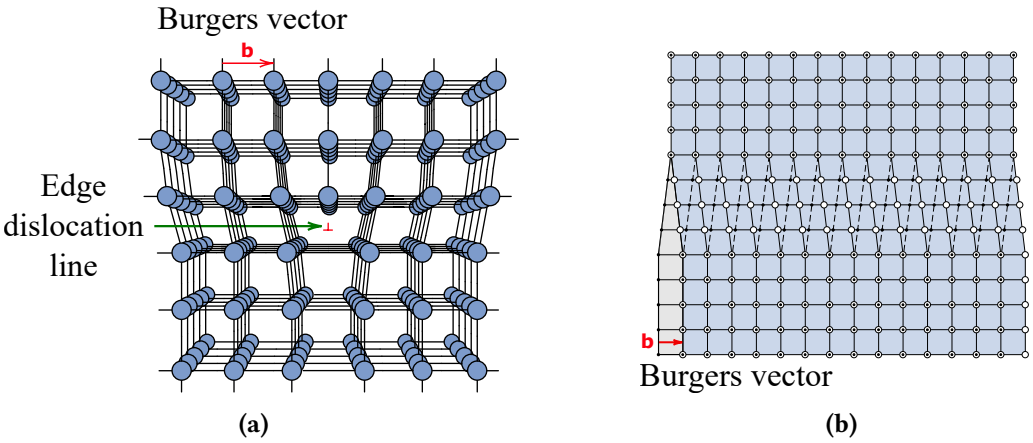
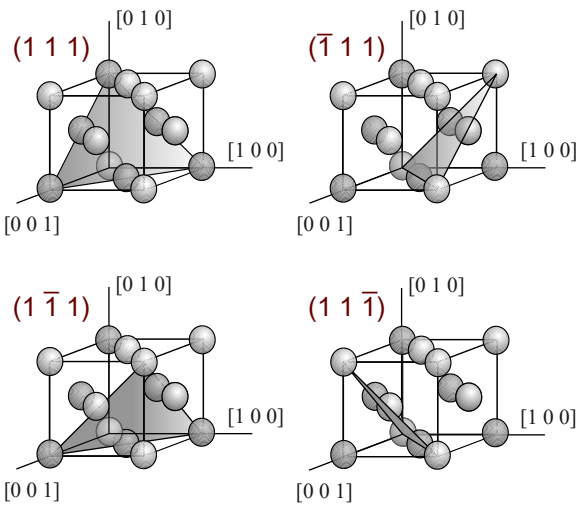


Figure 2.2 – Atom positions around: a) edge, and b) screw dislocation. Adapted from Callister & Rethwisch [2010].

When a sufficiently large shear stress is applied to a crystal, plastic deformation is produced by the motion of dislocations. This process is known as slip and occurs in metals within individual grains by dislocations moving along crystallographic planes [Askeland & Wright, 2014]. Experimental observations on single crystals show that slip tends to occur on preferred slip systems, which are a combination of the most densely packed planes and the directions in which atoms are packed closest together [Dunne & Petrinic, 2005]. In Face Centred Cubic (FCC) materials, as is the case of both Waspaloy and RR1000, the most densely packed planes are the diagonal planes of the unit cell. Figure 2.3 presents a schematic representation of an FCC crystal type along with a full list of possible slip systems. The full family of slip systems in an FCC crystal may be written as $\langle 1\bar{1}0\rangle\{111\}$, and is formed by 12 such systems.

Deformation by slip is described by Schimid's law in terms of slip systems and a critical resolved shear stress (CRSS) needed to overcome resistance to dislocation motion [Kiwanuka, 2013], i.e. slip occurs on a slip system when the resolved shear stress reaches a critical value. Figure 2.4 illustrates Schimid's law, containing slip plane normal, $\boldsymbol{n}$, slip direction, $\boldsymbol{s}$, and loaded in direction $\boldsymbol{t}$. Considering Fig. 2.4 and an applied tensile stress, σ, the resolved shear stress acting on the slip plane and in the slip direction, τ, may be mathematically formulated according to Eq. 2.1.



Slip System	Slip Plane	Slip Direction
1	(1 1 1)	[1 1̄ 0]
2	(1 1 1)	[0 1 1̄]
3	(1 1 1)	[1 0 1̄]
4	(1̄ 1 1)	[1 1 0]
5	(1̄ 1 1)	[0 1 1̄]
6	(1̄ 1 1)	[1 0 1]
7	(1 1̄ 1)	[1 1 0]
8	(1 1̄ 1)	[0 1 1]
9	(1 1̄ 1)	[1 0 1̄]
10	(1 1 1̄)	[1 1̄ 0]
11	(1 1 1̄)	[0 1 1]
12	(1 1 1̄)	[1 0 1]

Figure 2.3 – Schematic of FCC crystal type showing slip systems.

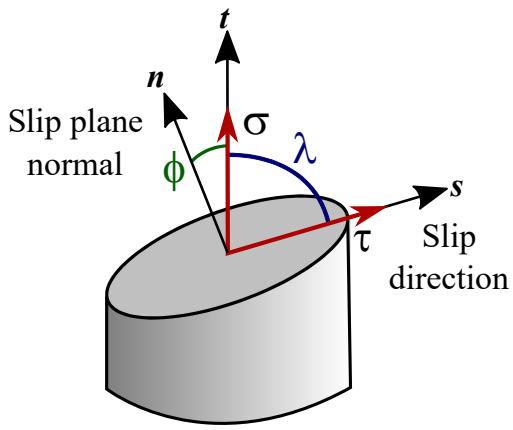


Figure 2.4 – Illustration of Schimid's law considering a single crystal. Adapted from Dunne & Petrinic [2005].

$$\tau = \sigma \cos\phi \cos\lambda = \sigma\,(\boldsymbol{t}\cdot\boldsymbol{n})(\boldsymbol{t}\cdot\boldsymbol{s})\ . \tag{2.1}$$

Depending on the loading condition, different slip systems can be activated, and some slip systems will dominate plastic deformation depending on their Schmidt factors. The dislocation motion is associated with the mechanisms of hardening and strengthening. Crystals work harden during plastically straining as dislocation glide stops and dislocations become stored. Dislocations storage happens for two reasons: either they are stored for the compatible deformation of various parts of the specimen, or they accumulate by randomly trapping each other [Ashby, 1970]. Considering the plastic bending of a crystal to a curvature K illustrated in Fig. 2.5. A simple geometric

relationship exists between the deformation, described by the curvature, and the density of dislocations $\rho_{GND} = k/\boldsymbol{b}$ of Burgers vector $\boldsymbol{b}$. These dislocations are termed Geometrically Necessary Dislocations (GNDs) as they are needed to accommodate plastic shear strain gradients and lead to lattice curvature [Nye, 1953; Fleck & Hutchinson, 1994; Arsenlis & Parks, 1999; Dunne, Rugg & Walker, 2007].

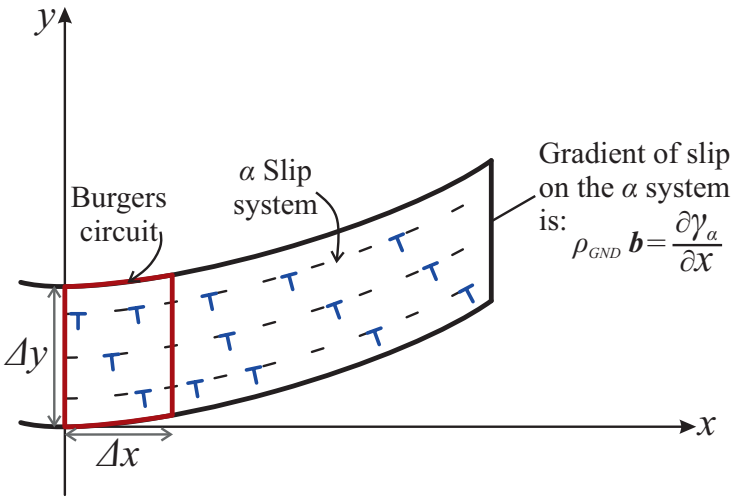


Figure 2.5 – Diagram illustrating the relationship between deformation, described by the curvature, and GNDs density. Adapted from Ashby [1970].

By contrast, the deformation of a single crystal by pure tension is uniform, and dislocations are not geometrically necessary. Dislocations still accumulate in such conditions leading to crystal work hardening. However, their density cannot be predicted by a simple geometric argument as they accumulate by random encounters in the crystal resulting in mutual trapping. These dislocations are referred to as Statistically Stored Dislocations (SSDs) [Ashby, 1970]. The total density in a crystal can therefore be decomposed into a geometrically-necessary part and a statistically-stored part. The geometrically-necessary part is the minimum dislocation needed to accommodate the lattice curvature, anything above the geometric minimum necessary would thus incorporate some statistical component, comprised of dislocation dipoles, i.e. self-terminating dislocation structures with no geometric consequence [Arsenlis & Parks, 1999]. When the density of GNDs exceed that of SSDs, the former controls the work hardening of the material [Ashby, 1970].

As an initially soft metal with low dislocation density is plastically deformed due to cyclic stress/strain, the density of dislocations can increase rapidly. This increase in dislocation density leads to a decrease in dislocation mobility. Therefore, if dislocations are constrained to move or glide and slip is minimised, the material is said to harden cyclically and the cyclic yield strength becomes greater than the monotonic yield strength [Stephens et al., 2000]. In contrast, for initially hard and high dislocation density metals, plastic straining can cause the existing dislocation structures to rearrange into configurations of less resistance to deformation, allowing for greater dislocation mobility. Dislocations are then able to circumnavigate around microstructural barriers that generally tend to restrict deformation, such as precipitates and grain boundaries. As a result, the material softens, and the cyclic yield strength is less than the monotonic yield strength. Both hardening and softening can occur either at a global scale, such as a net section area, or at a very localised region, such as notches, cracks or vicinity of metallurgical discontinuities [Stephens et al., 2000]. It is important to note that dislocation density is also highly dependent on the manufacturing process and thermo-mechanical history of the material, affecting material hardness directly.

2.2 Multiaxial fatigue testing

Lanza [1886] pioneered multiaxial fatigue experiments by observing combined cyclic loading back in 1886. He discussed his test results for combined in-phase bending and torsion and pointed out the need for further work. Later, Mason [1917] conducted an extensive study of cyclic strains under combined fully reversed torsional and bending stresses on mild steel. At the time, multiaxial fatigue was still in its infancy and the term itself had not yet been coined. A significant contribution was made by Mason and co-workers in the early 1920s [Mason, 1923]. Their work, published in 1923, is considered the pioneer in detailed elastic-plastic analysis in the high cycle fatigue regime. They use a bilinear representation for the cyclic stress-strain curve in the case of round bars under alternating torsion or bending [Garud, 1981*b*]. In addition, Mason

& Delaney [1921] published the first report on out-of-phase combined bending and torsion.

A more systematic multiaxial fatigue test programme was conducted in the 1930s by Gough & Pollard [1935], who designed and built high speed testing machines to investigate the combined effects of bending and torsional stresses (with and without mean stresses) on fatigue life. This set of experiments was used as a benchmark for the early multiaxial fatigue criteria, such as the empirical proposition of Gough [1949] (for ductile steels and cast-irons) and the first stress-based multiaxial criteria. Yet another extensive investigation of fatigue strength under combined bending and torsion was published by Nishihara & Kawamoto [1941, 1944, 1945]. Their experimental data has been widely used for benchmarking.

Advances in material testing equipment and techniques during the past 40 years have enabled the development of more realistic multiaxial fatigue tests by applying loads representative of service life, at different temperatures, test frequencies and load phase difference. Among the most used techniques, cruciform specimens and thin-walled tubular specimens have been broadly used for fatigue testing under biaxial stress states [Bonnand et al., 2011]. However, tension-torsion specimens pose limitations for probing the entire principal stress plane, σ_1 vs σ_2, since only 2 of the 4 quadrants can be investigated. Nevertheless, using internally pressurised tubular specimens, it is possible to access more of the principal stress plane.

Figure 2.6 illustrates the regions of the principal stress plane, σ_1 vs σ_2, that can be probed depending on the test configuration. The combination of cruciform specimens and axial-torsional specimens, internally pressurised, allows the investigation of almost the entire principal stress plane. However, for cruciform specimens the assessment of the biaxial compression region is challenging due to potential specimen buckling limitations. In the literature, examples of fatigue life investigation using tubular specimens are available in Andrews & Ellison [1973]; Found et al. [1985]; Kalluri & Bonacuse [1993].

Cruciform specimens and biaxial test rigs allow the investigation of a broad range of biaxiality. However, specimens are expensive, and testing is complex [Makinde et al., 1992; Boehler et al., 1994; Hannon & Tiernan, 2008].

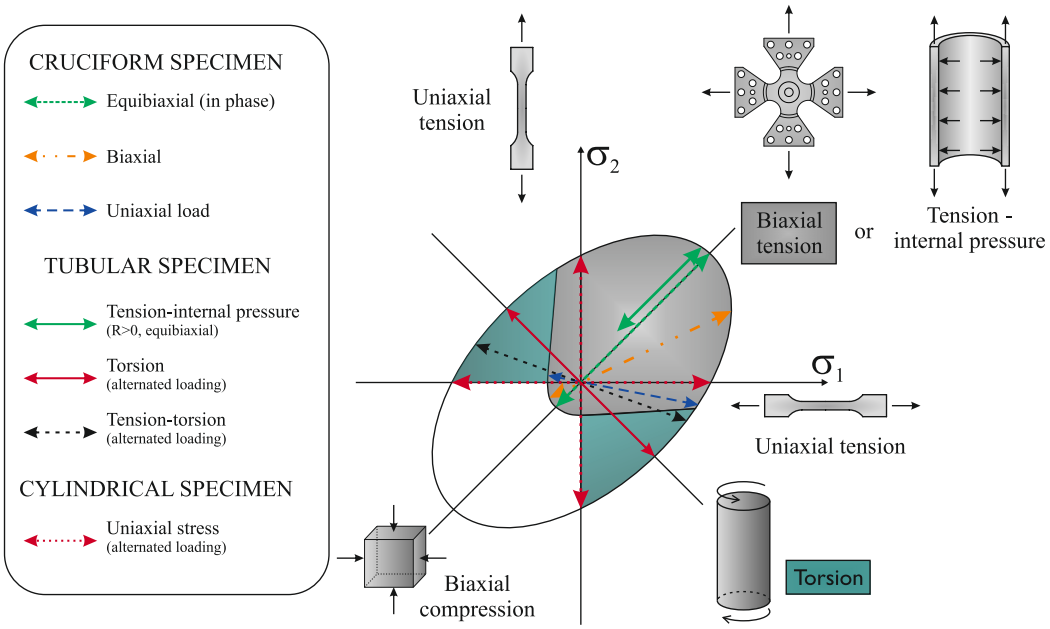


Figure 2.6 – Possible stress domain and corresponding experiments. Adapted from Bonnand et al. [2011].

2.3 Non-proportional loading

Non-proportional loading is defined as any time varying stress/strain path that changes the orientation of the principal stress/strain axes with respect to the axes of the component [Socie & Marquis, 1999]. Consequently, dislocations move in different directions, interact with each other and generate an additional cyclic hardening, named non-proportional hardening [Kanazawa et al., 1979; Fatemi & Shamsaei, 2011; Bees et al., 2014]. For low cycle fatigue regime, a direct effect of this is a noticeable reduction in fatigue life, especially important for engineering components classified as critical, such as compressor and turbine discs in aero-engine whose failure may be hazardous to the safety of the aircraft. However, for high cycle fatigue regime, the additional hardening can be beneficial to the material, leading to longer lives.

Non-proportional loading causes some unique effects and changes the deformation behaviour of the material. Doong et al. [1990] listed a few of them, including: increased cyclic hardening, partial recovery of hardening after loading is changed from non-proportional to proportional, and abrupt increase of hardening upon the sudden change of loading direction (cross-hardening effect). According to Doong et al. deformation features such as partial recovery of non-proportional hardening and cross-hardening behaviour of metals are either ignored or poorly modelled. In addition, many of the models that include the effect have complex mathematical formulations and require a large number of material constants, which limit their application in routine engineering analysis. The inability of models to effectively model the non-proportional hardening behaviour appears to result from the lack of consideration of material anisotropy that occurs in many materials after plastic deformation.

It is widely reported in the literature that many metallic materials exhibit additional strain hardening when non-proportionally loaded [Jayaraman & Ditmars, 1989; Doong et al., 1990; Bettge et al., 1995; Calloch & Marquis, 1997; Kang et al., 2005; Wang et al., 2008]. Pattison [2012] carried out strain- and stress-controlled tests with Waspaloy and found that on average this material exhibits an additional hardening of 24% as a result of a variety of non-proportional loadings paths at room temperature. Pattison also points out that this additional hardening potentially becomes more significant as the plastic strain is increased. Bees et al. [2014] and Bees [2016] obtained comparable results with RR1000, where for load paths at 90° out-of-phase, the most critical loading condition, an additional hardening of over 20% was observed. 90° out-of-phase loading paths promote continuous rotation of the maximum shear stress plane in all directions generating severe interaction of slip systems [Shamsaei, 2010].

2.4 Multiaxial fatigue modelling

Fatigue lives are commonly divided into different regimes based on the number of cycles to failure and the level of plasticity involved. Cyclic loading conditions where plasticity can be observed macroscopically and fatigue lives are up to 10^5 cycles are considered to be in the Low Cycle Fatigue (LCF) regime. In contrast, in the High Cycle Fatigue (HCF) regime, plasticity takes place only at the mesoscopic level and the bulk behaviour of the material is elastic [Mamiya et al., 2009]. For this second regime, fatigue lives commonly range between 10^5 and 10^7 cycles. Fatigue lives in the excess of 10^8 cycles are considered part of the Very High Cycle Fatigue (VHCF) regime. This is a relatively new field of research, which gained momentum at end of the twentieth century and presents considerable differences to the other two fatigue regimes. For instance, under VHCF conditions plasticity is retrained to the microscale and cracks usually initiate sub-surface, associated with interior defects such as inclusions, pits, and pores [Wang et al., 2002; Doquet et al., 2019].

The fatigue phenomenon is usually broken down into three different phases: crack nucleation (or initiation), microstructural sensitive short crack growth and long crack growth. Fatigue cracks initiate from the gradual accumulation of slip at the surface of the material, where there is less physical restraint. Although sub-surface initiation can occur due to the presence of significant defects such as brittle inclusions within the material [Suresh, 1998; Wang et al., 2002; Pattison, 2012; Doquet et al., 2019]. The repetition of cyclic loads induces the creation of persistent slip bands (PSB) and the formation of extrusion-intrusion type features orientated on the grain crystallographic planes. The accumulation of irreversible cyclic plastic strain within the PSB structures leads to the initiation of microcracks of dimensions comparable to or smaller than the characteristic microstructural size scale, i.e comparable to material grain size and interparticle spacing [Suresh, 1998; Socie & Marquis, 1999; Agbessi et al., 2016]. The crack growth process continues with an incremental extension on each loading cycle,

related to the formation of striations seen on typical fatigue fracture surfaces. As short cracks lengthen to long cracks, they become less sensitive to microstructural variations and their growth rate decreases. The resulting dominant macrocrack then propagates in a stable manner until the ultimate fatigue fracture.

Each of these phases are treated and modelled differently. Long cracks are usually modelled according to linear elastic fracture mechanics (LEFM) and the power-law proposed by Paris & Erdogan [1963]. Short cracks, however, cannot be analysed by LEFM as the size of the plastic zone at the crack tip is large with respect to the length of the crack. Also, overall applied stress levels may be high with respect to the yield strength of the material [McEvily et al., 1991; Miller, 1991]. Therefore, short cracks require elastic-plastic analysis to quantify their behaviour [Miller, 1982]. The portion of fatigue life spent in each of the three phases presented above depend directly on the stress/strain levels and related fatigue regime. In the HCF regime, most of the fatigue live is spent in the crack initiation phase, usually in the excess of 90% of the total life to failure [Suresh, 1998; Agbessi et al., 2016]. For higher stress levels, under the LCF regime, crack propagation tends to dominate the fatigue life of the material. However, some materials are initiation-dominated irrespective of the fatigue regime, such as certain Nickel-based superalloys [Manonukul & Dunne, 2004].

There exist numerous standards and preferred methods for fatigue testing and specimen geometries. For instance, tension-torsion tests with thin-walled tubular specimens are commonly used to investigate multiaxiality effects. However, although numerous different approaches have been proposed for modelling, there is no universal consensus on the most efficient criterion for predicting multiaxial fatigue failure. Most of the criteria proposed are limited to certain materials and/or specific loading conditions. This section reviews theories grouped as stress-, strain- and energy-based criteria. These groups are further divided into sub-groups. For stress- and strain-based theories, the most well-known empirical, extended yield criteria, invariant based, integral approaches and critical plane approaches are highlighted. Finally, for the third group, theories based

on elastic strain energy density, on plastic strain energy density and on the combination of both are discussed.

The parameters reviewed in the following sections were proposed taking into account a particular fatigue regime. For instance, stress-based criteria are better suited to HCF analysis, as the material deforms primarily elastically under such conditions. On the other hand, stresses associated with LCF conditions are high enough to cause appreciable plastic deformation. Therefore, for LCF, fatigue life is better characterised by strain-based parameters. Lastly, energy-based criteria were proposed to bridge the gap between stress- and strain-based approaches and can be used for both HCF and LCF regimes, depending on the energy measure adopted.

2.4.1 Stress-based criteria

The very first propositions on multiaxial fatigue were basically empirical criteria proposed on the attempt of correlating fatigue data obtained with the initial multiaxial fatigue tests, mostly combined torsion and bending tests. Haigh [1923] extended his theory of elastic limit for ductile metals to combined alternating stresses. His formulation takes into account the elastic shear strain energy density and the hydrostatic stress effect, modified by a material constant, to distinguish between tensile and compressive stresses. Based on the extensive set of experiments of Gough & Pollard [1935], Gough [1949] developed two empirical relations that could be applied to the design of shafts under mixed torsion and bending loading. The first relation describes an ellipse quadrant for ductile materials, and the second an ellipse arc for brittle cast irons. Guest [1937, 1940] proposed a single empirical relation for in-phase fully reversed combined stressing, which could derive both of Gough's relations and sufficiently describe the experimental data of Gough & Pollard [1935]. Nishihara & Kawamoto [1941, 1944, 1945] conducted an investigation of fatigue strengths under combined torsion and bending and proposed an empirical relation for in-phase loading that could also be used for out-of-phase loading cases.

All the presented empirical criteria were devised with the objective of fitting a particular experimental data set. Hence, they have limited application for materials and stress states different than those initially considered. Wang [2004] concluded that Gough's formulation presents good correlation for proportional loading. However, the model does not fit in with the experimental data under non-proportional loading from the publications of Papadopoulos [1997] and Carpinteri & Spagnoli [2001]. Nishihara & Kawamoto [1945] presented a good collapse of high-cycle fatigue experimental data for different materials (hard steel, mild steel, cast iron and duralumin) with different phase angles.

Initially, the multiaxial fatigue problem was addressed using yield theories, where a general equivalent stress could be used to quantify fatigue damage. While many yield criteria have been suggested, the three most famous are the maximum normal stress theory, the maximum shear stress theory [Tresca, 1868] and the octahedral shear stress theory (distortion energy – von Mises [1913]). The drawback of these straightforward criteria is that they are not suitable for out-of-phase or non-proportional loading conditions as these formulations have a fixed tension-torsion relation [Bannantine et al., 1990; Socie & Marquis, 1999; Fatemi & Shamsaei, 2011]. Figure 2.7 illustrates a comparison between the effect of various ratios of bending and shear stress according to these three theories and a set of test data from Gough & Pollard [1935]. The plot shows that better correlation is obtained with the octahedral shear stress than with the maximum shear stress or the maximum principal stress, when comparing tension and torsion data. Most of the known yield criteria when extended to fatigue predict a constant ratio between the fatigue strength in bending and the fatigue strength in torsion, b/t. However, test results obtained by Gough & Pollard [1935] showed that the ratio b/t is strongly material dependent, and thus the application of yield criteria to multiaxial fatigue is limited.

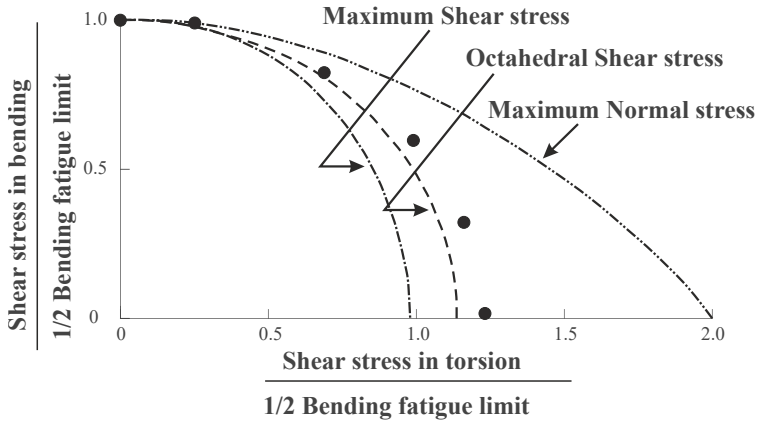


Figure 2.7 – Correlation of bearable stress amplitude for a given number of cycles in HCF regime under bending and torsion. Adapted from Socie & Marquis [1999].

In the group of Stress Equivalent/Stress Invariant approaches, criteria are formulated taking into account the invariants of the stress tensor and/or invariants of the deviatoric stress tensor. Generally, these formulations directly relate the second invariant of the deviatoric stress tensor and the first invariant of the stress tensor. Sines [1955, 1959] after a thorough analysis of a large set of experiments, with numerous materials, concluded that for high cycle fatigue regime static shear stress has no effect on either fatigue strength in torsion or fatigue strength in bending. However, for low cycle fatigue regime, a static shear stress does influence fatigue life. These considerations are valid as long material yielding does not occur, i.e. $\tau_a + \tau_{mean} < \tau_{yield}$. In addition, Sines concluded that mean hydrostatic stress affects fatigue life. In most cases, a tensile mean normal stress reduces fatigue life, whereas a compressive mean normal stress increases life. Based on these conclusions, Sines proposed that the alternating shear stress should be used as the damage parameter. Hence, his formulation is based on the octahedral shear stress (which takes into account the effect of slippage in material planes) and the hydrostatic stress (which represents the mean normal stress effect).

Similar to Sines' formulation, the stress based criterion proposed by Crossland [1956] also considers the amplitude of the second invariant of the deviatoric stress tensor, which corresponds to the amplitude of von Mises equivalent stress. But in contrast, the mean stress effect is introduced in Crossland's formulation through the

maximum value of the first invariant of Cauchy's stress tensor, i.e. the maximum hydrostatic stress. More recently invariant-based criteria for high cycle fatigue have been proposed by associating the normal stress measure with new methodologies to calculate the shear stress amplitude. For instance, Gonçalves et al. [2005] proposed a criterion that considers the shear stress amplitude, calculated with the minimum circumscribing ellipsoid method, and the maximum principal stress of the stress history (a contrasting feature as most models in this class consider the hydrostatic stress). Cristofori & Tovo [2009] followed the same trend and introduced a stress invariant criterion based on the association of a new formulation for the equivalent amplitude of the deviatoric component and the hydrostatic stress.

The third class of stress-based methods is based on the search for critical planes (one or more), where a particular damage parameter reaches its maximum magnitude. This methodology have gained great attention over the past 40 years as it mathematically describes the physical phenomenon and is capable of predicting damage and also crack orientation (for ductile materials cracks typically nucleate along slip planes, where the maximum shear stress occurs [Brown & Miller, 1973; Socie & Marquis, 1999]). In addition, they account for the hydrostatic effect through the normal stress or strain term.

Findley [1958, 1959] took Gough & Pollard [1935] set of experiments into account and proposed one of the first multiaxial fatigue criteria based on the critical plane approach. According to his formulation, failure occurs on planes where the sum of shear stress amplitude (parameter governing crack progression) and the maximum normal stress modified by a material parameter is maximum. Matake [1977] proposed a similar criterion considering that failure occurs on the planes of maximum shear stress amplitude that presents the maximum normal stress. Papadopoulos [1997] concluded after a comparative study that Matake's formulation correctly predicts the torsional and normal mean stress effects, an improvement when compared with Findley's criterion.

McDiarmid made great contribution to multiaxial fatigue research with substantial amount of experimental and analytical work. His first proposition was rather complicated [McDiarmid, 1991], with critical planes defined by maximum shear stress range. McDiarmid later reformulated his initial proposition by considering the reverse shear fatigue strength for case A and case B crack growth. As introduced by Brown & Miller [1973], type A cracks propagate along the surface and type B cracks propagate away from the surface. According to Karolczuk & Macha [2005], McDiarmid's proposition correlated well experimental data for proportional bending with torsion. Furthermore, the criterion also performed well for non-proportional loading conditions with zero and non-zero mean stresses. However, the criterion was inefficient for the ratio of $\tau_a/\sigma_a = 0.5$ and phase difference of 90°, when any plane experiences a maximum shear stress range.

Integral approaches form the last class of stress-based criteria; in this class an effective shear stress is obtained by averaging the resolved shear stress acting on all cutting planes of a representative volume element. In comparison with the critical plane approach, the integral approach defines fatigue damage as the integral value of the shear stresses acting on all planes rather than the amplitude of the shear stress acting on a single critical plane. Important propositions were made by Socie [1987], Fatemi & Kurath [1988], Papadopoulos [1995], and more recently by Morel & Huyen [2008].

Papadopoulos [1997] proposed his formulation based on mesoscopic scale approach (scale of the metal grains of a metallic aggregate). As localised plastic strain developing in some crystals are the main cause of fatigue nucleation, Papadopoulos' approach evaluates the crystal plastic strain range by linking it to the usual macroscopic quantities. Thus, the criterion is based on an average measure of the plastic strain accumulated in all the flowing crystals within an elementary volume. Equivalently this criterion is based on the integration of the resolved shear stress over all possible directions in the current examined plane [Papuga, 2011]. In his paper, Papadopoulos [1997] recommends the use of his criterion for ductile metals. Recently Papuga [2011] assessed this criterion and

concluded that for brittle materials Papadopoulos' formulation give non-conservative predictions, even for simple uniaxial cases with the presence of mean stress.

2.4.2 Strain-based criteria

Strain based criteria are widely used for low cycle fatigue, where mesoscopic plasticity plays an important role. Due to the cyclic plasticity involved in this life regime, mean and amplitude stresses are cycle dependent and thus cyclic stress-strain behaviour is also of interest. In situations where multiaxial stress (strain) fields exist, a correlating parameter or fatigue theory is needed to fit the multiaxial fatigue data to the uniaxial case. The most popular of these strain-based theories are strain versions of the classical failure theories aforementioned. The strain based static yield criteria mirror the stress-based yield criteria presented in the previous section.

Many researchers have shown the validity of the octahedral shear strain theory for a wide variety of materials and stress states but mostly for in-phase tests. Recently Shamsaei et al. [2011]; Shamsaei, Gladskyi, Panasovskyi, Shukaev & Fatemi [2010] investigated the use of this formulation and concluded that the criterion can correlate axial, torsional, and in-phase constant amplitude data, but cannot correlate out-of-phase as well as variable amplitude strain conditions. As noted with the stress based static yield theories, strain-based theories always predict a constant ratio of axial fatigue ductility/shear fatigue ductility.

Critical plane approaches have also been extended to consider strain quantities as the controlling parameter. Brown & Miller [1973] proposed a theory based on a physical interpretation of mechanisms of fatigue crack growth. According to them, failure under multiaxial fatigue is governed by the maximum shear stress range. In addition, the tensile normal strain acting on the plane of maximum shear strain benefits propagation (opening of crack tip). Their theory was adopted as the formulation basis for numerous critical plane theories that followed next. For instance, the widely used parameter

proposed by Fatemi & Socie [1988] is also based on the theory proposed by Brown & Miller, considering that tensile normal stress in the maximum shear stress plane accelerates fatigue crack growth by separating the crack surfaces and consequently reducing frictional forces. The mathematical details of these model are presented in Chapter 4.

2.4.3 Energy-based criteria

Energy based criteria are generally classified into three different groups, depending on the kind of strain energy density per cycle assumed as the damage parameter. For high-cycle fatigue applications, elastic strain energy is usually assumed as the damage parameter. In contrast, for low cycle fatigue regimes, plastic strain energy is adopted as the parameter controlling the damage. Lastly, a combination of plastic and elastic strain energies is used for improved predictions over a wider range of fatigue lives, i.e. for both high and low cycle fatigue regimes. Due to the limitations of space just the most widely used energy-based criteria are presented in this chapter. For a complete review of them please see Macha & Sonsino [1999].

Smith, Watson & Topper [1970] developed an energy-based damage parameter, SWT, for predicting fatigue life under uniaxial tension-compression conditions. This parameter was modified for proportional and non-proportional multiaxial loading conditions of materials that fail predominantly by crack growth on planes of maximum tensile strain or stress, according to crack Mode I. Socie [1987] modified the SWT, transforming it into a critical plane approaches, considering only stresses and strains occurring on a particular plane. Lopez-Crespo et al. [2015] conducted an investigation of the fatigue behaviour of tubular specimens made of St52-3N steel under proportional and non-proportional biaxial loading conditions. They assessed Wang-Brown, Fatemi-Socie and Smith-Watson-Topper parameters in terms of crack orientation and fatigue life predictions. Under proportional loading, better crack orientation prediction was obtained with Smith-Watson-Topper criterion, followed by Wang-Brown and Fatemi-

Socie. However, for non-proportional conditions, the Fatemi-Socie parameter gave the best predictions. Finally, regarding fatigue life predictions, Fatemi-Socie formulation performed the best under both proportional and non-proportional loadings, followed by Wang-Brown and Smith-Watson-Topper parameters.

Garud [1981*a*] proposed a criterion where plastic strain energy (energy dissipated) is assumed as the damage parameter controlling the fatigue crack initiation life. This theory is mathematically expressed as the plastic work for a cycle, i.e. the sum of energies from all stress state components in a cycle. Garud simplified his initial formulation considering a plane-stress state and applied it to in-phase and non-proportional out-of-phase tension torsion test data for a 1% Cr-Mo-V steel. As an example of a parameter that combines the elastic and plastic strain energies, Xia [1993] and Xia et al. [1996] proposed a criterion based on the sum of the two quantities. As elastic strain energy alone cannot influence fatigue damage accumulation in the low cycle fatigue regime and considering that plastic strain energy is minimal in high cycle fatigue. The elastic strain energy in the interval of positive stresses in a cycle provides a way to introduce the mean stress effect into the criterion.

2.5 Micromechanics approach

A large body of research has been focused on the role of higher length-scale microstructural features, such as grains and inclusions, on deformation and fatigue behaviour of Nickel-based superalloys [Kumar et al., 2006]. Evidences suggest that grain and precipitate size play an important role on the deformation and strength behaviour of Nickel-based superalloys, leading to homogeneous or inhomogeneous deformation depending on the combination of grain and precipitate size [Antolovich & Jayaraman, 1983; Lerch et al., 1984]. As fatigue cracks tend to initiate within localised slip bands, grain and slip band size affects cyclic behaviour, influencing initiation life and crack propagation. In addition, precipitate morphology also affects fatigue life by assisting

or hindering crack propagation, acting as obstacles to deflect crack, reducing crack propagation rate and consequently leading to longer fatigue life [Mughrabi et al., 1997; Ott et al., 1999].

The formulations discussed in the literature review presents limitations when it comes to represent the micro-mechanical aspects of fatigue crack formation. Hence, the third key component of this research thesis focusses on micromechanical based methods that involve explicit modelling of elastic–plastic behaviour of individual grains in polycrystalline Nickel-based superalloys under uniaxial and multiaxial cyclic loading conditions, with emphasis on loading amplitudes near the macroscopic yield point. In many respects, the current understanding of the early stages of fatigue crack formation in the grain/phase scale is still in its infancy [McDowell & Dunne, 2010]. Despite substantial advances in atomistic modelling of the inelastic behaviour of metallic materials, there is a substantial gap between the length and time scales of atomistic modelling and those scales necessary to quantify the role of microstructure in formation of fatigue cracks. In this sense, fatigue is one of the most challenging problems, since the loading is non-monotonic, and the number of cycles required is often in hundreds of thousands. Modelling and simulation specific to dislocation structures in fatigue such as cells or persistent slip bands in single crystals has provided progress in addressing cyclic deformation aspects [Polák et al., 2003; Polák, 2007; Mughrabi, 2009; McDowell & Dunne, 2010]. Quantitative relationship between such dislocation structures and crack nucleation is still in its early developments.

Crystal-plasticity modelling has been shown a powerful tool to link dislocation substructure under cyclic loading to engineering application requiring prediction of fatigue life of components based on crack initiation (macro-crack, at which the microstructure plays a less pronounced role in affecting variability of subsequent crack growth). However, the implementation of crystal-plasticity models requires the investigation of numerous micro-mechanics aspects, which might be a lengthy process. In addition, advanced microscopy techniques are required for identifying and characterizing relevant

statistical representations of microstructure attributes, which are fundamental for the proper calibration and validation of the model.

Successful applications of micromechanical modelling for fatigue crack nucleation prediction have been proposed recently. For instance, Dunne, Wilkinson & Allen [2007] successfully captured the full-field stress and strain distributions of an FCC Nickel-based superalloy under cyclic loading conditions, accurately spotting crack nucleation sites based on predicted bands of persistent slip. Korsunsky et al. [2007] investigated the effects of localised crystal slip within an idealised Nickel-based superalloy and compared numerous classical criteria for the prediction of thermo-mechanical fatigue crack initiation. They positively concluded that energy dissipation per cycle is a convenient parameter for accurately predicting fatigue lives. In parallel, McDowell [2007] extended Fatemi & Socie [1988]; Fatemi & Kurath [1988] damage parameter for microstructure-sensitive fatigue analysis of Nickel-based superalloys and obtained good correlation in both low cycle and high cycle regimes. Based on the argument that cracks form due to dislocation pile up and constrained plastic flow [Stroh, 1953, 1954], Wan et al. [2014] proposed a criterion for predicting crack nucleation based on stored energy density. Their criterion has recently being implemented by Chen [2018] for investigating fatigue lives of RR1000 under complex multiaxial load paths and good collapse of experimental data has been reported.

3 Experimental Work

The accuracy of multiaxial fatigue criteria for predicting fatigue life is directly dependent on the quality of their calibration and the assumption of a stabilised material cyclic behaviour – especially important for LCF as criteria variables are calculated over a single load cycle. Usually, these criteria are calibrated considering the fatigue response of a material characterised by the stress- and/or strain-life relationship, and the deformation behaviour as described by the cyclic stress-strain response. This chapter describes the experimental programme used to calibrate and benchmark the multiaxial fatigue criteria investigated in the following chapters. A combination of uniaxial and multiaxial load-controlled tests was carried out with two Nickel-based superalloys used for the manufacturing of aero-engine discs, namely Waspaloy and fine grain (FG) RR1000. The first section of this chapter focusses on Waspaloy and presents the biaxial and uniaxial fatigue test programmes conducted with this material. The second section reports tension-torsion tests carried out with FG RR1000 under numerous non-proportional load paths. With the exception of the initial biaxial fatigue tests with Waspaloy, which were previously conducted by Dr Robert Paynter, the entire experimental work, with both Waspaloy and RR1000, as well as the post-processing of experimental data were performed solely by the Thesis author as part of this doctorate research project.

3.1 Waspaloy

The first Nickel-based superalloy investigated was Waspaloy, a proprietary age -hardening polycrystalline superalloy developed in the 1950s. Waspaloy has since been widely used in aircraft engine components that require considerable strength and oxidation resistance at high operating temperatures [Xue, 2010]. Until the late 1990s, Waspaloy was still the best superalloy available for the majority of hot gas turbine applications due to its elevated creep resistance and high fatigue strength [Bloch & Soares, 2001].

The specimens used in the test programme were sourced from a fleet high-pressure turbine disc. Specimen blanks were removed from the bore area of the forging in the axial direction. Waspaloy for turbine discs is generally prepared by ingot metallurgy, which includes three melting steps followed by annealing and hot working to achieve the desired compositional homogeneity and grain size. This process is described in details in Benz [1999] and Reed [2006]. A metallographic sample was prepared for the determination of grain size. The sample was etched using a solution of Hydrochloric Acid (37%) and Hydrogen Peroxide 100 (>30%) and then analysed in an Alicona Infinite-Focus microscope (see Fig. 3.1). Grain measurement was performed according to the Heyn linear intercept procedure as presented in [ASTM E112-13, 2013] and as a result, an average grain diameter of $45\mu m$ was obtained.

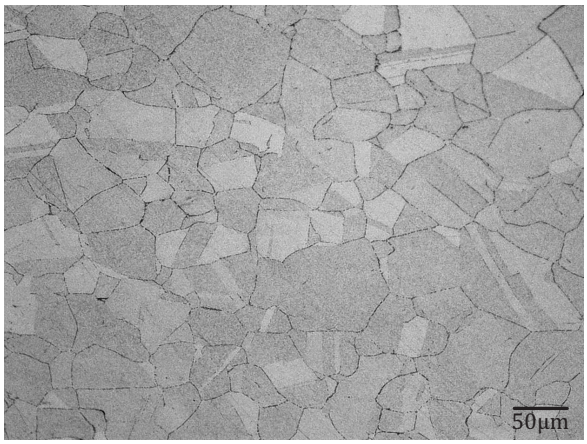


Figure 3.1 – Waspaloy grain morphology - 20x magnification.

In terms of its mechanical properties, the axial hardening curve for Waspaloy at room temperature was obtained from Pattison [2012], who used deformation-controlled tests with thin-walled tubular specimens. The material has a Poisson's ratio of $\nu = 0.284$ and Young's modulus of E=222 GPa. Figure 3.2 presents the axial monotonic and fully reversed ($R = -1$) cyclic stress-strain response of the material. The cyclic hardening curve was modelled using the Ramberg-Osgood power law for cyclic loading to fit the stabilised plastic strain and stress test data, as is defined by:

$$\frac{\Delta\varepsilon}{2} = \frac{\Delta\,\sigma}{2E} + \left(\frac{\Delta\sigma}{2K'}\right)^{\frac{1}{n'}} , \tag{3.1}$$

where K' and n' are the axial fatigue strength coefficient and the cyclic axial strain hardening exponent, respectively. These parameters can be obtained by fitting true stress versus plastic strain in a log-log scale [Mousa, 2011; Shamsaei, 2010]. In terms of true plastic strains and true stress, Eq. 3.1 can be rewritten as:

$$\sigma = K'(\varepsilon^p)^{n'} . \tag{3.2}$$

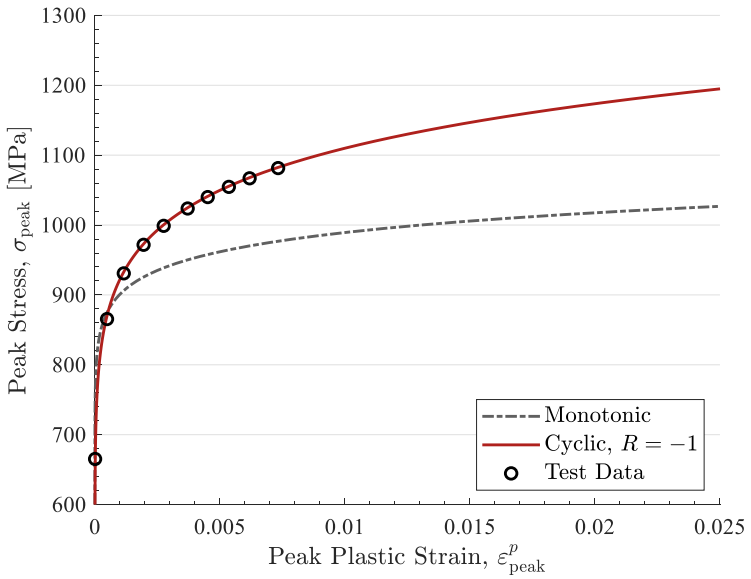


Figure 3.2 – Hardening curve for Waspaloy at room temperature, fully reversed cyclic ($R = -1$) vs monotonic response. Adapted from Pattison [2012].

3.1.1 Biaxial Fatigue tests

Biaxial fatigue tests were performed using a servo-hydraulic rig, designed and built in the University of Oxford. In total eleven cruciform specimens were used to investigate a wide range of biaxiality ratios, with an initial quasi-static cycle to produce limited plastic deformation, followed by fatigue cycling in the elastic regime until failure. All tests were load controlled and carried out at the same load ratio, $R = F_{min}/F_{max} = 0.05$, due to physical limitations of the testing machine. This means that in every test there was a mean stress applied to the material, which, according to Socie & Marquis [1999] and Brown & Miller [1973], directly impacts crack growth. A tensile mean stress reduces fatigue life as it opens the crack tip and facilitates its shearing process.

3.1.1.1 Biaxial test rig

Figure 3.3 presents the biaxial rig consisted of two independent frames carrying hydraulic actuators such that the perpendicular load vectors meet at the centre of the specimen. The horizontal load path (assumed here as the x-direction) has two actuators working in opposite direction, with capacity of 100 kN each. The vertical load path (y-direction) has a fixed clamp at the top and an actuator at the bottom capable of providing up to 350 kN. A set of springs connect both frames and allows vertical movement of the horizontal actuators according to the deformations of the specimen, so that the loads are almost perpendicular at all loads. The complexity of the tests and the size of the actuators and specimen mean that tests can only be carried out at relatively low frequency, 0.5Hz. Each actuator has its own dedicated PID controller and these were connected to each other with PC based software to allow fully synchronised loading and potentially complex load sequences, although only proportional in-phase loading was considered.

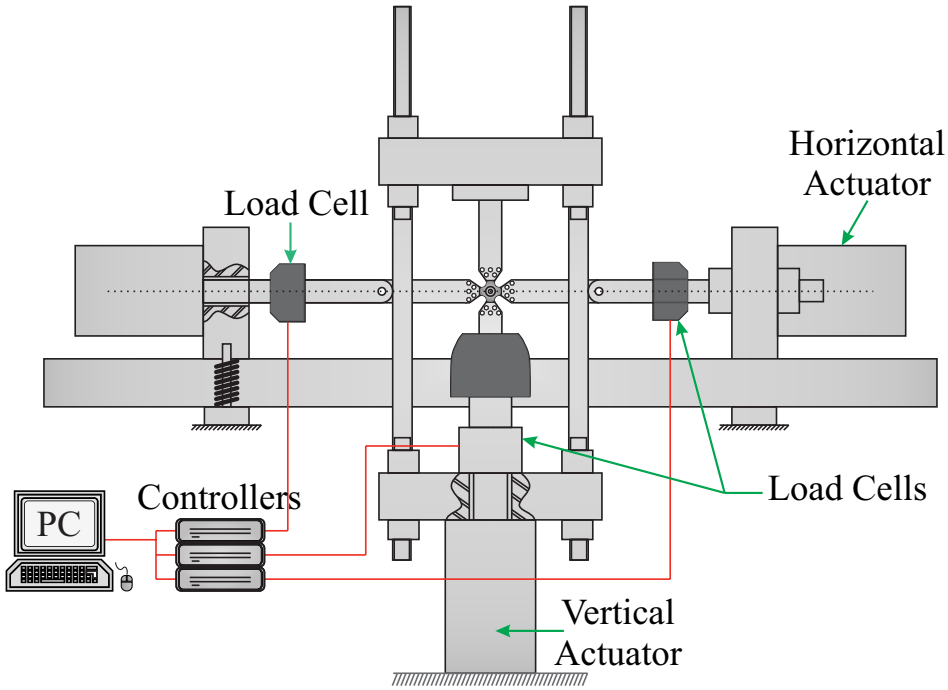


Figure 3.3 – Biaxial test rig.

Strain gauges were connected to the measurement system, and each channel balanced before the specimens were clamped into place. Hence, changes in loads occurring during the clamping process could be monitored. In addition, strain gauges on the arms of the specimen were used to monitor bending due to misalignment of the rig. If a moderate tension is applied to the horizontal axis, then the difference between strain gauges at the top and bottom of the specimen arms shows whether bending is present. The tests were terminated based on the presence of visible cracks. In this sense, the tests were carefully set up on tight displacement limits, if tripped the tests would automatically stop and an inspection of the specimen would be performed. If visible cracks were spotted, then the current fatigue life would be recorded and considered as final.

3.1.1.2 Cruciform specimens

Cruciform specimens were used with a reduced thickness gauge section at the centre. Its geometry is akin to a Maltese cross, with 190mm across. The arms are 28mm wide at the

narrow point, widening to 88mm to include five M12 mounting bolt holes and an 8mm alignment hole. The arms are 12mm thick at the bolting location; the central portion is 7mm thick, ultimately enclosing the 2mm thick, 15mm diameter gauge section. The centre portion (excluding the gauge section) was shot peened to increase the fatigue strength of the external edges between the arms and hence to inhibit failure away from the gauge section. In total 12 strain gauge rosettes were mounted on both front and back face of the gauge section and at the narrow point of the arms. The outputs from these were recorded, together with the applied loads, to determine specimen calibration. A schematic representation of the specimen and loads applied is shown in Fig. 3.4.

The arms of the specimen were clamped between two plain faced jaws, thus the force is transmitted primarily by friction. To reduce the chance of slip, the faces of the specimen were abraded with coarse silicon carbide paper and cleaned with solvents to remove any grease. The jaws were clamped with five bolts per arm; these were tightened to at least 60kN per bolt. The highest arm load was 175kN, so that a coefficient of friction of at least 0.3 is needed to prevent slip at the jaws. If slip does occur, then a portion of the load is carried by the bolts in 'bearing bolt' mode.

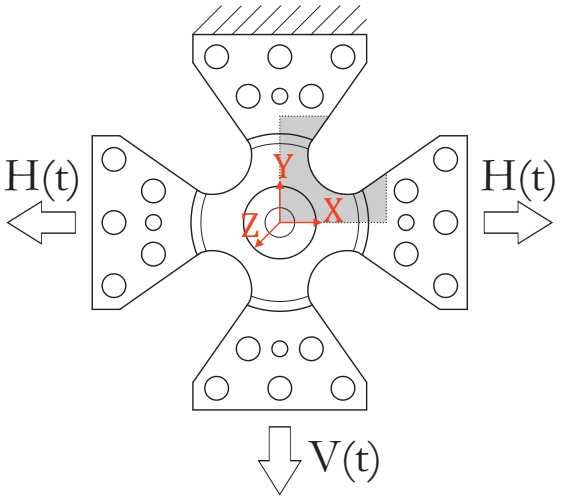


Figure 3.4 – Cruciform specimen, applied loads and definition of x–y–z coordinate system. Grey shaded area represents FE cut section.

3.1.1.3 Load combination

The load conditions were set to have the same maximum principal stress in each case, varying the other in-plane principal stress. As the gauge section is only 2mm thick and 15mm across, the assumption is made that the local behaviour at gauge section surface is equivalent to plane stress conditions, i.e. the out-of-plane stress is zero. The following combinations were investigated:

- Equal biaxial tension (EB): Equal load applied to each arm ($\sigma_1 = \sigma_2$);
- Pure shear (PS): Stresses on the two axes are equal and opposite ($\sigma_1 = -\sigma_2$);
- Single Actuator (Uniaxial Load – UL): Load applied on one axis only ($F_y = 0$, but $\sigma_2 \neq 0$) ;
- Uniaxial Stress (US): Both axes are used to create an uniaxial equivalent stress state at the gauge section ($F_y > 0$, but $\sigma_2 = 0$);
- Minimum von Mises (Mv): The combination of loads that gives the minimum von Mises equivalent stress (octahedral shear stress) at the gauge section, i.e. for a given σ_1, σ_2 is calculated to give the minimum von Mises equivalent stress under biaxial tension.

In order to parametrically compare the different load conditions, a measure of biaxiality can be used. Biaxiality of loading can be defined in a number of different ways based on load, stress or strain. This investigation adopts the definition based on strain proposed by Itoh et al. [1994], which considers the largest magnitude of strain ratio. Mathematically defined in Eq. 3.3:

$$\Phi_\varepsilon = \begin{cases} \dfrac{\varepsilon_2}{\varepsilon_1}, & \text{if } |\varepsilon_2| > |\varepsilon_3| \\ \dfrac{\varepsilon_3}{\varepsilon_1}, & \text{if } |\varepsilon_2| \leq |\varepsilon_3| \end{cases} . \tag{3.3}$$

The intention of the experimental programme is to investigate the effect of strain biaxiality, i.e. to keep one of the maximum principal strains fixed and adjust the other over a range. In Fig. 3.5, ε_x is kept constant and ε_y varies over $[-\varepsilon_x, \varepsilon_x]$. ε_z is simply obtained by strain relationships. The plot has in the abscissa the $\varepsilon_y/\varepsilon_x$ ratio and in ordinates each of the strain components ($\varepsilon_x, \varepsilon_y$ and ε_z – represented by the dotted and dashed curves) and the biaxiality ratio (Φ_ε – represented by the solid black curve). The figure illustrates a wide range of biaxiality ratio, from ν to 2ν, that cannot be achieved, as there is discontinuity at the point where the in-plane strain exceeds the magnitude of the through-plane strain. Finally, the red circles on the solid black curve represents the experimental tests performed.

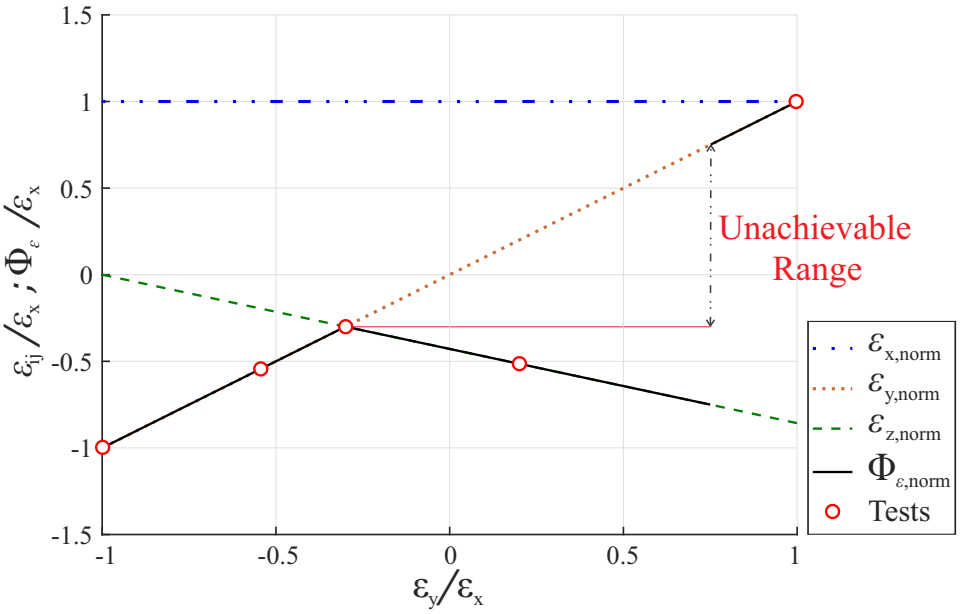


Figure 3.5 – Strains and Biaxiality Ratio, Φ_ε, as strain ratio $\frac{\varepsilon_y}{\varepsilon_x}$ varies.

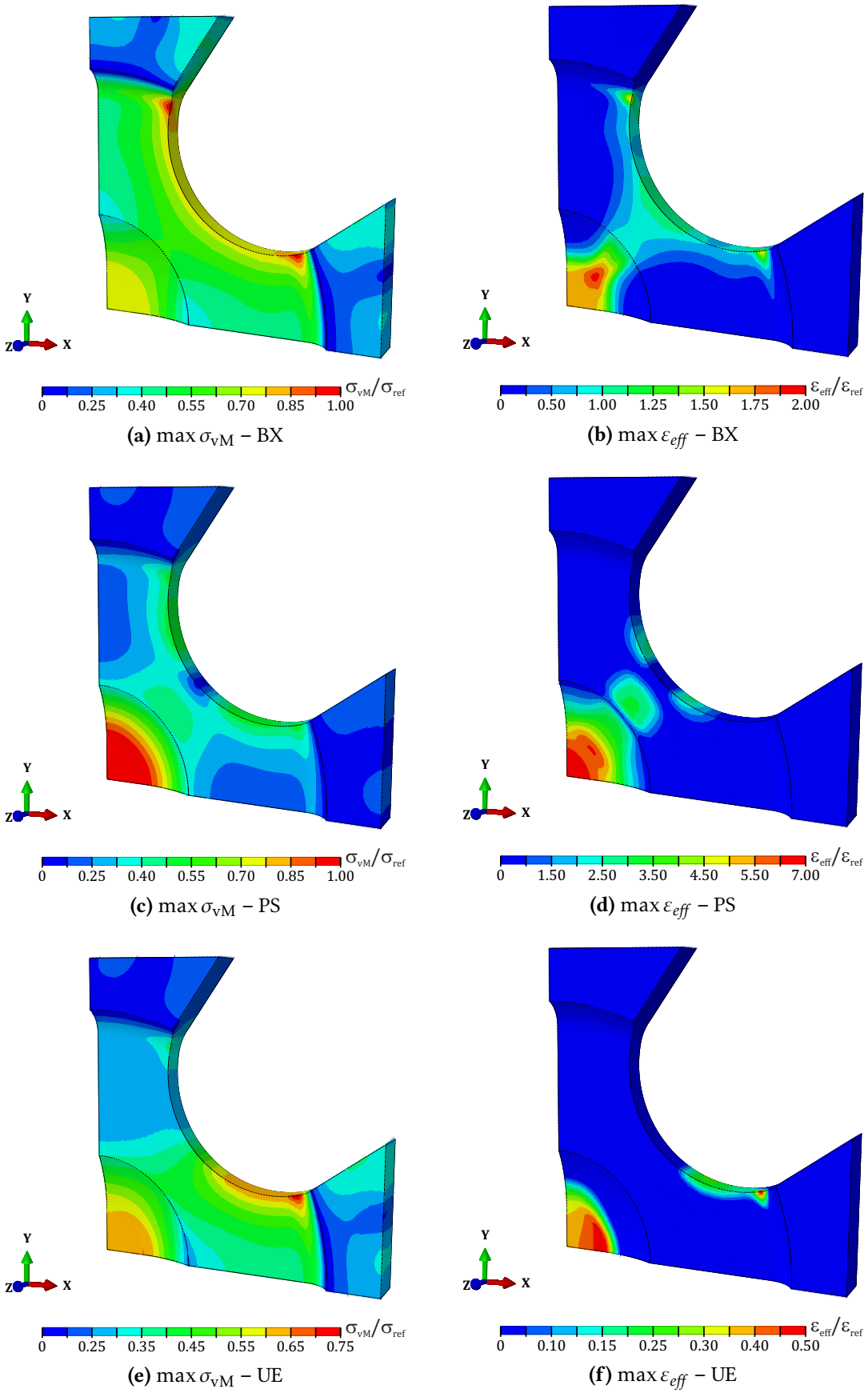
3.1.1.4 Finite element modelling

Finite element modelling was employed to analyse the specimen and to establish the relationship between load and stress or strain, not obvious for the cruciform specimen. Then, this was used to set the experimental conditions, estimating the loads required for each test. Actual strain gauge readings were used to confirm whether the required value

was achieved. Due to the symmetry of the problem only one eighth of the specimen was simulated with appropriate boundary conditions imposed to the symmetry planes. A structured mesh was created with 159,792 linear hexahedral elements, 180,700 nodes and reduced Gauss integration points. In order to more accurately describe the stress/strain field, a more refined mesh was applied to the region were failure was expected to occur. Thus, the gauge region presents elements of 0.125mm, amounting to 10,776 elements and 12,454 nodes.

Simulations of each load combination were performed in two steps, first as a quasi-static elastic analysis and then as a full cycle elasto-plastic analysis, considering the maximum von Mises equivalent stress and the maximum effective plastic strain respectively. The specimen cut used to illustrate the FE results are represented by the grey area in Fig. 3.4 (only the region of interest is displayed, i.e. the clamp region was cropped out). The plastic behaviour was modelled considering Waspaloy stabilised cyclic response presented in Fig 3.2. Although the available cyclic response is for $R = -1$ and not for the load ratio of $R = 0.05$ used in the test programme, it provides a good starting point for calculating the stresses seen at such a complicated specimen geometry.

Figures 3.6a and 3.6b present the elastic and plastic analysis of the biaxial loading case. This highlighted that yielding first occurs at the edge of the specimen, between the arms (Fig. 3.6a). However, as the next step demonstrates in Fig. 3.6b, this was not a practical issue because at full load greater plastic strain occurs within the gauge section, with the maximum effective plastic strain concentrated near the edge. Figures 3.6c and 3.6d show that during the elastic step of pure shear the maximum von Mises occurs at the edge of the gauge section, and for the plastic step the maximum plastic strain occurs at the exact centre of the specimen. Lastly the result for the uniaxial equivalent loading case shows that for the elastic step the maximum von Mises also occurs at the edge of the specimen, between the arms (Fig. 3.6e) , and during the plastic step the maximum plastic strain is located at the edge of the test zone, in the direction of the greater load (Fig. 3.6f).



(a) max σ_{vM} – BX **(b)** max ε_{eff} – BX

(c) max σ_{vM} – PS **(d)** max ε_{eff} – PS

(e) max σ_{vM} – UE **(f)** max ε_{eff} – UE

Figure 3.6 – FE Model: Elastic (max σ_{vM}) and Elasto-Plastic (max ε_{eff}) analysis.

3.1.1.5 Experimental results

Initial tests compared different biaxialities at the same $\sigma_{\mathrm{x,peak}}$, but different $\sigma_{\mathrm{y,peak}}$ for each test. Further tests for pure shear and uniaxial stress cases were run at lower peak stresses. It was observed from strain-gauge readings that in most cases yielding occurred during the first cycle, but no "reversed yielding" took place when load was removed ($R = 0.05$), as predicted by the elasto-plastic FE analysis. Hence no further plasticity was detected on strain gauge readings for subsequent load cycles at the same load level, although the material was loaded to the (work hardened) elastic limit each time.

As mentioned previously, nominal stress and strain levels were used to set the experimental conditions (estimating the loads required for each test), and actual strain gauge readings were used to confirm whether the required values were achieved. An elastic relationship was established to correlate the loads applied by the actuators and the stresses seen at the gauge section. The data for this was obtained from both the FE modelling, above, and measurements during the elastic loading phase of testing. The normalised compliance response found for the rosette located at the centre of the gauge section is $c_p = 0.0117\mu\varepsilon/kN$ for the axis parallel to loading and $c_n = -0.0063\mu\varepsilon/kN$ for the normal direction (the ratio $r_\varepsilon = c_n/c_p = -0.538$). Hence, for any combination of loads the normalised nominal strains can be calculated by:

$$\varepsilon_{\mathrm{x}} = 0.0117L_{\mathrm{x}} - 0.0063L_{\mathrm{y}} \quad , \tag{3.4}$$

and

$$\varepsilon_{\mathrm{y}} = -0.0063L_{\mathrm{x}} + 0.0117L_{\mathrm{y}} \quad , \tag{3.5}$$

where L_H and L_V are the horizontal and vertical nominal loads, respectively.

Assuming a plane stress state at the gauge section, the nominal stress state at the

centre of the specimen can be calculated by:

$$\sigma_x = \frac{E}{1-\nu^2}\left(\varepsilon_x + \nu\varepsilon_y\right) \quad , \tag{3.6}$$

and

$$\sigma_y = \frac{E}{1-\nu^2}\left(\varepsilon_y + \nu\varepsilon_x\right) \quad , \tag{3.7}$$

Table 3.1 summarises the results obtained after testing of 11 specimens. Note that stress and strain levels presented in Table 3.1 are nominal, calculated using Eqs. 3.4–3.7. The map of peak stresses in the two principal directions (σ_1 vs σ_2) shown in Fig. 3.7 graphically represents the test cases shown in Tab. 3.1. It gives a diagrammatical summary of the load conditions, with life to failure ('000 cycles) shown below each case point. von Mises and elastic strain energy contours were plotted in Fig. 3.7 as guides to represent the initial elastic domain of Waspaloy. Table 3.2 presents the actual stress and strain ranges seen during the tests, i.e. it presents the average strain amplitude and average mean strain measured with strain gauge rosettes and the actual residual and peak stresses obtained with the elastic-plastic Finite Element analysis, considering the peak loads measured by the load cells of the biaxial rig. Critical residual and peak stresses for each test condition were obtained from the points of maximum von Mises equivalent stress in the gauge section. The actual strain and stress values, presented in Tab. 3.2 and illustrated in Fig. 3.8, were used as input for the fatigue life prediction analysis presented in Chapter 4.

Both Tables (3.1 and 3.2) present similar stress ranges. However, the results obtained with the elastic-plastic FE analysis show that there was a significant level of residual stresses for the single actuator (CX01 and CX04) and pure shear (CX05, CX10 and CX11) test cases. Therefore, for these test cases the actual peak stresses are considerably different than the nominal ones.

The first two specimens (CX01 and CX02) were tested to gain experience with the

test and establish the limits of the specimen and rig. Initially the first test was carried out under quasi-static single actuator and equi-biaxial conditions and the second trial specimen was used to check the symmetry of the rig. The specimen was mounted rotated 90° from its normal orientation and taken through an elastic cycle on each actuator axis, then rotated to its normal orientation and the elastic cycle repeated. It could be concluded that strains are symmetrical on the strain gauges, and slight mismatches in calibrations of the actuator load cells could be adjusted by reducing the gain for the vertical axis.

The second pure shear test (CX06) was considered a run-out (510,000 cycles) as subsequent cyclic loading progressed uneventfully. The uniaxial equivalent test with low stress (CX09) was adjusted to give a maximum principal strain equivalent to the equi-biaxial tests (CX02, CX03) for comparison of results at different levels of biaxiality. The maximum von Mises for this case was below the yield stress of the material and subsequent fatigue loading gave a life of 658,164 (not a run-out). Strain gauges often failed before the specimen failed. As the crack that causes eventual failure develops, the load transfers to different parts of the specimen and is manifested as a drop in strains for the surviving gauges - both mean and amplitude.

Table 3.1 – Test results based on nominal stress and strain values.

Exp. №	Load Case	Peak Load [kN]		Norm. Peak Strain		Norm. Peak Stress			Biaxiality Ratio			Cycles, $2N_f$
		Horizontal	Vertical	ε_x	ε_y	σ_x	σ_y	σ_{vM}	Load	Strain	Stress	
CX01	Uniaxial Load	127	0	1.489	-0.801	1.372	-0.412	1.618	0.00	-0.54	-0.30	87,765
CX02	Equi-Biaxial	170	170	0.921	0.921	1.286	1.286	1.286	1.00	1.00	1.00	65,426
CX03	Equi-Biaxial	170	170	0.921	0.921	1.286	1.286	1.286	1.00	1.00	1.00	57,884
CX04	Single Actuator	117	0	1.372	-0.738	1.264	-0.379	1.490	0.00	-0.54	-0.30	97,560
CX05	Pure Shear	90	-90	1.623	-1.623	1.264	-1.264	2.189	-1.00	-1.00	-1.00	25,789
CX06	Pure Shear	51	-51	0.920	-0.920	0.716	-0.716	1.241	-1.00	-1.00	-1.00	510,000[a]
CX07	Uniax Equiv	129	39	1.264	-0.359	1.264	0.000	1.264	0.30	-0.28	0.00	154,396
CX08	Min von Mises	148	103	1.084	0.273	1.264	0.632	1.095	0.70	0.25	0.50	107,004
CX09	Uniax Equiv	94	28	0.920	-0.261	0.920	0.000	0.920	0.30	-0.28	0.00	658,164
CX10	Pure Shear	66	-66	1.182	-1.182	0.920	-0.920	1.594	-1.00	-1.00	-1.00	236,935
CX11	Pure Shear	90	-90	1.623	-1.623	1.264	-1.264	2.189	-1.00	-1.00	-1.00	21,684

[a] Runout

Table 3.2 – Test results based on strain gauge readings and FE analysis.

Exp. №	Load Case	Peak Load [kN]		Mean Strain			Strain Amplitude			Residual Stress		Peak Stress		Cycles, $2N_f$
		Horizontal	Vertical	ε_x	ε_y	ε_{xy}	ε_x	ε_y	ε_{xy}	σ_x	σ_y	σ_x	σ_y	
CX01	Uniaxial Load	126.33	8.07	1.396	-0.469	0.359	0.690	-0.367	0.132	-0.19	0.07	1.12	-0.23	87,765
CX02	Equi-Biaxial	169.34	172.67	1.049	1.098	1.075	0.445	0.436	0.436	-0.04	-0.04	1.18	1.23	65,426
CX03	Equi-Biaxial	170.73	170.98	1.180	1.143	1.141	0.450	0.452	0.459	-0.04	-0.04	1.20	1.21	57,884
CX04	Single Actuator	118.20	1.15	1.154	-0.676	0.199	0.662	-0.358	0.145	-0.17	0.07	1.08	-0.28	97,560
CX05	Pure Shear	92.32	-90.40	1.209	-1.121	0.241	0.327	-0.326	0.072	-0.42	0.42	0.80	-0.80	25,789
CX06	Pure Shear	52.15	-51.22	0.638	-0.622	0.014	0.444	-0.440	0.014	-0.04	0.04	0.66	-0.66	510,000[a]
CX07	Uniax Equiv	130.30	38.70	0.852	-0.301	0.261	0.612	-0.178	0.198	-0.08	0.02	1.19	0.01	154,396
CX08	Min von Mises	150.25	103.22	0.645	0.134	0.343	0.525	0.127	0.313	0.00	0.00	1.29	0.57	107,004
CX09	Uniax Equiv	96.41	28.33	0.502	-0.145	0.121	0.452	-0.133	0.144	0.03	0.00	0.97	-0.01	658,164
CX10	Pure Shear	67.74	-65.88	1.093	-1.035	0.069	0.584	-0.574	0.017	-0.16	0.16	0.74	-0.73	236,935
CX11	Pure Shear	93.00	-90.40	1.581	-1.365	0.170	0.342	-0.327	0.018	-0.42	0.42	0.81	-0.80	21,684

[a] Runout

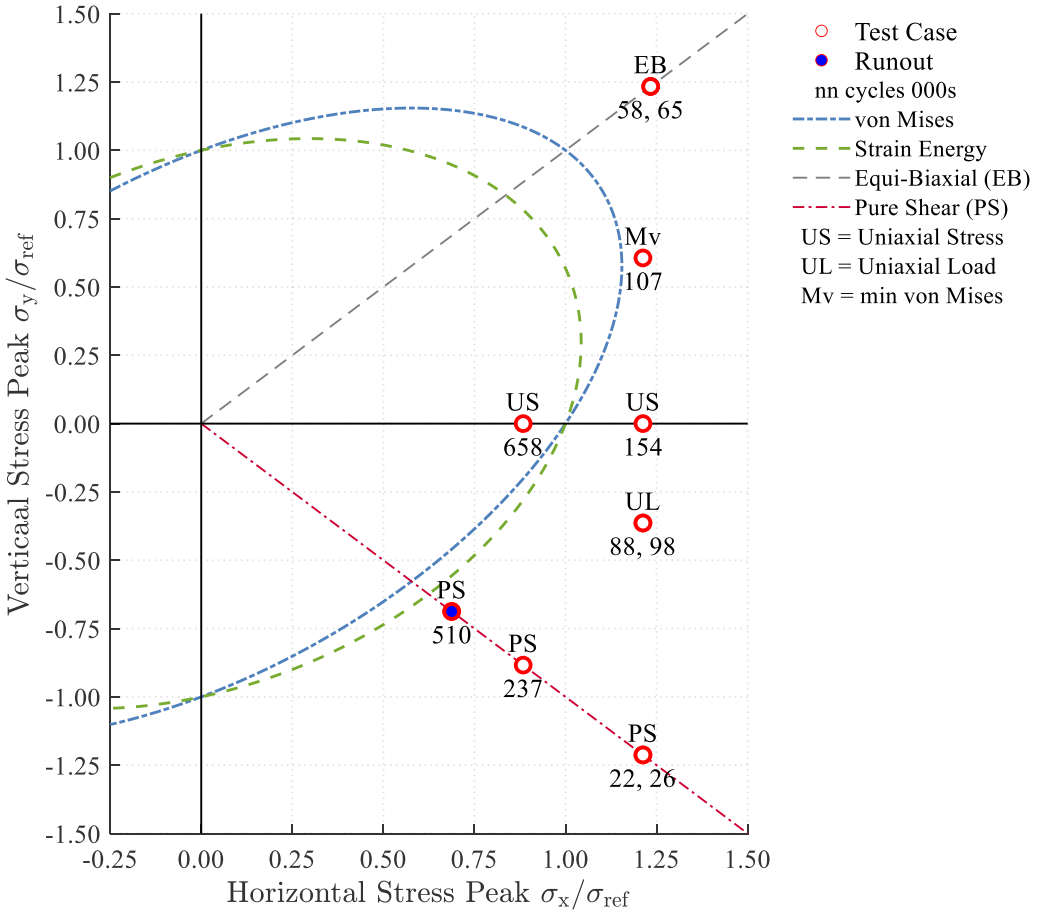


Figure 3.7 – Map of nominal peak stress combination considering $\sigma_3 = 0$. For cases with two test results, both values are given.

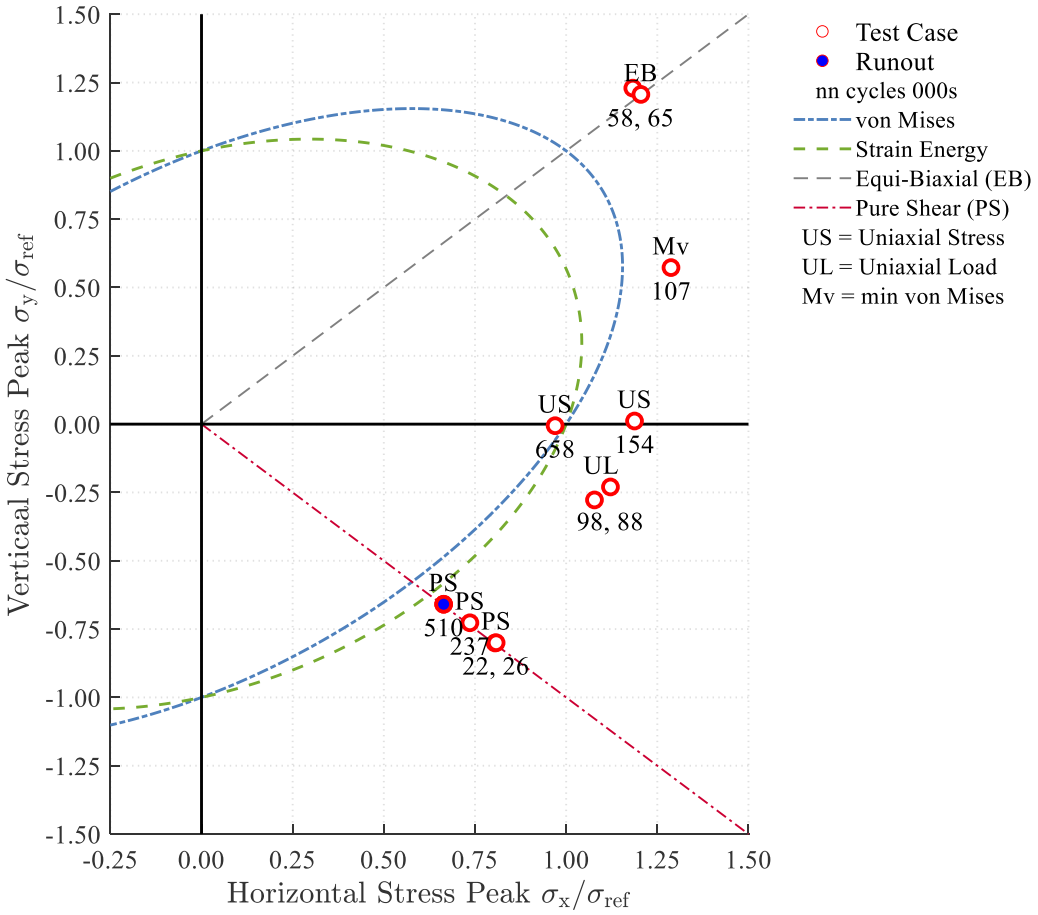
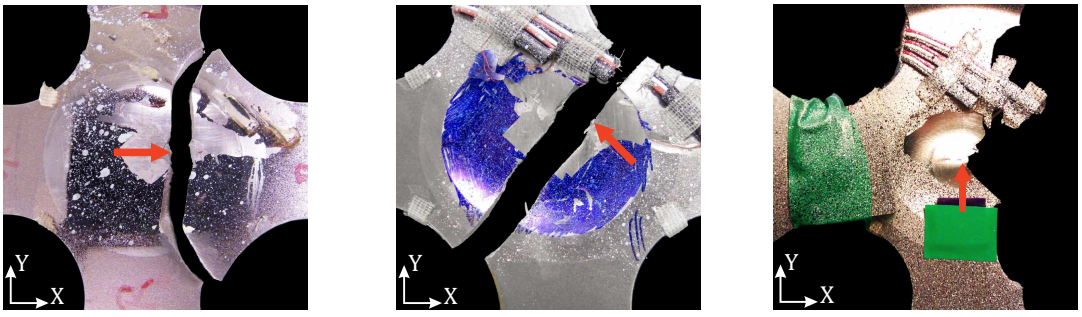


Figure 3.8 – Map of actual peak stress combination considering $\sigma_3 = 0$. For cases with two test results, both values are given.



(a) Uniaxial Load **(b)** Equi-biaxial Load **(c)** Pure Shear

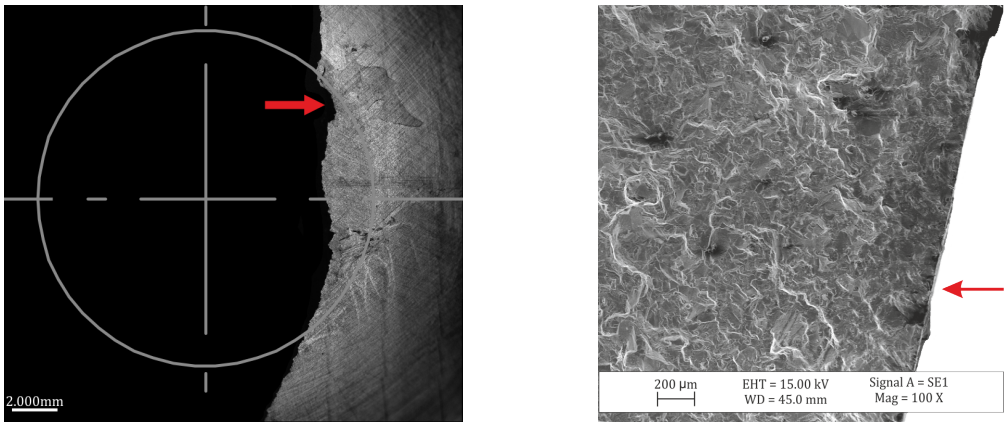
Figure 3.9 – Failure location for different loading conditions.

As the most heavily stressed point depends on biaxiality, cracks initiated in different regions depending on the test (always within the gauge section). In both single actuator and uniaxial equivalent tests crack initiated at the edge of the test region and as a final result one arm of the specimen pulled away from the remainder. For equi-biaxial loaded specimens the crack started at the stress concentration near the edge of the thin region and propagated diagonally along a 45° line, first towards the centre and then across the whole specimen. For pure shear conditions, cracks started at the centre of the gauge section. Therefore, results are coincident with the FE model, and cracks initiate where ε_{eff} is maximum, as illustrated in Fig. 3.9.

3.1.1.6 Fractography

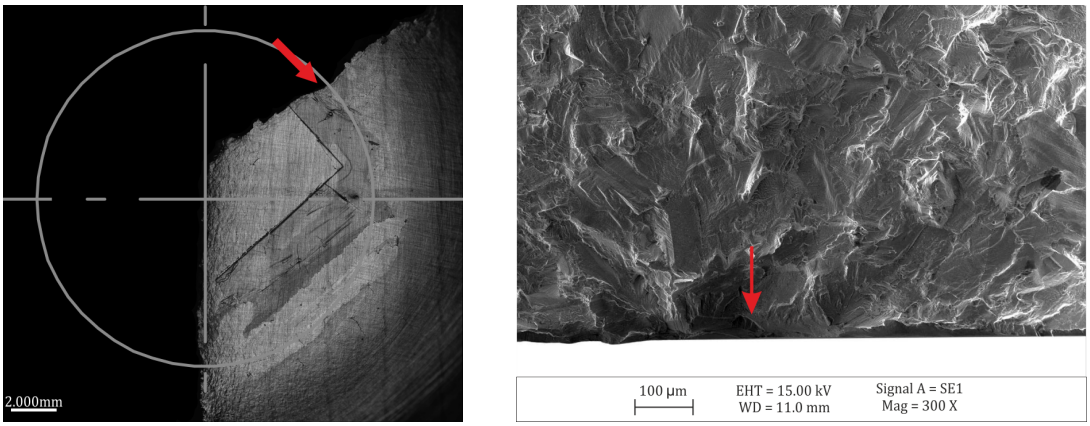
Fracture surface analysis of some of the broken specimens was conducted using an Alicona InfiniteFocus Microscope and a Carl Zeiss Evo LS15 Scanning Electron Microscope (SEM). The results obtained with the Uniaxial Load (CX04) specimen, Equi-biaxial (CX03) and Pure Shear (CX05) are illustrated in Figs. 3.10–3.12. The intention was to analyse the region where the cracks started in three steps. First a microscopy of the gauge section at 5x magnification was performed with the Alicona, Figs. 3.10a and 3.11a illustrate that for uniaxial load and equi-biaxial failure initiate at the edge of the gauge section, roughly at 45°. For the pure shear case, Fig. 3.12a shows that failure initiated next to the centre of the specimen.

After spotting the crack initiation site, the specimens were analysed at the SEM, Figs. 3.10b, 3.11b and 3.12b, as the second step of this investigation. Lastly, a profile of the fracture surface for each case specimen was obtained using the Alicona one last time (Fig. 3.13). It was concluded after this third step that the crack that had led the uniaxially loaded specimen to failure propagated at 45° from the initiation location. For the equi-biaxial and pure shear cases the propagation occurred at a shallower angle (almost at 90°).



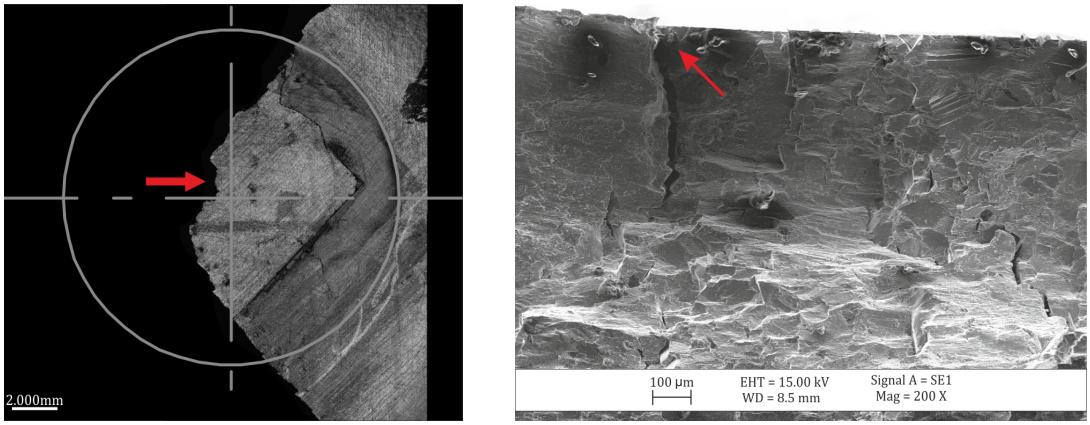
(a) Surface microscopy **(b)** SEM

Figure 3.10 – Failure location for uniaxial load (single actuator).



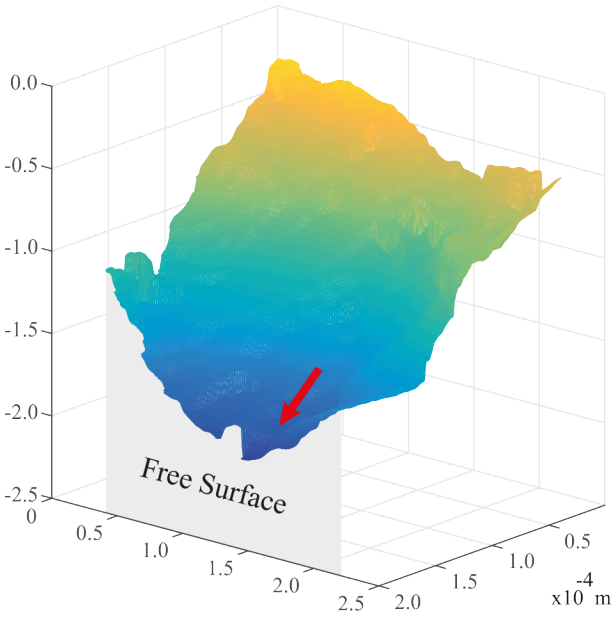
(a) Surface microscopy **(b)** SEM

Figure 3.11 – Failure location for equi-biaxial load.

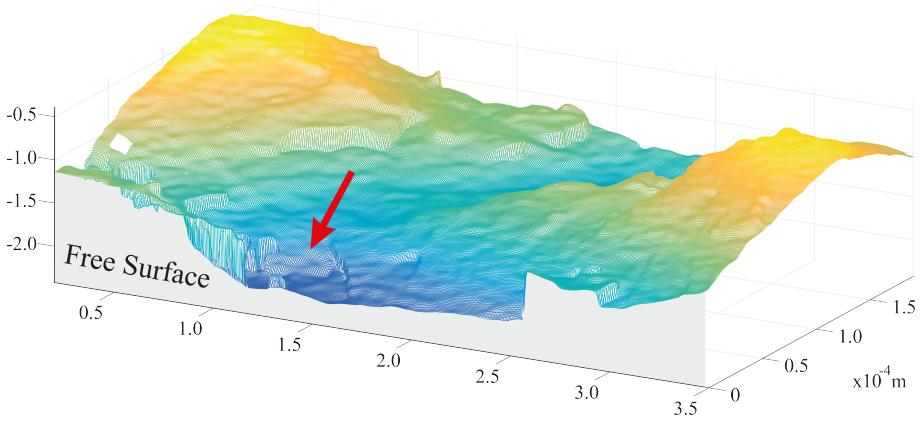


(a) Surface microscopy **(b)** SEM

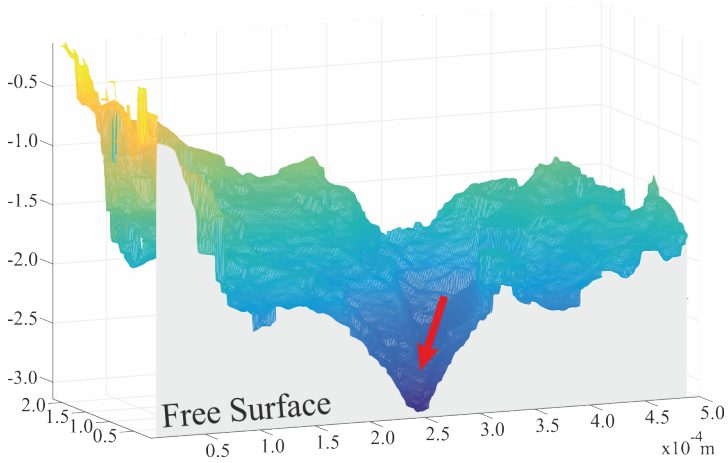
Figure 3.12 – Failure location for pure shear.



(a) Uniaxial Load



(b) Equi-biaxial Load



(c) Pure Shear

Figure 3.13 – Profile of fracture surface at magnification of 50x.

3.1.2 Uniaxial Fatigue tests

The biaxial test results presented in the previous section represent a great data set for benchmarking multiaxial fatigue criteria. However, the limited number of cruciform specimens and the focus on investigating the biaxiality of load effect meant that few specimens could be used for uniaxial fatigue testing. As most fatigue parameters depend on uniaxial data for calibration, a test programme using the same material was devised to improve fatigue life prediction performance and reduce data scatter caused by material variation.

Load controlled monotonic and cyclic tests were carried out with custom-designed specimens at room temperature. In total four specimens were used to characterise the axial monotonic and cyclic behaviour of Waspaloy. The monotonic test was performed under displacement control at 5mm/s. For the cyclic tests, both constant amplitude tests and a multiple amplitude step fatigue test were performed to characterise the material fatigue behaviour and obtain the material's cyclic hardening curve. The same test conditions of the biaxial test programme was used, i.e load ratio $R = F_{min}/F_{max} = 0.05$ and test frequency $f = 0.5$Hz, to complement the uniaxial equivalent data points presented in the previous section.

3.1.2.1 Axial test rig

The testing rig used for the uniaxial experimental programme consists of a single actuator capable of 100 kN and controlled by a CaTs3 digital servo-controller. Figure 3.14 illustrates the uniaxial test rig. Displacement and strain measurement for both test types (monotonic and cyclic) was performed live through an optical setup using a Virtual Instrument (VI) coded in LabView.

The optical setup consisted of a 4.1-megapixel 10-bit monochromatic camera (FLIR Grasshopper 3 – GS3U3-41C6M) with a reduced region of interest/capture to increase

frame rate to 120 frames captured per second. The increased frame rate is particularly important for the cyclic tests, as it impacts the quality of waveform shape measurement. The camera was paired with a telephoto micro lens AF Micro-Nikkor 200mm f/4D IF-ED, providing a 1:1 reproduction ratio.

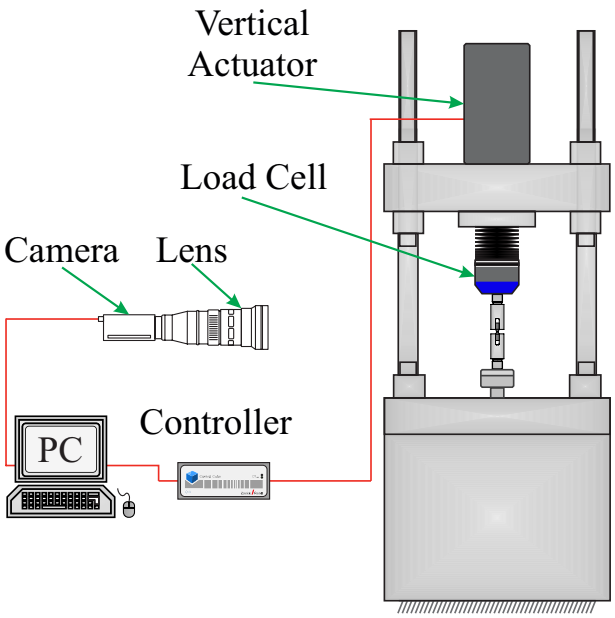


Figure 3.14 – Uniaxial test rig.

3.1.2.2 Custom-designed specimens

Hour-glass specimens with square cross-section were used for the tests. They were obtained from the clamping region of the cruciform specimens previously used in the biaxial fatigue tests. No plastic strain was observed in this region during the fatigue testing of the biaxial test programme. Thus, it is safe to assume that the material properties remained unaltered and that the clamping region is suitable for manufacturing new specimens.

Figure 3.15 illustrates the hour-glass specimen and the region where they were manufactured from. The geometry of the clamping region and the clamping holes restricted the design of the specimen and of its gauge section, which is only 2mm long and 6mm wide. Figure 3.16 presents the geometry of the specimen in detail. Waspaloy

is extremely hard and difficult to machine. Thus, the specimens were manufactured using wire erosion (EDM), which produced a smooth-surfaced gauge section, suitable for fatigue testing.

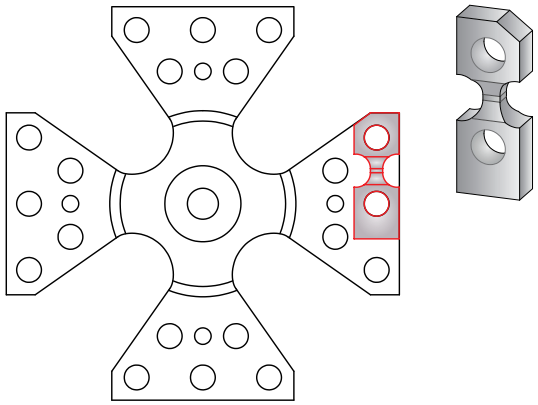


Figure 3.15 – Source region for the hour-glass specimen and geometry illustration.

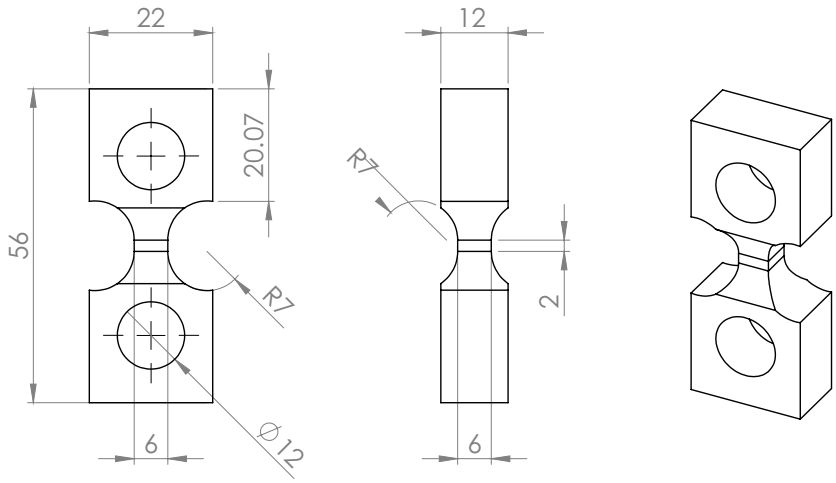


Figure 3.16 – Technical drawing of custom-designed Waspaloy specimen.

Gauge section roughness was measured using an Alicona InfiniteFocus Microscope and compared with the recommendation presented in ASTM E466-15 [2015] standard for load controlled uniaxial fatigue testing. Roughness is measured by the height of the irregularities with respect to an average line. Three roughness measures were considered to assess the surface finish of the specimens, according to ISO-4287 [1997] and Black & Kohser [2018]: 1) the arithmetic mean deviation of the assessed profile, $R_a = \frac{1}{n}\sum_{i=1}^{n} |y_i|$; 2) the root-mean-square (rms) value, $R_q = rms = \sqrt{\frac{1}{n}\sum_{i=1}^{n} {y_i}^2}$; and 3)

the average peak to valley height of the roughness profile, R_z.

Figures 3.17 and 3.18 present the surface roughness measured at the gauge section along the x- and y-directions, respectively. In both directions the arithmetic mean deviation of the surface roughness was found to be below the maximum roughness of $R_a \leq 200$nm recommended in ASTM E466-15 [2015]. Therefore, surface finish was suitable for fatigue testing.

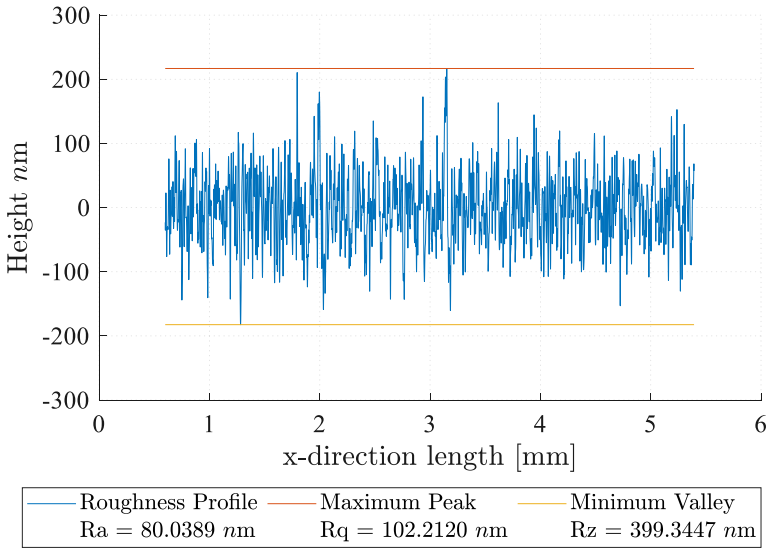


Figure 3.17 – Roughness profile at gauge-section along x-direction.

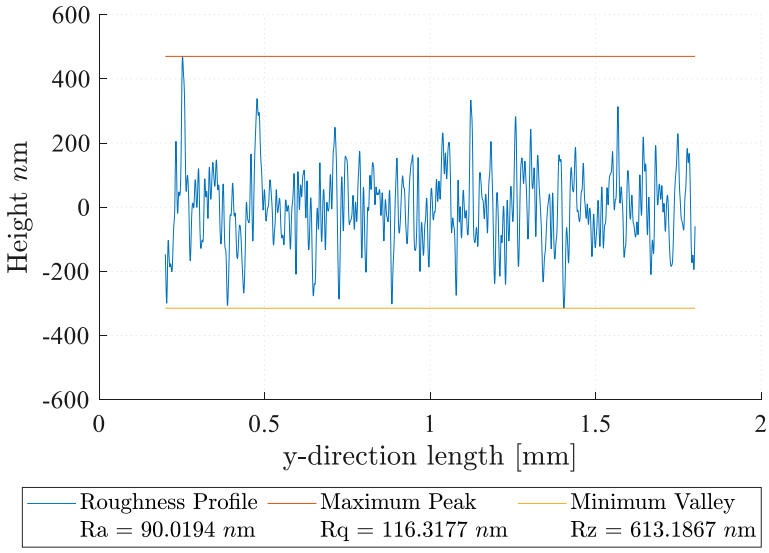


Figure 3.18 – Roughness profile at gauge-section along y-direction.

3.1.2.3 Optical strain measuring system

Advances in material testing equipment and techniques during the past 40 years have enabled the development of more realistic fatigue tests by applying loads representative of service life, at different temperatures and test frequencies. However, challenges remain for strain measurement in fatigue testing. Clip-on gauges (extensometers), for instance, have a fixed gauge length which can lead to significant errors at low strain conditions. Certain clip-on gauges require dimples in the specimen to be properly attached, which makes them unsuitable for use during fatigue testing because of the associated stress concentration. Electrical resistance bonded strain gauges are the most widely used method for obtaining surface strains from a component or specimen; however, the quality of the measurement is directly dependent on the quality of the bond and it may not survive long into the test. Moreover, bonded strain gauges only provide an averaged local measurement, corresponding to the region they are attached to. Aiming to overcome these limitations, an optical system capable of tracking specimen deformation via edge detection was developed for the uniaxial tests with Waspaloy.

The optical system consists of the camera + lens apparatus described previously and a computer running the Virtual Instrument on LabView. The connection between them is made via USB3, which allows for fast data transferring. The VI was coded by the Thesis author to control image acquisition and processing, allowing the user to set capturing rate, region of interest and pixel to millimetres calibration. Each image frame captured is scanned for edges or sharp transitions in the pixel values (according to the grey scale) along a given line defined by the user on the VI. The y-coordinate associated with the pixel at the sharp transition is recorded and used for the displacement and strain measurement.

The specimens used in this investigation had the limits of their gauge section painted in matte black, so that the sharp transition between the black paint and the material bare surface (lighter shade of grey) could be identified as an edge. Therefore, two

points/edges were detected along each defined line, one point at the upper limit and another at the lower gauge section limit. Figure 3.19 presents a schematic representation of the custom-designed specimen, with gauge section limits painted in black, and how edges are detected along green lines defined in the VI. The red circles along the lines represent the edges detected. Multiple lines were defined during the tests, they were used to measure bending and to confirm whether deformation in the gauge section was uniform.

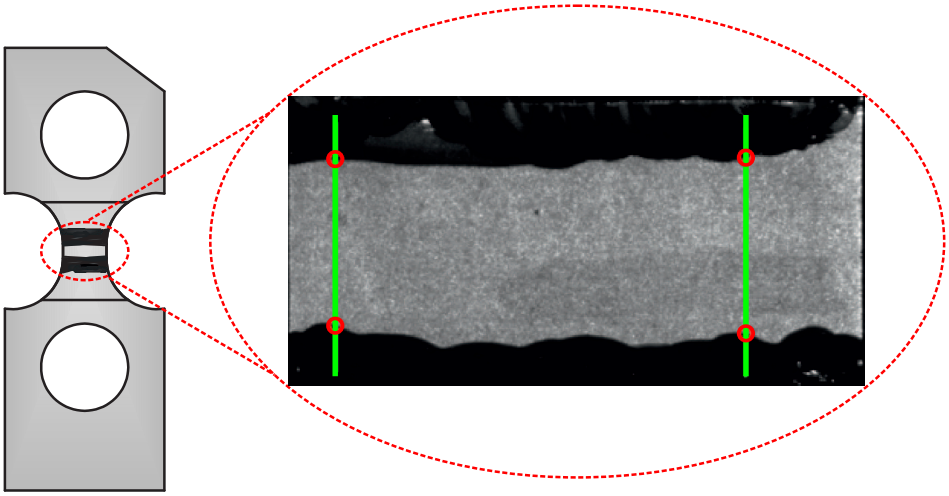


Figure 3.19 – Edge detection system in action.

Prior to each test, the distance between two points along a defined line in the y-direction is recorded on the VI and used during the tests as the reference distance/original length (ΔY_0). During the tests, the upper and lower boundaries of the gauge section displace according to the load applied. The y-coordinate of the upper and lower boundaries in the deformed configuration are used for calculating specimen displacement and strain. The difference between the two points after deformation gives the new distance ($\Delta Y = Y_{\text{upper}} - Y_{\text{lower}}$). Axial deformation is thus calculated according to the engineering strain formula:

$$\varepsilon_{yy} = \frac{\Delta Y - \Delta Y_0}{\Delta Y_0} \quad . \tag{3.8}$$

3.1.2.4 Test matrix

In total four tests were performed. First, a quasi-static test to obtain the monotonic hardening curve of Waspaloy at room temperature. Then, a cyclic multiple step test and two constant amplitude tests to obtain the stabilised cyclic stress-strain curve for Waspaloy. In the multiple step method, the load amplitude increases in steps of fixed number of cycles until specimen failure, and in the constant amplitude method, the specimen is cycled under a constant load amplitude until failure [Suresh, 1998].

The advantage of the constant amplitude method is that it provides a good representation of the hysteresis loop shape and stress-strain range for the tested load condition [Pattison, 2012]. However, this method requires numerous specimens to map the entire stress-strains curve and obtain the stabilised cyclic response of a material. In contrast, the multiple step method can provide a more accurate prediction of strain range for different stress range levels using a single specimen. The main disadvantage of this method is a loss of hysteresis loop shape definition.

For the multiple step test, each stress amplitude level was repeated for fifty cycles to obtain a pseudo-stabilised stress and strain condition. The stress amplitude was increase in steps of 50MPa from 450MPa in the first stress block up to a peak of 1400MPa, where specimen failure occurred. Had failure not occurred at this level, the test would have been continued beyond this amplitude. Figure 3.20 displays a schematic representation of the stress blocks applied at the same load ratio $R = 0.05$. For the two tests at constant amplitude, peak stresses were at 1000MPa and 835MPa.

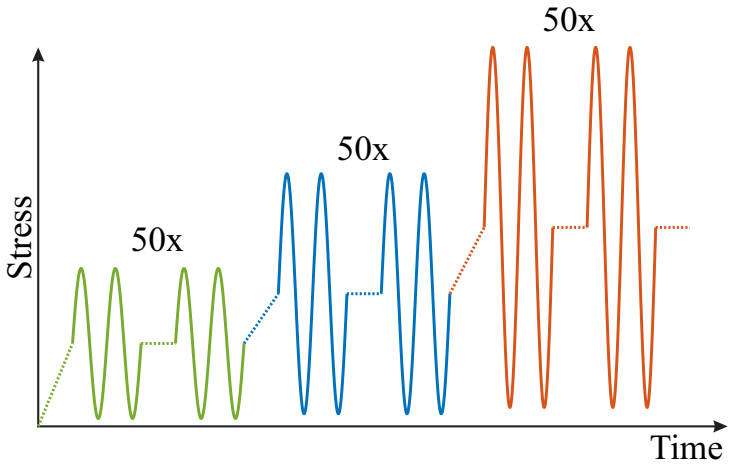


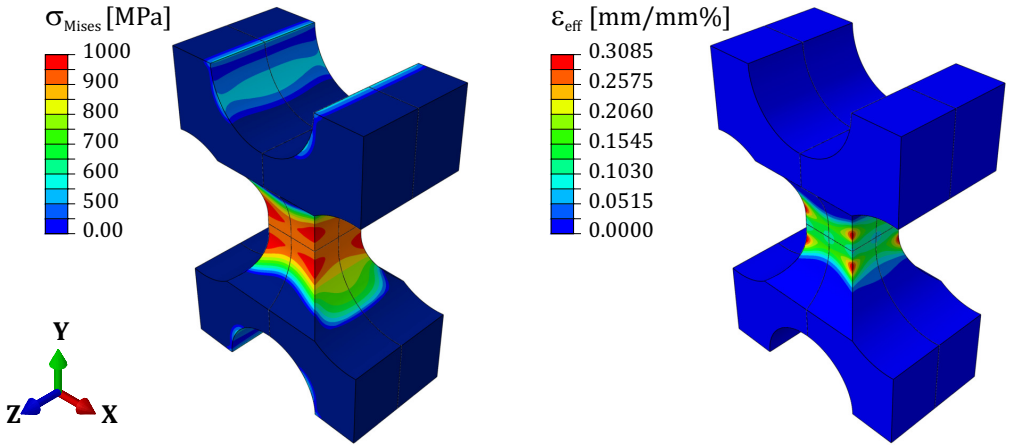
Figure 3.20 – Multiple step method – stress block schematic representation.

3.1.2.5 Finite Element Modelling

The specimen custom design was optimised using a finite element model calibrated with the test data obtained from the biaxial tests and the data available in Pattison's work [Pattison, 2012]. Elasto-plastic analysis of the monotonic and cyclic load conditions were performed considering the maximum von Mises equivalent stress and the maximum effective plastic strain.

Similar to the simulations carried out with the cruciform specimen, the square gauge section and symmetry of the custom-designed specimen allows the simulation to be modelled with just one eighth of the specimen. A structured mesh was created with 171,648 linear hexahedral elements (C3D8R), 183,358 nodes and reduced integration points. In order to more accurately describe the stress/strain state in the region were failure was expected to occur, a more refined mesh was defined. Thus, the gauge section presents elements of 0.100mm, amounting to 23,040 elements and 25,823 nodes.

Figure 3.21 illustrates the von Mises stress field and effective plastic strain seen on the specimen under monotonic axial load in the y-direction up to 36kN. Analysis of these results point out that the site of maximum von Mises stress and maximum accumulated plastic strain occurs above the gauge section, at the transition between



(a) max σ_{Mises} **(b)** max ε_{eff}

Figure 3.21 – Elasto-plastic FE model of uniaxial tests.

the gauge section and the 7mm fillet radius – used to reduce the specimen cross-section from 22mm down to 6mm (Fig. 3.16 presents the geometry of the specimen in detail). Post-processing of the stress and strain results shows that the critical regions (hot spots) are located at approximately 1.75mm from the centre of the specimen or 0.75mm from the end of the gauge section. A stress concentration factor $K_t = \sigma_{peak}/\sigma_{nominal} = 1.32$ is observed for this specimen, which could not be reduced, as its design was constrained by the original geometry of the cruciform specimens. The stress concentration factor was taken into account for properly correlating the uniaxial test programme results and the uniaxial equivalent (US) test case data from the biaxial programme reported in the previous section. In addition, the K_t factor is fundamental for predicting fatigue lives accurately.

3.1.2.6 Experimental Results

The material used in the tests came from the same batch as the one used by Pattison in his work [Pattison, 2012]. Pattison performed monotonic and cyclic tests with tubular Waspaloy specimens, using a clip-on gauge to measure deformation. In his work he presents both the monotonic and cyclic hardening curves for Waspaloy at room temperature. Pattison's results were used to validate specimen design and to

determine how accurate the strain measurements with the VI were.

Figure 3.22a presents the axial load measured by the test machine load cell vs the displacement measured by the linear variable displacement transducer (LVDT). Figure 3.22b shows the displacement measurement for the upper and lower edges detected in the gauge length, Y_1 and Y_0 respectively, and the actuator displacement (LVDT) until the failure of the specimen. Note that the difference between the two points is less than 2mm (the gauge length), this is due to the difficulty in painting the gauge section accurately. Therefore, in order to guarantee that the measurements were performed inside the gauge section, the black lines illustrated in Fig. 3.19 are slightly over the borders of the gauge section. Figure 3.22 illustrates how the LVDT measurements are not representative of what is seen on the specimen. The LVDT is located at the actuator at the top of the test machine crossbar. Therefore, it measures the displacement of the entire rig. In contrast, the optical system developed for this test programme is able to accurately measurement the actual displacement at the cross section of the specimen.

As only four specimens were manufactured for this test programme. The specimen used for the monotonic test was also used to calibrate the VI and to adjust the test machine PID values. However, loads for the calibration process were kept within the elastic domain of the material. Figure 3.23 presents the monotonic stress-strain response obtained with this specimen. The acquired curve lies between the cyclic and monotonic hardening curves presented by Pattison [2012], but closer to the cyclic response even though they are at different load ratios. This result could have been caused by the calibration procedure and/or the previous biaxial tests with the cruciform specimens.

Figure 3.24 presents the results obtained with the multiple step cyclic test. The cyclic hardening curve for the material was obtained from a Ramberg-Osgood least squares fit through the stabilised strain and stress amplitude test data as defined in Eq. 3.1. Stresses were calculated from load cell readings and strain amplitudes were

measured with the optical system. The use of the Ramberg-Osgood expression enables the extrapolation of the hardening behaviour beyond the levels attained in the test; however, the accuracy of the curve beyond the test limits cannot be quantified. Results confirm the cyclic hardening response presented by Pattison [2012] for Waspaloy.

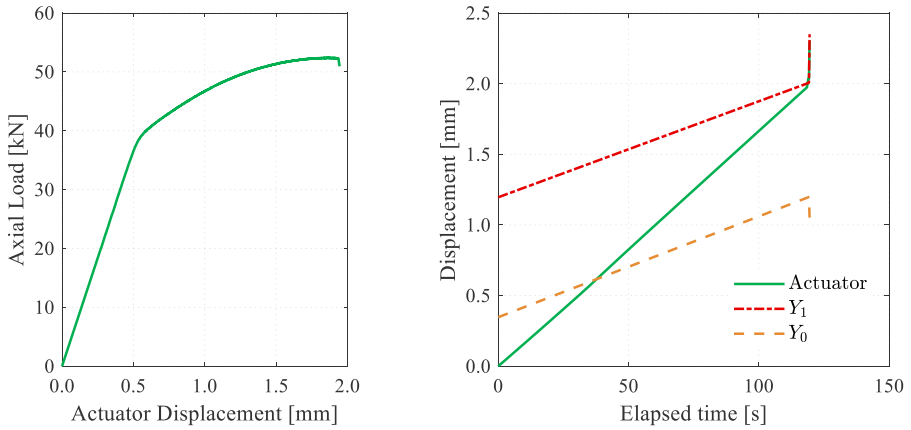


Figure 3.22 – Displacement measured by LVDT and the optical system.

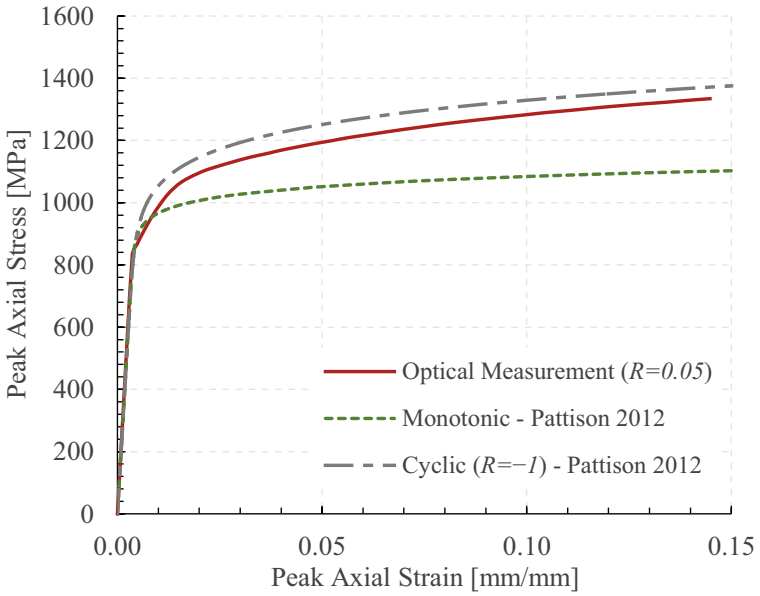


Figure 3.23 – Monotonic stress-strain response of Waspaloy.

Lastly, Fig. 3.25 presents how the constant amplitude uniaxial cyclic test data correlates with the uniaxial stress (US) tests performed with the cruciform specimens (CX07 and CX09). The axial stresses calculated for the uniaxial tests (UX), based on

load cell readings and specimen geometry, were adjusted considering the stress concentration factor, $K_t = 1.32$, obtained in the FE analysis presented previously. As the plot shows, once the stress concentration factor is considered, the two tests with the custom designed specimen lie along the same fitting curve as the results obtained with the US test cases. UX and CX above the markers represent the uniaxial and biaxial test programmes, respectively.

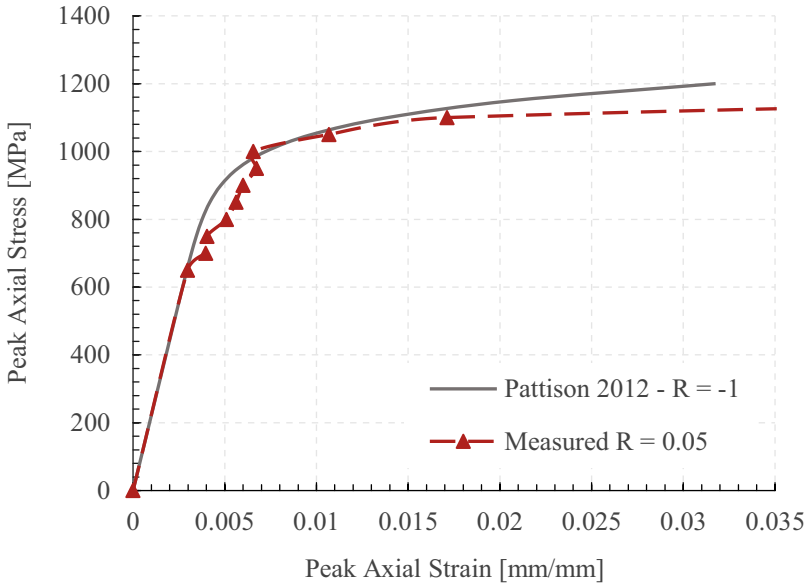


Figure 3.24 – Multiple step test stress-strain hardening curve.

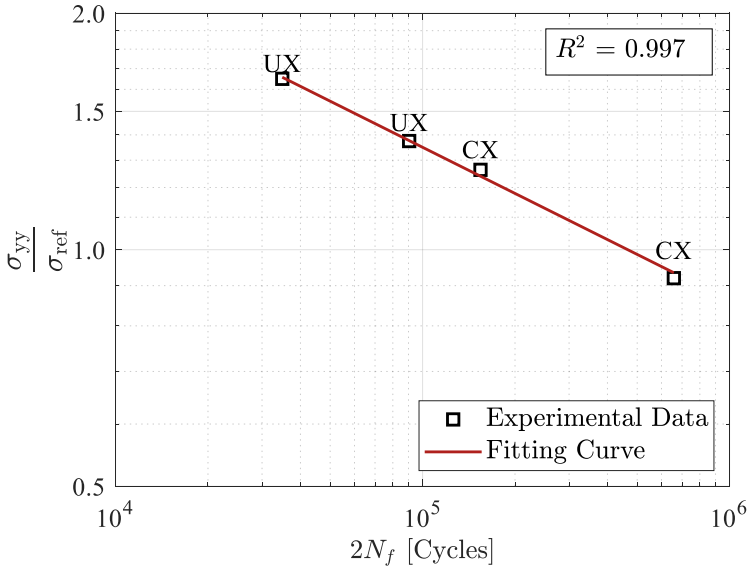
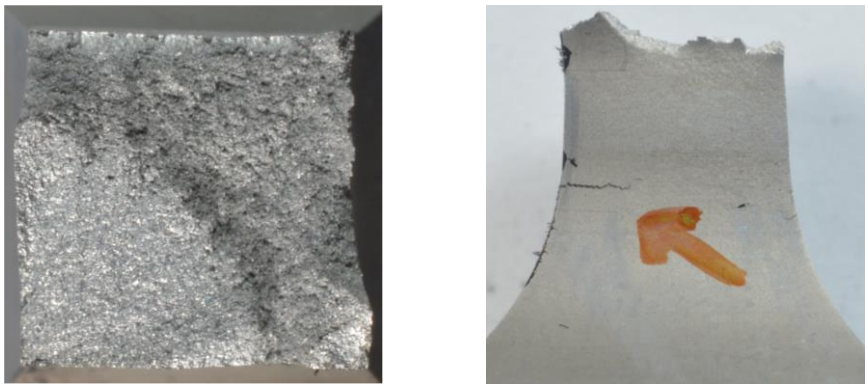


Figure 3.25 – Constant amplitude uniaxial fatigue tests. Cruciform and custom-designed specimens.

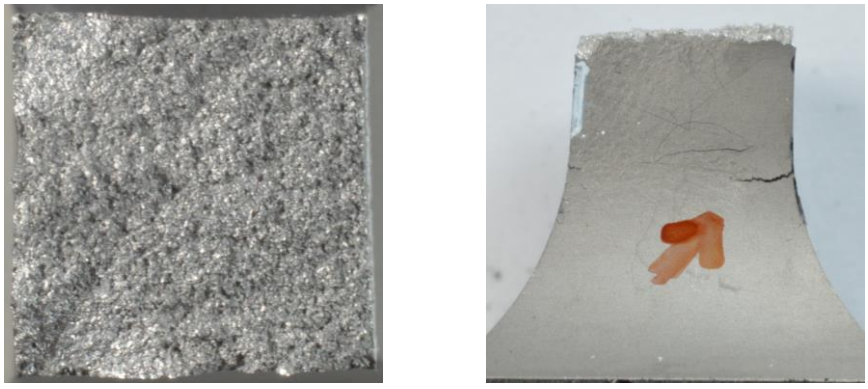
3.1.2.7 Fractography

Crack initiation and fracture surface analysis was performed with the two specimens used for the constant amplitude fatigue tests. Figures 3.26a and 3.27a present the fracture surface of specimens subjected to 30kN and 36kN respectively. Images show a longer crack propagation region for the test at lower stress level, and a more ductile fracture surface for the test at higher stress level. Figures 3.26b and 3.27b display cracks that initiated at the hot spots but did not dominate the failure of the specimens. This result confirms the predictions obtained from the FE analysis and presented in Fig. 3.21.



(a) Surface macro-photography **(b)** Crack at FE hotspot.

Figure 3.26 – Failure location, peak load at 30kN.



(a) Surface macro-photography **(b)** Crack at FE hotspot.

Figure 3.27 – Failure location, peak load at 36kN.

3.2 RR1000

This section introduces the second Nickel-based superalloy investigated, RR1000, and the experimental programme designed to explore its multi-axial deformation and fatigue behaviour under non-proportional loading conditions. Fine grain (FG) RR1000 is a powder-metallurgy (PM) superalloy developed by Rolls-Royce plc. for turbine disc applications and represents the current generation superalloy for this type of application. The ingot metallurgy process presented for Waspaloy cannot be applied to heavily alloyed grades such as RR1000, since the levels of segregation arising during melt processing and the significant flow stress at temperature cause cracking during thermal-mechanical working; instead, powder-processing is preferred [Reed, 2006].

Powder-processing can deliver better-defined compositional ranges and microstructural control; generating an enhancement in the operating temperature and performance rating [Bees, 2016]. Advantages of powder-processing include improved property uniformity due to the elimination of macro-segregation and the development of a fine grain size. Chen [2018] experimentally determined the average grain size for FG RR1000 to be approximately 5μm, with minimum grain size of 1μm and maximum of 20μm. This is an important aspect, as smaller grains have a crucial role on the accumulation of geometrically necessary dislocation due to higher strain gradients. Figure 3.28 presents the grain size distribution for RR1000 obtained by Chen. The disadvantages of PM are the extra cost associated with the production of the powder, which has to be handled to the highest standards to assure quality and minimise residual voids, pores, prior particle boundaries and cross-contamination. In addition, composition variation can lead to extra complexity of the probabilistic lifing method required [Reed, 2006]. Figure 3.29 illustrated the variation of yield stress at 650°C with the total fraction of strengthening phases ($\gamma' + \gamma''$). There is a clear distinction between the two materials investigated in this research project, Waspaloy and RR1000, where the latter presents considerably higher yield strength and improved low cycle fatigue properties.

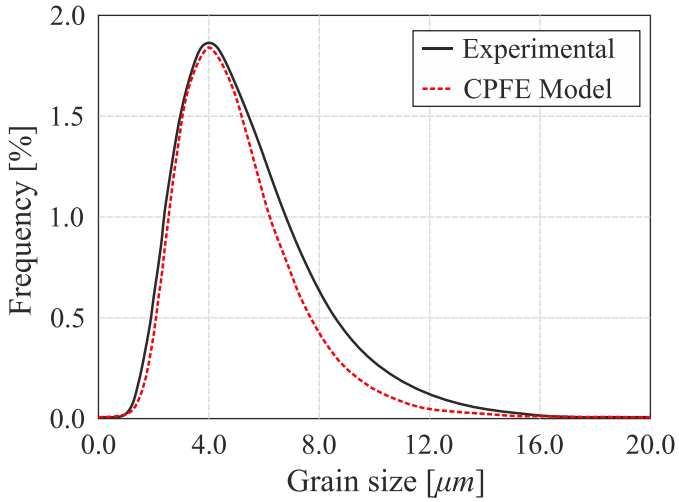


Figure 3.28 – Grain size distribution for RR1000. Adapted from Chen [2018].

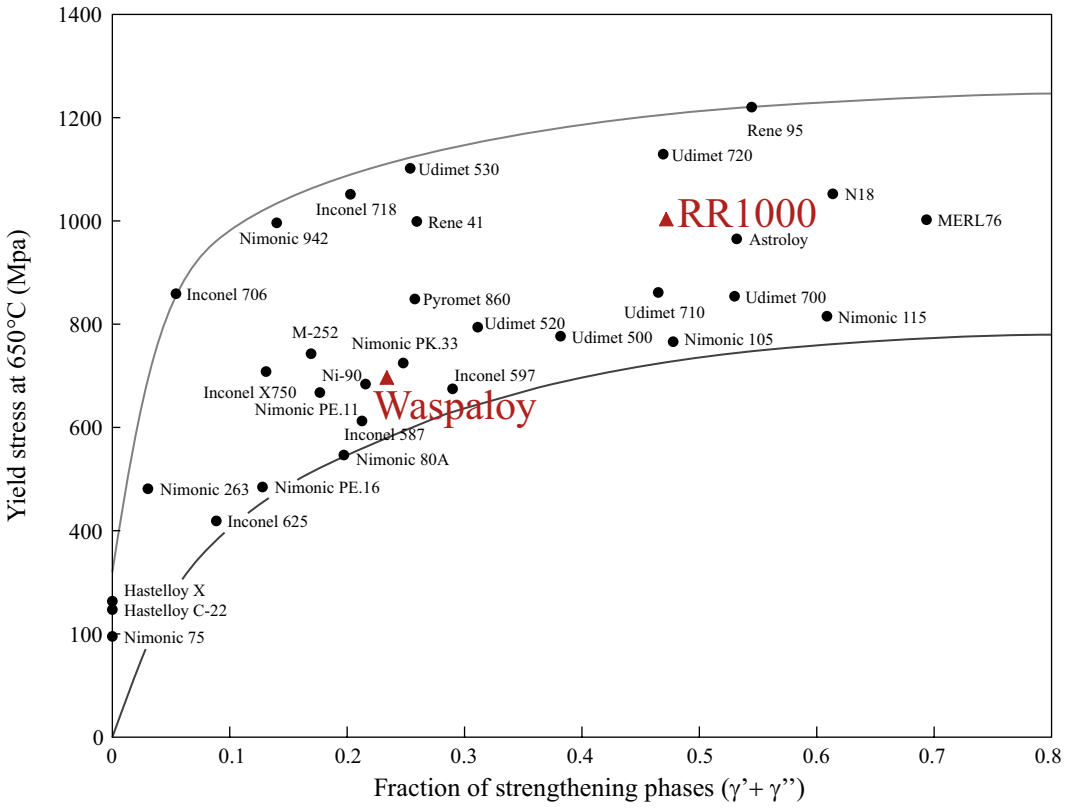


Figure 3.29 – Variation of the yield stress at 650°C with the total fraction of the γ' and γ'' – Adapted from Reed [2006].

The alloy used for this investigation came from fully heat-treated and annealed forgings, its chemical composition (in wt%) and the associated mechanical properties are given in Tabs. 3.3 and 3.4 respectively.

Table 3.3 – Chemical composition (in wt%) of RR1000 from Preuss et al. [2006].

Alloy	Cr	Co	Mo	Al	Ti	Ta	Hf
RR1000	14.3–15.2	14.0–19.0	4.2–5.3	2.8–3.2	3.4–4.2	1.3–2.2	0.0–1.0

Table 3.4 – Material Properties of RR1000.

Material Property	Value
Tensile strength at 0.1% total deformation, $\sigma_{0.1}$	1145 [MPa]
Shear strength at 0.1% total deformation, $\tau_{0.1}$	660 [MPa]
Young's Modulus, E	224100 [MPa]
Poisson's Ratio, ν	0.326
Hardening Modulus, h	4032 [MPa]

3.2.1 Non-proportional tension-torsion tests

The test programme is an extension of the work performed and published by Bees et al. [2014] and Bees [2016]. Bees et al. investigated the non-proportional hardening behaviour of RR1000 and modified Shamsaei & Fatemi [2010] and Itoh et al. [2013] formulations for predicting non-proportional hardening under various strain paths.

Based on the material constant proposed by Itoh et al. [2013], for evaluating the degree of reduction in fatigue life due to non-proportional hardening, Bees et al. [2014] pointed out a reduction in Low Cycle Fatigue (LCF) life of RR1000 dependent on strain range levels, and the need for further investigation. Therefore, the goal of this test programme is to identify and quantify load path dependency and the effects of non-proportional multiaxial loading - including additional cyclic hardening and cross-hardening - on RR1000 LCF life.

The test matrix designed consists of 6 non-proportional tension-torsion load paths. In total 16 fully reversed tests, i.e. without mean stresses ($R_\sigma = -1, R_\sigma = \sigma_{\min}/\sigma_{\max}$), were performed under load control at high stress levels (near the yield limit of the

material) and room temperature, avoiding creep effects. Due to their complexity and high-loads involved, tests were run at a maximum frequency of 1Hz.

3.2.1.1 Tension-torsion rig

An ultra-high stiffness tension-torsion servo-hydraulic test machine (Instron 8850) was used for all tests. The testing rig contains a rotary actuator providing up to 1000Nm and an axial actuator capable of 100kN. Both actuators are located at the top of the rig and connected to each other in the axial direction so that only the upper grip of the rig is movable, while the lower one is fixed to the machine frame. Manufactured by Instron Testing Systems, the test rig has an advanced testing environment (Wavematrix) that allows the configuration of complex load paths.

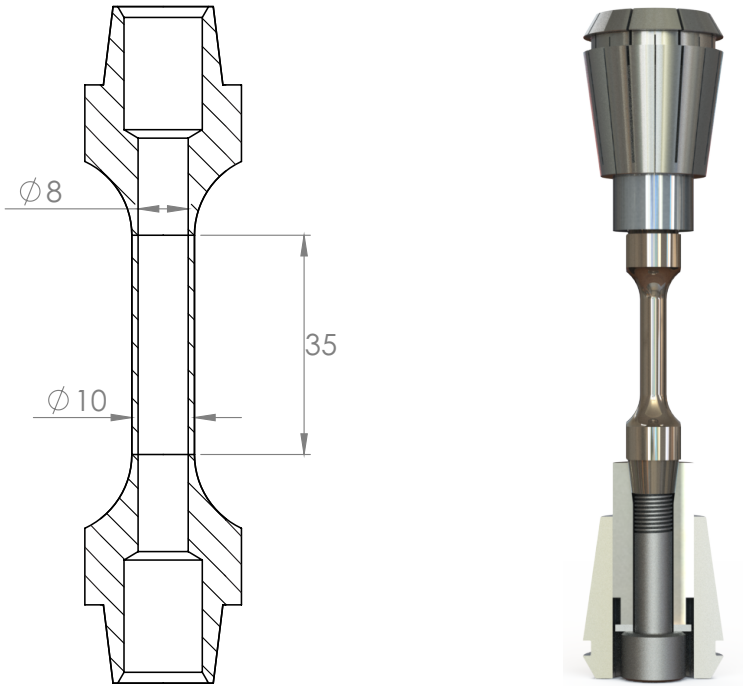
A camera setup was used for measuring strain fields and detecting the additional hardening caused by load non-proportionality, instead of clip-on extensometers and resistance strain gauges, due to their limitations presented in the previous section. The images collected during the tests were used to compare the different levels of non-proportional hardening seen for each load path.



Figure 3.30 – Axial torsional test rig with camera setup.

3.2.1.2 Tubular specimens

Thin-walled hollow cylindrical test specimens, sourced from a fleet high-pressure turbine disc, were used for the stress-controlled fatigue test programme. Specimen blanks were air quenched for 16 hours at 760° and manufactured according to Rolls-Royce specifications. The gauge section has nominal dimensions of 8mm and 10mm for the inner and outer diameters respectively, and 35mm for the gauge length. Specimens were internally reamed and honed (0.025 to 0.040μm), and externally polished (0.025 to 0.400μm) across the gauge length to a consistent surface finish. The individual test piece dimensions were measured and found to comply with requirements. Conical ends to the specimen ensure a uniform circumferential mechanical interface and enable the firm application of torsional loads across a fully reversed load cycle. Figure 3.31 illustrates the specimen geometry and gripping apparatus designed for fitting the specimen into the test rig.



(a) Geometry **(b)** Gripping apparatus.

Figure 3.31 – Tension-Torsion tubular specimen.

3.2.1.3 Load Paths

The constrained quantity of specimens available, 16, limited the number of load paths that could be investigated, as it is necessary to repeat each load condition at least a few times to confirm the real trend and effects of non-proportional hardening. Therefore, 6 load paths were carefully selected for investigation, considering the rotation factor proposed by Kanazawa et al. [1979] to quantify the degree of non-proportionality.

The Kanazawa factor is mechanistically based on the amount of slip experienced by critical planes in the material and is defined as the ratio between the minor and major axes of the minimum ellipsoid that circumscribe the load path. Figure 3.32 illustrates the load path dependency (LPD) factor, $F = b/a$, defining the degree of non-proportionality in a range from zero to one. For fully proportional/in-phase tests, $F = 0$, whilst for 90°out-of-phase tests, $F = 1$, representing the maximum degree of non-proportionality.

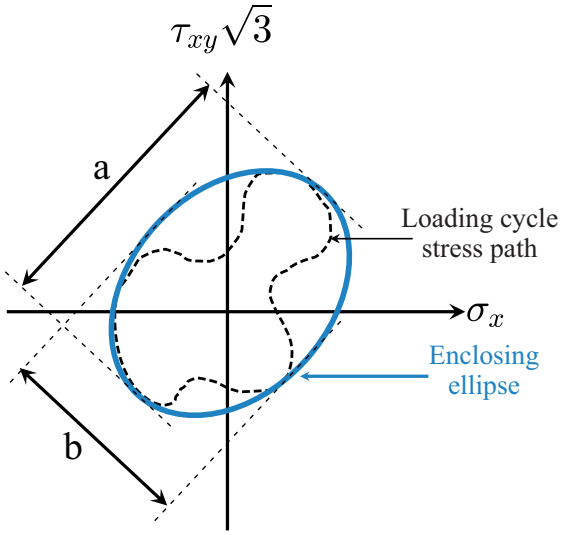


Figure 3.32 – Load path dependency factor, F, adapted from Pattison [2012].

Figure 3.33 illustrate the different load paths investigated in this work and their load sequence, where the red dashed arrow indicates the first loading step. The first condition tested was the 90° out-of-phase square load path, named 1SQ, as this is considered the most damaging load path and has been extensively investigated for

RR1000 by Bees et al. [2014] and Bees [2016]. The goal was to use Bees' test data as a benchmark to validate the experimental procedure and obtain more data points to accurately predict the non-proportional hardening behaviour of RR1000 under this test condition.

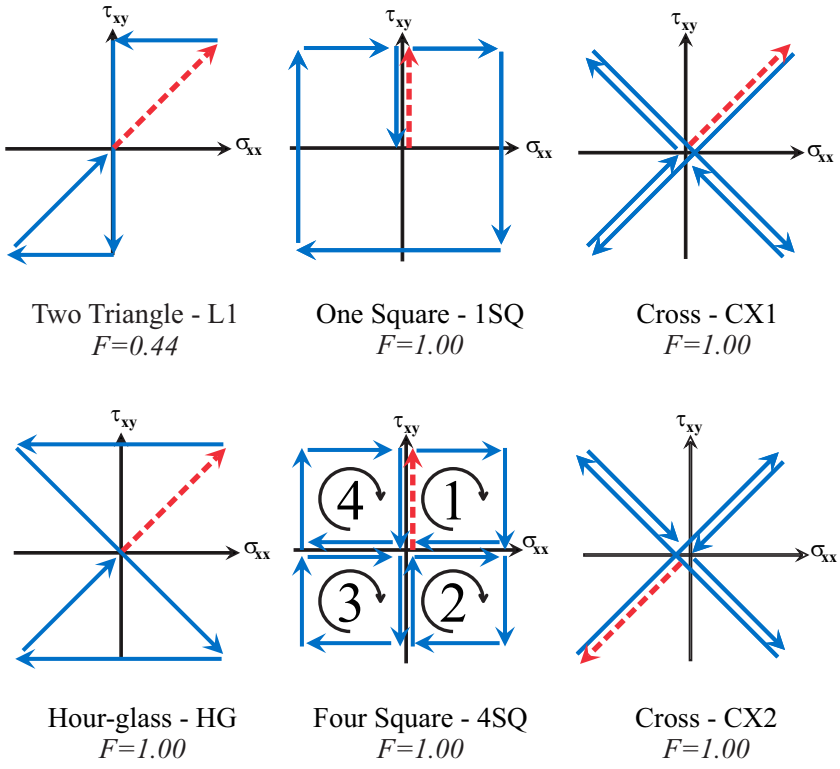


Figure 3.33 – Non-proportional load paths.

Doong & Socie [2008] point out that during out-of-phase loading, the loading sequence and load reversibility have a strong impact on fatigue life. Therefore, in order to investigate the cross-hardening effect caused by sudden changes of loading direction, a modification of the 1SQ load path was proposed. For this proposed load path, named four-square (4SQ), the load is completely removed before each change of direction. Both test conditions present the same LPD factor, $F = 1$.

Load cases 1SQ and 4SQ provide enough information for a fundamental analysis of non-proportional hardening and load path dependency. However, they are simplistic load paths that do not consider the real loading conditions that many components experience in service. Therefore, a load path more representative of the stresses seen

on HPT disc bore surfaces was selected from the research work presented by Bees [2016]. This load path, named two triangles (L1), presents the lowest degree of non-proportionality of all tests, $F = 0.44$, a value similar to the LPD factor obtained for non-proportional load paths with a phase difference of 45°.

Analogously to the extension of 1SQ load path to the 4SQ load path, the L1 test condition was adapted for the investigation of cross-hardening. As a result, an hourglass shaped (HG) load path was obtained, the material thus experiences load reversion in both torsional and axial directions, with $F = 1$. Lastly, two cross load paths (CX1) and (CX2), with $F = 1$, were assessed. These two cases present both the opportunity to assess cross-hardening, by contrasting them with the HG load path, and load path dependency, by investigating the effect of load sequence, as this is the only difference between the two cases, CX1 and CX2 – CX1 initiates its cycle with a proportional tension-torsion load, whilst CX2 initiates with a proportional compression-torsion load.

3.2.1.4 Stress-strain Formulae

Static yield parameters characterise the general multiaxial stress state through a scalar quantity, allowing the comparison to simple uniaxial test data. Thus, in order to set the test conditions and correlate the tension-torsion stress state to the uniaxial deformation behaviour of RR1000, the von Mises equivalent stress and strain were implemented. For the tension-torsion stress condition with only $\sigma_y \neq 0$ and $\tau_{xy} \neq 0$, von Mises equivalent stress reduces to:

$$\sigma_{vM} = \sqrt{\sigma_{yy}^2 + 3\tau_{xy}^2} \quad , \tag{3.9}$$

and the effective strain can be simplified to:

$$\varepsilon_{eff} = \sqrt{\varepsilon_{yy}^2 + \frac{1}{3}\gamma_{xy}^2} \quad . \tag{3.10}$$

For an idealised elastic/perfectly plastic material, the shear stress is uniform throughout the tubular specimen wall once yield has been exceed at the bore of the tube [Brown, 1978]. Equation 3.11 gives the average shear stress across the specimen wall thickness,

$$\tau_{\mathrm{xy},0} = \frac{3T}{2\pi\left(r_o^3 - r_i^3\right)} \quad , \tag{3.11}$$

where T is the torque applied and r_o and r_i are the outer and inner radii respectively. The normal stress, σ_{yy}, is calculate as follows:

$$\sigma_{\mathrm{yy}} = \frac{F_{\mathrm{yy}}}{\pi\left(r_o^2 - r_i^2\right)} \quad , \tag{3.12}$$

where F_{yy} is the axial load applied to the specimen.

Loads for all test conditions were set considering nominal values of von Mises stress, σ_{vM}. The normal and shear stresses where obtained using the relationships

$$\sigma_{\mathrm{yy}} = \frac{\sigma_{\mathrm{vM}}}{\sqrt{2}} \quad , \textit{and} \quad \tau_{\mathrm{xy},0} = \frac{\sigma_{\mathrm{yy}}}{\sqrt{3}} \quad . \tag{3.13}$$

Nominal loads for each test condition were calculated substituting in Eqs. 3.11 and 3.12 the results from Eq. 3.13 for each von Mises stress, σ_{vM}, level.

3.2.1.5 Finite element modelling

Finite element modelling was employed for an assessment of the specimen geometry and to estimate strain levels for each load path. The objective was to investigate possible design flaws that could lead to crack initiation outside the gauge section and to have a ballpark for the strain measurements performed using DIC. For that an isotropic hardening rule was adopted together with the stabilised cyclic hardening curve for RR1000 provided by Rolls-Royce plc. Specimen symmetry meant that an axisymmetric

model could be used. A mesh formed by 7,663 linear quadrilateral elements with reduced integration of type CGAX4R was defined, amounting to 8,078 nodes. Figure 3.34a presents the assigned mesh and the investigated surface paths plotted onto a 180° revolved projection of the specimen. A more refined mesh was applied to the gauge section and the fillet radius region.

Figure 3.35 shows von Mises equivalent stress, σ_{vM}, and the normal, σ_{yy}, and shear stresses, τ_{xy}, along the inner and outer surface paths (as presented in Fig. 3.34b). The case in point represents the instant of maximum tensile and torsional load of the L1 load path, i.e the end point of the red arrow illustrated in Fig. 3.33. At the gauge section – represented in Fig. 3.35 by the dotted line at y-distance equal to 17.5mm – the maximum normal stress is seen on the inner surface. However, as all load paths had a torsional load component, the maximum von Mises stress is always seen on the outer surface. Fractography results presented in the following sections confirm that fatigue cracks initiated indeed on the outer surface of the specimen.

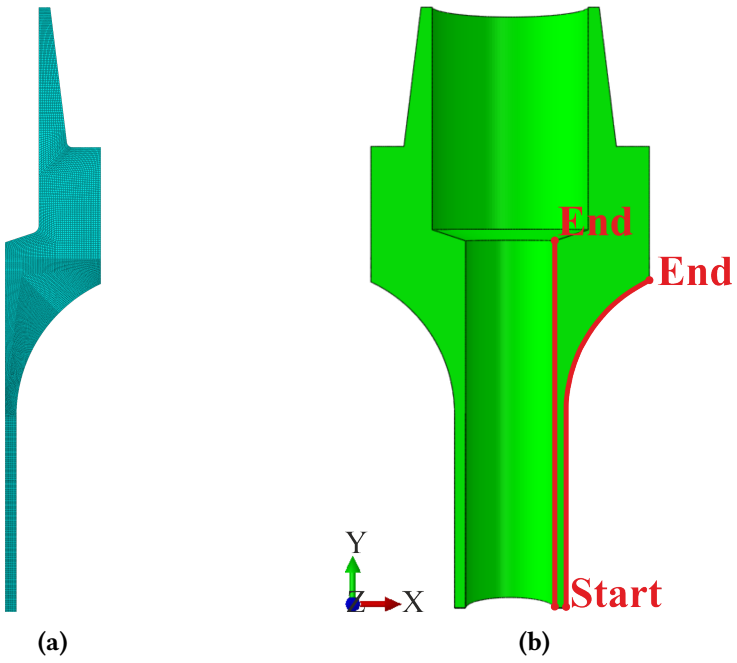
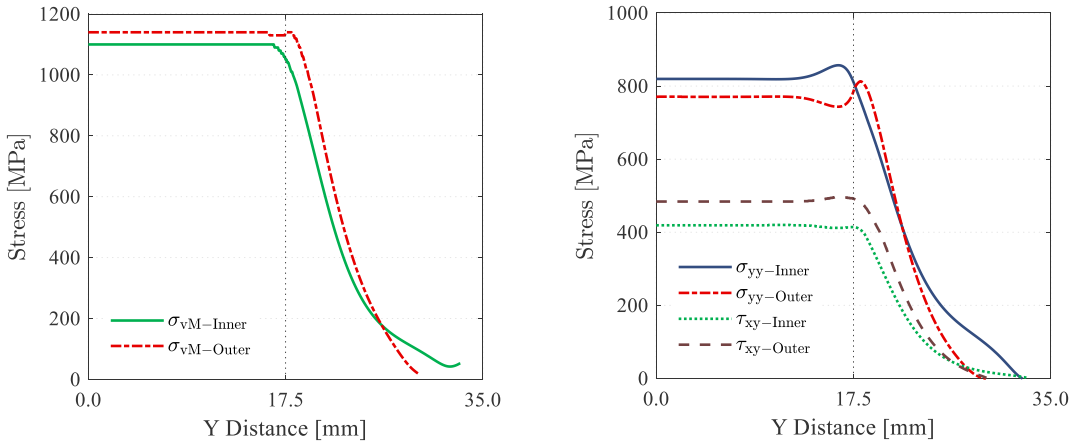


Figure 3.34 – a) Axisymmetric FE model of the specimen; b) Node paths used for the stress distribution investigation - inner and outer surface paths.



(a) σ_{vM} **(b)** σ_{xx} **and** τ_{xy}

Figure 3.35 – Stress distribution along inner and outer surface paths.

3.2.1.6 Experimental results

Table 3.5 presents the normalised normal, shear and von Mises peak stresses. These were calculated based on Eqs. 3.11 and 3.12, and the axial force and torque measured by the test machine load cell throughout the test. von Mises peak stresses were calculated using the formula presented in Eq. 3.9.

Peak strains were measured using DIC with Davis (illustrated in Fig. 3.36), and effective peak strain calculated according to Eq. 3.10. Figure 3.37 shows the cyclic stress-strain response for RR1000 with the proportional/in-phase (IP) and 90°out-of-phase (1SQ) power fit. The results obtained with the 1SQ and L1 test cases are superimposed in red for contrast. Both test data are in good agreement with the results presented by Bees et al. [2014], where the 1SQ data follows the non-proportional fitting and the L1 test data lies closer to the in-phase fitting curve.

A similar result is illustrated in Fig. 3.38, in the stress-life comparison. All test conditions with $F = 1$, i.e. with a phase shift of 90°, presented similar fatigue lives for equivalent stress levels. In contrast, the L1 test case, which presents $F = 0.44$, gave considerably longer fatigue lives, comparable to the results obtained by Bees [2016] for in-phase loading. Figure 3.38 also suggest that for stress levels near the yield strength of

RR1000, only a minor cross-hardening effect is observed, as the cross, CX1 and CX2, and the HG load paths gave similar fatigue lives. The same is observed in the comparison between 4SQ and 1SQ test cases.

Table 3.5 – Normalised peak stresses and total fatigue lives.

Load Path	Norm. Peak Stresses σ_{yy}	$\tau_{xy,0}$	σ_{vM}	Fatigue Life $2N_f$
One Square – 1SQ	0.639	0.329	0.856	12,903
	0.634	0.372	0.904	7,625
	0.680	0.393	0.962	4,992
	0.680	0.399	0.969	4,756
Four Squares – 4SQ	0.635	0.364	0.895	9,269
	0.680	0.389	0.957	4,398
Two Triangles – L1	0.598	0.346	0.847	52,302
	0.633	0.368	0.899	24,298
	0.678	0.389	0.956	13,293
Hourglass – HG	0.599	0.347	0.848	15,080
	0.630	0.365	0.893	8,366
	0.676	0.391	0.958	4,752
Cross – CX1	0.629	0.365	0.892	10,596
	0.675	0.385	0.949	5,432
Cross – CX2	0.630	0.366	0.893	9,094
	0.676	0.387	0.952	5,151

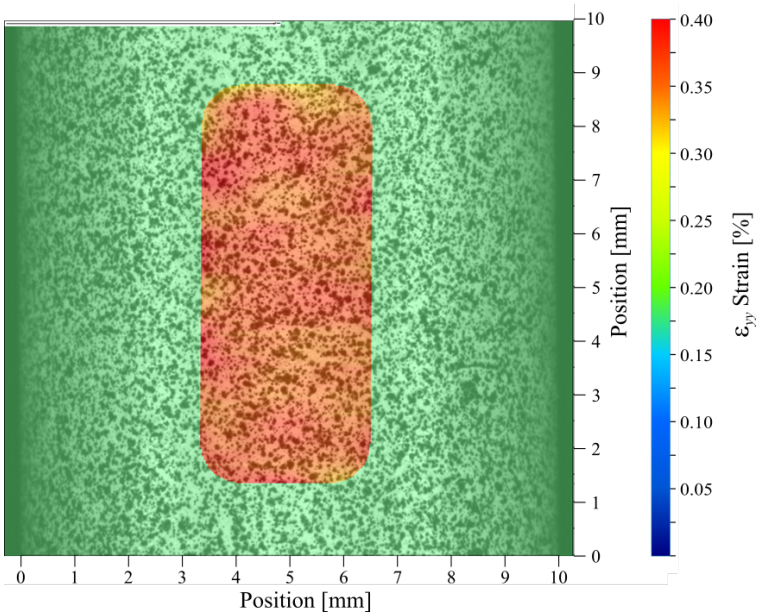


Figure 3.36 – 1SQ Load Path at $\sigma_{vM,peak}$ = 1125MPa – ε_{yy} peak strain.

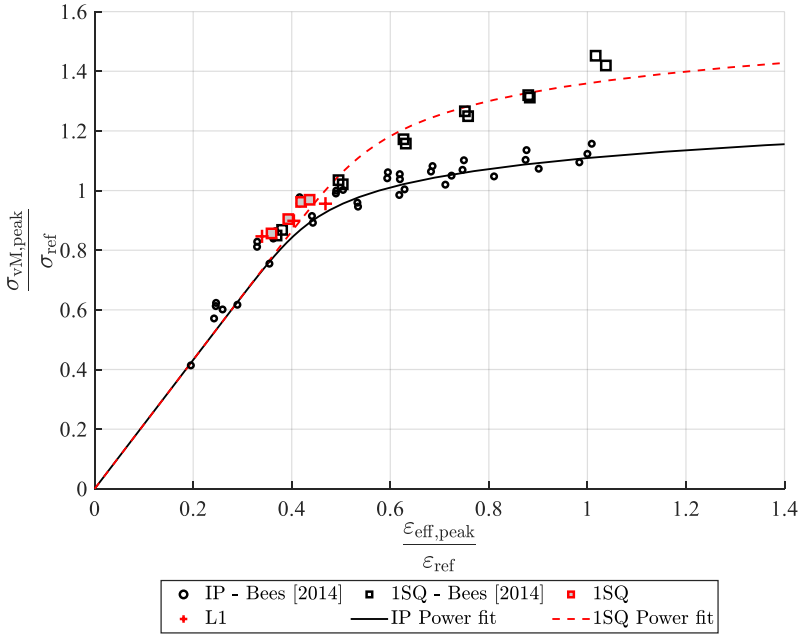


Figure 3.37 – Cyclic stress-strain response for RR1000 adapted from Bees et al. [2014] with current test data.

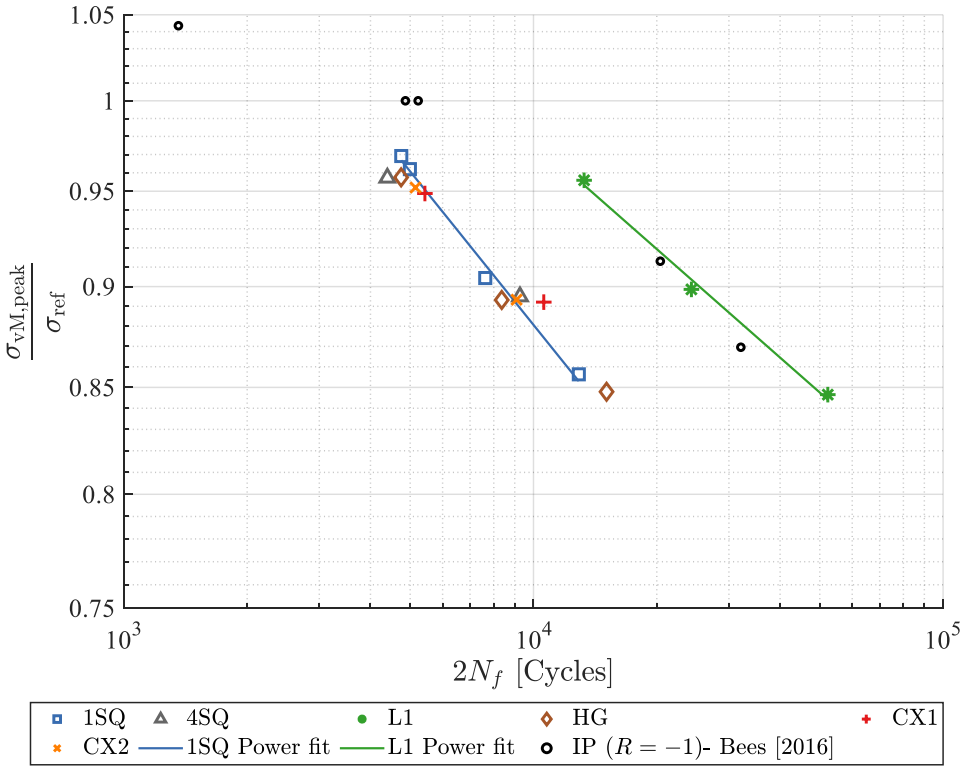


Figure 3.38 – Stress-life comparison with in-phase test data adapted from Bees [2016].

3.2.1.7 Fractography

It was presented in the Finite Element modelling of RR1000 section that the maximum axial stress, σ_{yy}, was observed on the inner surface of the specimen. Therefore, in order to investigate where the cracks that eventually led to the failure of the specimen were initiated, the failed specimens were checked under the microscope. It was noted that some of the specimens had a clear scratch mark along the inner surface, which most probably was created during the removal of the machine tool after the honing process. A close inspection showed that these marks were very shallow and did not impact crack initiation. Figure 3.39 shows the SEM analysis of the specimen tested under the CX2 load condition with maximum von Mises of 1125MPa. The red arrow points to the site of crack initiation and the green dashed line arrow points to the scratch mark. It was concluded that the scratch mark did not interfere in the crack initiation process.

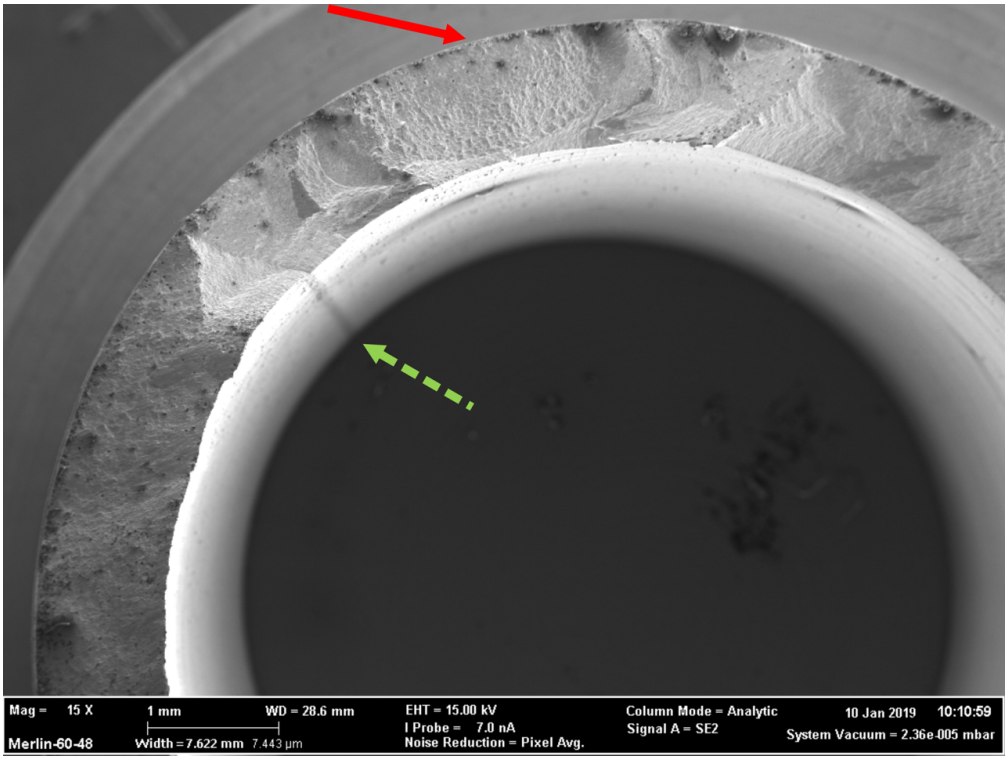
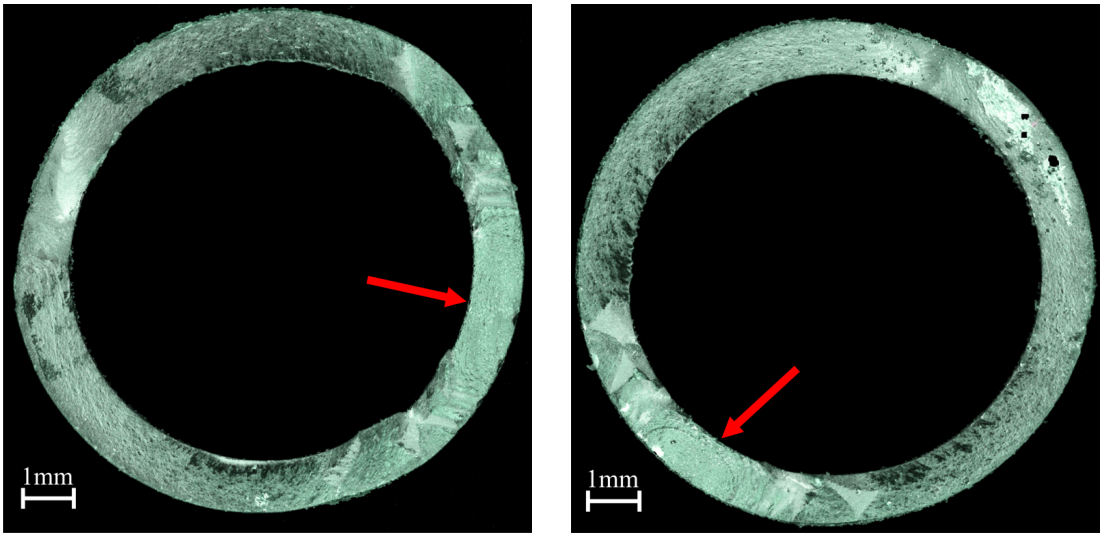


Figure 3.39 – SEM analysis of failed specimen – CX2 1125MPa.

All specimens displayed similar results. The only key difference observed was the size of the region where the crack propagated. Specimens tested at higher equivalent

stress levels had shorter crack propagation followed by ductile fracture. Figure 3.40 illustrates the crack propagation region for the hourglass load path cases.



(a) σ_{vM} **= 1000MPa** **(b)** σ_{vM} **= 1125MPa**

Figure 3.40 – Crack surface for HG load path.

3.3 Conclusions

This chapter presented the experimental data set that was used as the basis in this research project for comparing the performance of multiaxial fatigue parameters in predicting fatigue lives.

3.3.1 Conclusions for Waspaloy

Biaxial fatigue tests under a range of loading conditions with cruciform specimens were performed for the investigation of strain biaxiality effect. Finite Element modelling of the specimen was performed to set the test conditions and to predict stress-strain fields and failure location. Different biaxiality ratios with the same maximum principal stress were considered. Results demonstrate a variation in total life to failure and failure location, confirming the FE predictions.

In order to complement the biaxial test data, a uniaxial test programme was devised

considering a similar methodology. The obtained results present a strong correlation with the literature and the previous biaxial test data with cruciform specimens. An optical strain measurement system was developed for the uniaxial programme. The system proved to be accurate and reliable. However, a few drawbacks were identified: i) measurement along a line is not ideal, as due to Poisson effect a point in the surface of the specimen also moves in the X direction. (Movement in Z direction is not a problem as the depth of field is enough to cope with that); ii) for high plastic strain levels the paint used to delimit the gauge section starts to peel off the specimen and measurement is compromised; iii) at the current setup, only one of the four faces of the specimen can be monitored. Thus, it is not always possible to spot crack initiation.; iv) specimen design and alignment flaws – fatigue cracks initiated outside the gauge section, at the corners, at the transition between the gauge section and the fillet radius.

3.3.2 Conclusions for RR1000

The non-proportional deformation and fatigue behaviour of RR1000 was investigated under a range of load paths. Results indicate that RR1000 presents no load path dependency for stress levels near the yield strength of the material. On the other hand, fatigue lives and cyclic hardening are highly dependent on the degree of non-proportionality. Five of the six load paths investigated have the same degree of load non-proportionality, characterised by the LPD factor $F = 1$. A clear distinction is seen between these test cases and test case L1, which presents a lower factor, $F = 0.44$. The L1 test case presented fatigue lives approximately three times longer than test cases with the higher LPD factor ($F = 1$), and strain levels and fatigue lives comparable to in-phase tests.

The cylindrical geometry of the specimen and shine surface pose a significant challenge for strain measurements with DIC. For that reason, only a small section of the specimen gauge section could be used for measurement, as the camera setup did not have enough depth of field – depth variation is detect by the DIC system as spurious volumetric deformation.

4 Multiaxial Fatigue Damage Parameters

4.1 Overview

There is a variety of methodologies available for predicting the fatigue life of engineering components subjected to proportional and non-proportional multiaxial loading conditions. Gates [2016] created a flowchart to illustrate the general process flow for fatigue crack initiation analysis considering different life prediction methodologies. Figure 4.1 presents an adapted version of Gates' flowchart, which outlines some of the more specific steps required for a wider variety of analysis procedures.

As seen in Fig. 4.1, when considering crack initiation life, there are different classes of multiaxial fatigue parameters: stress-, strain-, and energy-based criteria. These approaches are characterised based on the parameter used to quantify fatigue damage. In addition, there exist a range of parameters, including those based on critical plane concepts, which relate fatigue damage to some combination of stress, strain, or energy quantities on the material plane where they are maximum. The main fatigue damage parameter classes are presented in the damage calculation step of the flowchart.

Fatigue testing are normally carried out in two forms, either under load control or under strain control. As a result, the input loading for a fatigue life analysis is either in the form of applied stress (for load-controlled tests) or strain history (for strain-controlled tests), but not both. Therefore, depending on the damage parameter chosen for the analysis, the constitutive behaviour of the material and its non-proportional hardening response have to be modelled in order to derive accurate strain response from a given stress history, or vice versa [Gates, 2016]. This is especially true in cases where plastic deformation play an important role, as it is the case for LCF regimes.

This chapter focusses on some of the most widely used multiaxial fatigue theories based on the four main classes presented in Fig. 4.1. Therefore, no attempt is made to review all the models that have been proposed so far. For a chronological review of multiaxial fatigue criteria propositions please see Garud [1981*b*]; You & Lee [1996]; Macha & Sonsino [1999]. For a more detailed review on stress based and strain based multiaxial criteria please refer to Fatemi & Shamsaei [2011]; Papadopoulos [1997]; Socie & Marquis [1999]; Wang [2004]. Finally, critical plane approaches have also been assessed in Lopez-Crespo et al. [2015]; Reis et al. [2009]; Wang [2004].

As the test programmes presented in Chapter 3 were all load controlled, an introductory assessment was performed using stress-based parameters and considering the stress levels obtained from the elasto-plastic FE analysis reported in Chapter 3. Stress-based parameters were subdivided into extended yield criteria and invariant based approaches. After that, aiming to better model the mechanisms governing fatigue failure, an extensive investigation of critical plane approaches was performed, including stress-, strain- and energy-based criteria.

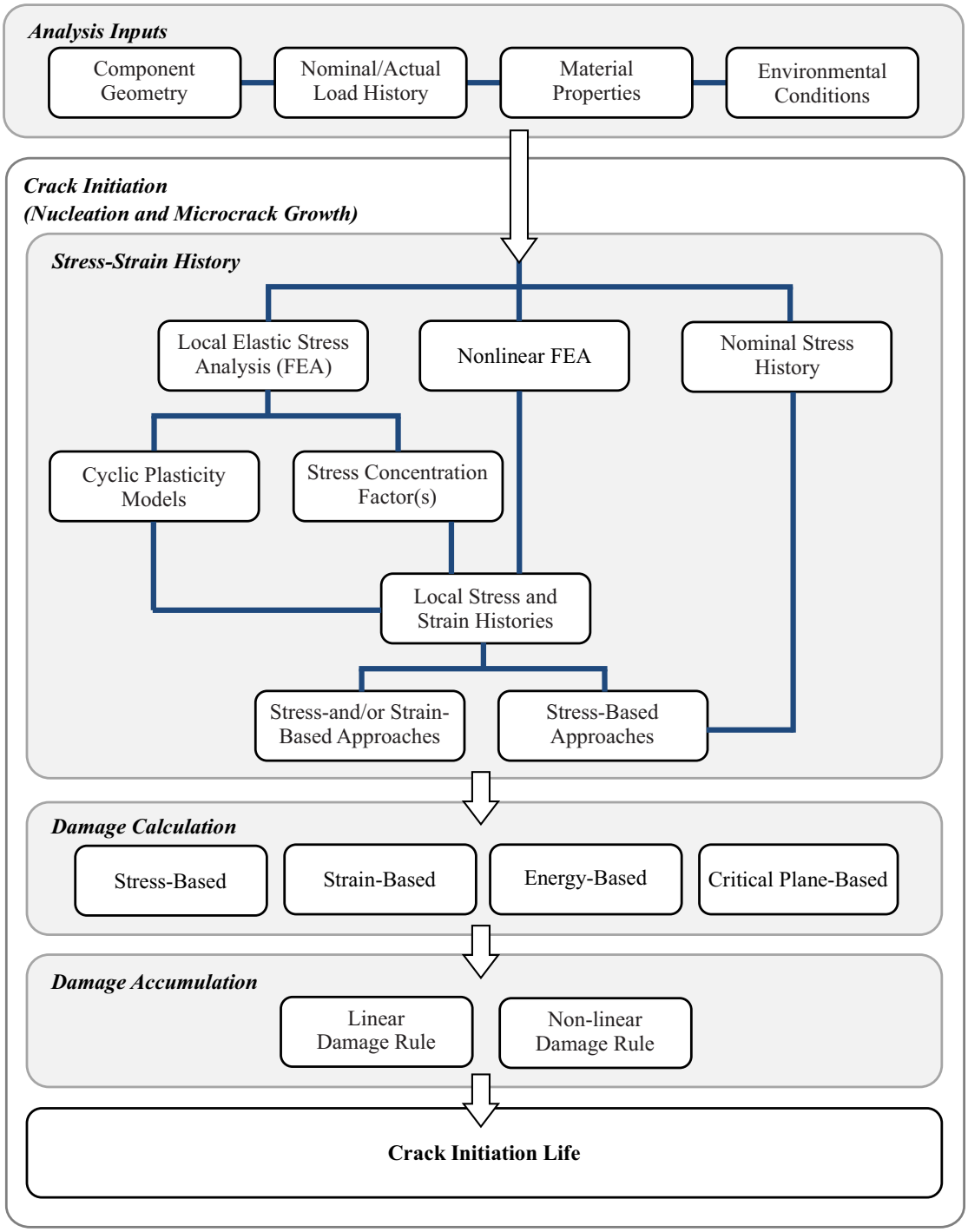


Figure 4.1 – Flowchart outlining the general steps for estimating the multiaxial variable fatigue life, adapted from Gates [2016]

4.2 Axial and torsional fatigue behaviour

The fatigue behaviour of materials is characterised in the form of a stress or strain parameter versus fatigue life, and a cyclic stress-strain curve. Such a characterisation is usually obtained using smooth specimens under uniaxial loading. Multiaxial fatigue assessment is then carried out with the help of an appropriate rule or criterion that reduces the complex multiaxial stress/strain state to an "equivalent" uniaxial stress/strain state. For high cycle fatigue regime, fatigue life is commonly estimated using a combination of stress-based theories and the relationship established by Basquin [1910]. For axial loading, this relationship is given by:

$$\frac{\Delta\sigma}{2} = \sigma_f' \left(2N_f\right)^b \quad , \tag{4.1}$$

and for torsional/shear loading by:

$$\frac{\Delta\tau}{2} = \tau_f' \left(2N_f\right)^{b_\gamma} \quad . \tag{4.2}$$

In terms of elastic axial and shear strain, Eqs. 4.1 and 4.2 can be rewritten as follows:

$$\frac{\Delta\varepsilon^e}{2} = \frac{\sigma_f'}{E} \left(2N_f\right)^b \quad , \tag{4.3}$$

and,

$$\frac{\Delta\gamma^e}{2} = \frac{\tau_f'}{G} \left(2N_f\right)^{b_\gamma} \quad . \tag{4.4}$$

where $\Delta\sigma$ and $\Delta\tau$ are the axial and shear stress ranges, and $\Delta\varepsilon^e$ and $\Delta\gamma^e$ the axial and shear elastic strain ranges, respectively. σ_f' and b are the axial fatigue strength coefficient and exponent, respectively. Analogously, τ_f' and b_γ are the shear fatigue

strength coefficient and exponent, respectively. N_f is the number of reversals ($2N_f$ refers to the number of cycles to failure).

However, many components and structures undergo a few cycles of high amplitude stress during their lifetime (i.e. take-off and landing of aircrafts, start-up and shutdown of power generation plants, etc.). Design for this life region (life typically $< 10^5$ cycles) is referred to as low cycle fatigue design for which localised cyclic plasticity plays an important role. For the past 60 years, cyclic strain has been the basis for low cycle fatigue design. Hence, predictions for low cycle fatigue regime are made by the association of strain-based criteria with the following strain-life relationship for axial loading:

$$\frac{\Delta\varepsilon}{2} = \frac{\Delta\varepsilon^e}{2} + \frac{\Delta\varepsilon^p}{2} = \frac{\sigma'_f}{E}\left(2N_f\right)^b + \varepsilon'_f\left(2N_f\right)^c \quad , \tag{4.5}$$

where $\Delta\varepsilon$ is the total axial strain range, and equal the sum of elastic and plastic strain ranges. ε'_f and c are the axial fatigue ductility coefficient and exponent, respectively. Similarly, for torsional/shear loading, strain-life curve is given by:

$$\frac{\Delta\gamma}{2} = \frac{\Delta\gamma^e}{2} + \frac{\Delta\gamma^p}{2} = \frac{\tau'_f}{G}\left(2N_f\right)^{b_\gamma} + \gamma'_f\left(2N_f\right)^{c_\gamma} \quad . \tag{4.6}$$

where $\Delta\gamma$ is the total shear strain range and equal the sum of elastic and plastic strain ranges. γ'_f and c_γ are the shear fatigue ductility coefficient and exponent, respectively. Eqs. 4.5 and 4.6 are a combination of Basquin's and Coffin-Manson's relationships. Figure 4.2 illustrates a typical strain-life ($\varepsilon - N$) curve in the log-log scale, considering Eq. 4.5. A similar curve can be obtained taking into account a torsional loading condition and Eq. 4.6.

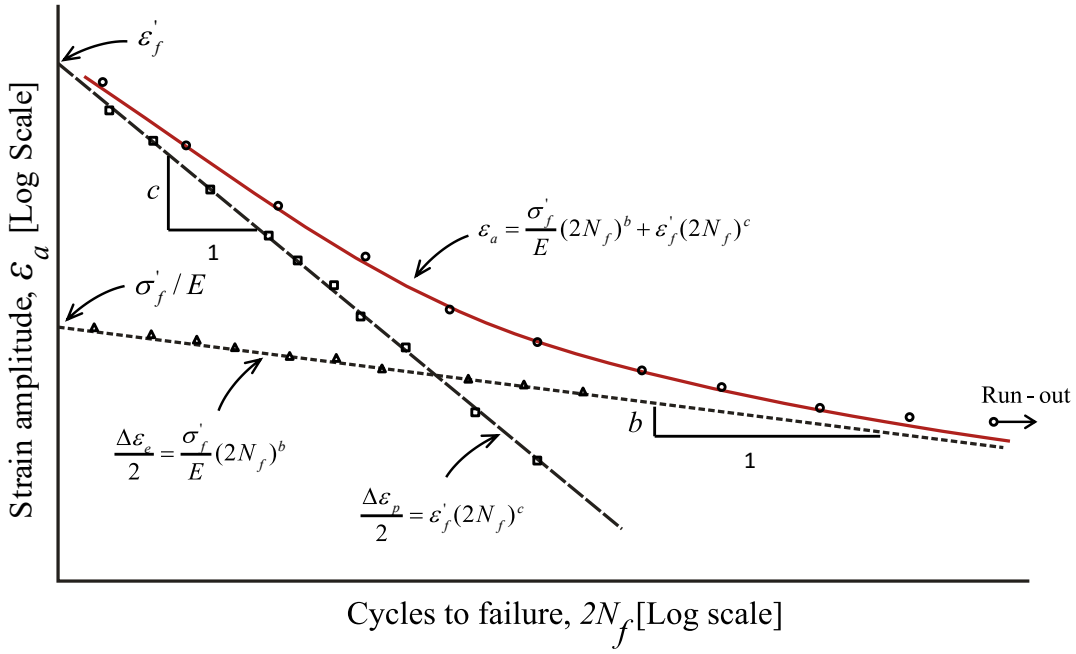


Figure 4.2 – Schematic representation of a typical strain-life curve. Adapted from Mousa [2011].

4.3 Stress-strain response modelling

The load conditions investigated in this research project were always very close or slightly above the yield strength of the Nickel-based superalloys considered. Therefore, a methodology to model the stress-strain response of the Nickel-based superalloys and determine plastic deformation was needed. Figure 4.3 illustrates the typical stress-strain response of a material subjected to cyclic loading, commonly referred to as hysteresis loop. Considering a "Masing-type" behaviour, i.e. assuming that the stabilised hysteresis loop curve of the material may be approximated by doubling the cyclic stress-strain response curve [Mousa, 2011; Ince, 2012], the hysteresis loop may be modelled using the Ramberg-Osgood power law for axial and torsional cyclic loading, respectively, as:

$$\frac{\Delta\,\varepsilon}{2} = \frac{\Delta\,\sigma}{2E} + \left(\frac{\Delta\,\sigma}{2K'}\right)^{\frac{1}{n'}} \quad , \tag{4.7}$$

and,

$$\frac{\Delta\gamma}{2} = \frac{\Delta\tau}{2G} + \left(\frac{\Delta\tau}{2K'_\gamma}\right)^{\frac{1}{n_\gamma{}'}} \quad , \tag{4.8}$$

where K' and n' are the axial fatigue strength coefficient and the cyclic axial strain hardening exponent, respectively. Analogously, K'_γ and $n_\gamma{}'$ are the torsional fatigue strength coefficient and the cyclic torsional strain hardening exponent, respectively.

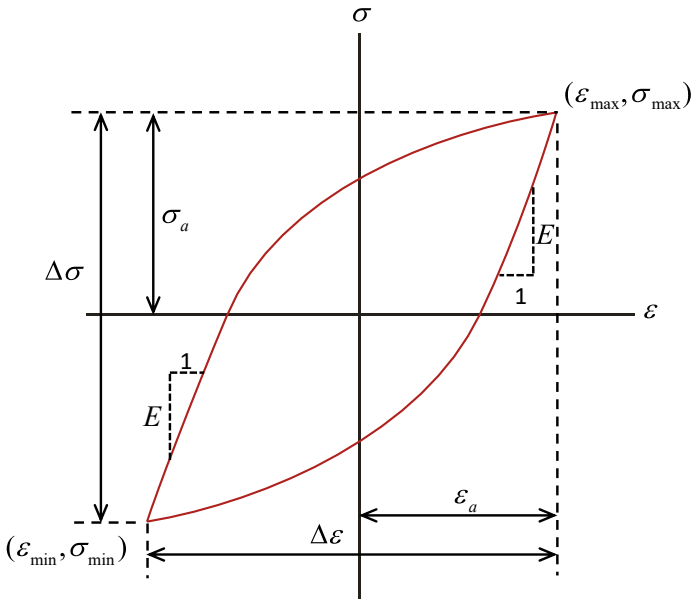


Figure 4.3 – Typical hysteresis loop. Adapted from Mousa [2011].

When a proportional multiaxial loading condition is considered, the elastic and plastic strain components can be calculated considering Hooke's law and Hencky's total deformation plasticity equation [Ince, 2012; Ince et al., 2014]:

$$\varepsilon_{ij} = \frac{1+\nu}{E}\sigma_{ij} - \frac{\nu}{E}\sigma_{kk}\delta_{ij} + \frac{3}{2}\frac{\varepsilon^p_{\text{eq}}}{\sigma_{\text{eq}}}S_{ij} \quad , \tag{4.9}$$

where ε_{ij} represents the total strain components, σ_{ij} the stress components of Cauchy's stress tensor and S_{ij} the deviatoric stress components, given by:

$$S_{ij} = \sigma_{ij} - \frac{1}{3}\sigma_{kk}\delta_{ij} \quad . \tag{4.10}$$

The remaining terms, σ_{eq} and ε^p_{eq}, are measures of equivalent stress and equivalent plastic strain, respectively. The octahedral shear stress and stress, also known as von Mises, are the most widely used equivalent stress and strain measures. They are expressed as follows:

$$\sigma_{\text{eq}} = \sigma_{\text{vM}} = \sqrt{\frac{3}{2} S_{ij} S_{ij}} \quad , \tag{4.11}$$

$$\varepsilon^p_{\text{eq}} = \varepsilon^p_{\text{vM}} = \sqrt{\frac{2}{3} \varepsilon^p_{ij} \varepsilon^p_{ij}} \quad , \tag{4.12}$$

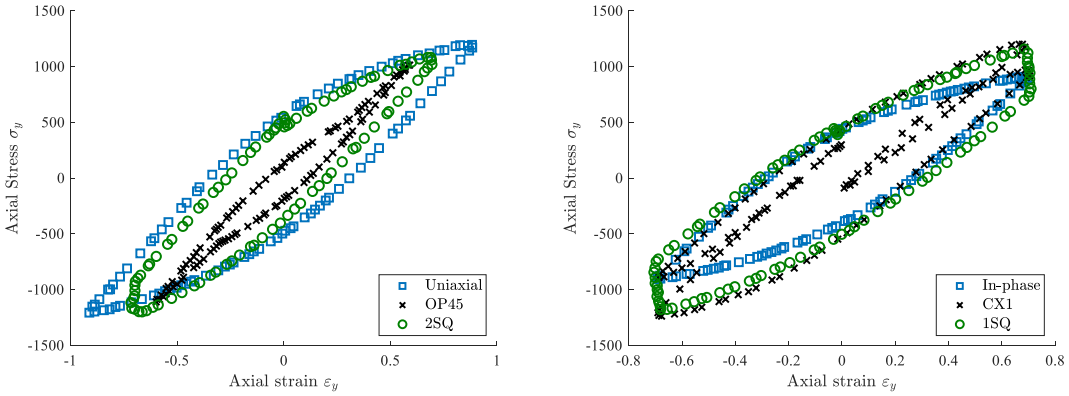
The relationship between these, for the multiaxial stress state, is an extension of Ramberg-Osgood power law for uniaxial loading:

$$\frac{\Delta\ \varepsilon^p_{eq}}{2} = \left(\frac{\Delta\ \sigma_{\text{vM}}}{2\bar{K}'} \right)^{\frac{1}{\bar{n}'}} \quad . \tag{4.13}$$

where the constants $\bar{K}'$ and $\bar{n}'$ are the equivalent cyclic strength coefficient and equivalent cyclic strain hardening coefficient, respectively, representing the intercept and slope of the best fit line to equivalent stress amplitude vs equivalent strain amplitude in a log-log scale.

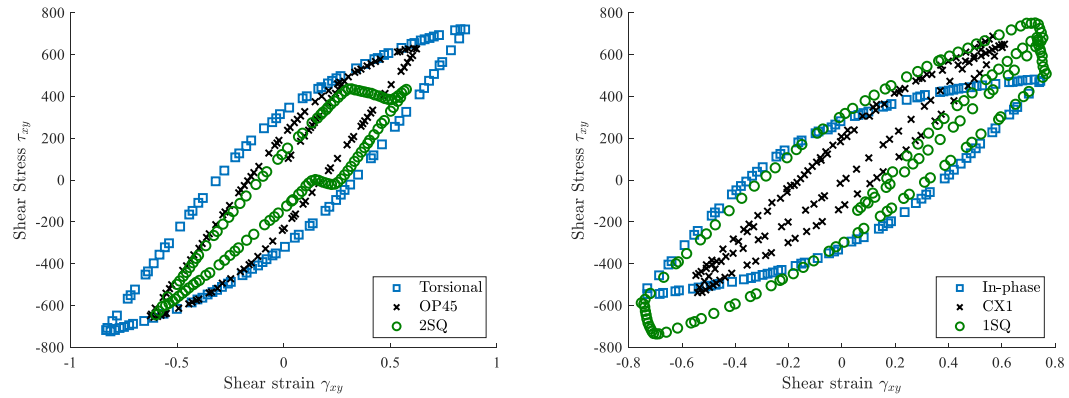
The more commonly used Mises equivalent stress and strain, though a good approximation, are only valid for isotropic material behaviour and cannot be used for non-proportional multiaxial loading, as during non-proportional loading the shape of the hysteresis loop is path dependent [Mousa, 2011]. Therefore, in order to use Hencky's plasticity equation for RR1000, a close inspection of RR1000 hysteresis loop was carried out to verify if the material exhibit an isotropic response under cyclic multiaxial loading. Figures 4.4 and 4.5 illustrate the axial and torsional hysteresis loops for RR1000, respectively. Seven different load conditions are presented: 1) uniaxial; 2) pure torsional; 3) in-phase/proportional; 4) trapezoidal waveforms 45° out-phase

(OP45); 5), two squares, tension-counter clockwise torsion and compression-clockwise torsion (2SQ); 6) CX1 (presented in chapter 3); trapezoidal waveforms 90º out-phase (1SQ).



(a) **(b)**

Figure 4.4 – Half-life hysteresis loops for RR1000 – Axial strain vs stress. Adapted from Bees [2016].



(a) **(b)**

Figure 4.5 – Half-life hysteresis loops for RR1000 – Shear strain vs stress. Adapted from Bees [2016].

As it can be observed in Figs. 4.4 and 4.5, the general response of RR1000 is isotropic, with the exception of the 2SQ load condition. However, this load condition was not investigated in this doctoral research project. Therefore, the only modification needed for the application of Hencky's formulation to the RR1000 test programme was a correction for the additional non-proportional hardening. For that, the correction proposed by Shamsaei, Fatemi & Socie [2010], that takes into account the additional hardening

and the severity of multi-axial loading to differentiate between the proportional and non-proportional load cases, was adopted. Shamsaei et al.'s correction is formulated as follows:

$$\frac{\Delta\,\varepsilon_{\mathrm{eq}}^{p}}{2}=\left(\frac{\Delta\,\sigma_{\mathrm{vM}}}{2\bar{K}'(1+\alpha F)}\right)^{\frac{1}{\bar{n}'}} \quad , \tag{4.14}$$

where F is the non-proportional factor proposed by Kanazawa et al. [1979] and illustrated in chapter 3 of this doctoral thesis. Table 4.1 summarises the non-proportional factor for each of the load paths investigated with RR1000. α is the material dependent non-proportional hardening coefficient, introduced by Socie & Marquis [1999] and found from the following relationship:

$$\alpha=\frac{\sigma_{OP}}{\sigma_{IP}}-1 \quad , \tag{4.15}$$

where σ_{OP} and σ_{IP} are the out-of-phase (non-proportional) and in-phase (proportional) stresses, respectively. For RR1000, $\alpha = 0.25$, which is fairly low in contrast to other materials such as stainless steel 304 that presents higher levels of additional non-proportional hardening with $\alpha = 0.90$ [Socie & Marquis, 1999; Bees, 2016].

Table 4.1 – Non-proportionality load factors for RR1000 load paths.

Stress Path	***F***
Two-triangles (L1)	0.44
Hourglass (HG)	1.0
One Square (1SQ)	1.0
Four squares (4SQ)	1.0
Cross – CX1	1.0
Cross – CX2	1.0

4.4 Critical plane search

For a loaded specimen, stress and strain magnitudes at a given point vary depending on the orientation of a plane passing through that point. In this work, stress and strain components on arbitrary planes are calculated using a coordinate transformation matrix with respect to plane orientation. The coordinate system, x – y – z, is shown in Fig. 4.6. The planes of interest are obtained by first rotating the coordinate system by an angle θ about the x-axis (Eq. 4.16) and then by an angle ϕ about the z axis (Eq. 4.17). The rotation matrix for rotations about x and z are given respectively by:

$$a_\theta = \begin{bmatrix} 1 & 0 & 0 \\ 0 & \cos\theta & \sin\theta \\ 0 & -\sin\theta & \cos\theta \end{bmatrix} , \tag{4.16}$$

$$a_\phi = \begin{bmatrix} \cos\phi & \sin\phi & 0 \\ -\sin\phi & \cos\phi & 0 \\ 0 & 0 & 1 \end{bmatrix} . \tag{4.17}$$

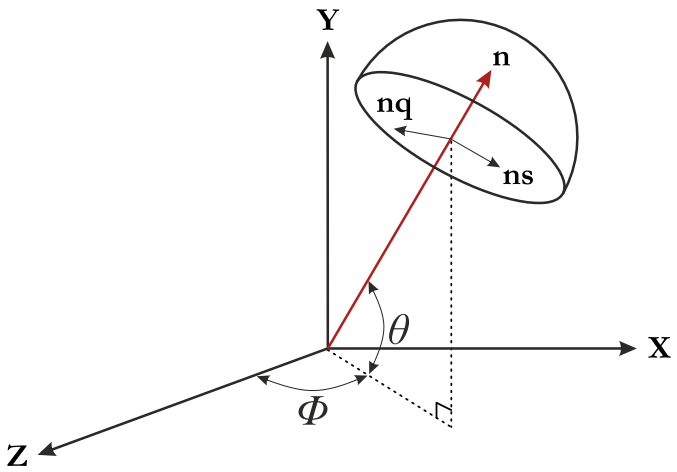


Figure 4.6 – Orientation of plane in three-dimensional co-ordinate system.

Finally, the general transformation matrix for rotations about x-axis first and then z-axis is defined as:

$$a_{\theta\phi} = a_{\theta} a_{\phi} = \begin{bmatrix} cos\theta & \sin\theta\cos\phi & \sin\theta\sin\phi \\ -\sin\theta & \cos\theta\cos\phi & \cos\theta\sin\phi \\ 0 & -\sin\phi & \cos\ \phi \end{bmatrix} \quad . \tag{4.18}$$

Consequently, the stresses and strains on specific planes can be calculated by:

$$\sigma'_{ij} = a_{\theta\phi}\sigma_{ij}a^{\mathsf{T}}_{\theta\phi} \quad , \tag{4.19}$$

$$\varepsilon'_{ij} = a_{\theta\phi}\varepsilon_{ij}a^{\mathsf{T}}_{\theta\phi} \quad , \tag{4.20}$$

where $a^{\mathsf{T}}_{\theta\phi}$ defines the transpose of the general transformation matrix presented in Eq. 4.18.

For the critical plane approaches investigated in this work, the critical plane is assumed as the plane experiencing the maximum amount of fatigue damage. For instance, this could be the plane of maximum shear strain range or the plane experiencing the maximum normal strain. In order to compute fatigue damage parameters on specific planes, stress and strain components need to be discretised in time – which is essential for non-proportional loading investigations as the principal stress/strain direction changes constantly with respect to the axes of the specimen – and expressed on the local coordinate system of that plane according to Eqs. 4.19 and 4.20.

It was shown in Chapter 3 that, for LCF tests with both Waspaloy and RR1000, cracks initiated on the free surface of the specimens from the points of maximum von Mises equivalent stress, as identified in the reported FE analyses. Therefore, the transformation of stress and strain tensors is computed using the loading histories from these hot spots. Eqs. 4.21 and 4.22 present the stress and strain tensors written in terms of the loading history discretised in time:

$$\sigma_{ij}^{(t)} = \begin{bmatrix} \sigma_{\mathrm{xx}}^{(t)} & \tau_{\mathrm{xy}}^{(t)} & 0 \\ \tau_{\mathrm{xy}}^{(t)} & \sigma_{\mathrm{yy}}^{(t)} & 0 \\ 0 & 0 & 0 \end{bmatrix} \quad , \tag{4.21}$$

$$\varepsilon_{ij}^{(t)} = \begin{bmatrix} \varepsilon_{\mathrm{xx}}^{(t)} & \gamma_{\mathrm{xy}}^{(t)} & 0 \\ \gamma_{\mathrm{xy}}^{(t)} & \varepsilon_{\mathrm{yy}}^{(t)} & 0 \\ 0 & 0 & \varepsilon_{\mathrm{zz}}^{(t)} \end{bmatrix} \quad . \tag{4.22}$$

the variation of stress and strain components in time subjected to a sinusoidal cyclic loading is given by:

$$\sigma_{ij}^{(t)} = \sigma_{ij,\mathrm{mean}} + \sigma_{ij,\mathrm{a}} \ \sin(\omega t - \varphi) \quad , \tag{4.23}$$

$$\varepsilon_{ij}^{(t)} = \varepsilon_{ij,\mathrm{mean}} + \varepsilon_{ij,\mathrm{a}} \ \sin(\omega t - \varphi) \quad . \tag{4.24}$$

where $\sigma_{ij,\mathrm{a}}$ represents the stress amplitude and $\sigma_{ij,\mathrm{mean}}$ the mean stress. Analogously, $\varepsilon_{ij,a}$ and $\varepsilon_{ij,m}$ represents the amplitude and mean strain, respectively. ω represents the loading frequency and φ the phase shift. For the tension-torsion non-proportional tests with RR1000 a phase shift φ is applied to the torsional command.

For each discretised time instant (Δt assumed as 1/360 in this work), the maximum and minimum stresses and strains are calculated on all possible failure planes by varying θ and ϕ in Eqs. 4.19 and 4.20 from 0° to 180° in steps of 1°. Once normal and shear stress and strain components are calculated for all possible directions, then, the fatigue damage parameters can be evaluated on each plane to determine the critical plane experiencing the maximum fatigue damage i.e. where the fatigue damage parameter is maximised [Ince, 2012].

4.5 Stress-based criteria

Stress-based criteria were initially proposed for the HCF regime where plasticity takes place only at the mesoscopic level and the macroscopic behaviour is elastic [Mamiya et al., 2009]. However, these parameters can be extended to the LCF regime for the assessment of materials that exhibit limited macroscopic plasticity and overall elastic behaviour. Although not ideal, these parameters can provide a good first estimation, with relative simplicity, for investigations with limited material data, as stresses can be easily calculated from load cell readings from experiments with standard specimen geometries. Strains on the other hand requires direct measurements or finite element modelling for their determination. Stress-based criteria are generally formulated taking into account the physical effects governing fatigue. In this sense, shear stress parameters are incorporated in order to capture plasticity and slippage on material planes, and normal stress functions introduce the effect of mean stress and nucleation of micro-cracks (opening/closing of them).

Stress based formulations are normally classified into certain classes according to the stress measure used to quantify the fatigue damage associated with a given load history [Mamiya et al., 2009; Araújo et al., 2011]. This section presents fatigue predictions obtained with propositions in the classes of equivalent stress /extended yield criteria and stress invariant approaches. Fatigue predictions obtained with stress-based critical plane parameters are analysed in the following section, along with strain- and energy-based critical plane parameters.

4.5.1 Static yield criteria

Static yield parameters characterise the general multiaxial stress state through a scalar quantity. Thus, in order to correlate the experimental results, a single parameter based on a combination of the loads direction can be used. Two simple candidate parameters were examined initially: von Mises equivalent stress and elastic strain energy equivalent

stress. These yield theories were extended to multiaxial fatigue and combined with Basquin's relationship for life prediction.

There are two main reasons why equivalent stress parameters adapted from static yield theories are used as candidates for the description of fatigue behaviour of materials under complex multiaxial stress states. The first one is the advantage of using non-complex and inexpensive uniaxial tests for model calibration. The second refers to the possibility of collapsing different loading conditions into one single curve by means of simple stress corrections and the relationship established between stress and fatigue life proposed by Basquin. The drawback of these straightforward criteria is that they are not suitable for out-of-phase or non-proportional loading conditions as these formulations have a fixed tension-torsion relation [Bannantine et al., 1990; Socie & Marquis, 1999; Shamsaei et al., 2011]. They require thus corrections for correlating non-proportional fatigue data.

4.5.1.1 Octahedral shear stress – von Mises criterion

Among the extended yield criterion theories, the most popular one is the octahedral shear stress theory, commonly termed as von Mises' theory, σ_{vM}. Equation 4.11 presents von Mises equivalent stress in its most general form. Expanding it, von Mises equivalent stress becomes:

$$\Delta\sigma_{vM} = \sqrt{\frac{\left(\Delta\sigma_x - \Delta\sigma_y\right)^2 + \left(\Delta\sigma_x - \Delta\sigma_z\right)^2 + \left(\Delta\sigma_y - \Delta\sigma_z\right)^2 - \ 6\ \left(\Delta\tau_{xy}^2 + \Delta\tau_{xz}^2 + \Delta\tau_{yz}^2\right)}{2}}. \tag{4.25}$$

Equation 4.25 is only valid for proportional or in-phase loading. During non-proportional or out-of-phase loading $\Delta\sigma_1 - \Delta\sigma_3 \neq \Delta\left(\sigma_1 - \sigma_3\right)$ so that no unique definition of the shear stress exists. The use of von Mises criterion for out-of-phase loading has often been shown not to be successful [Fatemi & Socie, 1988]. For the biaxial

programme, considering plane stress and no shear, von Mises equivalent stress can be expressed as:

$$\sigma_{\mathrm{vM}} = \sqrt{\sigma_{\mathrm{x}}^2 + \sigma_{\mathrm{y}}^2 - 2\sigma_{\mathrm{x}}\sigma_{\mathrm{y}}} \quad , \tag{4.26}$$

For proportional tension-torsion stress condition with only $\sigma_{\mathrm{y}} \neq 0$ and $\tau_{\mathrm{xy}} \neq 0$, Eq. 4.25 reduces to:

$$\sigma_{\mathrm{vM},IP} = \sqrt{\sigma_{\mathrm{y}}^2 + 3\tau_{\mathrm{xy}}^2} \quad , \tag{4.27}$$

and for non-proportional tension-torsion stress conditions considering Shamsaei et al.'s correction (Eq. 4.14), Eq. 4.27 becomes:

$$\sigma_{\mathrm{vM},OP} = (1 + \alpha F)\sqrt{\sigma_{\mathrm{y}}^2 + 3\tau_{\mathrm{xy}}^2} \quad . \tag{4.28}$$

Alternatively the von Mises equivalent stress amplitude can be calculated according to the Minimum Circumscribed Hypersphere (MCH) method proposed by Papadopoulos [1997], where the amplitude of the equivalent stress measure is assumed as the radius, $\boldsymbol{s}_a$, of the minimum hypersphere circumscribing the load path Ψ projected onto the deviatoric stress space π. Figure 4.7 illustrates the MCH method. The mean value of the shear stress is the length of the vector that points from the origin, O, to the centre of the minimum circumscribed hypersphere, $\boldsymbol{s}_m$.

To facilitate the calculation of von Mises equivalent stress amplitude, it can be rewritten in terms of the amplitude of the second invariant of the deviatoric tensor, i.e. $\sigma_{\mathrm{vM},a} = \sqrt{3J_{2,a}}$. However, as the definition of its amplitude and mean value is a complicated task, the following transformation rules for the deviatoric stresses presented by Papadopoulos [1997] and Balthazar & Malcher [2007] are adopted:

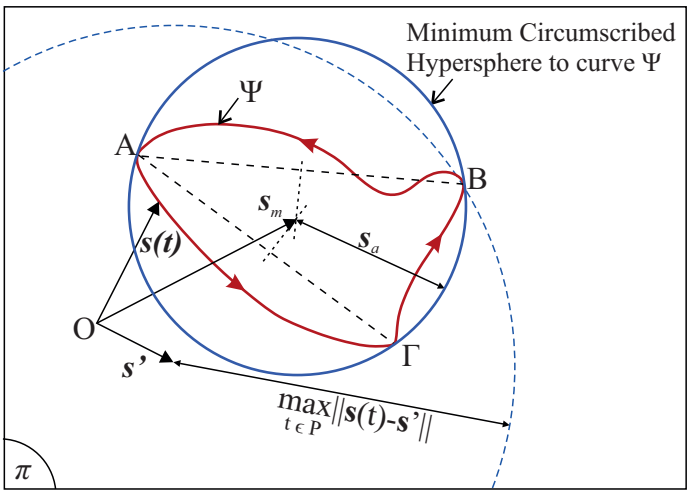


Figure 4.7 – Schematic representation of the Minimum Circumscribed Hypersphere. Adapted from Papadopoulos [1997].

$$s_1 = \frac{\sqrt{3}}{2}\sigma_x \; ; \; s_2 = \frac{1}{2}\left(\sigma_y - \sigma_z\right) \; ; \; s_3 = \sigma_{xy} \; ; \; s_4 = \sigma_{xz} \; ; \; s_5 = \sigma_{yz} \quad . \tag{4.29}$$

With the above transformation rules, the six components of the deviatoric stress tensor, $\boldsymbol{S}_{ij}$, may be mapped onto a vector of a five dimensional Euclidean space, $\boldsymbol{s}$, allowing the stress deviator to be fully described by fewer components in the transformed space [Papadopoulos, 1997; Balthazar & Malcher, 2007].

$$\boldsymbol{s} = [s_1 \;\; s_2 \;\; s_3 \;\; s_4 \;\; s_5]^\intercal \quad . \tag{4.30}$$

The length of vector $\boldsymbol{s}$ is given by its Euclidean norm, where:

$$\sqrt{J_2} = \sqrt{\frac{1}{2}\boldsymbol{S}_{ij} : \boldsymbol{S}_{ij}} = \sqrt{\boldsymbol{s} \cdot \boldsymbol{s}} \quad . \tag{4.31}$$

Hence, the length of the vector $\boldsymbol{s}_m$ that points to the centre of the hypersphere is equal to the mean value $\sqrt{J_{2,m}}$, whereas the radius of this sphere is equal to $\sqrt{J_{2,a}}$. The process of finding the centre, s_m, of the MCH to the load path ψ is mathematically formulated as a min-max problem given by:

$$s_m : \min_{\boldsymbol{s}'} \left\{ \max_{t \in P} \|\boldsymbol{s}(t) - \boldsymbol{s}'\| \right\} \quad , \tag{4.32}$$

where t denotes the time instant inside each period denoted as P. Once s_m has been determined, the von Mises equivalent stress amplitude can be obtained according to the following relationship with the amplitude of the second invariant, $\sqrt{J_{2,a}}$:

$$\frac{\sigma_{\mathrm{vM},a}}{\sqrt{3}} = \sqrt{J_{2,a}} = \max_{t \in P} \|\boldsymbol{S}(t) - \boldsymbol{S_m}\| \quad , \tag{4.33}$$

Figure 4.8 displays the collapse of the biaxial test data by von Mises parameter normalised against life to failure. It is clear that the parameter is able to provide a reasonable collapse of the uniaxial stress (US), uniaxial load (UL) and high stress pure shear (PS) test cases. However, despite the overall good correlation ($R^2 = 0.655$), the parameter shows significant scatter for the other test cases, with the low stress PS case the farthest from the best fit line.

Figures 4.9 and 4.10 illustrate the correlation of the RR1000 tension-torsion test data by von Mises parameter with and without the non-proportional correction presented in Eq. 4.28, where $\sigma_{\mathrm{vM,OP}} = (1 + \alpha F)\, \sigma_{\mathrm{vM,IP}}$. Figure 4.10 exhibits a clear distinction between test cases with non-proportionality factor $F = 1$ and the L1 test cases with $F = 0.44$. The adoption of a stress correction clearly improves substantially the collapse of the test data, achieving an almost perfect correlation of $R^2 = 0.9857$.

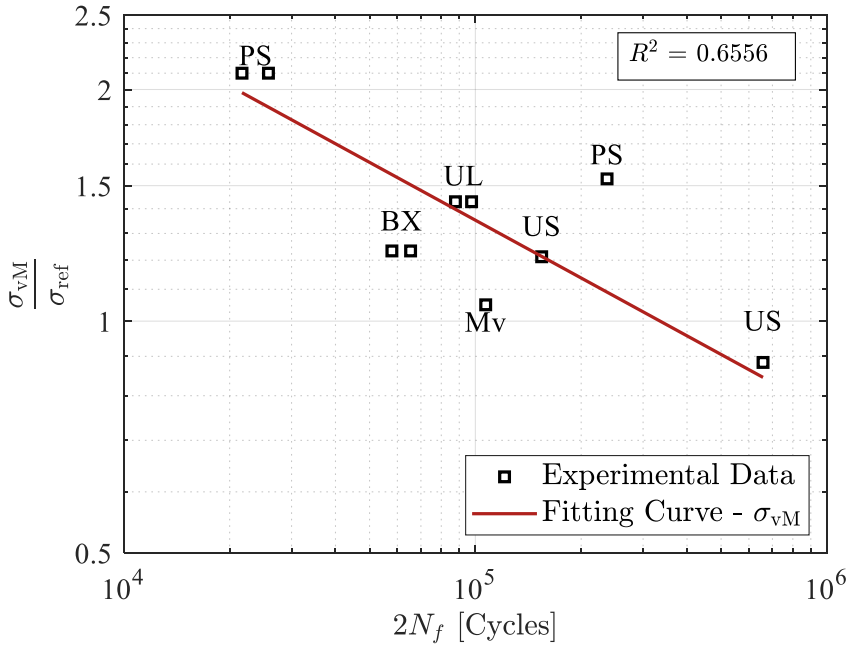


Figure 4.8 – Peak von Mises stress vs life – Waspaloy.

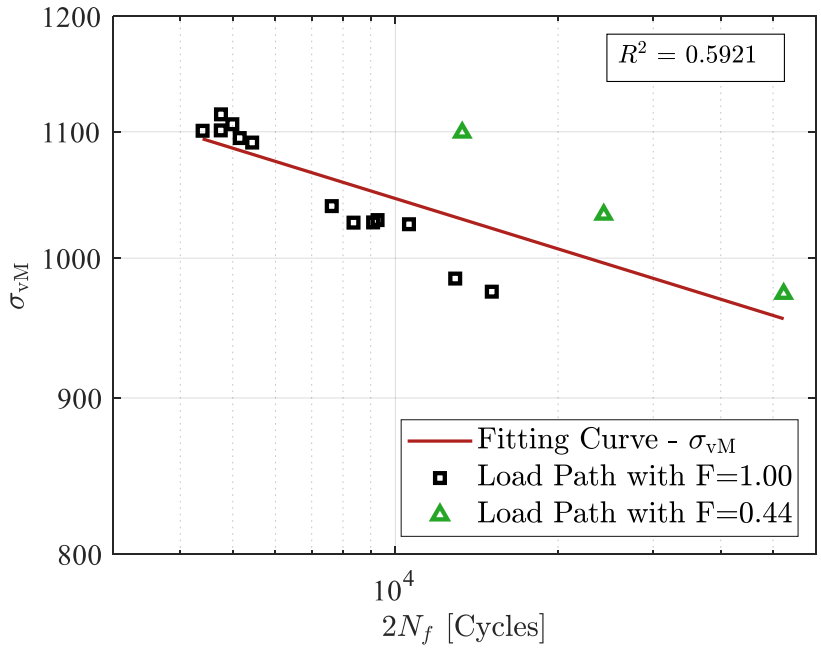


Figure 4.9 – Peak von Mises peak stress vs life, without non-proportional loading correction – RR1000.

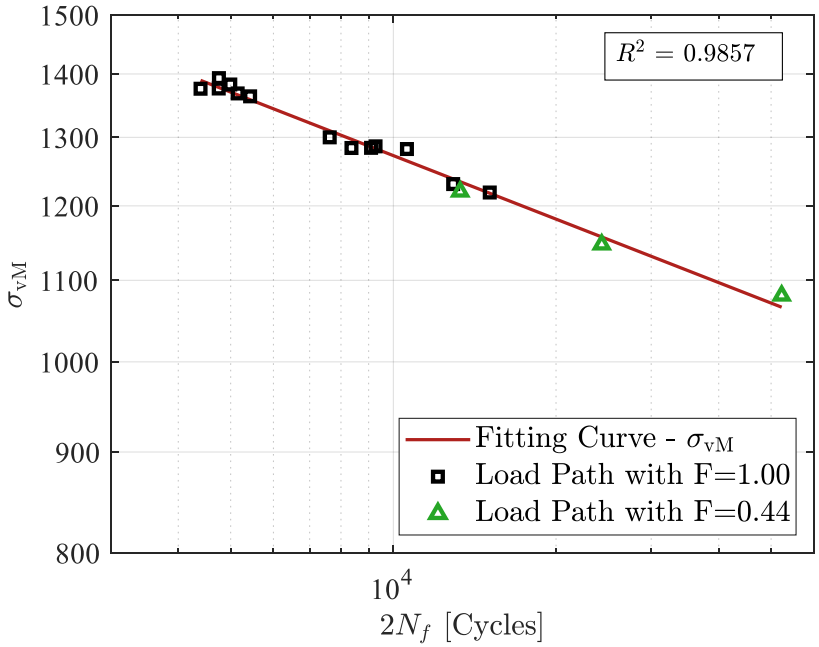


Figure 4.10 – Peak von Mises peak stress vs life, with non-proportional loading correction – RR1000.

4.5.1.2 Elastic strain energy density equivalent stress

Elastic strain energy is defined as the mechanical energy stored up in an elastically stressed system, i.e. in an elastic body, which is being deformed, the internal work per unit volume is completely transformed into strain energy. For an idealised elastic body, the stored energy is completely recoverable when the solid is returned to its original unstrained configuration. In order to quantify this behaviour, the strain energy is determined in terms of the resulting stress and strain fields within the elastic solid.

In its most general form, the elastic strain energy density is defined as the sum of the products of strain and stress, divided by 2:

$$U_e = \frac{1}{2}\sigma_{ij}\varepsilon_{ij} \quad . \tag{4.34}$$

Expanding Eq. 4.34, the elastic strain energy density can be rewritten as,

$$U_e = \frac{1}{2}\left(\sigma_x\varepsilon_x + \sigma_y\varepsilon_y + \sigma_z\varepsilon_z + \tau_{xy}\gamma_{xy} + \tau_{xz}\gamma_{xz} + \tau_{yz}\gamma_{yz}\right) \quad . \tag{4.35}$$

For the cases of uniaxial, equi-biaxial, and tension-torsion loading, U_e in Eq. 4.35 reduces to $U_{e,UX}$, $U_{e,EB}$, and $U_{e,TT}$ respectively:

$$U_{e,UX} = \frac{1}{2}\left(\sigma_x\varepsilon_x\right) \quad , \tag{4.36}$$

$$U_{e,EB} = \frac{1}{2}\left(\sigma_x\varepsilon_x + \sigma_y\varepsilon_y\right) \quad , \tag{4.37}$$

$$U_{e,TT} = \frac{1}{2}\left(\sigma_y\varepsilon_y + \tau_{xy}\gamma_{xy}\right) \quad , \tag{4.38}$$

which considering the stress and strain relationship given by Hooke's law for these stress states become:

$$U_{e,UX} = \frac{1}{2E}\left(\sigma_x^2\right) \quad , \tag{4.39}$$

$$U_{e,EB} = \frac{1}{2E}\left(\sigma_x^2 + \sigma_y^2 - 2\nu\sigma_x\sigma_y\right) \quad , \tag{4.40}$$

$$U_{e,TT} = \frac{1}{2E}\left(\sigma_y^2 + 2\left(1+\nu\right)\tau_{xy}^2\right) \quad . \tag{4.41}$$

An equivalent stress measure for collapsing the biaxial stress state is defined by equating Eq. 4.40 to Eq. 4.39, i.e. by defining a uniaxial stress measure with elastic strain energy equivalent to a biaxial stress state. The result is:

$$\sigma_{\mathrm{Ue,EB}} = \sqrt{\sigma_x^2 + \sigma_y^2 - 2\nu\sigma_x\sigma_y} \quad . \tag{4.42}$$

Analogously, the uniaxial stress with elastic strain energy equivalent to a tension-torsion loading case is calculated by equating Eq. 4.41 to Eq. 4.39, resulting in:

$$\sigma_{\mathrm{Ue,TT}} = \sqrt{\sigma_y^2 + 2\left(1+\nu\right)\tau_{xy}^2} \quad . \tag{4.43}$$

Considering the non-proportional loading correction, Eq. 4.43 becomes:

$$\sigma_{\mathrm{Ue,OP}} = (1 + \alpha F)\sqrt{\sigma_{\mathrm{y}}^2 + 2\,(1+\nu)\,\tau_{\mathrm{xy}}^2} \quad . \tag{4.44}$$

Figure 4.11 presents the correlation between this parameter normalised and the test data in cycles to failure, considering the nominal stress values presented for Waspaloy. The criterion provided good results with a correlation coefficient, R^2, of 0.868, an improvement with respect to von Mises parameter. However, the peak elastic strain energy parameter also failed to collapse the low stress PS test case. Figures 4.12 and 4.13 illustrates the collapse presented by the elastic energy parameter without and with the non-proportional loading correction, respectively. An even greater improvement can be observed in this case, with $R^2 = 0.986$ from just $R^2 = 0.596$ without correction.

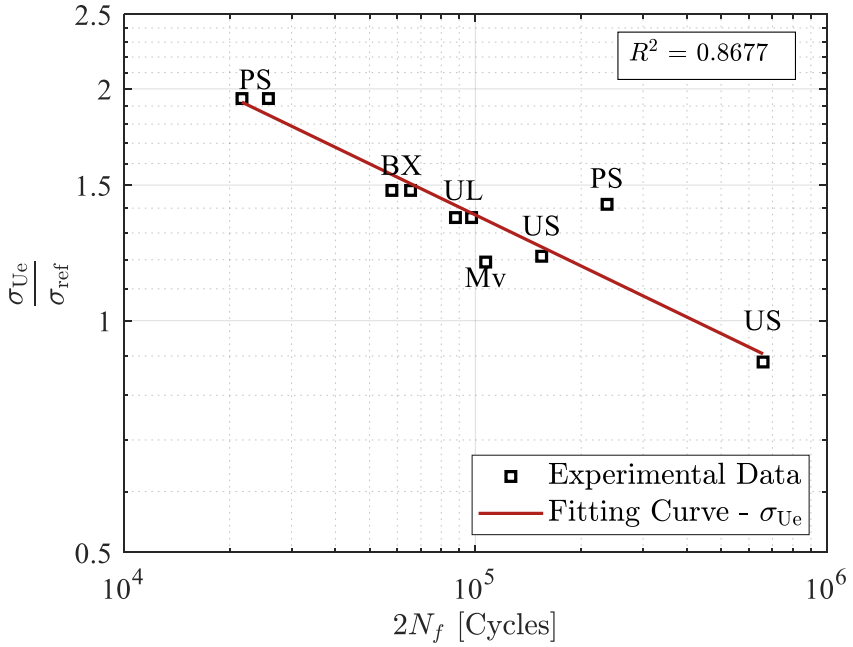


Figure 4.11 – Peak elastic strain energy equivalent stress vs life – Waspaloy.

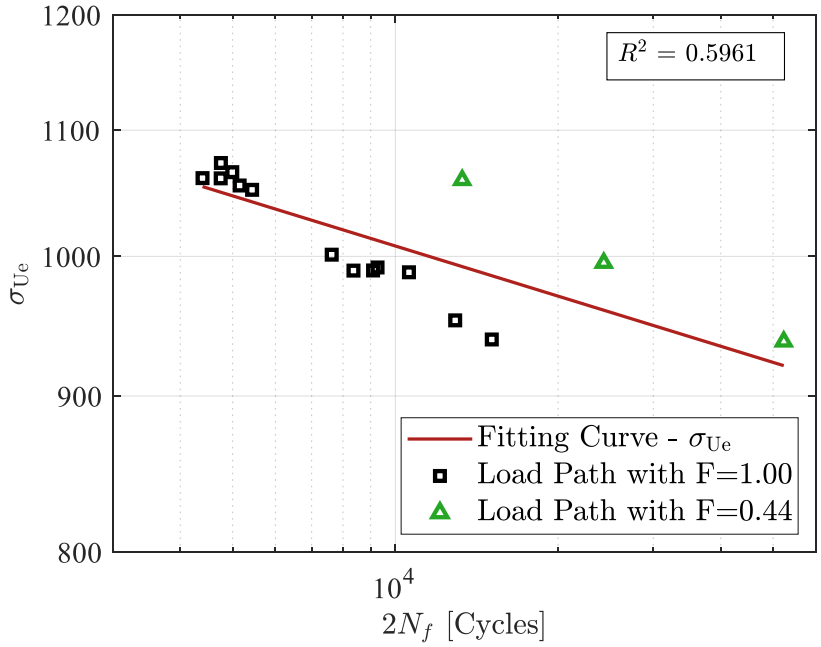


Figure 4.12 – Peak elastic strain energy equivalent stress vs life, without non-proportional loading correction – RR1000.

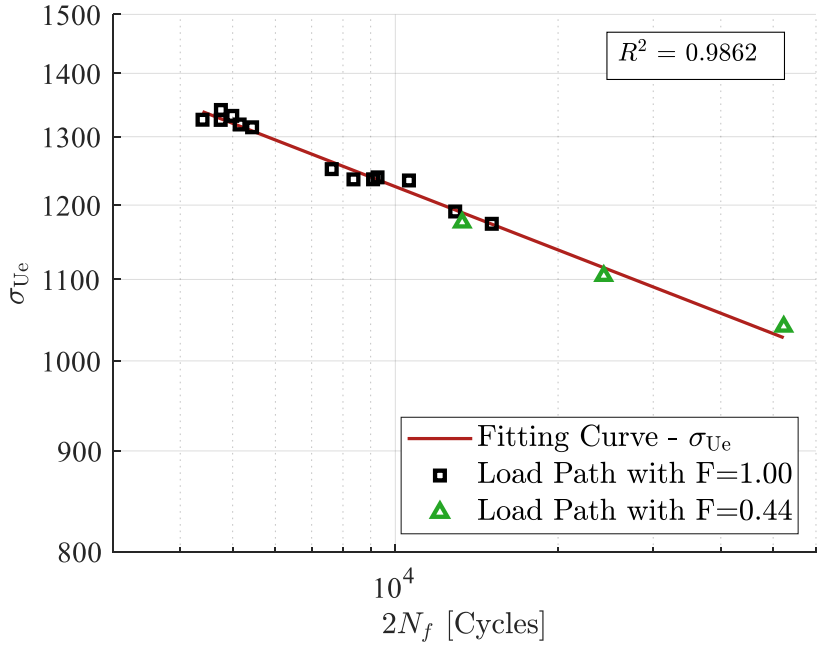


Figure 4.13 – Peak elastic strain energy equivalent stress vs life, with non-proportional loading correction – RR1000.

4.5.1.3 Walker stress

Walker [1970] proposed an effective stress to account for the effect of stress ratio on crack propagation and fatigue lives of aluminium alloys. This criterion was originally proposed as:

$$\sigma_{\mathrm{W}} = (\sigma_{\max})^{1-m} (\Delta\sigma)^{m} \quad . \tag{4.45}$$

In order to reduce scatter seen on the results presented by the elastic strain energy equivalent stress parameter and account for mean stress effects seen on the biaxial tests ($R = 0.05$), the energy parameter was associated with the Walker stress criterion [Walker, 1970], and formulated as:

$$\sigma_{\mathrm{W,Ue}} = \left(\sigma_{\mathrm{Ue,peak}}\right)^{1-m} (\sigma_{\mathrm{Ue,a}})^{m} \quad , \tag{4.46}$$

where $\sigma_{\mathrm{Ue,peak}}$ and $\sigma_{\mathrm{Ue,a}}$ are the peak and amplitude of the elastic strain energy equivalent stress, respectively. σ_W represents the Walker stress and m the Walker exponent, a fitting parameter used to collapse both mean stress and multi-axial effects. The exponent was optimised, considering the entire data set, to $m = 0.645$ for Waspaloy and $m = 0.40$ for RR1000.

Figure 4.14 shows a considerable improvement in the collapse of the Waspaloy biaxial test data in comparison with the elastic strain energy parameter alone (Fig. 4.11). Scatter was reduced specially for the pure shear loading condition at a lower stress level and the minimum von Mises load cases. Figures 4.15 and 4.16 present the analogous analysis for RR1000. As the tension-torsion test programme was carried out without mean stresses, i.e. $R = -1$, there is not a significant improvement in the collapse of test data by the implementation of the Walker parameter. It can be concluded thus that it is the non-proportional loading correction factor that drives improvement in correlation.

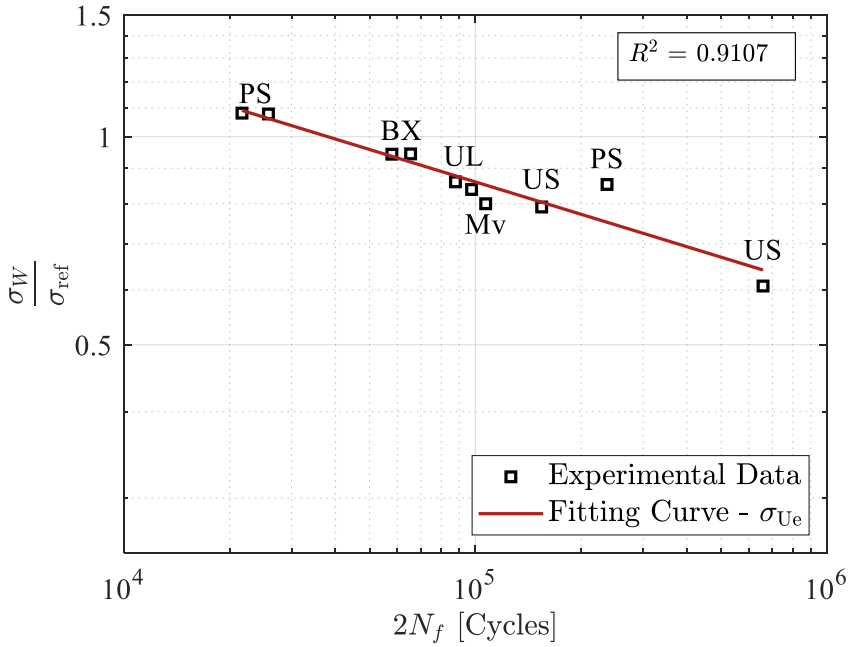


Figure 4.14 – Walker stress with elastic strain energy equivalent stress – Waspaloy.

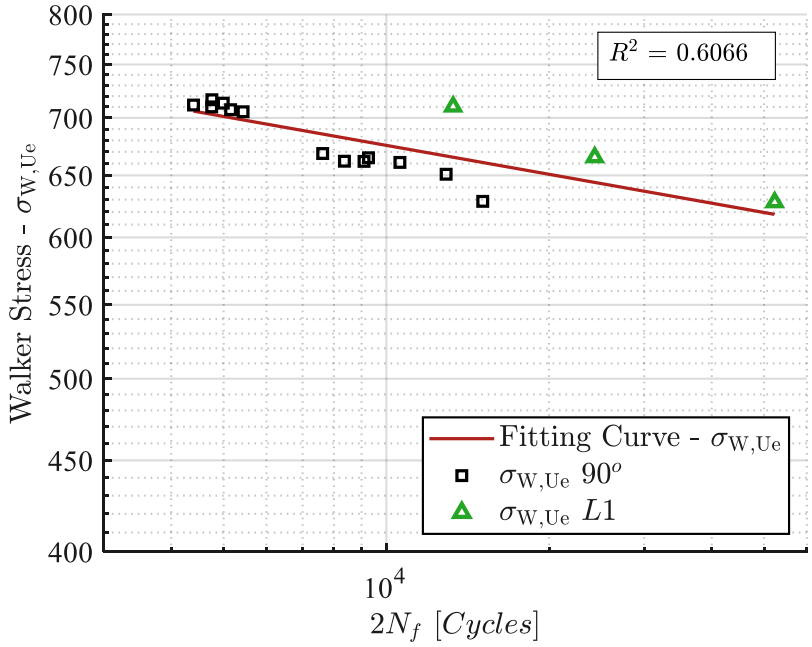


Figure 4.15 – Walker stress with elastic strain energy equivalent stress, without non-proportional loading correction – RR1000

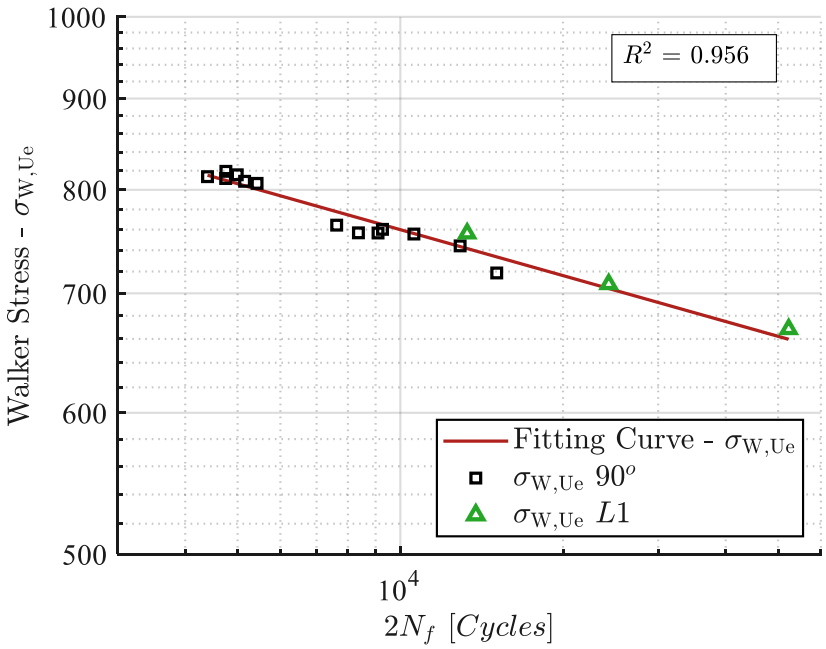


Figure 4.16 – Walker stress with elastic strain energy equivalent stress, with NP correction – RR1000

4.5.2 Invariant-based approaches

Stress Invariant approaches, criteria are formulated taking into account the invariants of the stress tensor and/or of the deviatoric stress tensor. Generally, these formulations directly relate the second invariant of the deviatoric stress tensor $\left(J_2 = \frac{1}{2} S_{ij} : S_{ij}\right)$ and the first invariant of the stress tensor ($I_1 = tr\left(\sigma_{ij}\right) = 3\sigma_{\mathrm{h}}$, where σ_{h} is the hydrostatic stress). In general, this class of multiaxial fatigue models is formulated as:

$$f(\tau) + \kappa g(\sigma) \leq \lambda \quad , \tag{4.47}$$

where $f(\tau)$ and $g(\sigma)$ are shear and normal stress functions respectively. κ and λ represent material parameters, obtained with two independent tests (generally fully reversed or repeated torsion and tension tests).

As these models are typically calibrated under tension-torsion conditions, they tend to give less accurate life predictions outside the calibration region. Figure 4.17 represents how the results of this class of formulations are normally presented, in a

shear stress amplitude vs measure of normal stress plot. The light grey shade area corresponds to the calibration region (tension-torsion) and is delimited by the uniaxial tension and uniaxial compression dashed lines. The darker grey shade area delimited by the equi-biaxial line is of particular interest for the biaxial test programme with Waspaloy, as many test cases lie in this region. Different line fonts exemplify fatigue life thresholds, i.e. a test case below a line is predicted to have a longer life than the threshold of the line. On the other hand, a point above it represents a test case with shorter life.

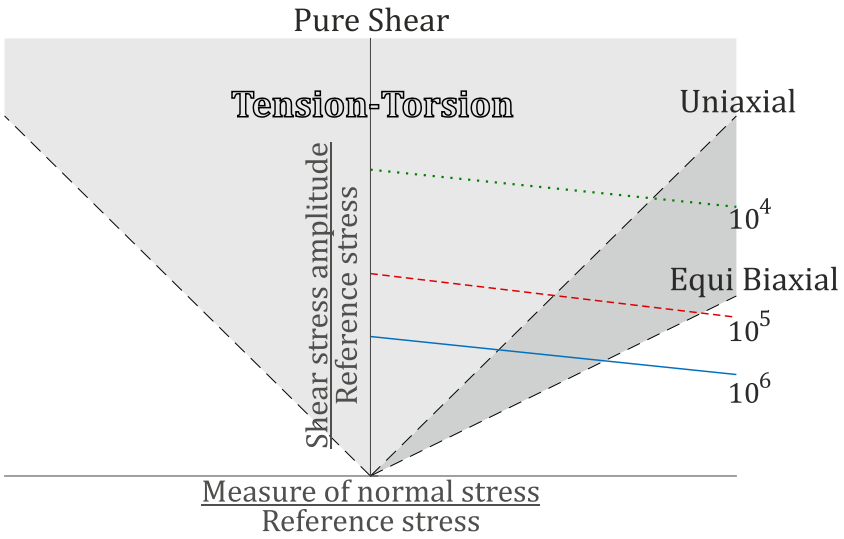


Figure 4.17 – Typical result representation of stress based multiaxial fatigue models.

The main issue with parameters based on stress tensor invariants is that they are not able to distinguish between proportional and non-proportional stress paths. Therefore, in order to overcome this limitation and improve fatigue life prediction for non-proportional loading conditions, the measure of shear stress amplitude proposed by Mamiya et al. [2009] and referred to as the Maximum Prismatic Hull (PH) was adopted. In this method, the maximum rectangular Prismatic Hull enclosing the stress history projected onto deviatoric stress space is used to define the shear stress amplitude. Figure 4.18 illustrates the use of the maximum PH. This method provides the same shear stress amplitudes for proportional load paths as other formulations such as von Mises effective stress and the widely used Minimum Circumscribed Hypersphere

(MCH) presented by Papadopoulos [1997] and mathematically determined previously. However, the PH method is more efficient computationally and can be used for complex non-proportional load paths.

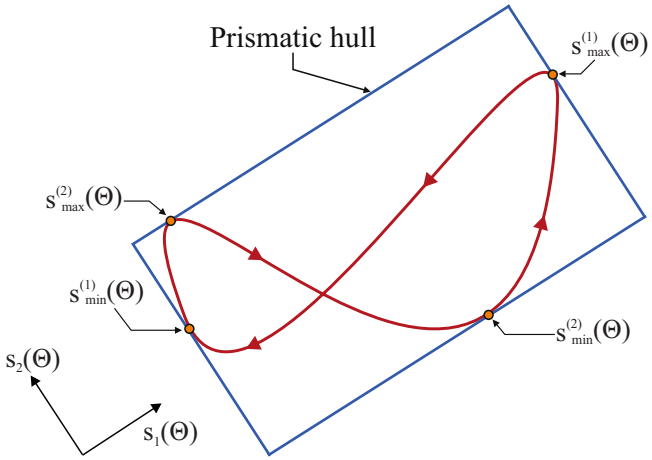


Figure 4.18 – Stress path s and its boundary points tangent to a Θ-oriented prismatic hull. Adapted from Mamiya et al. [2009]

Similar to the transformation rules presented in Eq. 4.29 for the mathematical definition of the MCH method. The PH method adopts the following transformation rules to represent the deviatoric stress components through the five-dimensional vector $\boldsymbol{s}$ [Mamiya et al., 2009]:

$$s_1 = \frac{1}{\sqrt{6}}\left(2\sigma_x - \sigma_y - \sigma_z\right);\ s_2 = \frac{1}{\sqrt{2}}\left(\sigma_y - \sigma_z\right);\ s_3 = \sqrt{2}\sigma_{xy};\ s_4 = \sqrt{2}\sigma_{xz};\ s_5 = \sqrt{2}\sigma_{yz} \quad . \tag{4.48}$$

An equivalent shear stress amplitude, $\tau_{eq,a}$, can be calculated according to the PH method by taking into account all the prismatic hulls which enclose the path of vector $\boldsymbol{s}$ and are tangent to it [Carpinteri et al., 2014]. For a given prismatic hull with orientation Θ at time instant t along a time interval $[0, T]$, the half value of its sides, a_i (with $i = 1, \ldots, 5$), can be evaluated as follows:

$$a_i(\Theta) := \frac{1}{2}\left(\max_t s_i(t) - \min_t s_i(t)\right) \quad , \tag{4.49}$$

and the corresponding equivalent shear stress as:

$$\tau_{\mathrm{eq},a}(\Theta) := \max_{\Theta} \sqrt{\sum_{i=1}^{5} a_i^2(\Theta)} \quad . \tag{4.50}$$

According to Mamiya et al. [2009] the terms a_i in Eq. 4.49 can be understood as shear stress amplitudes defined in five mutually orthogonal directions, with resultant $\tau_{\mathrm{eq},a}$ given by Eq. 4.50. In their work, Mamiya et al. [2009] also present an algorithm for computing the equivalent shear stress amplitude defined in Eq. 4.50.

4.5.2.1 Crossland

The stress invariant based criterion proposed by Crossland [1956] considers the amplitude of the second invariant of the deviatoric stress tensor, J_{2a} (which corresponds to the amplitude of von Mises equivalent stress and the effect of slippage in material planes) and the maximum value of the first invariant of Cauchy's stress tensor, i.e. the maximum hydrostatic stress, $\sigma_{\mathrm{h,max}}$. This last term accounts for the mean stress effect. The criterion is given by:

$$\sqrt{J_{2a}} + \kappa \sigma_{\mathrm{h,max}} \leq \lambda \quad . \tag{4.51}$$

According to Eq. 4.51, fatigue crack under cyclic loading initiates when the left side of the equation is greater than the right side. Where κ and λ are material constants, based on fatigue strength, determined under fully reversed uniaxial (σ_{-1}) and torsional (τ_{-1}) tests with smooth specimens respectively:

$$\kappa = 3\left(\frac{\tau_{-1}}{\sigma_{-1}}\right) - \sqrt{3} \quad ; \quad \lambda = \tau_{-1} \quad . \tag{4.52}$$

For non-proportional loading, the second invariant of the deviatoric stress tensor,

$J_{2,a}$, is replaced by the shear stress amplitude calculated using the PH method (Eq. 4.50). Therefore, Eq. 4.51 becomes:

$$\frac{\tau_{\text{eq},a}}{\sqrt{2}} + \kappa\sigma_{h,\max} \leq \lambda \quad . \tag{4.53}$$

Figure 4.19 presents the fatigue life predictions obtained with Crossland's formulation for Waspaloy, considering the typical representation exemplified in Fig. 4.17. The dashed black lines connect test cases with the same $\sigma_{\text{x,peak}}$, in order to illustrate the biaxiality effect when $\sigma_{\text{y,peak}}$ is changed. It is concluded that in general the model presents good correlation with experimental data both within and outside the tension-torsion calibration region. Fatigue lives are correctly predicted to lower when the magnitude of $\sigma_{\text{y,peak}}$ increases.

Figures 4.20 and 4.21 display the experimental against predicted life of the biaxial and tension-torsion test data for Crossland parameter, respectively. The black dashed lines represent the factor of three scatter bands. For proportional loading the shear stress amplitude calculated for Crossland parameter is given by von Mises equivalent stress amplitude (Eq. 4.51). It was anticipated thus that the overall correlation for the Waspaloy test data would be improved by the implicit use of the weighted mean stress correction in the form of the maximum hydrostatic stress, similarly to the results obtained with Walker parameter. In addition, good fatigue life prediction was obtained for the RR1000 test data (Fig. 4.21) using this parameter and the PH method. However, the parameter was not able to collapse the test data the same way the extended yield criteria did, and conservative predictions were obtained for L1 test cases with $F = 0.44$.

The main advantage of this stress-based formulation is that it only requires two material parameters (σ_{-1} and τ_{-1}), which can easily be obtained from uniaxial and torsional load-controlled tests. The main drawback of it is that it requires an alternative measure of shear stress for non-proportional load and that it incorrectly predicts fatigue damage for static loads, even for conditions with no shear stresses involved, due to the

additive foundation of the formulation (Eq. 4.51).

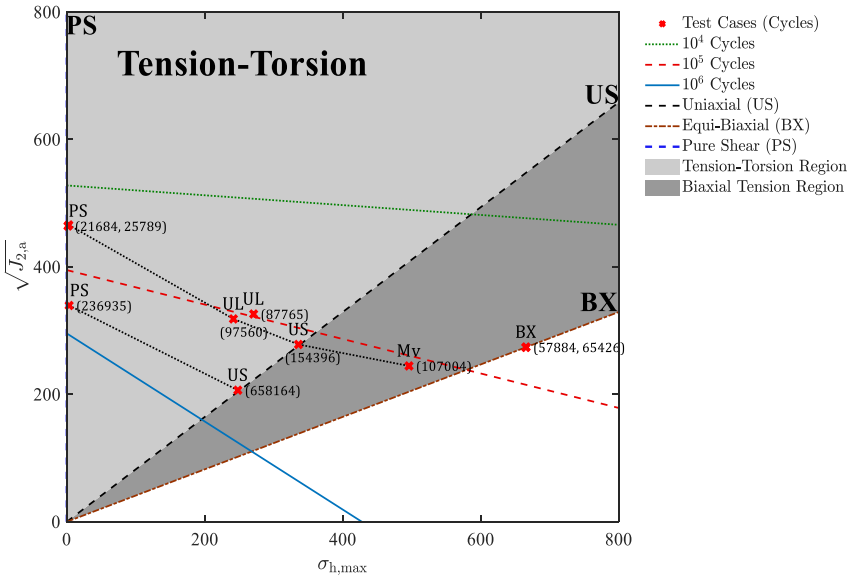


Figure 4.19 – Fatigue life prediction with Crossland parameter – Waspaloy.

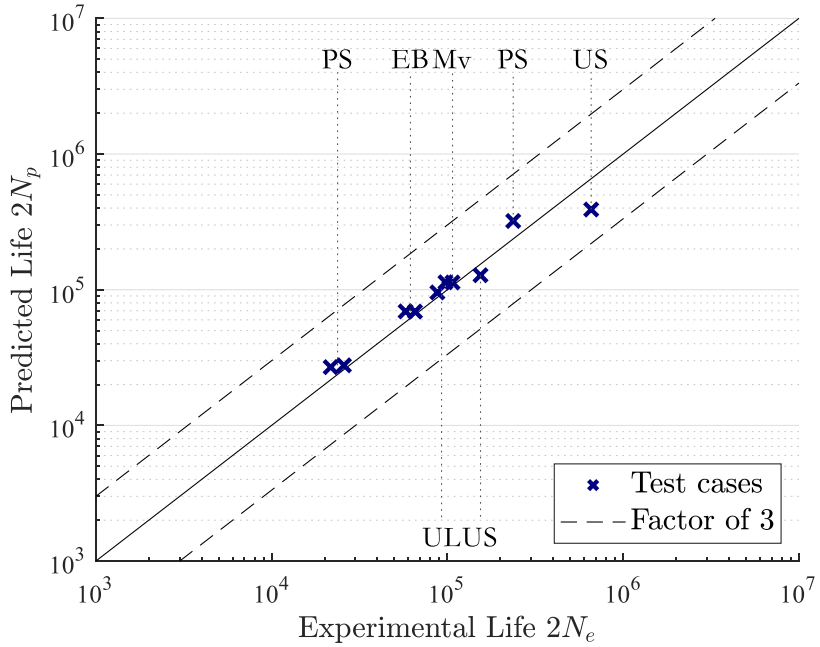


Figure 4.20 – Crossland parameter: experimental vs predicted life – Waspaloy.

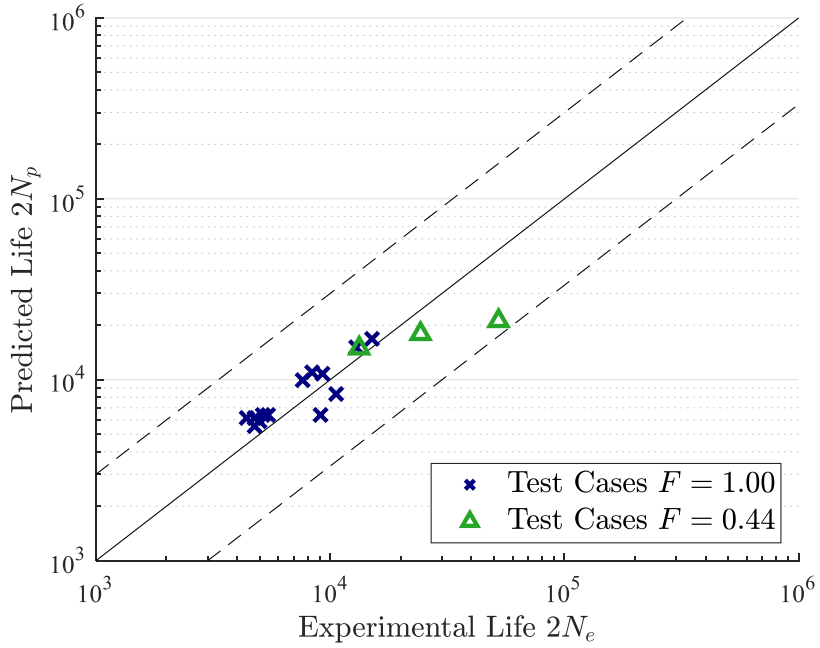


Figure 4.21 – Crossland parameter: experimental vs predicted life – RR1000.

4.6 Critical Plane approach

The critical plane approach was developed considering the physical phenomenon of fatigue crack initiation and growth. The process of localised, reversed crystallographic slip by which fatigue cracks initiate and propagate, tends to occur on particular material planes [Pattison, 2012]. Therefore, numerous multiaxial fatigue formulations use the critical plane concept to assess the stress-strain state at different orientations in a material, searching for a plane where a particular damage parameter is maximum. This is of particular use for non-proportional loading due to the rotation of the principal axes with respect to the specimen axes over the load cycle. This section presents and assess the performance of stress-, strain- and energy-based critical plane approaches.

4.6.1 Stress-based criteria

4.6.1.1 Matake

Matake [1977] proposed a criterion where failure occurs on the planes of maximum shear stress amplitude (parameter governing crack progression), considering the maximum value over time of the stress normal to that plane (parameter controlling the crack tip opening/closing and hydrostatic effect). The parameter is mathematically formulated as:

$$\tau_{a,max} + \kappa\sigma_{n,max} = \lambda \quad , \tag{4.54}$$

where $\tau_{a,max}$ and $\sigma_{n,max}$ are the maximum shear stress amplitude and the maximum normal stress respectively. The material parameters, κ and λ, are calculated as:

$$\kappa = 2\left(\frac{\tau_{-1}}{\sigma_{-1}}\right) - 1 \quad ; \quad \lambda = \tau_{-1} \quad . \tag{4.55}$$

Figure 4.22 shows the predictions for Waspaloy obtained with Matake model. In contrast to the results representation with Crossland parameter (Fig. 4.19), for Matake parameter the uniaxial and equi-biaxial dotted lines are coincident. Papadopoulos [1997] concluded after a comparative study that Matake's formulation behaved correctly under mean torsion loads. The same conclusion can be drawn from Fig. 4.23, where a good collapse of the PS load conditions was obtained and PS test case points lie correctly on the y-axis of Fig. 4.22. In addition, Matake's proposition gives the most conservative prediction for Waspaloy for the uniaxial stress (US) and uniaxial load (UL) conditions. Lastly, Figure 4.24 presents the collapse of the tension-torsion RR1000 test data with Matake parameter. Fatigue lives were correctly predicted to be longer for L1 load cases with $F = 0.44$ than for test cases with $F = 1.00$. However, the model presents a tendency to be slightly over optimistic for L1 test conditions. Nonetheless, Matake

parameter gives better predictions for RR1000 than Crossland parameter, as fatigue lives predicted with the former parameter are in closer agreement with experimental observations and reduced scatter can be observed in Fig. 4.24 vs Fig. 4.21.

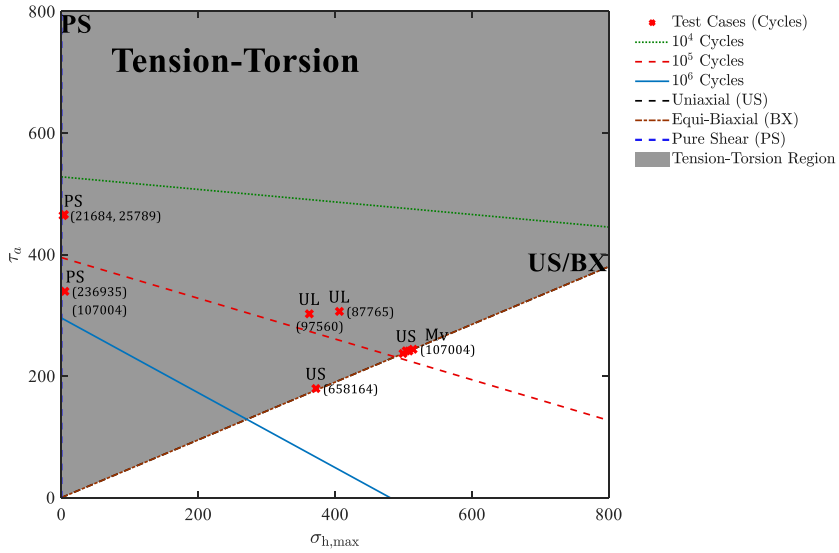


Figure 4.22 – Fatigue life prediction with Matake parameter – Waspaloy.

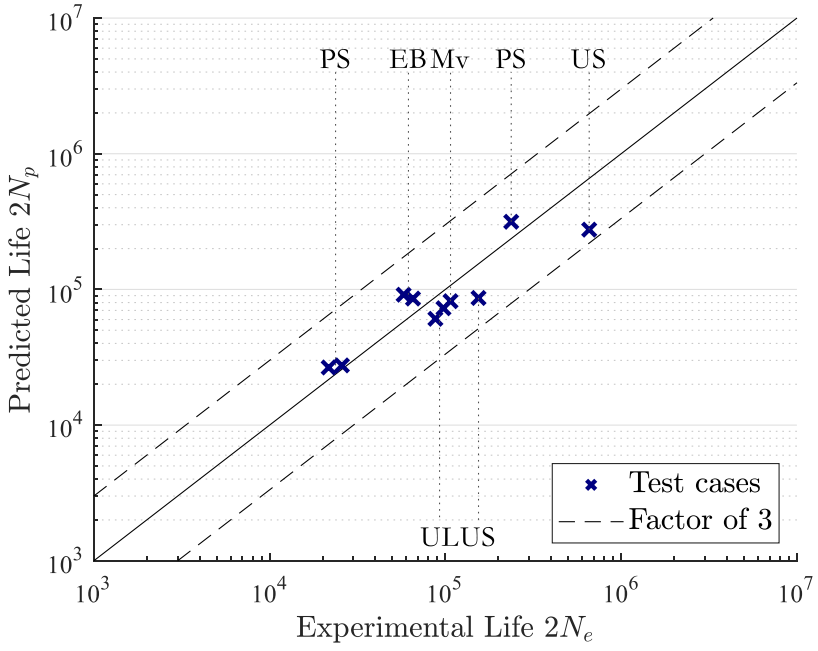


Figure 4.23 – Matake parameter: experimental vs predicted life – Waspaloy.

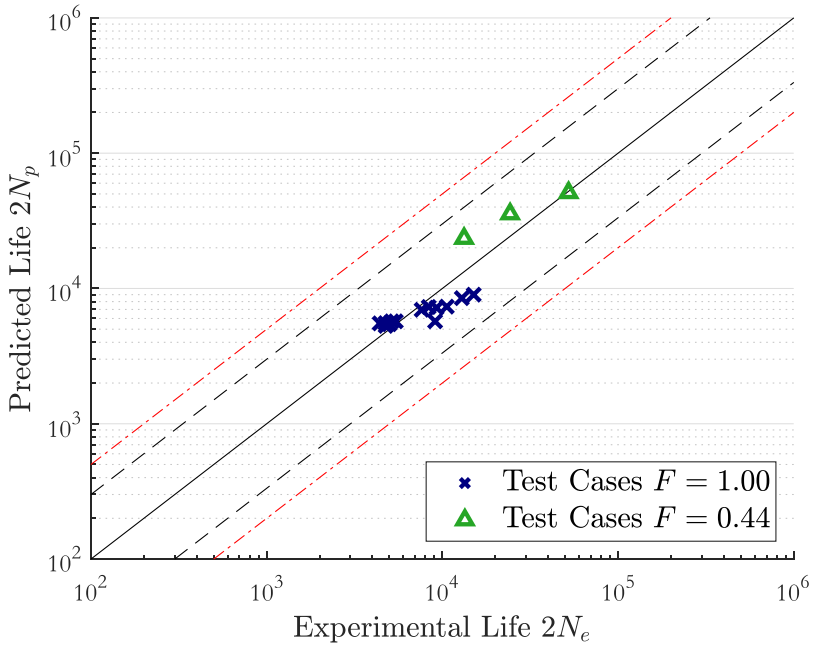


Figure 4.24 – Matake parameter: experimental vs predicted life – RR1000.

4.6.2 Strain-based criteria

4.6.2.1 Kandil-Brown-Miller

Brown & Miller [1973] proposed a theory based on a physical interpretation of mechanisms of fatigue crack growth. According to them, failure under multiaxial fatigue is governed by the maximum shear stress range. In addition, the tensile normal strain acting on the plane of maximum shear strain benefits propagation (by opening the crack tip). Originally, Brown and Miller represented graphically their criterion by contours of constant life. Later Kandil et al. [1982] proposed a specific formulation of the theory for shallow cracks that propagate parallel to the shear stress acting on the free surface:

$$\Delta\hat{\gamma} = (\Delta\gamma_{\max}^{\alpha} + S\Delta\varepsilon_{\mathrm{n}^{\alpha}})^{\frac{1}{\alpha}} \quad , \tag{4.56}$$

where $\Delta\hat{\gamma}$ is the equivalent shear strain range, $\Delta\gamma_{\max}$ is taken as the maximum shear strain range and $\Delta\varepsilon_{\mathrm{n}}$ is the normal strain range on the plane of maximum shear strain

range. S represents a material dependent parameter, describing the influence of the normal strain on material crack growth. Similar to the material constants for stress-based formulations, S is also determined by correlating axial and torsional fatigue data.

Finally, Wang & Brown [1996*a*,*b*] introduced a mean stress term to the formulation, and assuming $\alpha = 1$, the equivalent shear strain amplitude was expressed as:

$$\frac{\Delta\hat{\gamma}}{2} = \frac{\Delta\gamma_{\max}}{2} + S\Delta\varepsilon_n \quad . \tag{4.57}$$

For fatigue life prediction, this formulation is expressed as follows:

$$\frac{\Delta\gamma_{\max}}{2} + S\Delta\varepsilon_n = [(1+\nu) + S(1-\nu)]\frac{\sigma_f'}{E}\left(2N_f\right)^b + (1.5 + 0.5S)\,\varepsilon_f'\left(2N_f\right)^c \quad , \tag{4.58}$$

where,

$$S = \frac{\frac{\tau_{f'}}{G}(2\mathrm{N_f})^{b_\gamma} + \gamma_f'(2\mathrm{N_f})^{c_\gamma} - (1+\nu)\frac{\sigma_f'}{E}(2\mathrm{N_f})^b - 1.5\varepsilon_f'(2\mathrm{N_f})^c}{(1-\nu)\frac{\sigma_f'}{E}(2\mathrm{N_f})^b + 0.5\varepsilon_f'(2\mathrm{N_f})^c} \quad . \tag{4.59}$$

4.6.2.2 Fatemi-Socie

Based on the work of Brown & Miller [1973], Fatemi & Socie [1988] concluded that tensile normal stress in the maximum shear stress plane accelerates crack growth by separating the crack surfaces and consequently reducing frictional forces. They also recognised that the inclusion of the maximum stress term on the critical plane, instead of normal strain, was necessary to adequately account for the additional hardening caused by non-proportional loading. The Fatemi-Socie damage parameter may be interpreted as the cyclic shear strain modified by the normal stress to include the crack

closure effects, and formulated as:

$$\frac{\Delta\gamma_{\max}}{2}\left(1+\kappa\frac{\sigma_{\mathrm{n,max}}}{\sigma'_{\mathrm{yield}}}\right)=\frac{\tau'_f}{G}\left(2N_f\right)^{b_\gamma}+\gamma'_f\left(2N_f\right)^{c_\gamma} \quad , \tag{4.60}$$

where $\frac{\Delta\gamma_{\max}}{2}$ is the maximum shear strain amplitude and $\sigma_{\mathrm{n,max}}$ is the maximum normal stress on the plane where $\frac{\Delta\gamma_{\max}}{2}$ occurs. The material parameter κrepresents the influence of the normal stress, $\sigma_{\mathrm{n,max}}$. In addition, σ'_{yield} represents the cyclic yield strength of the material and is included to make the maximum normal stress component dimensionless and proportional to the shear strain.

The material parameter κ is expressed in the following way:

$$\kappa=\left[\frac{\frac{\tau_{f'}}{\mathrm{G}}\left(2\mathrm{N_f}\right)^{b_\gamma}+\gamma'_{\mathrm{f}}\left(2\mathrm{N_f}\right)^{c_\gamma}}{\left(1+\nu\right)\frac{\sigma'_f}{E}\left(2\mathrm{N_f}\right)^{b}+1.5\varepsilon'_f\left(2\mathrm{N_f}\right)^{c}}-1\right]\frac{\sigma'_{\mathrm{yield}}}{\sigma'_f\left(2\mathrm{N_f}\right)^{b}} \quad . \tag{4.61}$$

Figures 4.25 display the experimental against predicted life of the Waspaloy biaxial test data for both Wang-Brown (WB) and Fatemi-Socie (FS) parameters. It is observed that both parameters present comparable predictions (an expected result as both parameters search for the similar critical planes, where $\Delta\gamma$ is maximum and modified by a normal stress/strain measure). These two criteria show their best predictions for the pure shear (PS) condition, uniaxial load (UL) and uniaxial stress (US). Their worst predictions are for the equi-biaxial case (EB), minimum von Mises (Mv), US with lower strain range and PS with lower stress range. Nevertheless, both strain-based parameters present good correlation, with almost all their predictions within the factor of three scatter bands for Waspaloy.

Figure 4.26 shows the results obtained with the analogous analysis for RR1000 test data, where markers with filled faces represent L1 test cases with $F = 0.44$ and red dashed lines represent the factor of five scatter bands. This time there is a clear distinction between the two parameters, with FS parameter giving less conservative

predictions than WB criterion. Despite both parameters presenting good results and accurately predicting longer lives for L1 test cases, WB parameter presented a better collapse of the tension-torsion test data within the factor of three scatter bands.

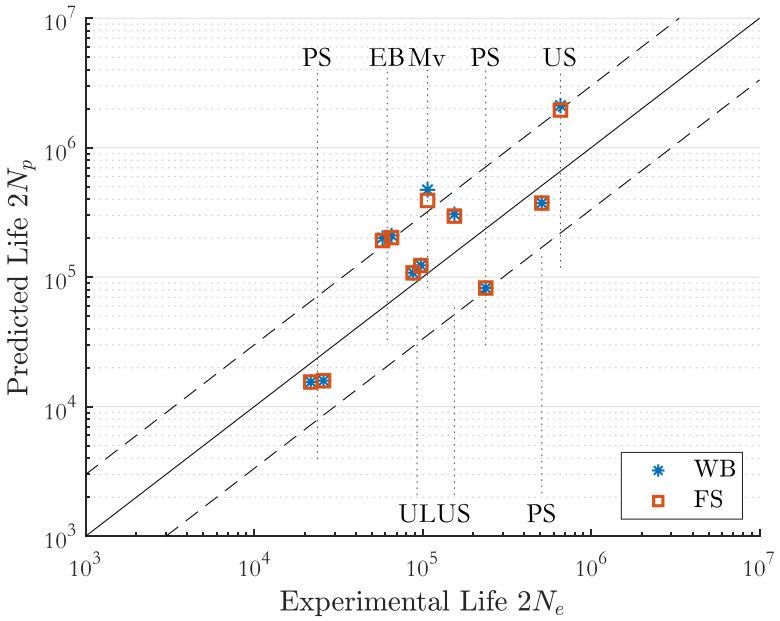


Figure 4.25 – WS and FS parameters: experimental vs predicted life – Waspaloy.

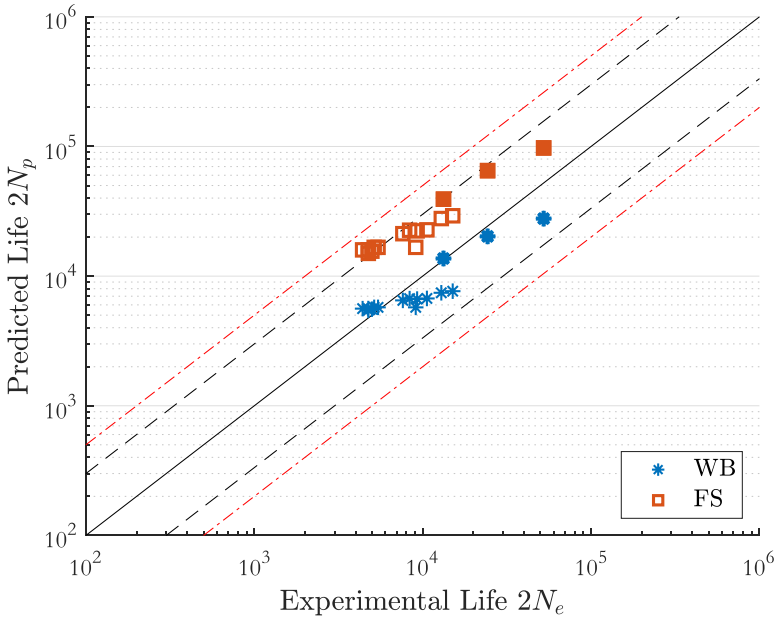


Figure 4.26 – WS and FS parameters: experimental vs predicted life – RR1000.

4.6.3 Energy-based criteria

As reviewed in Chapter 2, energy-based criteria are generally classified into three different groups, depending on the kind of strain energy density per cycle assumed as the damage parameter. In the first group, elastic strain energy is considered as the damage parameter, and the criteria are used for high cycle fatigue regimes. Secondly, for low cycle fatigue regimes, plastic strain energy is considered as the damage parameter. The last group is based on a combination of elastic and plastic strain energies for both high and low cycle fatigue regimes.

Figure 4.27 illustrates how elastic and plastic energy density that can be obtained from a hysteresis loop, where ΔW_e and ΔW_p represent the elastic and plastic strain energy densities, respectively. The total energy density, ΔW_t, is given by the summation of the two terms:

$$\Delta W_t = \Delta W_e + \Delta W_p \quad . \tag{4.62}$$

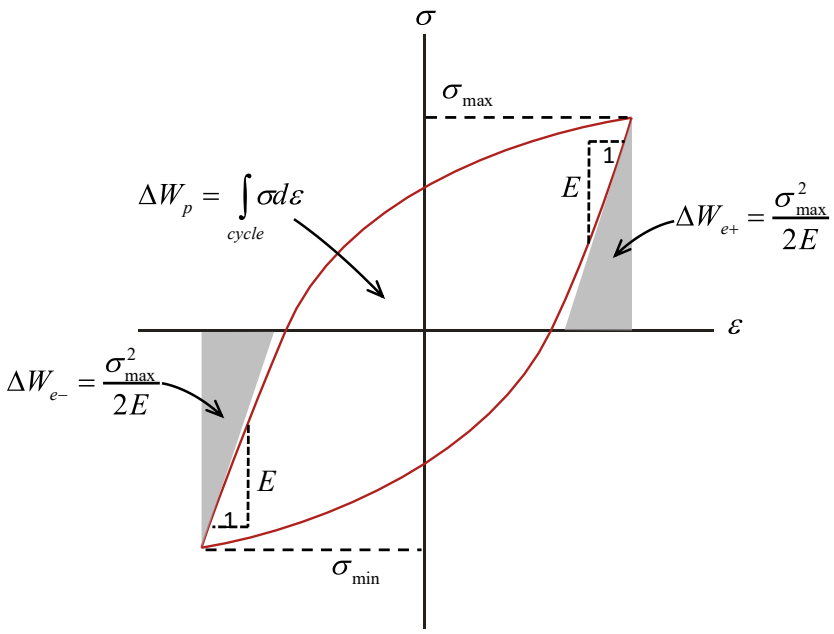


Figure 4.27 – Hysteresis loop energy densities. Adapted from Mousa [2011].

Analogous to the Coffin-Manson strain-life curve presented in Section 4.2, an energy-life curve can be obtained for axial loading conditions:

$$\Delta W_A = E'_e (2\mathrm{N_A})^B + E'_f (2\mathrm{N_A})^C \quad , \tag{4.63}$$

where W_A and is the energy due to purely axial loading, and E'_e and E'_f are the energy-axial fatigue strength and axial fatigue toughness coefficients, respectively. B and C are the energy-axial and axial fatigue toughness exponents, respectively.

For torsional/shear loading conditions, the energy-life curve is defined as:

$$\Delta W_T = W'_e (2\mathrm{N_T})^{B_\gamma} + W'_f (2\mathrm{N_T})^{C_\gamma} \quad , \tag{4.64}$$

where W_T is the energy due to purely torsional loading, and W'_e and W'_f are the energy-torsional fatigue strength and torsional fatigue toughness coefficients, respectively. Correspondingly, B_γ and C_γ are the energy-torsional and torsional fatigue toughness exponents.

The coefficients and exponents for Eqs. 4.63 and 4.64 can be obtained similarly to the coefficients for Coffin-Manson relationship presented in Eqs. 4.5 and 4.6, but using axial and torsional energy-life curves. Figure 4.28 illustrates the energy-life curve for axial loading. The obtained lives $2\mathrm{N_A}$, from axial energy, and $2\mathrm{N_T}$, from torsional energy, are them combined for fatigue life prediction [Mousa, 2011]:

$$2\mathrm{N_f} = \frac{\Delta W_A}{\Delta W_t} 2\mathrm{N_A} + \frac{\Delta W_T}{\Delta W_t} 2\mathrm{N_T} \quad , \tag{4.65}$$

where ΔW_t is the total energy density.

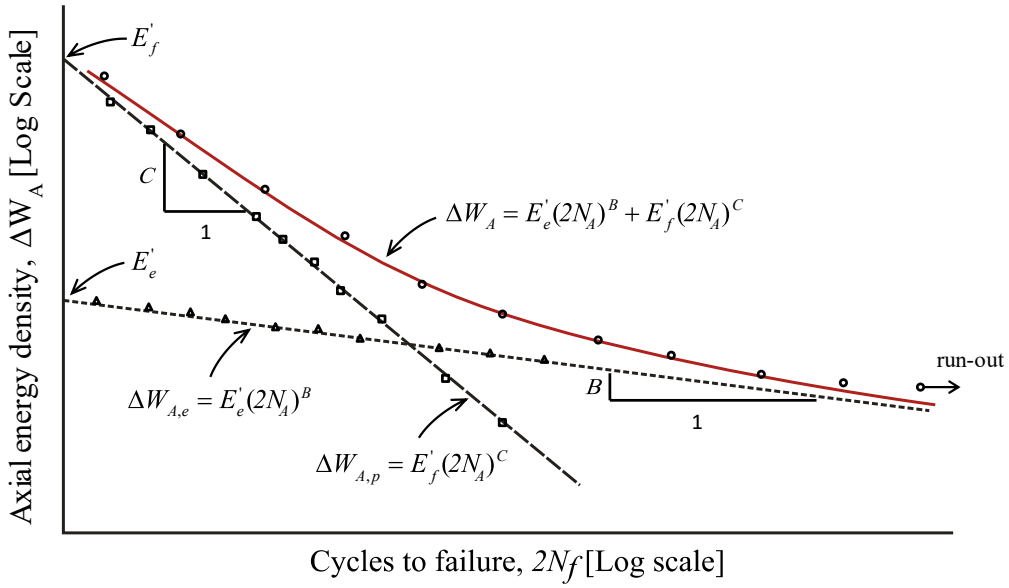


Figure 4.28 – Energy-life curve. Adapted from Mousa [2011].

4.6.3.1 Smith-Watson-Topper

The first of the energy-based damage parameter considered was proposed by Smith, Watson & Topper [1970], SWT, for predicting fatigue life under uniaxial tension-compression conditions with mean stresses. The parameter was originally defined as:

$$\sigma_{n,max}\frac{\Delta\varepsilon}{2} = \frac{\sigma_{f'^2}}{E}(2N_f)^{2b} + \sigma_{f'}\varepsilon_{f'}(2N_f)^{b+c} \quad . \tag{4.66}$$

This parameter was modified for proportional and non-proportional multiaxial loading conditions of materials that fail predominantly by crack growth on planes of maximum tensile strain or stress, i.e. by Mode I. In these materials, cracks nucleate in shear, but early life is controlled by crack growth on planes perpendicular to the maximum principal stress and strain.

Socie [1987] proposed a modification to the SWT parameter in order to take into account only stresses and strains occurring in the critical plane. This became the most

well-known form of the parameter and is mathematically represented by:

$$\sigma_{\mathrm{n,max}}\frac{\Delta\varepsilon_{\mathrm{n,max}}}{2}=\frac{\sigma_{\mathrm{f}'2}}{\mathrm{E}}\left(2\mathrm{N_f}\right)^{2b}+\sigma_{\mathrm{f}'}\varepsilon_{\mathrm{f}'}\left(2\mathrm{N_f}\right)^{b+c} \quad . \tag{4.67}$$

where $\frac{\Delta\varepsilon_{\mathrm{n,max}}}{2}$ represents the maximum normal strain, and accordingly $\sigma_{\mathrm{n,max}}$ is calculated on the plane where $\frac{\Delta\varepsilon_{\mathrm{n,max}}}{2}$ occurs.

4.6.3.2 Liu

Liu [1993] proposed a criterion based on the virtual strain energy concept. He used two different formulations depending on the failure mode, one for tensile failure, ΔW_I, and another one for shear failure, ΔW_{II}. The first criterion, ΔW_I, considers the axial work, $\Delta\sigma\Delta\varepsilon$, as the main damage parameter, and assumes as the critical plane the plane in which this parameter reaches its maximum value. On the other hand, for the second criterion, ΔW_{II}, the critical plane is the one that maximises the shear work, $\Delta\tau\Delta\gamma$:

$$\Delta W_I=\left(\Delta\sigma\Delta\varepsilon\right)_{\mathrm{max}}+\left(\Delta\tau\Delta\gamma\right) \quad , \tag{4.68}$$

and,

$$\Delta W_{II}=\left(\Delta\sigma\Delta\varepsilon\right)+\left(\Delta\tau\Delta\gamma\right)_{\mathrm{max}} \quad . \tag{4.69}$$

For fatigue life prediction, these formulations are expressed as:

$$\Delta W_I=4\sigma_f'\varepsilon_f'\left(2N_f\right)^{b+c}+\frac{4\sigma_f'^2}{E}\left(2N_f\right)^{2b} \quad , \tag{4.70}$$

and,

$$\Delta W_{II} = 4\tau'_f \gamma'_f \left(2N_f\right)^{b_\gamma + c_\gamma} + \frac{4\tau'^2_f}{G}\left(2N_f\right)^{2b_\gamma} \quad , \tag{4.71}$$

4.6.3.3 Glinka-Ince

Two formulations were proposed by Ince & Glinka [2014], based on the search for specific planes experiencing the maximum amount of a generalised strain energy (GSE). The GSE damage parameter includes both the normal and shear strain energy terms:

$$W^*_{gen} = \left(\tau_{\max}\frac{\Delta\gamma^e}{2} + \frac{\Delta\tau}{2}\frac{\Delta\gamma^p}{2} + \sigma_{\mathrm{n,max}}\frac{\Delta\varepsilon^e_{\mathrm{n}}}{2} + \frac{\Delta\sigma_{\mathrm{n}}}{2}\frac{\varepsilon^p_{\mathrm{n}}}{2}\right)_{\max} \quad . \tag{4.72}$$

This formulation takes into account the effects of mean stress and non-proportional hardening through the elastic shear and normal strain energy terms by including the maximum shear stress, $\tau_{\max}$, and the maximum normal stress, $\sigma_{\max}$, in the formulation of the damage parameter. In addition, the shear strain energy terms reflect the initiation and growth of cracks, and the normal strain energy terms accelerate crack growth.

The shear strain energy terms in Eq. 4.72 can be normalised with the shear stress amplitude, $\frac{\Delta\tau}{2}$ and the normal strain energy terms can be normalised with the normal stress amplitude, $\frac{\Delta\sigma}{2}$ to transform the generalised strain energy parameter to the form of generalised strain amplitude (GSA):

$$\frac{\Delta\varepsilon^*_{gen}}{2} = \left(\frac{\tau_{\max}}{\Delta\tau/2}\frac{\Delta\gamma^e}{2} + \frac{\Delta\gamma^p}{2} + \frac{\sigma_{\mathrm{n,max}}}{\Delta\sigma_{\mathrm{n}}/2}\frac{\Delta\varepsilon^e_{\mathrm{n}}}{2} + \frac{\varepsilon^p_{\mathrm{n}}}{2}\right)_{\max} \quad . \tag{4.73}$$

Based on Basquin's relationship presented in Eqs. 4.1 and 4.2, and assuming a fatigue life of one cycle, i.e. $2N_f = 1$ (one cycle equals to two reversals), the shear and normal stress amplitudes become:

$$\frac{\Delta\sigma}{2} = \sigma'_f\left(2N_f\right)^b = \sigma'_f \quad , \tag{4.74}$$

and,

$$\frac{\Delta\tau}{2} = \tau'_f \left(2N_f\right)^{b_\gamma} = \tau'_f \quad . \tag{4.75}$$

Substituting Eqs. 4.74 and 4.75 into Eq. 4.73, the multiaxial fatigue damage parameter based on the generalised strain amplitude becomes:

$$\frac{\Delta\varepsilon^*_{gen}}{2} = \left(\frac{\tau_{\max}}{\tau'_f}\frac{\Delta\gamma^e}{2} + \frac{\Delta\gamma^p}{2} + \frac{\sigma_{\mathrm{n,max}}}{\sigma'_f}\frac{\Delta\varepsilon^e_{\mathrm{n}}}{2} + \frac{\varepsilon^p_{\mathrm{n}}}{2} \right)_{\max} \quad . \tag{4.76}$$

Figure 4.29 illustrates the collapse of Waspaloy biaxial test data by the energy-based parameters, SWT, Liu (I and II), GSE and GSA. Best predictions were obtained with SWT and Liu parameters. Almost all predictions obtained with SWT and Liu lie within the factor of three scatter bands. Comparing the two of them, the SWT parameter gives more conservative predictions, which is a desirable characteristic for the safe design of complex engineering components. On the other hand, better agreement with the experimental data is obtained with Liu, despite conservative predictions for the pure shear cases. Good correlation is also obtained with the GSE and GSA parameters. However, GSE parameter is in better correlation with the experimental data due to its lower scatter and more conservative predictions.

Figure 4.30 presents predicted against experimental life for RR1000 test data, once again filled marker faces represent L1 test cases with $F = 0.44$. Best and almost identical predictions are obtained with Liu I and GSE parameters, which collapse all test data within the factor of three scatter bands. Despite the similar formulation, the GSA parameter gives over conservative response, especially for L1 test cases, which lie closer to the factor of five scatter bands. In contrast to the conservative response obtained for Waspaloy, SWT parameter gives non-conservative predictions for RR1000, especially for L1 test cases. Only Liu and GSE parameters predicted longer lives for cases with $F = 0.44$ than cases with $F = 1.00$. However, Liu II parameter presents, in general,

over optimistic results for RR1000 and predicted runouts (lives > 10^6) for L1 test cases.

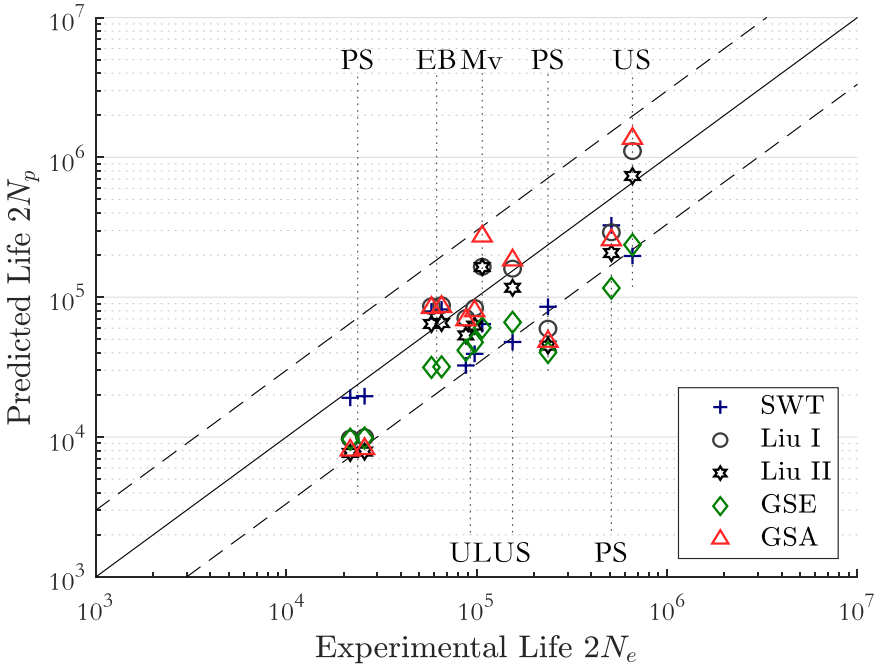


Figure 4.29 – SWT, Liu and Ince-Glinka parameters: experimental vs predicted life – Waspaloy

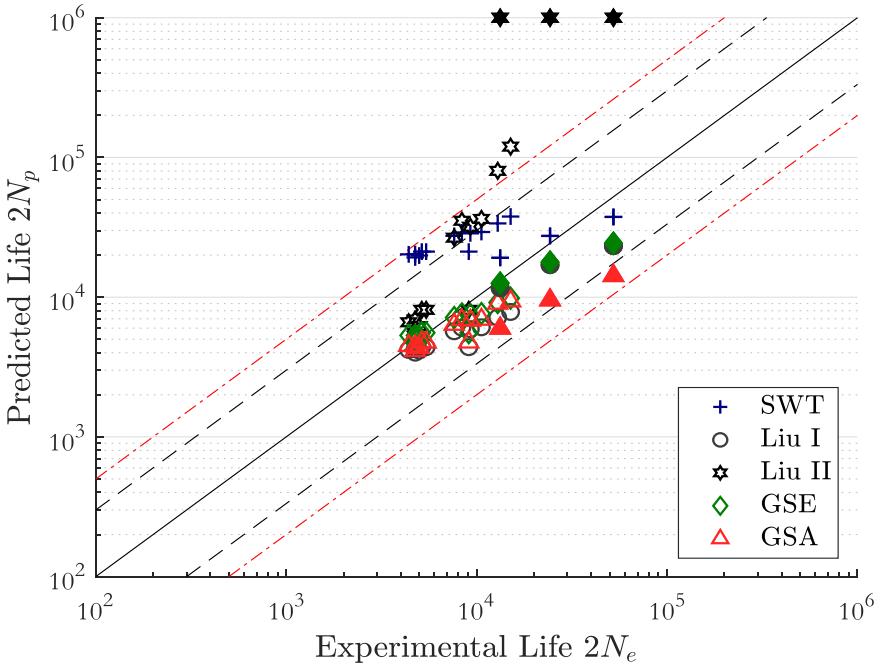


Figure 4.30 – SWT, Liu and Ince-Glinka parameters: experimental vs predicted life – RR1000.

4.7 Conclusion

A wide range of stress-, strain- and energy-based multiaxial fatigue criteria was investigated. Most of them could provide a reasonable collapse of both Waspaloy biaxial and RR1000 non-proportional tension-torsion test data. Regarding extended yield criteria, the best correlation with Waspaloy test data is obtained using Walker strain combined with elastic strain energy equivalent stress. For RR1000, excellent correlation is obtained for all equivalent stress methods, as long the Shamsaei et al. non-proportional correction factor is considered. The stress invariant based formulation proposed by Crossland with the PH method gives good correlation for both Waspaloy and RR1000, but it does not predict correctly the longer lives experimentally observed for L1 test cases with lower degree of non-proportionality, $F = 0.44$.

Considering critical plane approaches, the best correlation was obtained with Matake parameter. This could be justified by the input loading for fatigue life analysis in the form of applied stress, calculated from the load measurements of the tests carried out during this doctoral research project. Strains, on the other hand, were calculated using Hencky's total plasticity equation and the strain-controlled cyclic test data presented by Pattison [2012] for Waspaloy and Bees [2016] for RR1000. Therefore, the calibration of strain- and energy-based criteria were sub-optimal and inaccuracies from strain calculations and strain-life curve determination were carried forward during the evaluation of the parameters. Nevertheless, considering strain-based parameters, good predictions are obtained with Wang-Brown parameter for both Waspaloy and RR1000.

In terms of energy-based approaches, the best results were obtained with Liu I parameter for both materials, and GSE for RR1000 only. In an attempt to characterise the fatigue behaviour of Waspaloy under both proportional (in-phase) and non-proportional (out-of-phase) loading at room temperature and elevated temperature, Pattison [2012] used a hyperbolic co-tangent to correlate numerous stress-, strain and energy-based parameters to initiation life. The objective of his research was the assessment of how

alternative multiaxial damage parameters perform as direct replacements to Walker Strain parameter. Similar to the conclusions presented here, Pattison pointed out that the Liu parameter performed the best in collapsing the fatigue data points to the initiation life curve. However, they note that this parameter is not ideal, since there is no explicit mean stress correction term.

Therefore, to conclude, Tab. 4.2 summarises the performance of each criterion ascertained by a least square fit on the total absolute residual error, δ, as defined in Eq. 4.77. Test runouts were excluded from this fitting procedure.

$$\delta = \sum_{i=1}^{Test\ cases} \left| log_{10}\left(\frac{N_{i,predicted}}{N_{i,experimental}}\right)\right| \quad , \tag{4.77}$$

Table 4.2 – Absolute residual error for each criterion and material.

Parameter	**δ Waspaloy**	**δ RR1000**
von Mises - σ_{vM}	2.23	0.46
Elastic Strain - σ_{Ue}	1.14	0.44
Walker Stress - $\sigma_{\mathrm{W,Ue}}$	1.02	0.79
Crossland	0.79	1.81
Matake	1.59	1.71
Fatemi-Socie	3.33	6.72
Wang-Brown	3.50	1.96
Smith-Watson-Topper	2.93	7.27
Liu I	2.25	2.51
Liu II	2.50	9.61
Glinka-Ince – GSE	3.81	1.56
Glinka-Ince – GSA	2.89	2.69

5 Crystal Plasticity Modelling

5.1 Overview

The previous chapter, Chapter 4, presents results obtained with classical multiaxial fatigue criteria for the prediction of fatigue lives of Waspaloy and RR1000 specimens. Despite the good predictions presented in the analysis, none of the investigated models account for the damage phenomena happening in the material microstructure. Some models, such as those proposed by Fatemi-Socie and Ince-Glinka, are formulated considering an initial theoretical fatigue short crack that is influenced by normal stresses, opening or closing the crack, and by shear stresses that rub the surfaces of the crack depending on the loading condition, i.e. a tensile stress would facilitate crack growth/propagation and a compressive stress would hinder the process by increasing surface friction. However, these models are not truly mechanistic based, as they use a series of approximations and assumptions, making them akin to fitting parameters and not physical models. Therefore, this chapter adopts a different take on the investigation of multiaxial fatigue by modelling it at the grain scale through a crystal plasticity framework.

As classical plasticity models are insensitive to the length-scale of the fatigue nucleation process, a different approach and a change of length-scale are needed

to investigate the fatigue phenomena at the grain level. This chapter presents the formulation and implementation of a gradient-based crystal plasticity framework for the simulation of the non-proportional tension-torsion tests with RR1000 presented in Chapter 3. This approach takes into account the density of dislocations as its length-scale dependency parameter. The crystal plasticity framework and the results obtained with it are presented in the following sections.

5.2 Crystal plasticity framework

The crystal plasticity framework proposed by Dunne, Rugg & Walker [2007]; Dunne et al. [2012] is used to analyse the behaviour of the face centred cubic Nickel-based superalloy RR1000. The model incorporates explicit coupling of statistically stored dislocations (SSDs) and geometrically necessary dislocations (GNDs), presented in detail in Chapter 2 of this thesis. The crystal plasticity model was implemented within the commercial finite element software, Abaqus, via a user material subroutine (UMAT), which allows the implementation of general constitutive equations into Abaqus. The Crystal Plasticity Finite Element (CPFE) model describe the deformation behaviour of each crystal orientation assuming crystallographic slip via dislocation glide as the primary deformation mode, twinning is neglected in this CPFE model. Crystal orientation rotates with deformation and critical resolved shear stress increases according to a modified Taylor hardening law built into the model, the mechanical response and lattice texture change accordingly.

5.2.1 Crystal slip rule

Large deformation processes are generally comprised of stretch, which provides shape change, and rigid body rotation and translation, which neither contributes to shape change nor internal stresses [Dunne & Petrinic, 2005]. Figure 5.1 illustrates an imaginary material that undergoes combined stretch and rigid body displacement in three

configurations: the undeformed reference configuration, before any load is applied to the material (often referred to as initial or global configuration); an intermediate configuration; and the deformed configuration, after the load is applied (also known as current or local configuration). Variables in upper-case refer to the undeformed configuration coordinates, and lower-case variables correspond to deformed configuration coordinates.

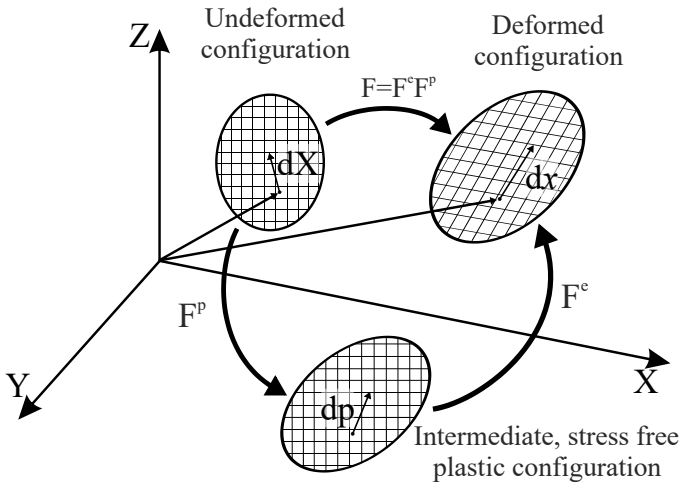


Figure 5.1 – Schematic diagram of the multiplicative decomposition of the deformation gradient. Adapted from Jones [2016].

The deformation gradient is defined as a second-order tensor that maps the line vector $d\boldsymbol{X}$ in the undeformed reference configuration (Lagrangian) to the line vector $d\boldsymbol{x}$ in the deformed configuration of the material (Eulerian), including both stretch and rigid-body rotation and translation:

$$\boldsymbol{F} = \frac{\partial \boldsymbol{x}}{\partial \boldsymbol{X}} \quad . \tag{5.1}$$

The intermediate configuration is a virtual state introduced for separating the elastic and plastic deformations when modelling large deformations, as strains usually go beyond the elastic limit of the material. Therefore, the deformation gradient can be decomposed as proposed by Lee [1969]:

$$\boldsymbol{F} = \boldsymbol{F}^e \boldsymbol{F}^p \quad , \tag{5.2}$$

where $\boldsymbol{F}^p$ represents the plastic deformation gradient and maps the line vector $d\boldsymbol{X}$ from the undeformed configuration to the line vector $d\boldsymbol{p}$ in the intermediate configuration via purely plastic deformation. $\boldsymbol{F}^e$ is the elastic deformation gradient and maps the intermediate configuration to the deformed configuration, accounting for the material's elastic stretch and rigid body rotation and translation. Therefore, $\boldsymbol{F}^p$ and $\boldsymbol{F}^e$ are mathematically formulated as:

$$\boldsymbol{F}^p = \frac{\partial \boldsymbol{p}}{\partial \boldsymbol{X}} \quad , \tag{5.3}$$

and,

$$\boldsymbol{F}^e = \frac{\partial \boldsymbol{x}}{\partial \boldsymbol{p}} \quad . \tag{5.4}$$

For Finite Element modelling it is generally more convenient to consider plasticity in terms of plastic strain rate, as plasticity is an incremental process. Analogously to the process of formulating the deformation gradient, $\boldsymbol{F}$, the velocity gradient, $\boldsymbol{L}$, can be defined considering a spatially varying velocity field, i.e. one for which material point velocities vary spatially [Dunne & Petrinic, 2005]. The increment in velocity, $d\boldsymbol{v}$, occurring over an incremental change in position, $d\boldsymbol{x}$, in the deformed configuration is given by the relation:

$$d\boldsymbol{v} = \frac{\partial \boldsymbol{v}}{\partial \boldsymbol{x}} d\boldsymbol{x} \quad . \tag{5.5}$$

The velocity gradient, describing the spatial rate of change of the velocity, can be defined as:

$$\boldsymbol{L} = \frac{\partial \boldsymbol{v}}{\partial \boldsymbol{x}} \quad , \tag{5.6}$$

and taking into account the time rate of change of the deformation gradient:

$$\dot{\boldsymbol{F}} = \frac{\partial}{\partial t}\left(\frac{\partial \boldsymbol{x}}{\partial \boldsymbol{X}}\right) = \frac{\partial \boldsymbol{v}}{\partial \boldsymbol{X}} = \frac{\partial \boldsymbol{v}}{\partial \boldsymbol{x}}\frac{\partial \boldsymbol{x}}{\partial \boldsymbol{X}} = \boldsymbol{L}\boldsymbol{F} \quad , \tag{5.7}$$

or in terms of $\boldsymbol{L}$:

$$\boldsymbol{L} = \dot{\boldsymbol{F}}\ \boldsymbol{F}^{-1} \quad . \tag{5.8}$$

The velocity gradient, thus, maps the deformation gradient, $\boldsymbol{F}$, onto the rate of change of the deformation gradient, $\dot{\boldsymbol{F}}$. The decomposition of the velocity gradient into its symmetric (stretch related) and antisymmetric (rigid-body rotation related) parts may be written as:

$$\boldsymbol{L} = \mathrm{sym}\,(\boldsymbol{L}) + \mathrm{asym}\,(\boldsymbol{L}) \quad , \tag{5.9}$$

where,

$$\mathrm{sym}\,(\boldsymbol{L}) = \boldsymbol{\Phi} = \frac{1}{2}\left(\boldsymbol{L} + \boldsymbol{L}^{T}\right) \quad , \tag{5.10}$$

and,

$$\mathrm{asym}\,(\boldsymbol{L}) = \boldsymbol{\omega} = \frac{1}{2}\left(\boldsymbol{L} - \boldsymbol{L}^{T}\right) \quad , \tag{5.11}$$

the symmetric part, $\boldsymbol{\Phi}$, and antisymmetric part, $\boldsymbol{\omega}$, are the rate of deformation and rate of continuum spin, respectively. Analogous to the multiplicative decomposition presented for the deformation gradient, the velocity gradient may also be decomposed

into its elastic and plastic components, $\boldsymbol{L}^e$ and $\boldsymbol{L}^p$, respectively:

$$\boldsymbol{L} = \boldsymbol{L}^e \boldsymbol{L}^p \quad . \tag{5.12}$$

The crystal plasticity framework proposed by Dunne, Rugg & Walker [2007]; Dunne et al. [2012], follows Asaro & Rice [1977] expression for the plastic velocity gradient, defined in terms of slip rate, $\dot{\gamma}$, and the Schmid tensor:

$$\boldsymbol{L}^p = \sum_{k=1}^{N_s} \dot{\gamma}^k \boldsymbol{s}^k \otimes \boldsymbol{n}^k \quad , \tag{5.13}$$

with $k = 1, \ldots, 12$, representing the number of slip systems seen in face centred cubic (FCC) crystals, ($[111] < 110 >$ family). $\dot{\gamma}^k$ is the slip rate on the k^{th} slip system, and s^k and n^k are the slip direction and normal to the k^{th} slip system, respectively. Cottrell [1953] proposed an expression for the slip rate, $\dot{\gamma}$, produced by the glide of density of mobile dislocations, ρ_m, with an average velocity, $\bar{v}$, formulated as:

$$\dot{\gamma}^k = \rho_m \boldsymbol{b} \bar{v} \quad , \tag{5.14}$$

where $\boldsymbol{b}$ represents the Burgers vector.

As the time taken for a dislocation to unpin from an obstacle is much greater than the time taken to glide between pinning points, the average dislocation velocity, $\bar{v}$, and the shear strain rate, must be dominated by the waiting time between pinning events. Considering the hypothesis proposed by Seeger [1955] that dislocation glide velocity is determined by the rate at which thermal activation allows unpinning of obstacles, and Gibbs [1969] consideration that all obstacles have the same strength. The average dislocation glide velocity, as formulated by Granato et al. [1964], is given by the product of the jump length of the thermal activation event, d, and the rate of successful activation, $\bar{\Gamma}$:

$$\bar{v} = d\,\bar{\Gamma} \quad , \tag{5.15}$$

and,

$$\bar{\Gamma} = \Gamma_{\text{forward}} - \Gamma_{\text{backward}} \quad . \tag{5.16}$$

The net probability of thermal activation, $\bar{\Gamma}$, is the difference between the probability that a dislocation segment encountering an obstacle will be activated over it (Γ_{forward}) and the probability that it will subsequently make the reverse jump from its new equilibrium position (Γ_{backward}). Gibbs [1969] expression for the rate of successful activation events is given by:

$$\Gamma = \frac{\upsilon \boldsymbol{b}}{2l} \exp\left(-\frac{\Delta G}{kT}\right) \quad , \tag{5.17}$$

where υ is the frequency of attempts (successful or otherwise) of dislocations to jump energy barriers, l is the pinning distance, ΔG is Gibbs free energy. Lastly, k and T are Boltzman constant and the temperature, respectively.

Gibbs free energy is a measure of the spontaneity of a process. For $\Delta G < 0$ the reaction is spontaneous, for $\Delta G > 0$ the reaction is non-spontaneous, and if $\Delta G = 0$ the system is in equilibrium. Under a stress field, Gibbs [1969] formulated Gibbs free energy as:

$$\Delta G = \Delta F - \tau \Delta V \quad , \tag{5.18}$$

where ΔF represents Helmholtz free energy, i.e. the amount of maximum energy available to perform work. τ is the resolved shear stress acting on the slip plane and ΔV is the thermodynamic activation volume. Replacing Eq. 5.18 into Eq. 5.17, the rate of successful forward activation becomes:

$$\Gamma_{\text{forward}} = \frac{v\boldsymbol{b}}{2l}\ \exp\left(-\frac{\Delta F}{kT}\right)\exp\left(\frac{\tau\Delta V}{kT}\right) \quad , \tag{5.19}$$

and for backward activation:

$$\Gamma_{\text{backward}} = \frac{v\boldsymbol{b}}{2l}\ \exp\left(-\frac{\Delta F}{kT}\right)\exp\left(-\frac{\tau\Delta V}{kT}\right) \quad . \tag{5.20}$$

Considering that $\sinh(x)=\frac{e^{x}-e^{-x}}{2}$ and replacing Eqs. 5.19 and 5.20 into Eq. 5.16, the net probability of thermal activation, $\bar{\Gamma}$, becomes:

$$\bar{\Gamma} = \frac{v\boldsymbol{b}}{2l}\ \exp\left(-\frac{\Delta F}{kT}\right)\sinh\left(\frac{\tau\Delta V}{kT}\right) \quad , \tag{5.21}$$

and the average velocity can thus be written as:

$$\bar{v} = \ d\ \frac{v\boldsymbol{b}}{l}\ \exp\left(-\frac{\Delta F}{kT}\right)\sinh\left(\frac{\tau\Delta V}{kT}\right) \quad . \tag{5.22}$$

Therefore, assuming that $d \approx l$, as suggested by Dunne, Rugg & Walker [2007], the slip rate, $\dot{\gamma}$, presented in Eq. 5.14 can be rewritten as:

$$\dot{\gamma}^{k} = \ \rho_{m} v\boldsymbol{b}^{2}\ \exp\left(-\frac{\Delta F}{kT}\right)\sinh\left(\frac{\Delta V}{kT}\left|\tau^{k}-\tau_{c}^{k}\right|\right) \quad . \tag{5.23}$$

τ^{k} represent the resolved shear stress on the k^{th} slip system and τ_{c}^{k} is the corresponding critical resolved shear stress. A slip system is considered active when $\tau^{k} \geq \tau_{c}^{k}$. Busso et al. [2000] and Dunne, Rugg & Walker [2007] argue that the predominant pinning mechanisms, i.e. the overall slip resistance in each active system, are due to forest obstacles arising from both statistically stored (SSDs) and geometrically necessary dislocations (GNDs) at low strain gradients. A length-scale dependent mechanical response can thus be introduced by making the pinning distance, l, dependent on the dislocation density within the activation volume [Jones, 2016]. Therefore, strain rate

and subsequent plastic deformation decreases as GND density increases.

Dunne, Rugg & Walker [2007] defined the activation volume as $\Delta V = l\boldsymbol{b}d$, i.e. the activation volume is bounded by the pinning distance, l, Burgers vector magnitude, $\boldsymbol{b}$, and the thermal activation jump length needed to overcome the energy barrier, d. Considering the argument above that the majority of pinning points are produced by other dislocations, Dunne et al. considered that the jump length, d, may be approximate to the Burgers vector, $\boldsymbol{b}$. Therefore, the activation volume becomes:

$$\Delta V = l\boldsymbol{b}^2 \quad , \tag{5.24}$$

where the pinning distance is equal to the mean free distance between dislocations:

$$l = \frac{1}{\sqrt{\psi\left(\rho_{GND} + \rho_{SSD}\right)}} \quad , \tag{5.25}$$

in which ρ_{GND} and ρ_{SSD} are the overall densities of GNDs and SSDs, respectively. The coefficient ψ represents the probability of pinning, indicating that not all dislocations (SSDs and GNDs) necessarily act as pinning points. Substituting Eqs. 5.24 and 5.25 into Eq. 5.23, the slip rate, $\dot{\gamma}$, can ultimately be reformulated as:

$$\dot{\gamma}^k = \rho_m v \boldsymbol{b}^2 \exp\left(-\frac{\Delta F}{kT}\right) \sinh\left(\frac{b^2\left|\tau^k - \tau_c^k\right|}{kT\sqrt{\psi\left(\rho_{GND} + \rho_{SSD}\right)}}\right) \quad . \tag{5.26}$$

5.2.2 Evolution of SSD and GND densities

The plastic deformation rate, $\boldsymbol{D}^p$, is the symmetric part of the plastic velocity gradient, $\boldsymbol{L}^p$, formulated as:

$$\boldsymbol{D}^p = \mathrm{sym}\left(\boldsymbol{L}^p\right) = \frac{1}{2}\left(\boldsymbol{L}^p + \boldsymbol{L}^{pT}\right) \quad . \tag{5.27}$$

In the current crystal plasticity framework, the evolution of SSDs density, ρ_{SSD}, is taken to evolve linearly with the accumulated slip rate as:

$$\dot{\rho}_{SSD} = \lambda \dot{p} \quad , \tag{5.28}$$

where λ is the hardening coefficient, experimentally determined to ensure appropriate polycrystal hardening. $\dot{p}$ represents the effective plastic strain rate, calculated based on the plastic deformation rate, $\boldsymbol{D}^p$:

$$\dot{p} = \sqrt{\frac{2}{3}\boldsymbol{D}^p : \boldsymbol{D}^p} \quad . \tag{5.29}$$

The existence of geometrically necessary dislocations GNDs is the result of strain gradients which are needed to accommodate the lattice curvatures and are necessary to maintain lattice continuity [Arsenlis & Parks, 1999]. In this study, the evolution of geometrically necessary dislocation density is determined geometrically according to Nye [1953] second-order antisymmetric tensor, $\boldsymbol{\Lambda}$:

$$\boldsymbol{\Lambda} = \operatorname{curl}(\boldsymbol{F}^p) = \sum_{k=1}^{12} \rho_{Gs}^k \boldsymbol{b}^k \otimes \boldsymbol{m}^k + \rho_{Get}^k \boldsymbol{b}^k \otimes \boldsymbol{t}^k + \rho_{Gen}^k \boldsymbol{b}^k \otimes \boldsymbol{n}^k \quad . \tag{5.30}$$

Nye's dislocation tensor, $\boldsymbol{\Lambda}$, provides a description for the state of dislocation of a region for which the Burger's vector circuit is open, i.e. for a path that fails to close due to the introduction of a dislocation in the plane. Therefore, the dislocation vector field can be decomposed into three components: screw dislocations parallel to the slip direction, $\boldsymbol{m}^k$, on the k^{th} slip system, and edge dislocation components oriented parallel to the plane normal, $\boldsymbol{n}^k$, and to $\boldsymbol{t}^k = \boldsymbol{n}^k \times \boldsymbol{m}^k$, respectively. Where $\boldsymbol{m}^k$, $\boldsymbol{t}^k$ and $\boldsymbol{n}^k$ form an orthogonal unit vector set. ρ_{Gs}^k is the density of screw components of the GNDs. Analogously, ρ_{Get}^k and ρ_{Gen}^k represent the densities of edge components of the GNDs parallel to $\boldsymbol{t}^k$ and $\boldsymbol{n}^k$, respectively [Busso et al., 2000]. The thirty-six independent GND

components, twelve components of screw dislocation and twenty-four components of edge dislocation, can be determined in matrix form as:

$$\boldsymbol{A}\rho_{GND} = \bar{\boldsymbol{\Lambda}} \quad , \tag{5.31}$$

where $\bar{\boldsymbol{\Lambda}}$ is a nine-dimension column vector containing the components of Nye's tensor, $\boldsymbol{\Lambda}$. $\boldsymbol{A}$ represents a linear operator (9×36) containing the basis tensors, $\boldsymbol{b}^k \otimes \boldsymbol{m}^k$, $\boldsymbol{b}^k \otimes \boldsymbol{t}^k$ and $\boldsymbol{b}^k \otimes \boldsymbol{n}^k$, such that the rows in $\boldsymbol{A}$ incorporate the nine components for each calculated tensorial product, for each of the thirty six GND components. ρ_G is the thirty-six-dimension column vector containing the screw and edge dislocation densities in the twelve slip systems.

Arsenlis & Parks [1999] presented two methods to solve Eq. 5.31 and obtain an unique solution for ρ_{GND}. The first method, termed L_2 minimisation, is geometrically motivated through Eq. 5.32 and involves the minimisation of the sum of the squares of the resulting dislocation densities. The second method, referred to as L_1 minimisation, is an energetically motivated approach, which calculates a set of dislocation with minimum line energy to support measured lattice curvature [Wilkinson & Randman, 2010]. As both methods yield similar results, the mathematically simpler, L_2, was adopted over L_1 for the implementation of GNDs into Dunne et al.'s crystal plasticity framework.

$$\rho_{GND} = \sqrt{\sum_{\alpha=1}^{12} \left(\rho_{Gs}^{\alpha}\right)^2 + \left(\rho_{Get}^{\alpha}\right)^2 + \left(\rho_{Gen}^{\alpha}\right)^2} \quad , \tag{5.32}$$

Considering the L_2 minimisation and Eq. 5.31, the GND density, for any given value of Nye's tensor, can be explicitly calculated as:

$$\rho_{GND} = \boldsymbol{A}^{-1}\bar{\boldsymbol{\Lambda}} \quad , \tag{5.33}$$

however, $\boldsymbol{A}$ is a 9×36 matrix. Thus, in order to invert it, the right pseudo-inverse of $\boldsymbol{A}$ may be considered, that is,

$$\boldsymbol{A}^{R-1} = \boldsymbol{A}^T \left(\boldsymbol{A}\boldsymbol{A}^T \right)^{-1} \quad . \tag{5.34}$$

Therefore, Eq. 5.33 becomes:

$$\rho_{GND} = \boldsymbol{A}^{R-1} \bar{\boldsymbol{\Lambda}} \quad , \tag{5.35}$$

where $\boldsymbol{A}^{R-1}$ is the 9×9 right pseudo-inverse of $\boldsymbol{A}$.

5.2.3 Hardening rule

A modification of Taylor [1934*a*,*b*] dislocation-based hardening rule is adopted for the evolution of the critical resolved shear stress on the k^{th} slip system, considering SSD and GND densities:

$$\tau_c^k = \tau_{c0}^k + G \cdot \boldsymbol{b} \cdot \sqrt{\rho_{SSD} + \rho_{GND}} \quad , \tag{5.36}$$

where τ_{c0}^k and τ_c^k are the initial and updated critical resolved shear stress on the k^{th} slip system, and G is the shear modulus of the material. The hardening rule presented in Eq. 5.36 does not explicitly include kinematic hardening, even though it has a significant impact on cyclic plasticity and dissipated energy [Moosbrugger & Morrison, 1997]. However, the GNDs density, ρ_{GND}, provides a contribution to kinematic hardening through the establishment of back stresses [Chen, 2018].

5.2.4 Stored energy criterion

Wan et al. [2014] proposed an energy-based criterion that considers local slip accumulation, SSD and GND densities, and the stress field for predicting both the site and

number of cycles for crack nucleation. Stroh [1953, 1954] long argued that local stored energy may be adopted as a failure criterion, as the energy associated with dislocation pile up and constrained plastic flow eventually leads to crack nucleation. Wan's criterion considers thus the locally stored energy rate developed over an area, where GND density, ρ_{GND}, provides implicit length-scale dependency. The energy associated with plastic deformation, $\dot{U}$, per loading cycle per unit volume at a microstructural point may be calculated as:

$$\dot{U} = \oint_{\text{cycle}} \boldsymbol{\sigma} : \boldsymbol{\varepsilon}^p \quad , \tag{5.37}$$

where the integration is carried out over a complete saturated cycle. Wan et al. [2014] hypothesised that the volume within which the energy is stored through the creation of dislocation structure may be written in terms of the mean free distance between dislocations presented in Eq. 5.25:

$$\Delta V_s = \frac{\Delta A_s}{\sqrt{(\rho_{GND} + \rho_{SSD})}} \quad , \tag{5.38}$$

where ΔA_s is the corresponding unit area resulting from dislocation structure (i.e. where dislocation interaction stresses are not negligible) [Wan et al., 2014, 2016; Jiang et al., 2016]. According to Wan et al. [2014] and Chen et al. [2018] the exact contribution of plastic energy associated with storage and dissipation are not known, but they assumed that roughly 5% of the total energy associated with plastic deformation is stored as dislocation structures. The remaining 95% is accepted to be energy dissipated as heat. Therefore, the stored energy density per cycle, $\dot{G}$, can be written considering a stored fraction, ζ, as:

$$\dot{G} = \frac{\dot{U}\Delta V_s}{\Delta A_s} = \oint_{\text{cycle}} \frac{\zeta \ |\boldsymbol{\sigma} : \boldsymbol{\varepsilon}^p|}{\sqrt{(\rho_{GND} + \rho_{SSD})}} \quad . \tag{5.39}$$

The critical stored energy density is assumed as the stored energy required to drive fatigue crack nucleation and may be written in its general form as:

$$G = \oint_{\text{cycle}} \dot{G} dN \quad . \tag{5.40}$$

Assuming a steady-state situation, i.e. a saturated rate of accumulation of stored energy due to plastic shakedown (steady slope for the accumulation rate), Eq. 5.40 may be simplified to:

$$G = G_0 + \dot{G} N_f \quad , \tag{5.41}$$

where G_0 represents the stored energy accumulated in the first few cycles before cyclic saturation, as it is assumed that SSD and GND densities evolve at a higher rate during initial load cycles. Therefore, Wan's criterion (Eq. 5.41) requires knowledge of the critical stored energy density and the length scale measure for predicting fatigue crack nucleation.

5.3 Crystal plasticity implementation

The crystal plasticity framework presented in section 5.2 was implemented in the finite element software Abaqus through a user defined material model (UMAT) subroutine initially developed and provided by Prof Fionn Dunne. As part of this research project, this initial UMAT subroutine was optimised and further developed by the thesis author for the inclusion of GNDs density and Wan et al. criterion. The UMAT implicitly integrates the constitutive equations using the Newton-Raphson iterative method, where quantities are written at the end of the time increment and stress is forced to converge back onto the yield surface using a plastic corrector term [Jones, 2016].

At the beginning of each time increment, Δt, Abaqus calls the UMAT at each inte-

gration point and provides the UMAT with the stress field, σ_t; state dependent variables defined by the user, $SDVs_t$; and the deformation gradient, both at the beginning and end of the time increment, $\boldsymbol{F}_t$ and $\boldsymbol{F}_{t+\Delta t}$ respectively. Given this input, the UMAT provides Abaqus with the updated stress field, $\sigma_{t+\Delta t}$; the material Jacobian, $\frac{\partial \Delta\sigma}{\partial \Delta\varepsilon}$; the updated state variables at the end of the time increment, $SDVs_{t+\Delta t}$; and the total velocity gradient, $\boldsymbol{L}_{t+\Delta t}$, calculated considering the deformation gradient and the time increment. Box 5.1 presents a summary of the UMAT implementation, adapted from [Jones, 2016], for ease of reference.

As presented in Box 5.1, the resolved shear stress, τ^k, is compared with the critical resolved shear stress for each slip system, τ_c. If the yield condition is met, i.e. if $\tau^k > \tau_c$, then a subroutine with the slip rule presented in Eq. 5.26 is called for the determination of the plastic velocity gradient, $\boldsymbol{L^p}$, and the differential of the strain tensor increment, required to define the material Jacobian. This process is embedded in a Newton-Raphson loop within the overall time increment, and iterates until the stress residual, ψ, is reduced to a tolerance $\leq 10^{-12}$ MPa. Once the stress residual has been reduced to the tolerance, the stress at the end of the time increment can be found from the stress used in the last Newton-Raphson loop, $\sigma_{t+\Delta t} = \sigma^{n+1}$. Lastly the Jacobian is updated at the end of the time increment.

Box 5.1 – UMAT implementation summary – Adapted from [Jones, 2016].

1. Determination of total velocity gradient, $\boldsymbol{L}$, considering:

$$\boldsymbol{L} = \dot{\boldsymbol{F}}\,\boldsymbol{F}^{-1}\,.$$

2. Determination of the rates of deformation and continuum spin using the symmetric and asymmetric parts of $\boldsymbol{L}$:

$$\mathrm{sym}(\boldsymbol{L}) = \boldsymbol{\Phi} = \frac{\mathbf{1}}{\mathbf{2}}(\boldsymbol{L} + \boldsymbol{L}^{\boldsymbol{T}})$$

and,

$$\mathrm{asym}(\boldsymbol{L}) = \boldsymbol{\omega} = \frac{\mathbf{1}}{\mathbf{2}}(\boldsymbol{L} - \boldsymbol{L}^{\boldsymbol{T}})$$

3. Stress at the end of the time increment, $\sigma_{t+\Delta t}$ is given in terms of an elastic trial stress, $\boldsymbol{\sigma}^{\boldsymbol{trial}}$, and plastic corrector term, $\boldsymbol{D\Delta\varepsilon^p}$, where $\boldsymbol{D}$ is global elastic constitutive matrix:

$$\sigma_{t+\Delta t} = \boldsymbol{\sigma}^{\boldsymbol{trial}} - \boldsymbol{D\Delta\varepsilon^p}$$

4. Calculation of the resolved shear stress on the k^{th} slip system, τ^k, based on the elastic trial $\boldsymbol{\sigma}^{\boldsymbol{trial}}$:

$$\tau^k = (\boldsymbol{s}^k \otimes \boldsymbol{n}^k) : \sigma_{t+\Delta t}$$

5. Determination of active slip systems considering the critical resolved shear stress, τ_c,:

$$\boldsymbol{if}\ \frac{\tau^k}{\tau_c} > \mathbf{1}\ \text{, then slip system is active.}$$

6. If the yield condition in (5) is met, then the plastic corrector term, $\boldsymbol{D\Delta\varepsilon^p}$, is $> \mathbf{1}$. The plastic strain increment, $\Delta\varepsilon^p$, is given by:

$$\boldsymbol{\Delta\varepsilon^p} = \mathrm{sym}(\boldsymbol{L})\boldsymbol{\Delta t} = \boldsymbol{\Phi\Delta t}\ \ ,$$

if $\boldsymbol{\Delta\varepsilon^p} > \mathbf{0}$ then a Newton-Raphson iterative loop within the overall time increment is needed to determine the stress and Jacobian at the end of the time increment, $\sigma_{t+\Delta t}$ and $\frac{\partial\Delta\sigma}{\partial\Delta\varepsilon}$.

7. Determination of the stress residual, ψ, for the Newton-Raphson iterative loop:

$$\psi = \sigma_{t+\Delta t} - \boldsymbol{\sigma}^{\boldsymbol{trial}} + \boldsymbol{D\Delta\varepsilon^p} = \mathbf{0}$$

8. The plastic strain increment, $\boldsymbol{\Delta\varepsilon^p}$, is given in terms of the constitutive equation for $\boldsymbol{L^p}$ by:

$$\boldsymbol{\Delta\varepsilon^p} = \boldsymbol{\delta}\,\boldsymbol{sym}\left(\sum_{\boldsymbol{k}} \rho_m \upsilon \boldsymbol{b^2} \exp\left(-\frac{\Delta F}{kT}\right) \sinh\left(\frac{b^2|\tau^k - \tau_c^k|}{kT\sqrt{\psi(\rho_{GND} + \rho_{SSD})}}\right) \Delta t(\boldsymbol{s}^k \otimes \boldsymbol{n}^k)\right)$$

9. Determine the stress increment:

$$\boldsymbol{\delta\sigma} = [\boldsymbol{I} + \boldsymbol{DP}]^{-\mathbf{1}}(\boldsymbol{\sigma}^{\boldsymbol{trial}} - \sigma_{t+\Delta t} - \boldsymbol{D\Delta\varepsilon^p})$$

where $\boldsymbol{P} = \sum_{\boldsymbol{k}} \rho_m \upsilon \boldsymbol{b^2} \exp\left(-\frac{\Delta F}{kT}\right)\left(\frac{b^2|\tau^k - \tau_c^k|}{kT\sqrt{\psi(\rho_{GND}+\rho_{SSD})}}\right) \cosh\left(\frac{b^2|\tau^k - \tau_c^k|}{kT\sqrt{\psi(\rho_{GND}+\rho_{SSD})}}\right) \Delta t(\boldsymbol{s}^k \otimes \boldsymbol{n}^k) \otimes (\boldsymbol{s}^k \otimes \boldsymbol{n}^k)$

10. Update the stress at the end of the time increment:

$$\boldsymbol{\sigma^{n+1}} = \boldsymbol{\sigma^n} + \boldsymbol{\delta\sigma}$$

If $\psi \leq 10^{-12}$ MPa, then $\sigma_{t+\Delta t} = \boldsymbol{\sigma^{n+1}}$

11. Determine the Jacobian at the end of the time increment:

$$\mathrm{J} = \frac{\partial\Delta\sigma}{\partial\Delta\varepsilon} = [\boldsymbol{I} + \boldsymbol{DP}]^{-\mathbf{1}}\boldsymbol{D}$$

5.3.1 Microstructurally representative volume element model

A microstructurally representative volume element (RVE) of RR1000, characterised by Chen [2018], was used for the investigation. Chen performed a statistical measurement of RR1000 grain size and used it as an input for the three-dimensional microstructure construction software, DREAM.3D, developed by Groeber & Jackson [2014]. Figure 5.2 presents the grain size distribution for RR1000 and the RVE with 168 surface grains constructed by Chen, using synthetic instantiation optimisation techniques. The grain size distribution of the microstructure was set so that the macroscopic response of the model would match experimental data at similar test conditions. According to Chen, RR1000 minimum, mean and maximum grain sizes are approximately 1μm, 5μm and 20μm, respectively. A random microstructure texture for the RVE was generated considering the distribution presented in Fig. 5.3a. Figure 5.3b presents the pole figures for the simulated texture of the RVE. Table 5.1 summarises the material properties for RR1000 crystal slip used in the UMAT for calculating the expressions presented in Section 5.2.

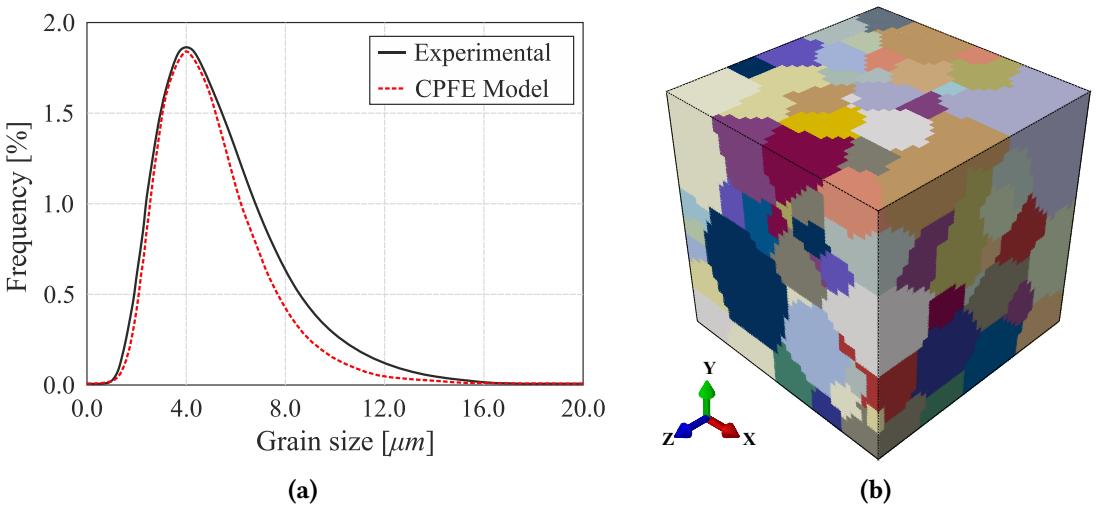
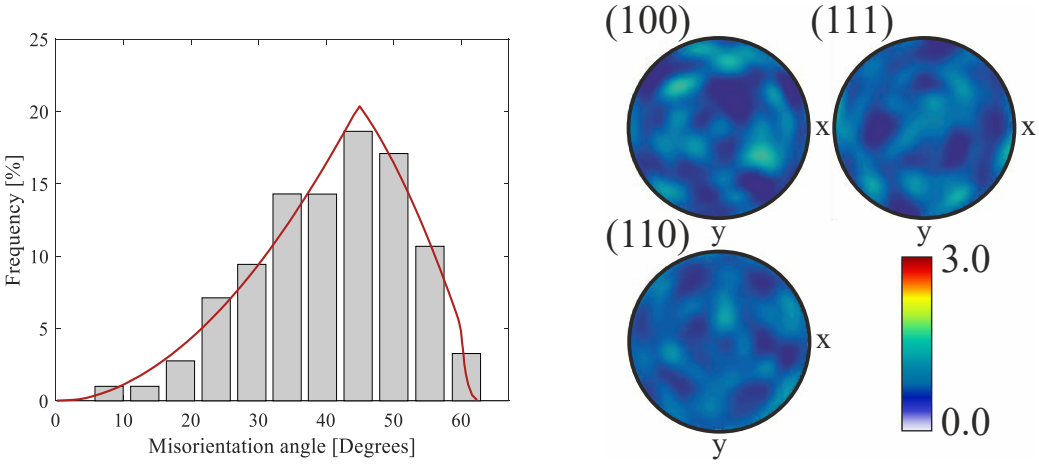


Figure 5.2 – a) Statistical grain size distribution; b) Microstructurally representative volume element. Adapted from Chen [2018].



(a) (b)

Figure 5.3 – a) Misorientation distribution of the RVE; b) RVE texture information pole figures. Adapted from Chen [2018].

Table 5.1 – Material properties for RR1000 crystal slip.

Parameter	**Value**
Elastic modulus – E [MPa]	210E+3
Shear modulus – $\boldsymbol{G}$ [MPa]	90E+3
Density of mobile dislocations, $\rho_m[\mu m^{-2}]$	0.05
Attempt frequency – υ	1.0E+11
Burgers vector – $\boldsymbol{b}$ [μ m]	3.5072E-4
Helmholtz free energy – ΔF [pJ]	3.456E-8
Boltzman constant – k [pJ/K]	1.381E-11
Critical resolved shear stress – τ_c [MPa]	450
Operating temperature - K	293
Hardening coefficient – λ [μm^{-2}]	150

5.3.2 Mesh discretisation

The RVE presented in Fig. 5.2b was discretised using 64,000 twenty-node hexahedral quadratic element with reduced integration (C3D20R). Grain boundaries are assumed to be rigid, i.e. the grain boundary between two grains is considered to be the common surface between their elements in the FE model. Figure 5.4 presents the mesh used for the simulations, each hexahedral quadratic element has its height, width and depth equal to 0.675μm. The accuracy of the CPFE model is strongly dependent on its mesh

density, where a finer mesh results in more accurate solutions. However, finer mesh requires longer computational time to reach the problem solution. Therefore, there is a trade-off between solution accuracy and computational cost. The element dimensions used in the analysis were selected from a mesh convergence study initiated by Chen [2018] and further developed as part of this thesis.

Figure 5.5 describes the total accumulated slip distribution across the microstructure after one stress-controlled uniaxial load cycle for three different mesh densities. Fine mesh represents results obtained with quadratic elements of 0.45μm, medium mesh represents elements of 0.675μm, and coarse mesh uses elements of 1.0125μm. Results show similar and close correlated accumulated slip distribution across the different resolutions, although a larger right tail bin appeared in the coarse mesh model. Figure 5.6 illustrates the spatial distribution of accumulated plastic slip for the medium and coarse meshes. The results imply that grain misorientation dictates the strain gradients adjacent to the boundary. Furthermore, similar contour plots can be observed for the different mesh discretisation, yet the medium-refined mesh provides better resolution (i.e. smoother distribution) for capturing plastic slip and dislocation density accumulation at the grain boundaries, as highlighted by the points of maximum accumulated plastic slip in Fig. 5.6. Hence, in order to obtain an optimum balance between computational cost and result accuracy, the medium resolution mesh was adopted for the simulations investigated in this chapter.

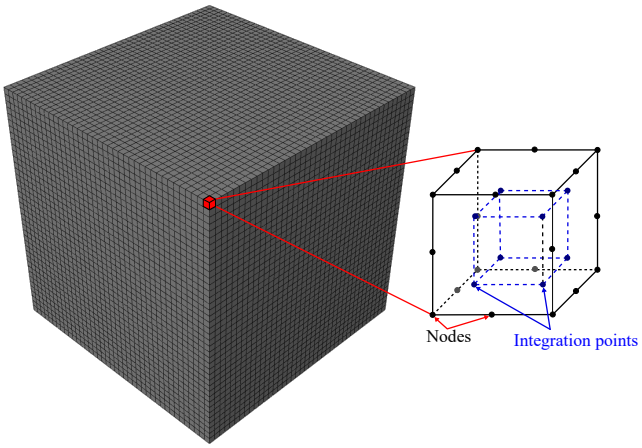


Figure 5.4 – RVE mesh and illustration of C3D20R element.

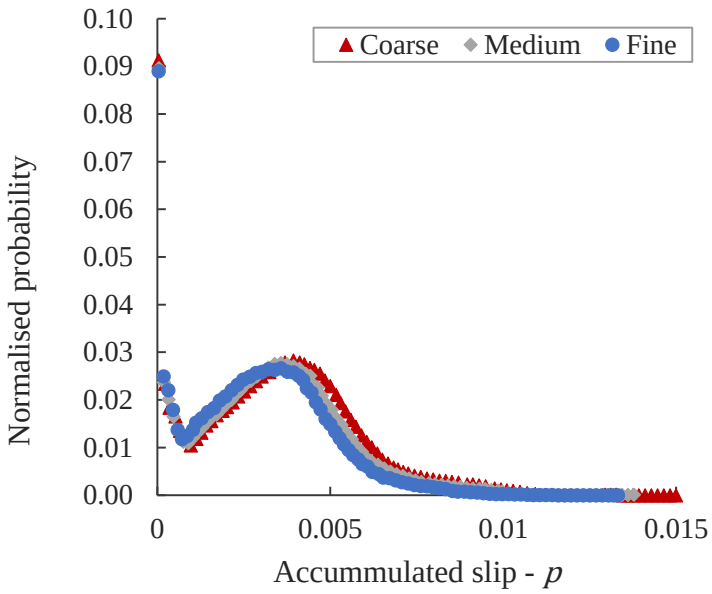


Figure 5.5 – Mesh convergence study. Adapted from Chen [2018].

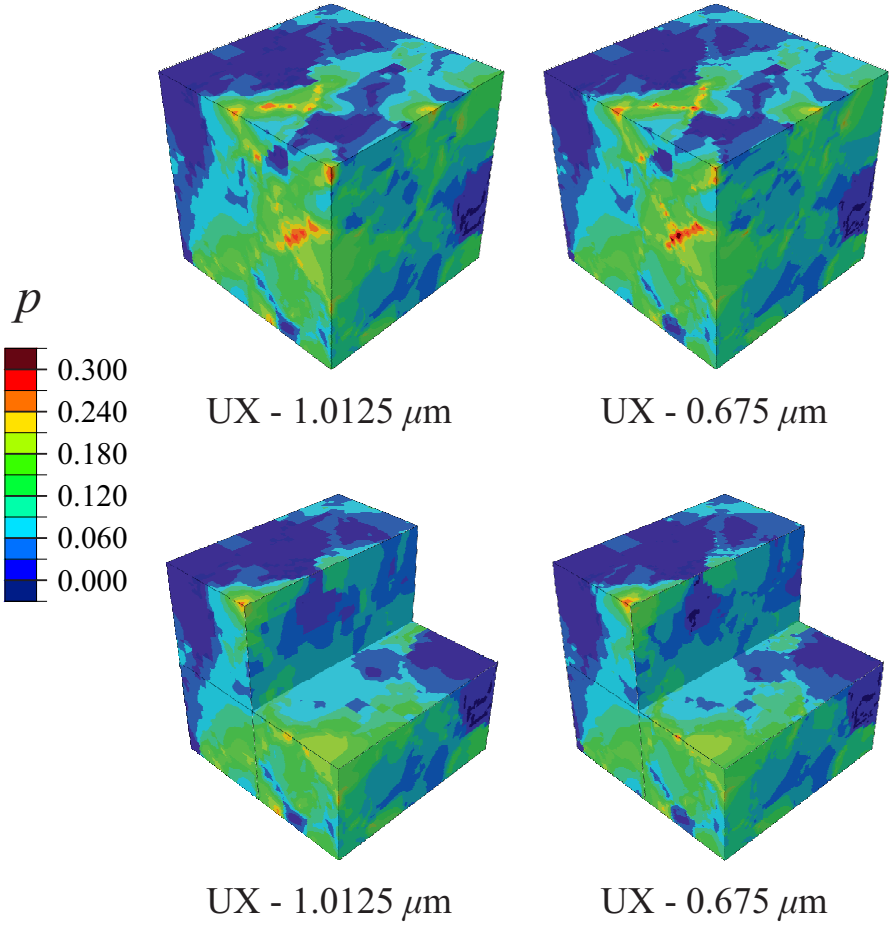


Figure 5.6 – Accumulated plastic slip, p, after 1 load cycles at $\sigma_{\text{vM,peak}}$ = 1150MPa.

5.3.3 Boundary conditions and loads

Restriction of displacement in the x-direction was applied to the back face of the RVE, on the y-z plane. In addition, the nodes at the bottom left and right vertexes of the RVE back face are fixed in the y-directions. Lastly, a z-direction displacement constrain is also applied to the node at the bottom right vertex of the back face. Figure 5.7 illustrates the applied boundary conditions.

The elements containing the constrained nodes at the vertexes were defined as purely elastic and a considerably larger stiffness was assigned to them to ensure solution convergence. Due to the material properties associated to these elements, the stresses seen in them and in the region immediately around them are the highest in the RVE. Therefore, in order to annihilate their influence on the results, a cube formed by the 9x9x9 elements surrounding the nodes at the vertexes were excluded from the post-processing analysis. An alternative to this approach would be the implementation of periodic boundary conditions. However, this would add another layer of complication to the model, leading to even longer simulation times.

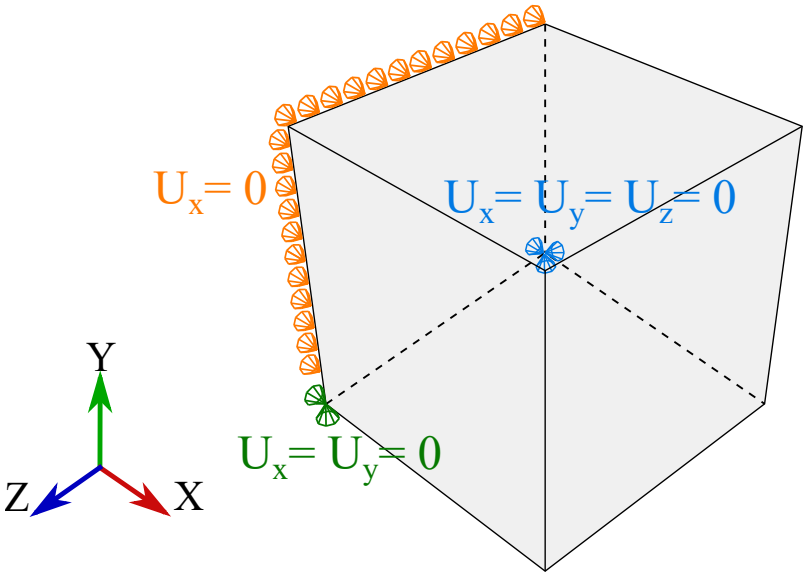
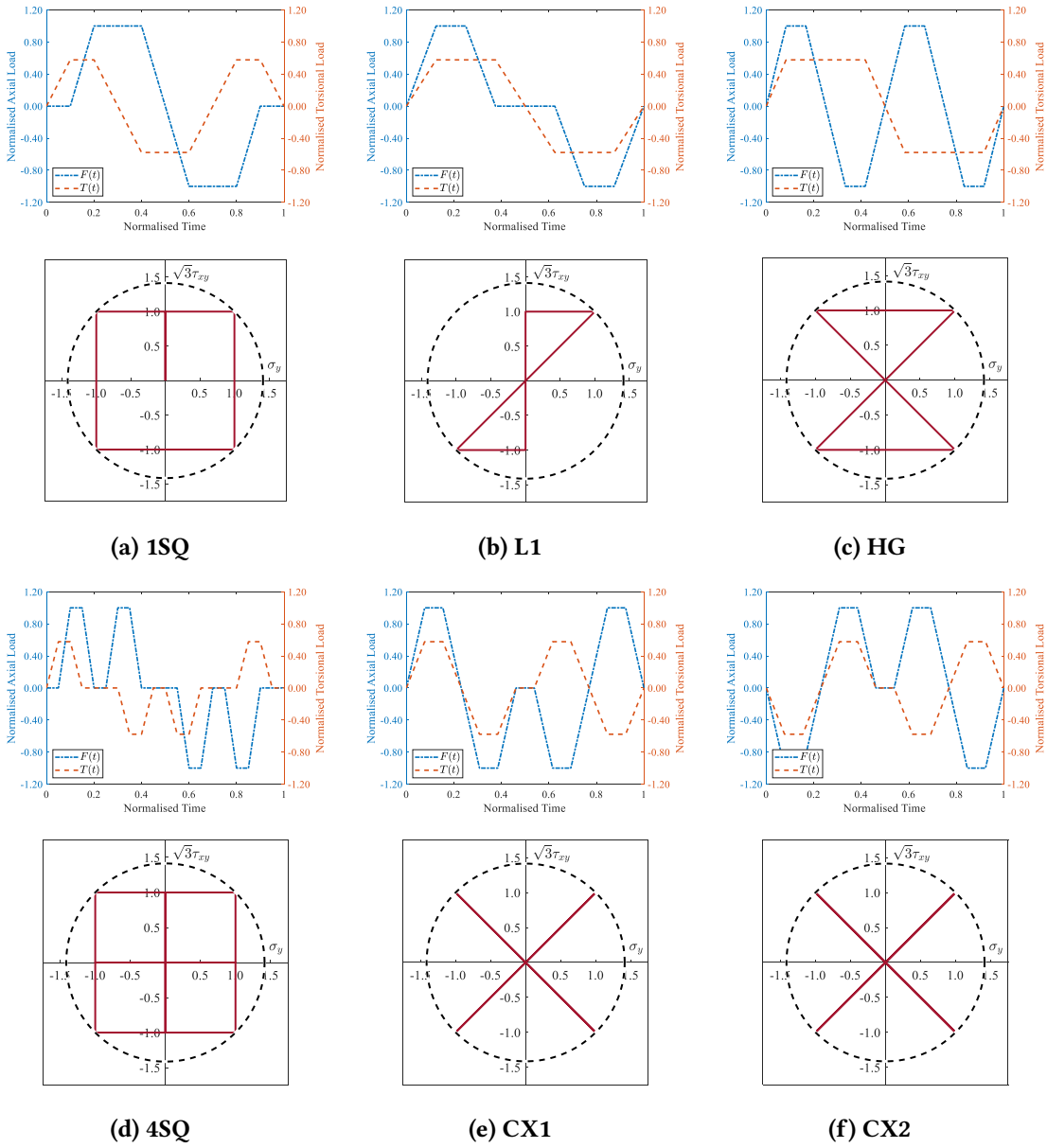


Figure 5.7 – Boundary conditions applied to the RVE.

A total of nine load path were implemented in the CPFE model for assessing its performance in predicting fatigue lives of RR1000 under multiaxial load conditions. Initially, uniaxial, pure torsion and in-phase tension-torsion loading conditions were simulated for calibrating the model against the results obtained by Chen [2018] in her doctoral thesis. After that, the six non-proportional load paths experimentally investigated in chapter 3 were discretised and implemented in Abaqus. Each load condition was simulated with GND densities coupled and uncoupled, and at two different von Mises peak stress: 1050MPa and 1150MPa with load ratio $R = -1$. These load levels were selected for two reasons. First, they are the nominal stress values selected by Bees [2016] for his multiaxial fatigue tests with RR1000 and for the simulations carried out by Chen. Second, these nominal peak stresses are comparable to the stress levels measured with the tension-torsion tests presented in this research project (Chapter 3). Figure 5.8 shows the load path discretisation used in the Abaqus UMAT.

It should be noted that the computational cost of running CPFE simulations poses a severe limitation to the number of fatigue load cycles that can be simulated. For load paths with greater number of reversals, such as the 4SQ and CX1 load paths, the simulation of a single load cycle could take as much as 35 hours to complete. Therefore, simulations were restricted to a maximum of ten load cycles, meaning that fatigue crack nucleation and crack failure would have to be extrapolated from this small number of load cycles. However, as the results present in the following section, the material quickly reaches a steady state (steady slope for the accumulation rate) and fatigue life predictions can be made with good accuracy.



(a) 1SQ **(b) L1** **(c) HG**

(d) 4SQ **(e) CX1** **(f) CX2**

Figure 5.8 – Load discretisation for Abaqus UMAT.

5.3.4 Model Calibration

Initial simulations were carried out to confirm the accuracy of the CPFE model in describing the macroscopic cyclic hardening behaviour of RR1000 and to identify how the coupling of GND densities, ρ_{GNDs}, impact the simulated stress-strain response of RR1000. Kiwanuka [2013] presents the importance of GND coupling for the accurate description of lattice rotation (and hence GND density) at locations of significant heterogeneity, such as grain boundaries, where the conventional crystal plasticity have

shown to be problematic. As RR1000 is a fine-grained material (Fig. 5.2a), the role of GNDs is thought to be particularly important for the evolution of stored energy density. Therefore, in order to investigate its impact on the crystal-plasticity framework proposed by Dunne et al., the hardening parameters presented by Chen [2018] were kept the same, so that a comparison solely based on the introduction of GND densities could be carried out.

Figure 5.9 illustrates the hysteresis loops obtained for a fully reversed uniaxial strain-controlled, $R = -1$, simulation against experimental data with strain amplitude $\frac{\Delta\varepsilon_{yy}}{2} = 0.90\%$. The red dots in Fig. 5.9 represent the experimental fatigue data obtained by Bees [2016] and previously presented in Chapter 4 of this doctoral thesis. The black dashed line and the green solid line are the response for the GND-uncoupled model for the first and fifth load cycles, respectively. The GND-uncoupled model is able to accurately describe the macroscopic cyclic behaviour of RR1000 during the first load cycle. However, for subsequent cycles, the model predicts exaggerated peak stresses, indicating that the parameters calibrated by Chen [2018] might be over non-conservatives.

Figure 5.10 presents a comparison between the GND-uncoupled model against the GND-coupled model for fully reversed uniaxial strain-controlled simulations with strain amplitude $\frac{\Delta\varepsilon_{yy}}{2} = 0.80\%$. The two model configurations provide contrasting hysteresis loop shapes and peak stresses, where clear distinctions can be observed already in the very first load cycle. Interestingly the hysteresis loop obtained with the GND-uncoupled model for the 5th load cycle lies closely to the hysteresis loop obtained for the first load cycle with the GND-coupled configuration. The explanation for that is the introduction of GND densities explicitly on both the hardening rule and slip rule of the material, which increases the hardening process of RR1000.

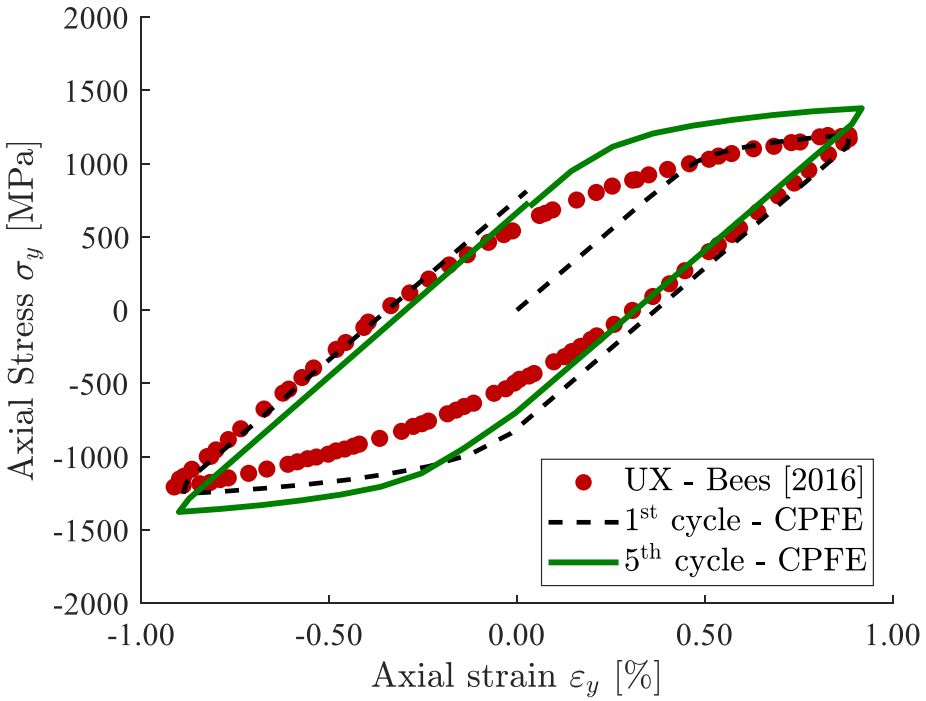


Figure 5.9 – Cyclic response for uniaxial strain controlled with $\frac{\Delta\varepsilon_{yy}}{2}$ = 0.90%. GND-uncoupled CPFE model.

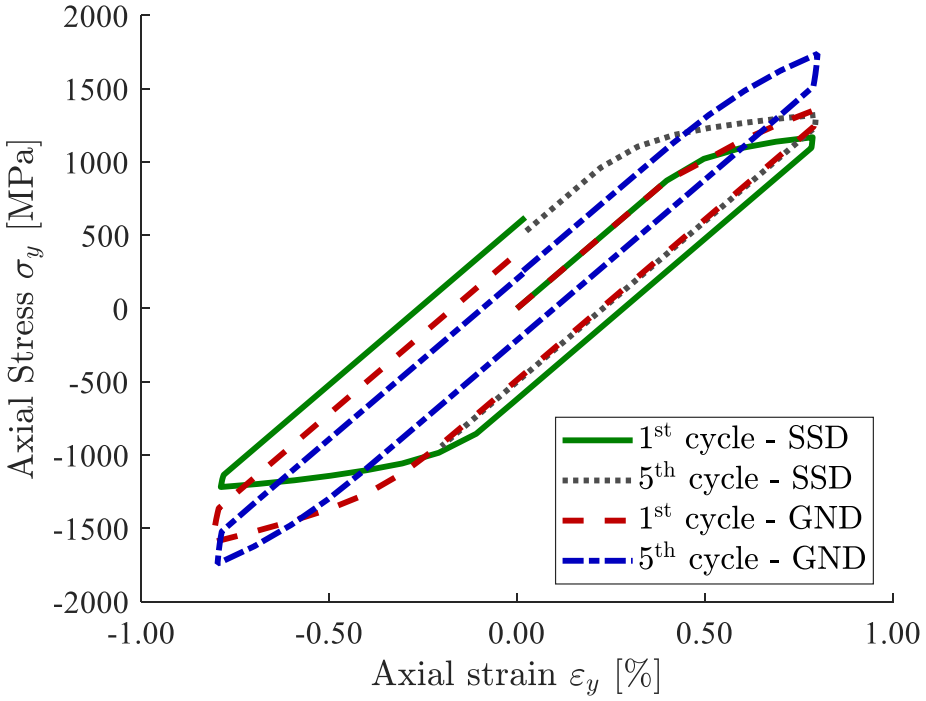


Figure 5.10 – Cyclic response for uniaxial strain controlled with $\frac{\Delta\varepsilon_{yy}}{2}$ = 0.80%. GND-uncoupled (SSD in the legend) vs GND-coupled (GND in the legend) CPFE model.

A second calibration procedure was performed to verify if the stress distribution seen in the RVE, due to the grain size and misorientation configuration adopted, are representative of the loads applied. Figure 5.11 illustrates the von Mises peak stress distribution for the first peak loading point of the 1SQ load path for both GND-couple and uncoupled configurations, represented in Fig. 5.11 by GND and SSD respectively. The normalised histogram illustrates the response of 4096 elements of the RVE at nominal peak von Mises of 1050MPa and 1150MPa. The stress range observed for the simulations at 1050MPa range from 935MPa to 1180MPa and mean of 1045MPa for the uncoupled configuration, and ranges from 962MPa to 1160MPa and mean of 1035MPa for the GND-coupled model. For the 1150MPa simulations, von mises peak stresses range from 985MPa to 1370MPa and mean of 1155MPa for the uncoupled model and range from 1055MPa to 1300MPa, with mean of 1163MPa for the GND-coupled configuration. Therefore, both configurations present stress distributions representative of the loads applied, with the uncoupled configuration presenting slightly wider stress ranges.

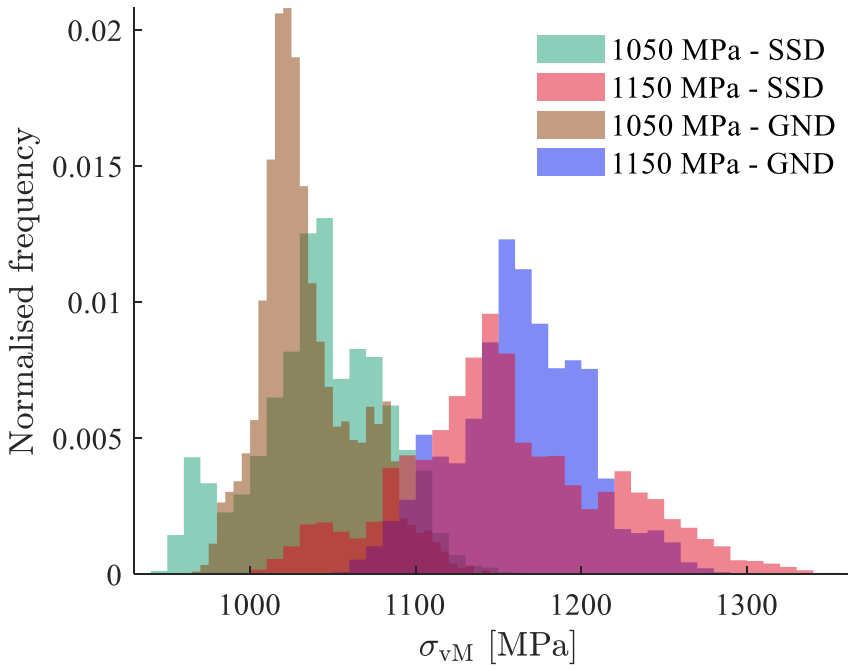


Figure 5.11 – Frequency distribution of peak von Mises equivalent stress for the CPFE model under 1SQ load path.

5.4 Results

A total of thirty-six simulations were performed, considering two model configurations (with and without accumulated GND densities), nine load paths and two peak von Mises stress levels (1050MPa and 1150MPa). Uniaxial, pure torsion and proportional load conditions were used for calibrating the CPFE model and the stored energy density parameter. The results obtained with these three proportional load paths are presented as reference point for the assessment of the six non-proportional load paths used for the RR1000 experimental programme. Figures 5.12–5.15 present the evolution of accumulated plastic slip against load cycles for the material points exhibiting the maximum value by the end of the 10^{th} cycle, these points are referred to as hotspots in the following discussion. A combination of quantitative and qualitative assessment was performed for selecting the hotspots. First, the top 10 centroids exhibiting the highest level of accumulated plastic slip were identified. Then, a careful and pragmatic analysis was performed to identify which of these element centroids was located in the region where a fatigue crack was most likely to nucleate, i.e. where not only the parameter been investigated was maximised but also where σ_{vM} and dissipated energy levels were considerably high and affecting a significant volume of material. An analogous procedure was adopted for the investigation of accumulated GND density and accumulated stored energy.

Each figure (Figs. 5.12–5.15) represents one model configuration at a particular von Mises nominal peak stress. Figures are further divided into two, plots on the left illustrate the results for the proportional load cases and the L1 load path, as RR1000 exhibits similar response under this load path and under proportional tension-torsion tests, as presented in Chapter 3. The plots on the right present the non-proportional load paths with $F = 1$, i.e. load paths with degree of non-proportionality equal to that of 1SQ (90° out-of-phase) load path.

Clearly from Figs. 5.12–5.15, different load path result in different levels and rates

of accumulated plastic slip, evidencing the material load path dependency. Figures 5.12 and 5.13 illustrate the evolution for the model with GND density switched off with maximum applied von Mises stress of 1050MPa and 1150MPa, respectively. Similar response is obtained for both stress levels. For the proportional plots (on the left), maximum accumulated slip is observed for the pure torsion loading condition, followed by L1 load path. If plastic slip was considered solely as a fatigue life prediction parameter, the pure-torsion case would give the shortest lives and the uniaxial test case the longest. This is the opposite of what Bees [2016] concluded from his experimental work on RR1000 at the same load conditions. Bees shows that RR1000 lives under pure torsion loading are roughly three times longer than lives obtained under uniaxial testing. He also reports similar lives for proportional tension-torsion and pure torsion loading paths. Regarding the five non-proportional load paths with $F = 1$ (plots on the right of Fig. 5.12 and 5.13), similar accumulated slip is observed for 4SQ, CX1 and CX2 load paths. The greatest slip accumulation is seen for the HG loading condition, at levels and rates comparable to L1 load path. However, it is important to recap that these two load paths give very distinct fatigue lives, where L1 gives lives similar to the in-phase test cases and HG lives similar to the other non-proportional load paths with $F = 1$.

Figure 5.14 and 5.15 show the evolution of plastic slip with the GND-coupled model configuration at nominal von Mises peak stress of 1050MPa and 1150MPa, respectively. A clear distinction can be observed on the accumulation of plastic slip with the introduction of GND density. Accumulation for the GND-coupled model exhibit an almost linear behaviour, whilst for the model without GNDs, slip accumulation have a logarithmic response, saturating after a few number of cycles. Overall, the total levels of plastic deformation are lower with GND density than without it (Fig. 5.12 and 5.13), illustrating the additional hardening introduced by this parameter. Considering the plots on the left, the accumulation of slip for the pure torsional load case is now closer to that observed for the in-phase tension-torsion load path. However, the greatest accumulation of plastic slip is still observed for the L1 test case, as if this load path was

the most damaging one. Considering now the results with the non-proportional load paths with $F = 1$ (right-hand side), a closer collapse is seen for the 1SQ, 4SQ, CX1 and CX2 cases, with the HG load path once again with the highest level of accumulated slip and further away from the other loading conditions. Clearly, the accumulated plastic slip, as a parameter on its own, is not capable of distinguishing the variations in fatigue lives observed for RR1000 under the load paths investigated in this doctoral thesis.

Figures 5.16 and 5.18 present the field contour plots of accumulated plastic slip for GND-uncoupled and GND-coupled configurations at $\sigma_{\text{vM,peak}} = 1150\text{MPa}$, respectively. Figures 5.17 and 5.19 illustrate a cut view for the contour plot of the same parameter for the two model configurations. Plastic slip accumulates at different hotspots depending on the load path and model configuration. For instance, for 1SQ load path without GNDs, maximum accumulated plastic slip occurs at the bottom of the RVE's left face, and for the GND-coupled 1SQ simulation, maximum slip occurs at the top face and roughly at the middle of left and front faces. As GNDs promote lattice rotation the hotspot of accumulated plastic slip shift between the two model configurations. In the previous evolution analysis, SQ4, CX1 and CX2 presented similar slip levels. The same observation can be made regarding their plastic slip hotspots and its distribution in the RVE, especially for the GND-coupled configuration.

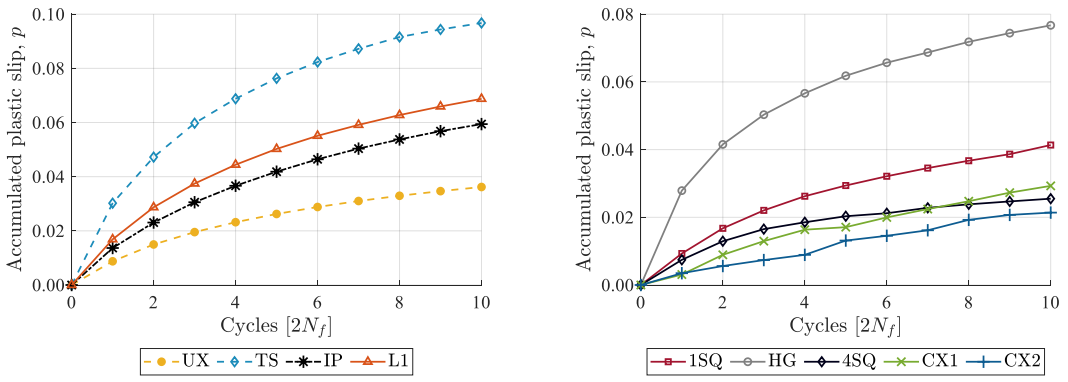


Figure 5.12 – Accumulated plastic slip, p, evolution at $\sigma_{\text{vM,peak}} = 1050\text{MPa}$. GND-uncoupled configuration.

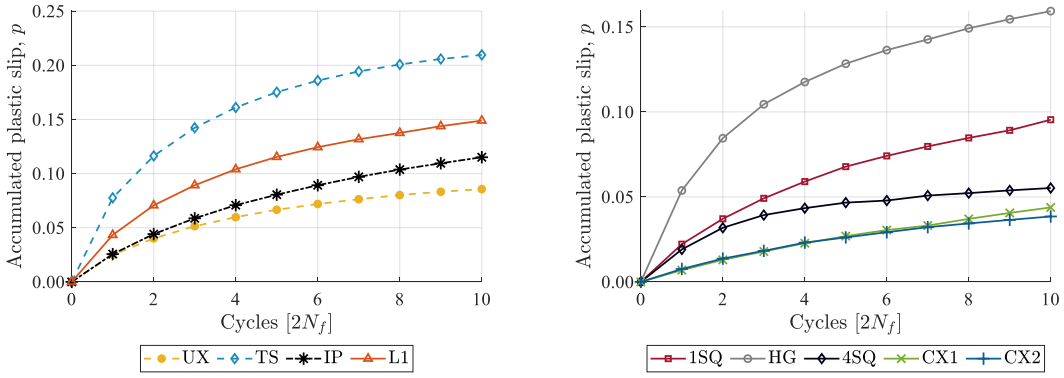


Figure 5.13 – Accumulated plastic slip, p, evolution at $\sigma_{\mathbf{vM,peak}}$ = 1150MPa. GND-uncoupled configuration.

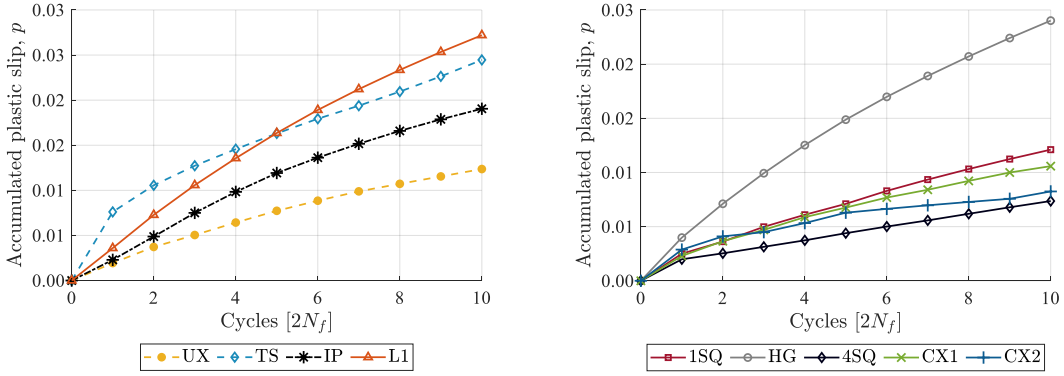


Figure 5.14 – Accumulated plastic slip, p, evolution at $\sigma_{\mathbf{vM,peak}}$ = 1050MPa. GND-coupled configuration.

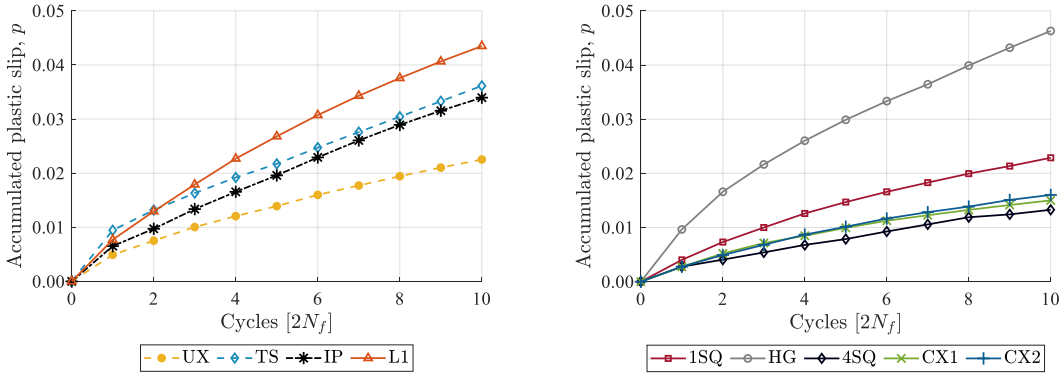


Figure 5.15 – Accumulated plastic slip, p, evolution at $\sigma_{\mathbf{vM,peak}}$ = 1150MPa. GND-coupled configuration.

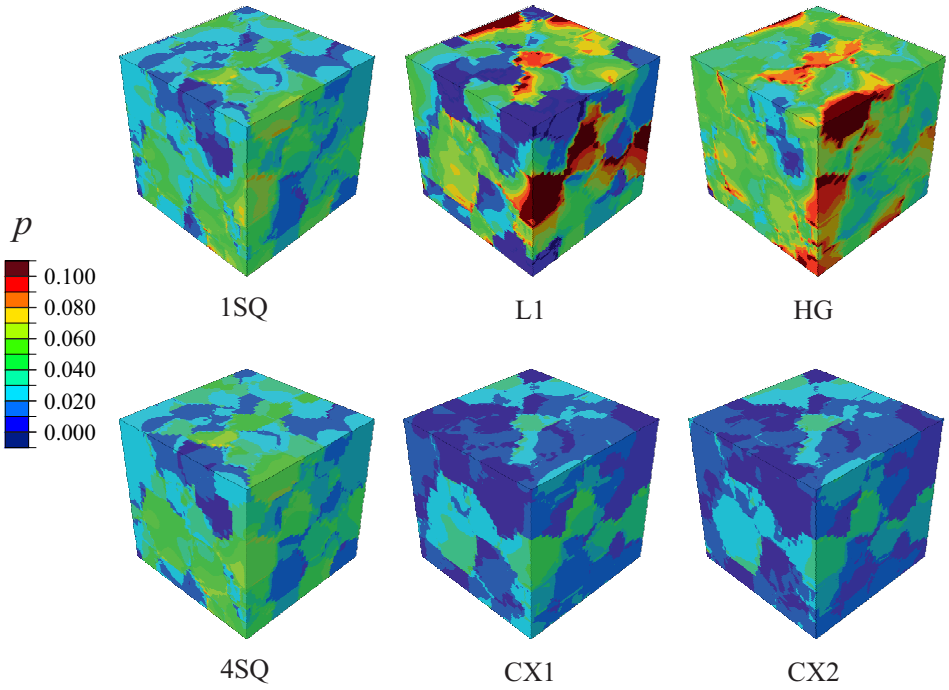


Figure 5.16 – Accumulated plastic slip, p, after 10 load cycles at $\sigma_{vM,peak}$ = 1150MPa. GND-uncoupled model.

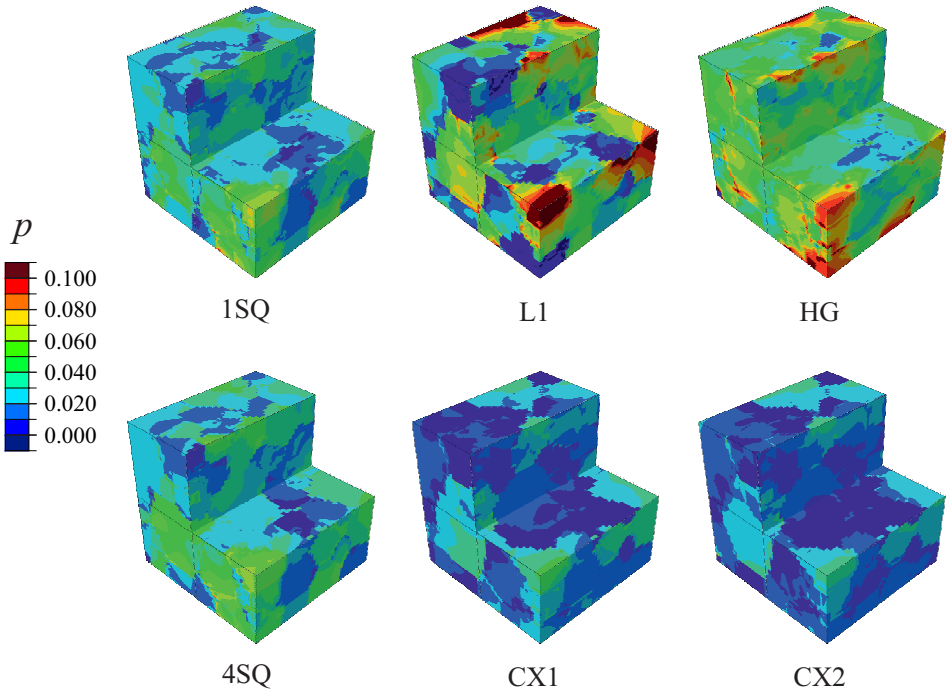


Figure 5.17 – Cut view - Accumulated plastic slip, p, after 10 load cycles at $\sigma_{vM,peak}$ = 1150MPa. GND-uncoupled model.

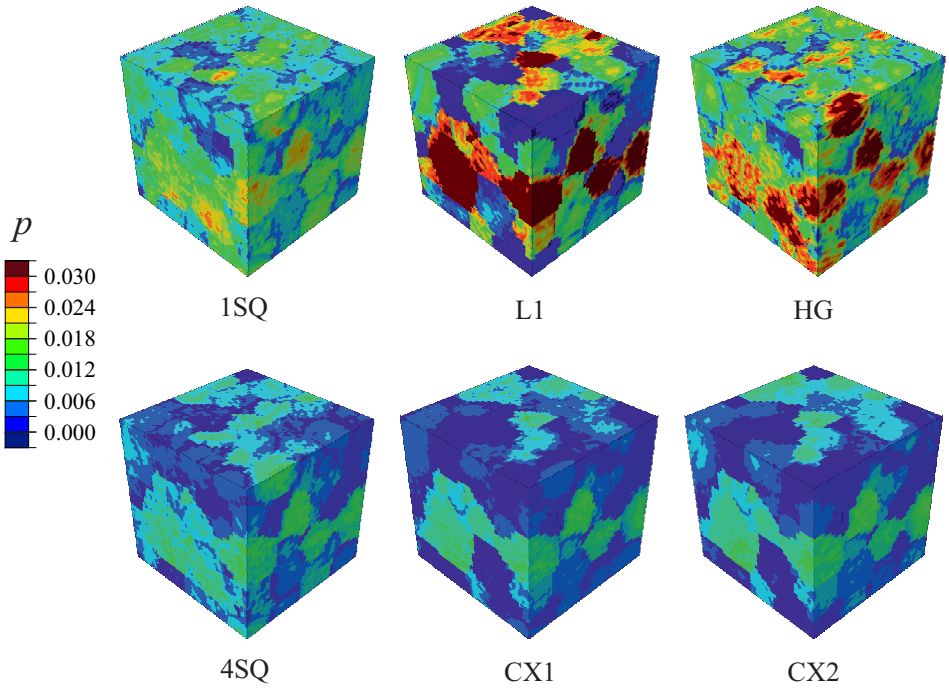


Figure 5.18 – Accumulated plastic slip, p, after 10 load cycles at $\sigma_{\mathrm{vM,peak}}$ = 1150MPa. GND-coupled model.

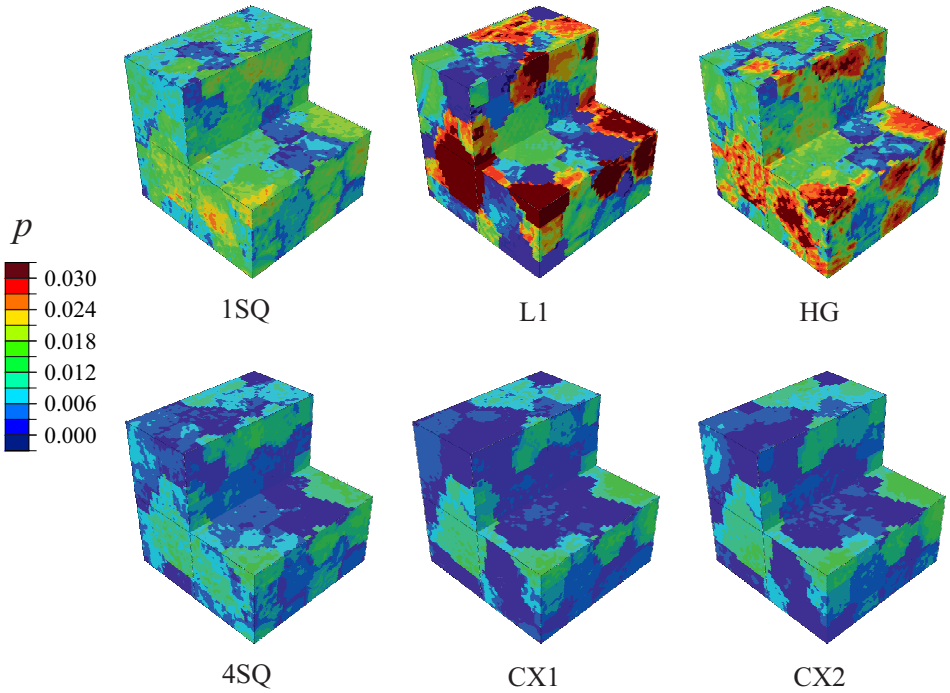


Figure 5.19 – Cut view - Accumulated plastic slip, p, after 10 load cycles at $\sigma_{\mathrm{vM,peak}}$ = 1150MPa. GND-coupled model.

Analogous to the analysis presented previously for plastic slip, an assessment of GND density evolution at the predicted highest hotspots has been carried out for investigating its impact on fatigue life prediction. Figures 5.20 and 5.21 present the evolution of GND density for the nine load paths simulated at maximum nominal von Mises of 1050MPa and 1150MPa, respectively. It is observed for the lower stress condition (1050MPa – Fig. 5.20) that GND density rapidly increases during the first load cycle and then stabilises, showing very little variation during the subsequent cycles. The only exception in Fig. 5.20 is CX1 load path, for which GND density continues to accumulate slowly after the first two cycles. Comparable densities are observed for L1, uniaxial and in-phase loading conditions, and for 4SQ, HG and CX2, accordingly. The highest accumulated GND densities are seen for the pure torsion and 1SQ loading conditions.

Regarding the highest stress level condition (1150MPa – Fig. 5.21), each load path presents a unique evolution curve with little stabilisation after the first load cycle, contrasting greatly with the results obtained with simulations at 1050MPa. In addition, the levels of GND density obtained for most load paths at 1150MPa are lower than those obtained at 1050MPa. Once again, the pure torsional load path attained the greatest value and stabilised quickly after the first load cycle. It is also observed that 1SQ and CX1 present a steep slope that seems to continue beyond the ten cycles simulated. It can be concluded, therefore, that this quantity by itself is not able to directly predict fatigue failure.

Figures 5.22 and 5.23 illustrate the field contour plots of GND densities at $\sigma_{\mathrm{vM,peak}} = 1150\mathrm{MPa}$. It is evident that different GND heterogeneity is generated for each loading path, showing considerable spatial variation. 1SQ and HG load paths present the greater number of hotspots, with higher levels of GND density distributed over the entire RVE. 4SQ and CX2 present both the lowest levels and spatial distributions of GND density. In contrast to accumulated plastic slip, it is possible to distinguish between CX1 and CX2 load path through the distribution and levels of GND density.

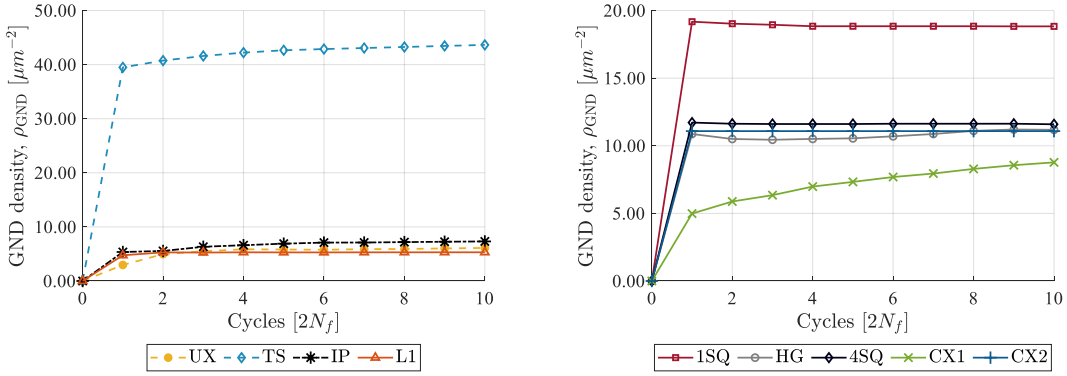


Figure 5.20 – GND density, ρ_{GND}, evolution at $\sigma_{vM,peak}$ = 1050MPa.

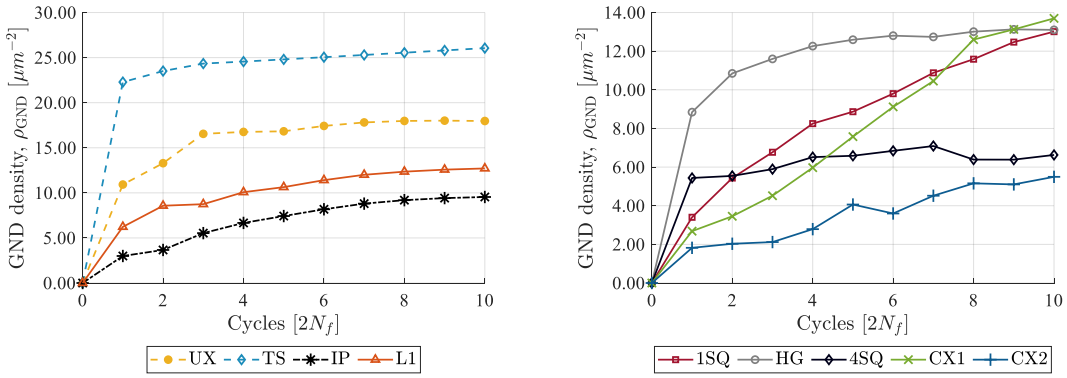


Figure 5.21 – GND density, ρ_{GND}, evolution at $\sigma_{vM,peak}$ = 1150MPa.

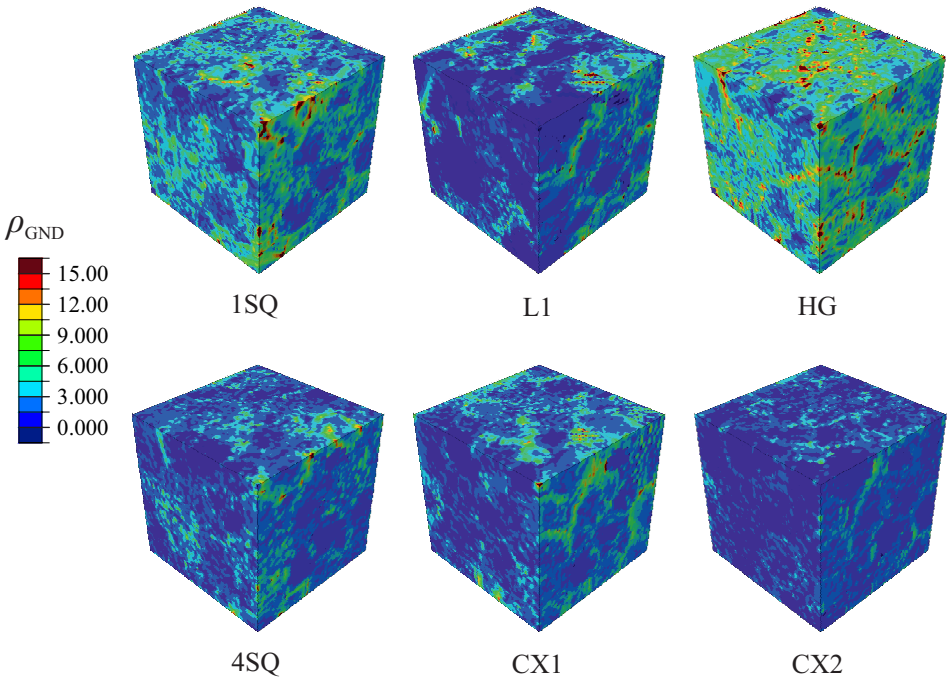


Figure 5.22 – Accumulated GND density, ρ_{GND}, after 10 load cycles at $\sigma_{vM,peak}$ = 1150MPa. GND-coupled model.

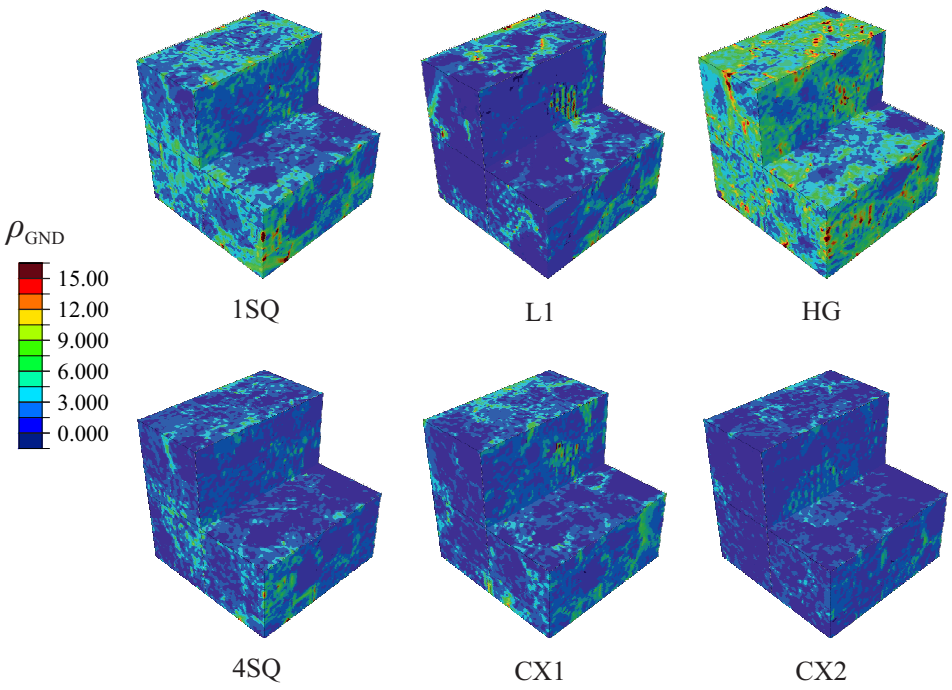


Figure 5.23 – Cut view - Accumulated GND density, ρ_{GND}, after 10 load cycles at $\sigma_{vM,peak}$ = 1150MPa. GND-coupled model.

Lastly, the stored energy criterion proposed by Wan et al. [2014] was evaluated, considering its evolution and ability to predict RR1000 fatigue lives under the investigated proportional and non-proportional loading conditions. As described in Eq. 5.39, the parameter explicitly considers stress, accumulated slip and the densities of SSDs and GNDs. Therefore, its performance is directly correlated with the evolutions of plastic slip and GND density presented previously. Figures 5.24–5.27 show the evolution of stored energy for both model configurations (with and without GND density) at 1050MPa and 1150MPa. It is found from Figs. 5.24 and 5.25 that CX1, CX2 and 4SQ present the lowest levels for this parameter and TS and HG present the highest. However, experimental results refute these findings, as the pure torsion load path exhibits the longest fatigue lives, and load paths with $F = 1$ the shortest.

Figures 5.26 and 5.27 present the analogous analysis considering GND-coupled simulations at 1050MPa and 1150MPa, respectively. Noticeably, this model configuration predicts a lower range of stored energy densities when considering all load paths. In addition, stored energy evolutions are closely grouped together, meaning that similar

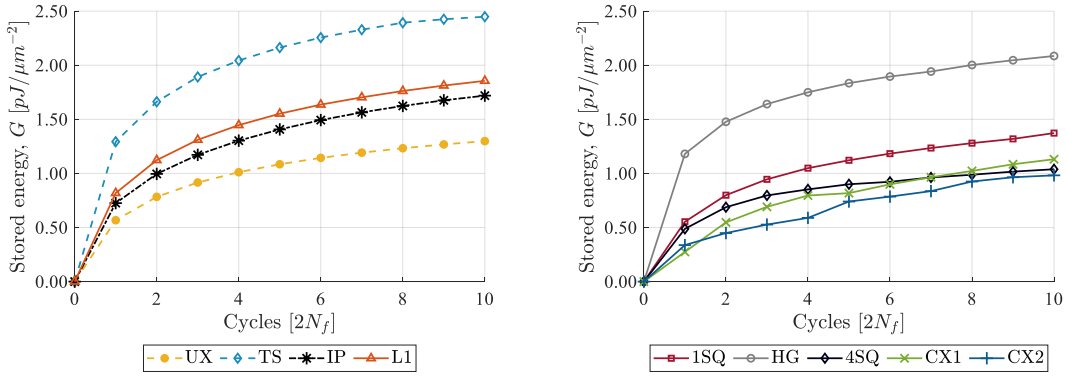


Figure 5.24 – Accumulated stored energy, G, evolution at $\sigma_{\text{vM,peak}}$ = 1050MPa. GND-uncoupled configuration.

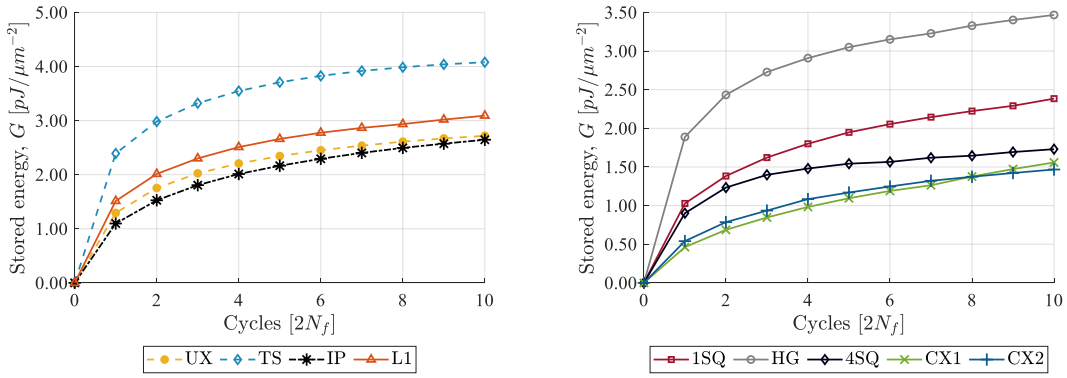


Figure 5.25 – Accumulated stored energy, G, evolution at $\sigma_{\text{vM,peak}}$ = 1150MPa. GND-uncoupled configuration.

fatigue lives are predicted for the group formed by 1SQ, 4SQ, CX1 and CX2, and the group of L1, pure torsion and in-phase load paths. These findings are now more representative of the experimental results for RR1000, except for the pure torsion load path, which experimentally exhibit the longest lives. Figures 5.28-5.31 illustrate the field contour plots of accumulated stored energy at $\sigma_{\text{vM,peak}}$ = 1150MPa for both model configurations (GND-uncloupled and coupled). The spatial distributions presented in Figs. 5.28-5.31 are very similar to the distributions seen for the accumulated slip contour plots presented in Figs. 5.16-5.19, illustrating the correlation between the stored energy criterion and accumulated plastic slip.

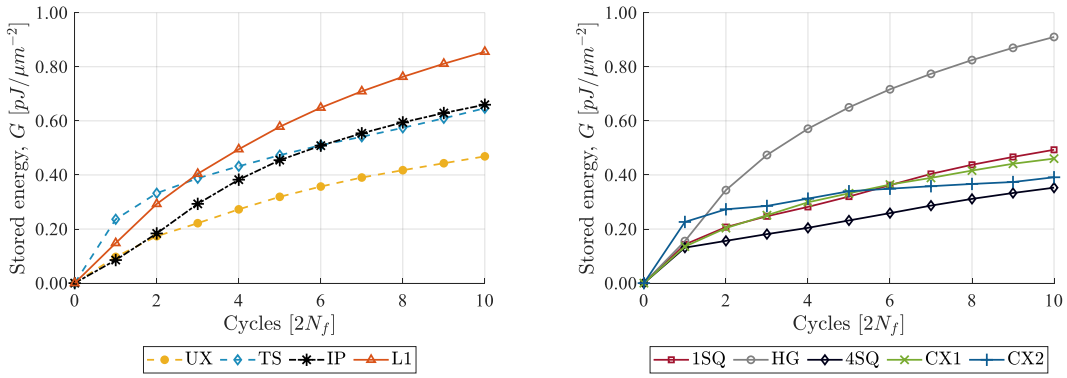


Figure 5.26 – Accumulated stored energy, G, evolution at $\sigma_{\text{vM,peak}}$ = 1050MPa. GND-coupled configuration.

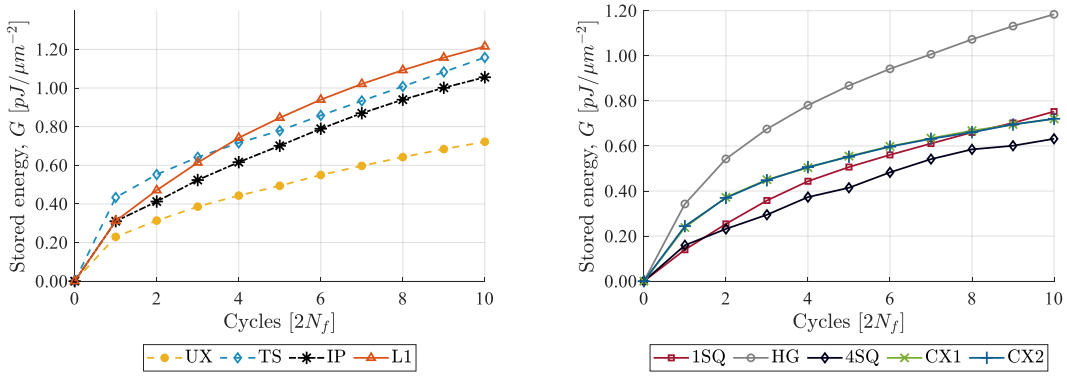


Figure 5.27 – Accumulated stored energy, G, evolution at $\sigma_{\text{vM,peak}}$ = 1150MPa. GND-coupled configuration.

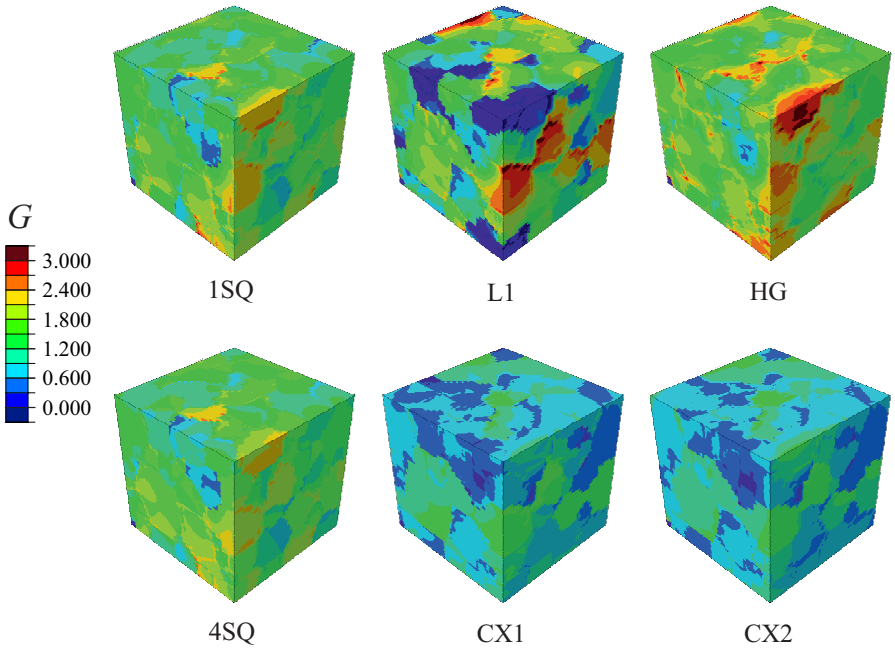


Figure 5.28 – Accumulated stored energy, G, after 10 load cycles at $\sigma_{\text{vM,peak}}$ = 1150MPa. GND-uncoupled model.

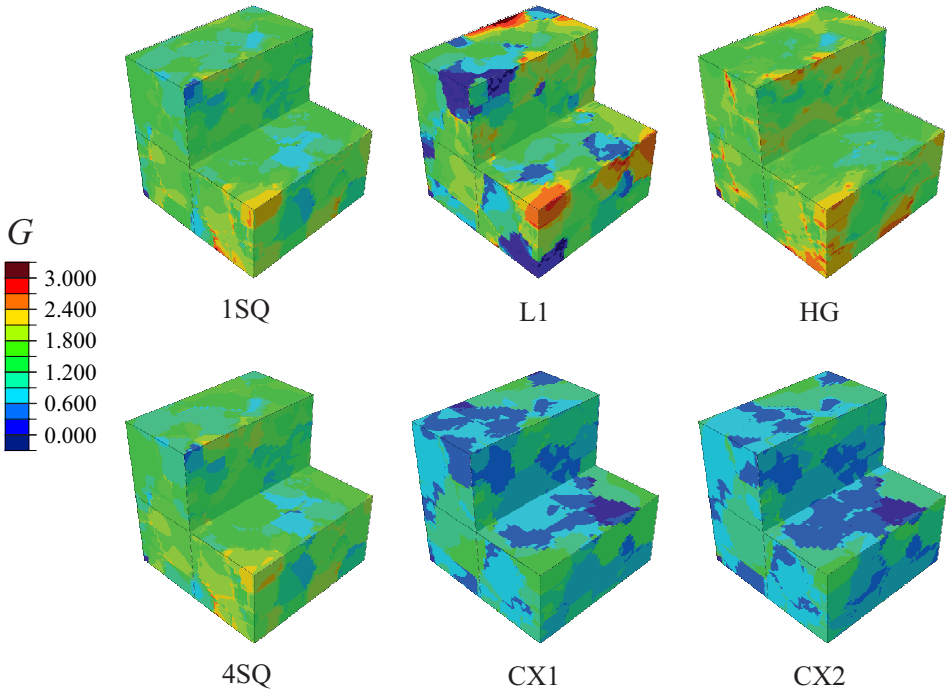


Figure 5.29 – Cut view - Accumulated stored energy, G, after 10 load cycles at $\sigma_{vM,peak}$ = 1150MPa. GND-uncoupled model.

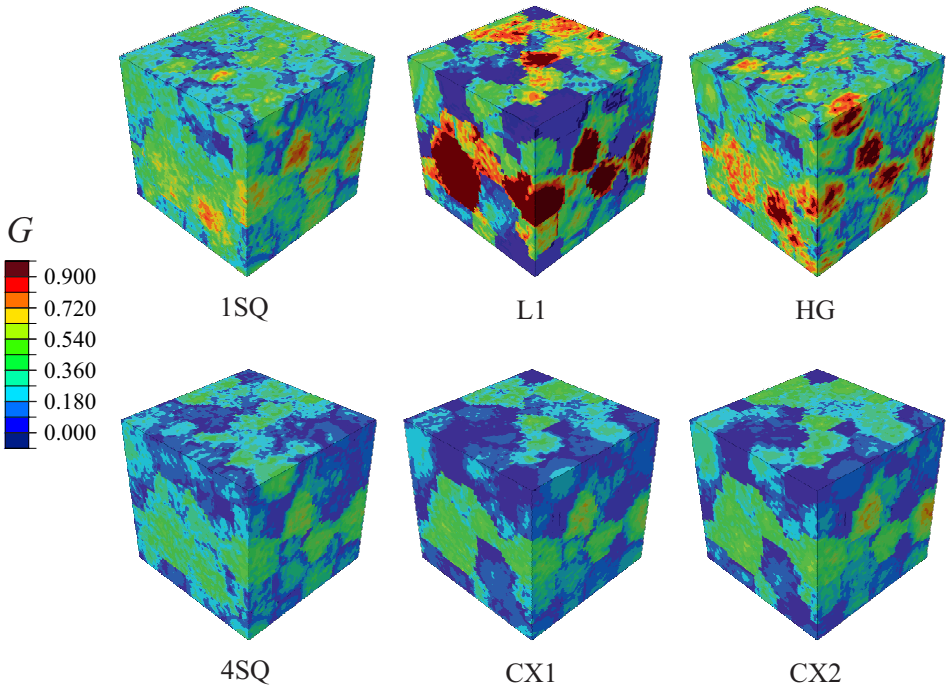


Figure 5.30 – Accumulated stored energy, G, after 10 load cycles at $\sigma_{vM,peak}$ = 1150MPa. GND-coupled model.

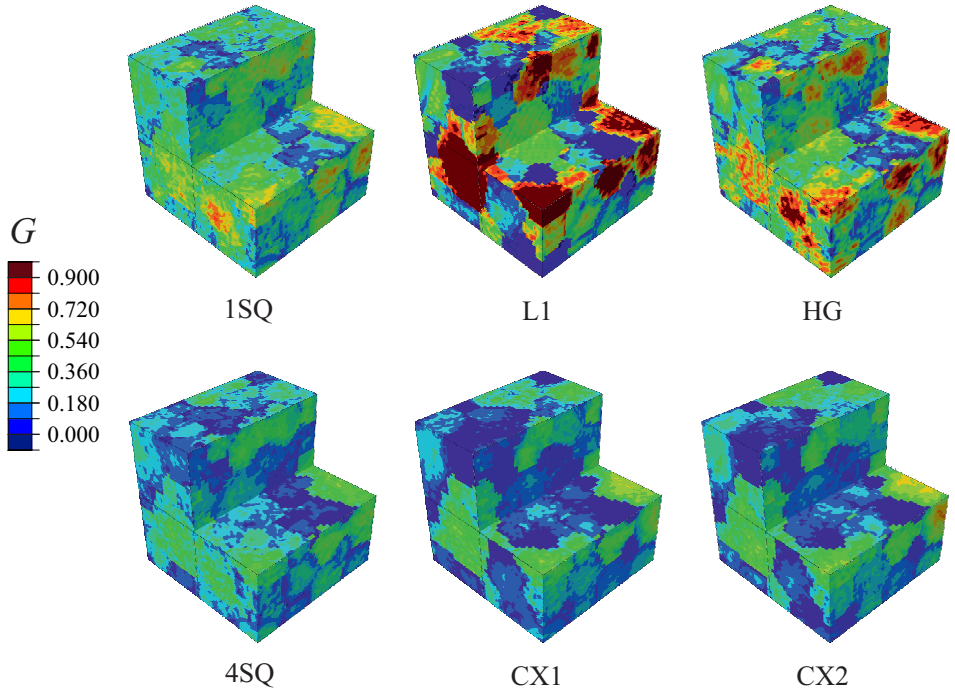


Figure 5.31 – Cut view - Accumulated stored energy, G, after 10 load cycles at $\sigma_{vM,peak}$ = 1150MPa. GND-coupled model.

In order to predict the number of cycles to failure for each load path, Eq. 5.41 and the critical stored energy value for RR1000 determined by Chen [2018] are considered. Chen simulated uniaxial tests at 1000MPa, 1050MPa and 1150MPa and compared the stored energy parameter with the experimental results presented by Bees [2016] to obtain a critical value of $G_c = 339J/m^2$. Table 5.2 summarises the fatigue lives predicted with Wan's stored energy criterion with the GND-coupled model configuration. A linear relationship between fatigue lives at 1150MPa and 1050MPa is assumed for interpolating the results for the actual stresses seen in the experimental programme described in Chapter 3.

Figure 5.32 presents the predicted life against experimental life. Excellent correlation is observed for the load paths with $F = 1$, i.e. 1SQ, HG, 4SQ, CX1 and CX2. All predictions for L1 load path lie outside the factor of three scatter band. This over conservative result was expected after the evolution analysis of the stored energy criterion and the quantities included in the formulation. The accumulated slip observed for L1 load path was the greatest of the non-proportional load paths, and the introduction

of GND coupling was not enough to correct the CPFE model response for this loading condition. A tentative explanation for this could be the texture adopted for the RVE microstructure, where the L1 load path had a greater activation rate of softer grains oriented preferably to the resolved shear stress, leading to a higher accumulation of plastic slip and dislocation density. As the stored energy accumulation is directly correlated to these parameters, the results for this load path were skewed from the other load paths.

Table 5.2 – Fatigue lives predicted in cycles – GND-coupled configuration.

Stress Level	1SQ	4SQ	L1	HG	CX1	CX2
1150 MPa	4504	2791	2863	5366	4706	4705
1050 MPa	6876	3963	3725	9606	7363	8660

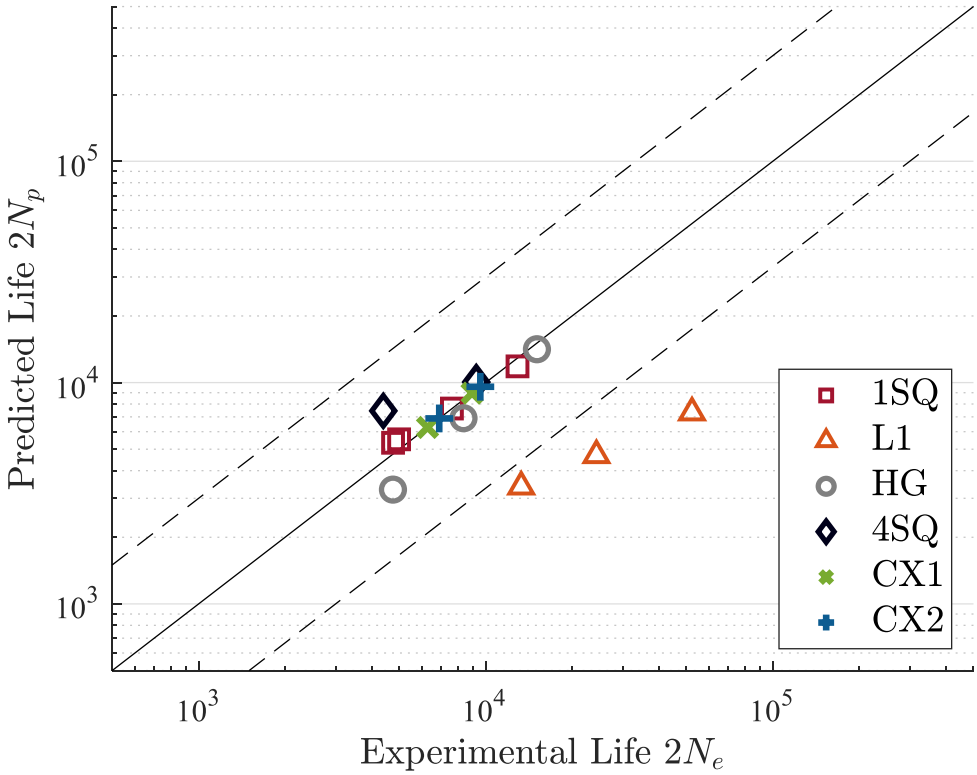


Figure 5.32 – Predicted versus experimental life – Stored energy criterion and GND-coupled CPFE model.

5.5 Conclusions

This chapter presents the formulation and implementation of a crystal plasticity framework and stored energy criterion for predicting fatigue lives of RR1000. The evolutions of accumulated plastic slip, GND density and stored energy density are assessed in their capacity to provide mechanistic and physical representation for RR1000 fatigue life scatter under non-proportional load path. It is concluded that neither accumulated slip nor GND density on their own are able to directly predict fatigue lives. However, their combination in the formulation of Wan et al.'s stored energy criterion represents an excellent parameter for accurately predicting fatigue lives under complex multiaxial loading conditions.

In order to compare the results obtained with the CPFE modelling approach against the multiaxial fatigue damage parameters presented in Chapter 4, the performance of Wan et al.'s criterion is also ascertained by a least square fit on the total absolute residual error, δ, as defined in Eq. 5.42. Table 5.3 summarises the absolute residual errors obtained for each load path. Residual errors for load paths with $F = 1$ are comparable to those obtained with the best performance parameters of Chapter 4. However, the poor predictions for L1 load path skewed the total absolute error to $\delta_{Wan} = 2.92$, a similar error level observed with the Liu I and Glinka (GSA) parameters.

$$\delta = \sum_{i=1}^{\text{Test cases}} \left| \log_{10} \left(\frac{N_{\text{i,predicted}}}{N_{\text{i,experimental}}} \right) \right| \quad . \tag{5.42}$$

Table 5.3 – Absolute residual error for each load path.

Load case	δ**RR1000**
One Square – 1SQ	0.0591
Four Squares – 4SQ	0.2642
Two Triangles – L1	2.1625
Hourglass – HG	0.2719
Cross – CX1	0.0105
Cross – CX2	0.1486
δ_{Wan}	2.92

6 Conclusion

This chapter presents the key findings obtained in this doctoral research project. First, the work undertaken in this thesis is summarised. Then, the main contributions and conclusions are highlighted. Finally, the last part of this chapter introduces suggestions for future work and extension of this research project.

6.1 Summary of Thesis

This doctorate thesis is set in the context of multiaxial fatigue testing and modelling and represents useful progress in the understanding and characterisation of multiaxial deformation and fatigue behaviour of Nickel-based superalloys. The primary aim was to implement and further develop methodologies for predicting fatigue lives of two Nickel-based superalloys. For that an extensive experimental programme was conducted with uniaxial and biaxial fatigue tests with Waspaloy, and non-proportional tension-torsion tests with RR1000. Although these two superalloys are used for high temperature application, the experimental programme was conducted at room temperature to isolate load multiaxiality effects from creep effects. The obtained test data was used for calibrating and benchmarking numerous multiaxial fatigue parameters and an extended crystal plasticity framework.

Chapter 1 detailed the motivation and industrial context of this project, introducing high pressure turbine (HPT) discs made of Nickel-based superalloys as the object of study. HPT discs, located directly after the combustion chamber, are subjected to complex mechanical and thermal loads. Therefore, understanding material multiaxial behaviour and appropriate techniques for modelling it are essential for the safe design of such critical components for aeroengine applications.

Chapter 2 focused on the literature review of this research study. This included the damage mechanisms associated with the fatigue phenomenon, differences between proportional and non-proportional loading, and the current state of the art for multiaxial fatigue testing and modelling considering different length scales. This chapter also set the background for subsequent chapters, in terms of the theory needed for formulating the multiaxial fatigue criteria.

Chapter 3 described the experimental programme carried out as part of this project. The first part of this chapter addressed various cyclic and monotonic tests with Waspaloy. It starts by describing the biaxial fatigue tests performed by Dr Robert Paynter, and the entire post processing of it, which was conducted as part of this doctorate thesis. The variation of biaxiality ratio, for the same maximum principal stress, was found to cause a significant change in fatigue life and failure location. Due to the limited availability of material data for Waspaloy at room temperature, a set of uniaxial monotonic and cyclic tests was devised and performed using a non-standard specimen geometry and an optical strain measurement system developed for it. The experimental data obtained was then used for calibrating multiaxial fatigue parameters. Despite the limitations in the design and machining of the specimen, the fatigue lives obtained are in good agreement with the biaxial tests with cruciform specimens and experimental data provided by Rolls-Royce plc.

The second part of Chapter 3 introduced non-proportional tension-torsion tests with RR1000. Tests were conceived to assess this Nickel-based superalloy under six

different load paths, where five of them have the same degree of non-proportionality and one load path, L1, has a lower degree. Experimental data reveals that RR1000 does not exhibit significant load path dependency at the stress levels investigated, as the five different load paths with the same degree of non-proportionality gave similar fatigue lives. However, the material seems to be strongly influenced by the degree of load non-proportionality. A clear distinction in terms of fatigue lives was observed between load paths with Kanazawa factor of $F = 1$ and the L1 load path, which exhibits $F = 0.44$. The limited number of specimens available, and the particular interest of the industrial sponsor in the most severe non-proportional loading conditions ($F = 1$), constrained to one the number of load path with lower F that could be investigated.

Chapter 4 evaluated several stress-, strain-, and energy-based multiaxial fatigue damage parameters in relation to the load controlled biaxial fatigue tests with Waspaloy and non-proportional tension-torsion fatigue tests with RR1000. The majority of multiaxial fatigue criteria investigated could provide a reasonable collapse of the experimental data for both materials. For Waspaloy, considering an absolute residual error $\delta \leq 2.5$, the best correlation was obtained with the elastic strain energy equivalent stress, the modified Walker stress and the invariant based criterion proposed by Crossland. Furthermore, for critical plane approaches, Matake's stress-based criterion and Liu I energy-based parameter gave the most accurate predictions for Waspaloy. Analogously for RR1000, excellent collapse of the test data was obtained with the yield criteria associated with Shamsaei et al. non-proportional correction factor. Among stress-based criteria, good correlation was obtained with Crossland's and Matake's formulation. For strain-based formulations, best correlation for RR1000 was seen for Wang-Brown model. Lastly, taking into account energy-based parameters, the best results were obtained with Liu I and GSE parameters.

It was also noted in Chapter 4 that the favourable performance of stress-based damage parameters is directly linked to test data available for calibration and input loading for fatigue analysis. All the tests performed in this research thesis were load-

controlled. Therefore, material parameter for strain-life curves and calibration of strain- and energy-based formulations were obtained with the assumptions presented in Chapter 4 and from nominal test data provided by Rolls-Royce plc, placing these classes of parameters at clear disadvantage against stress-based models.

Chapter 5 described the formulation of the crystal plasticity framework proposed by Dunne et al [2007; 2012] and the extension of this framework to include GNDs density. This chapter also presented a detailed description of the implementation of the framework into the finite element software Abaqus. Observations suggested that for RR1000, peak von Mises stress, accumulated plastic slip and GND density cannot be used as independent crack nucleation indicators accurately. Hence, this study adopted the critical stored energy criterion proposed by Wan et al. [6] for predicting fatigue lives under complex non-proportional load paths. This criterion provided excellent collapse of the non-proportional load paths with $F = 1$. However, poor predictions were obtained for L1 test case, with $F = 0.44$. A tentative explanation for this could be the texture adopted for the RVE microstructure, which resulted in the highest slip system activation for this load path.

Lastly, Tab. 6.1 summarises the performance of each criterion ascertained by a least square fit on the total absolute residual error, δ, as defined in Chapter 4 and 5.

Table 6.1 – Absolute residual error for each criterion and material investigated.

Parameter δ	**δWaspaloy**	**δRR1000**
von Mises - σ_{vM}	2.23	0.46
Elastic Strain - σ_{Ue}	1.14	0.44
Walker Stress - $\sigma_{W,Ue}$	1.02	0.79
Crossland	0.79	1.81
Matake	1.59	1.71
Fatemi-Socie	3.33	6.72
Wang-Brown	3.50	1.96
Smith-Watson-Topper	2.93	7.27
Liu I	2.25	2.51
Liu II	2.50	9.61
Glinka-Ince – GSE	3.81	1.56
Glinka-Ince – GSA	2.89	2.69
Wan et al.'s – Stored energy (CPFE)	x	2.92

6.2 Concluding remarks

The highlights of this doctorate thesis as well as the key conclusions from this study are presented below for the three main pieces of work: 1) Experimental work; 2) Multiaxial Fatigue Modelling; and 3) Micro-mechanical modelling of crack nucleation under multiaxial loading considering a CPFE framework.

6.2.1 Highlights

- Although RR1000 does not exhibit load path dependency for stress levels near the yield limit, fatigue lives and cyclic hardening for RR1000 are strongly dependent on the degree of load non-proportionality;

- If correctly calibrated, stress-based multiaxial fatigue parameters can be extended

to LCF applications with excellent accuracy;

- Overall, energy-based formulations provide the best collapse of LCF lives for both Waspaloy and RR1000;
- GND density is a fundamental parameter for the accurate prediction of fatigue lives of fine grain RR1000 under non-proportional loading through CPFE implementations.

6.2.2 Experimental work

- The Nickel-based superalloy Waspaloy exhibits a strong dependency on load biaxiality. Fatigue lives and crack initiation location were directly influenced by this parameter;
- The shortest fatigue lives for Waspaloy were observed for Pure Shear and Equibiaxial loading conditions;
- The developed optical strain measurement VI proved to be a reliable and accurate tool for live measurements during uniaxial fatigue testing;
- The non-proportional tension-torsion tests revealed that RR1000 presents strong dependency on the degree of load non-proportionality;
- It was shown that load paths with the higher Kanazawa factor of $F = 1$ gave the shortest fatigue lives, based on an equivalent peak stress basis;
- Load paths with similar degrees of non-proportionality gave similar fatigue lives for RR1000 for the stress levels investigated;
- RR1000 tests under L1 load path gave fatigue lives comparable to in-phase loading conditions for the tested stress levels;
- RR1000 non-proportional hardening is proportional to the applied stress range.

6.2.3 Multiaxial fatigue damage parameters

- Good fatigue life prediction was obtained with simple extensions of yield criteria to multiaxial fatigue data;
- Elastic strain energy equivalent stress provides substantial improvement for fatigue life predictions of Waspaloy over von Mises equivalent stress;
- The modification of Walker stress with elastic strain energy equivalent stress proved an excellent parameter for predicting biaxial fatigue lives of Waspaloy;
- The association of Shamsaei et al. non-proportional correction factor with extended yield criteria collapsed all test data with RR1000;
- Overall, the lowest absolute residual errors were obtained with stress- and energy-based approaches;
- Despite reliable results obtained with extended yield theories and stress-based formulations, theses parameters do not properly represent the physical behaviour of the material. They mostly act as fitting parameters;
- Fatigue life prediction with strain- and energy-based approaches were found to be very sensitive to model calibration. Therefore, these classes of parameters require careful calibration of their numerous material parameters.

6.2.4 Crystal plasticity modelling of RR1000

- The introduction of GND densities into Dunne et al.'s framework improves substantially fatigue life predictions for RR1000 test data;
- Strong dependency on GNDs density is observed for RR1000, due to its fine grain microstructure;
- Neither accumulated plastic slip nor GND density on their own are able to directly predict fatigue lives for RR1000;

- Excellent collapse of non-proportional load paths with $F = 1$ was obtained with Wan et al.'s criterion;
- The macroscopic response of the adopted RVE accurately represents RR1000 cyclic response;
- The use of one single RVE configuration can skew results. For instance, poor predictions were obtained for the pure torsion and L1 load paths;
- The main disadvantage of the crystal plasticity approach was found to be the overall time required for each simulation. On average, a single simulation of ten load cycles would take over 100 hours to complete.

6.3 Suggestions for future work

The extensive scope of this doctoral research and limited time meant that some areas could benefit from further investigation so that more general conclusions can be drawn. The areas where further research would prove to be beneficial are listed below.

6.3.1 Experimental work

- Perform strain-controlled tests with both Waspaloy and RR1000 for improved calibration of multiaxial fatigue parameters;
- Further tests with RR1000 under different stress levels. Initial tests focused on a narrow peak von Mises stress range, from 1000MPa to 1150MPa.
- Investigation of different degrees of non-proportionality for confirming RR1000 load path dependency trends.

6.3.2 Multiaxial fatigue damage parameters

- Extension of Liu's parameter for including mean stress effect for better collapse of Waspaloy biaxial test data;
- Extension of multiaxial fatigue damage parameters to the micro-scale, for use with the modified CPFE framework.

6.3.3 Crystal plasticity modelling of RR1000

- Improve hardening rule for GND-coupled CPFE model of RR1000;
- Investigate different microstructure realisations, including different texture and number of grains;
- CPFE modelling of Waspaloy biaxial test data – requires extensive material calibration;
- Simulation of load paths beyond 10 cycles for the investigation of GNDs density accumulation, especially for 1SQ and CX1 load paths that exhibit steep accumulation slopes;
- Further simulations at different stress levels, starting with peak von Mises stress of 1000MPa;
- Implementation of additional fatigue prediction criteria, such as the extension proposed by McDowell [2007].

References

Agbessi, K., Saintier, N. & Palin-Luc, T. [2016], 'Microstructure-based study of the crack initiation mechanisms in pure copper under high cycle multiaxial fatigue loading conditions', *Procedia Structural Integrity* **2**, 3210–3217.

Alexandrova, N., Alexandrov, S. & Vila, R. [2006], 'Analysis of stress and strain in a rotating disk mounted on a rigid shaft', *Theoretical and Applied Mechanics* **33**(1), 65–90.

Andrews, J. M. H. & Ellison, E. G. [1973], 'A testing rig for cycling at high biaxial strains', *Journal of Strain Analysis* **8**(3), 168–175.

Antolovich, S. D. & Jayaraman, N. [1983], The Effect of Microstructure on the Fatigue Behavior of NI Base Superalloys, *in* J. J. Burke & V. Weiss, eds, 'Fatigue', Springer US, Boston, MA, pp. 119–144.

Araújo, J. A., Dantas, A. P., Castro, F. C., Mamiya, E. N. & Ferreira, J. L. [2011], 'On the characterization of the critical plane with a simple and fast alternative measure of the shear stress amplitude in multiaxial fatigue', *International Journal of Fatigue* **33**(8), 1092–1100.

Arsenlis, A. & Parks, D. M. [1999], 'Crystallographic aspects of geometrically-necessary and statistically-stored dislocation density', *Acta Materialia* **47**(5), 1597–1611.

Asaro, R. J. & Rice, J. R. [1977], 'STRAIN LOCALIZATION IN DUCTILE SINGLE CRYSTALS ?', *J. Mech. Phys. Solids* **25**, 309 to 338.

Ashby, M. F. [1970], 'The deformation of plastically non-homogeneous materials', *Philosophical Magazine* **21**(170), 399–424.

Askeland, D. R. & Wright, W. J. [2014], *The Science and Engineering of Materials*, 7th edn, Cengage Learning, Boston MA.

ASTM E112-13 [2013], 'Standard Test Methods for Determining Average Grain Size', *ASTM International* .

ASTM E466-15 [2015], 'Standard Practice for Conducting Force Controlled Constant Amplitude Axial Fatigue Tests of Metallic Materials', *ASTM International* .

Balthazar, J. C. & Malcher, L. [2007], 'A review on the main approaches for determination of the multiaxial high cycle fatigue strength', *Mechanics of Solids in Brazil* (JANUARY 2007), 63–80.

Bannantine, J. A., Comer, J. J. & Handrock, J. L. [1990], *Fundamentals of metal fatigue analysis*, Prentice Hall, Englewood Cliffs, New Jersey.

Basquin, O. H. [1910], 'The exponential law of endurance tests', *Proc Am Soc Test Mater* **10**, 625–630.

Bees, M. R. [2016], The effect of loading proportionality on fatigue life, D.eng thesis, Swansea University.

Bees, M. R., Pattison, S. J., Fox, N. & Whittaker, M. T. [2014], 'The non-proportional behaviour of a nickel-based superalloy at room temperature, and characterisation of the additional hardening response by a modified cyclic hardening curve', *International Journal of Fatigue* **67**, 134–141.

Benz, M. G. [1999], Preparation of clean superalloys, *in* C. Briant, ed., 'Impurities in Engineering Materials', Routledge, New York, chapter Chapter 3, pp. 31–48.

Bettge, D., Österle, W. & Ziebs, J. [1995], 'Temperature dependence of additional cyclic hardening of a nickel-base superalloy during out-of-phase multiaxial deformation', *Scripta Metallurgica et Materiala* **32**(10), 1601–1606.

Black, J. T. & Kohser, R. A. [2018], *DeGarmo's materials and processes in manufacturing.*, John Willey & Sons.

Bloch, H. P. & Soares, C. [2001], Application of Hot Gas Turboexpanders, *in* 'Turboexpanders and Process Applications', Elsevier, pp. 85–272.

Boehler, J. P., Demmerle, S. & Koss, S. [1994], 'A new direct biaxial testing machine for anisotropic materials', *Experimental mechanics* **34**(1), 1–9.

Bonnand, V., Chaboche, J. L., Gomez, P., Kanouté, P. & Pacou, D. [2011], 'Investigation of multiaxial fatigue in the context of turboengine disc applications', *International Journal of Fatigue* **33**(8), 1006–1016.

Brown, M. W. [1978], 'Torsional stresses in tubular specimens', *The Journal of Strain Analysis for Engineering Design* **13**(1), 23–28.

Brown, M. W. & Miller, K. J. [1973], 'A Theory for Fatigue Failure under Multiaxial Stress-Strain Conditions', *Proceedings of the Institution of Mechanical Engineers* **187**(1), 745–755.

Busso, E. P., Meissonnier, F. T. & Dowd, N. P. O. [2000], 'Gradient-dependent deformation of two-phase single crystals', **48**, 2333–2361.

Callister, W. D. & Rethwisch, D. G. [2010], *Materials Science and Engineering: An Introduction*, 8th edn, John Wiley & Sons.

Calloch, S. & Marquis, D. [1997], Additional Hardening Due to Tension-Torsion Non-proportional Loadings: Influence of the Loading Path Shape, *in* 'Multiaxial Fatigue

and Deformation Testing Techniques', ASTM International, 100 Barr Harbor Drive, PO Box C700, West Conshohocken, PA 19428-2959, pp. 113–113–18.

Carpinteri, A., Ronchei, C., Spagnoli, A. & Vantadori, S. [2014], 'On the use of the Prismatic Hull method in a critical plane-based multiaxial fatigue criterion', *International Journal of Fatigue* **68**, 159–167.

Carpinteri, A. & Spagnoli, A. [2001], 'Multiaxial high-cycle fatigue criterion for hard metals', *International Journal of Fatigue* **23**(00), 135–145.

Castro, F. & Jiang, Y. [2016], 'Fatigue life and early cracking predictions of extruded AZ31B magnesium alloy using critical plane approaches', *International Journal of Fatigue* **88**, 236–246.

Chen, B. [2018], Understanding Microstructurally-Sensitive Fatigue Crack Nucleation in Superalloys, PhD thesis, Imperial College London.

Chen, B., Jiang, J. & Dunne, F. P. [2018], 'Is stored energy density the primary meso-scale mechanistic driver for fatigue crack nucleation?', *International Journal of Plasticity* **101**(December 2017), 213–229.

Cottrell, A. H. [1953], *Dislocations and Plastic Flow in Crystals*, Clarendon Press.

Cristofori, A. & Tovo, R. [2009], 'An invariant-based approach for high-cycle fatigue calculation', *Fatigue and Fracture of Engineering Materials and Structures* **32**(4), 310–324.

Crossland, B. [1956], Effect of large hydrostatic pressures on the torsional fatigue strength of an alloy steel, *in* 'Proc. Int. Conf. on Fatigue of Metals', Institution of Mechanical Engineers, London.

Cumpsty, N. [2003], *Jet Propulsion*, Cambridge University Press, Cambridge.

Doong, S. H. & Socie, D. F. [2008], 'Constitutive Modeling of Metals Under Nonproportional Cyclic Loading', *Journal of Engineering Materials and Technology* **113**(1), 23.

Doong, S. H., Socie, D. F. & Robertson, I. M. [1990], 'Dislocation substructures and nonproportional hardening', *Journal of Engineering Materials and Technology, Transactions of the ASME* **112**(4), 456–464.

Doquet, V., Hénaff, G., Palin-Luc, T. & Risbet, M. [2019], Fatigue Crack Initiation and Propagation, *in* 'Mechanics - Microstructure - Corrosion Coupling', Elsevier, pp. 65–90.

Dunne, F. P. E., Kiwanuka, R. & Wilkinson, A. J. [2012], 'Crystal plasticity analysis of micro-deformation, lattice rotation and geometrically necessary dislocation density', *Proceedings of the Royal Society A: Mathematical, Physical and Engineering Sciences* **468**(2145), 2509–2531.

Dunne, F. P. E., Wilkinson, A. J. & Allen, R. [2007], 'Experimental and computational studies of low cycle fatigue crack nucleation in a polycrystal', *International Journal of Plasticity* **23**(2), 273–295.

Dunne, F. P. & Petrinic, N. [2005], *Introduction to computational plasticity*, Oxford University Press on Demand.

Dunne, F. P., Rugg, D. & Walker, A. [2007], 'Lengthscale-dependent, elastically anisotropic, physically-based hcp crystal plasticity: Application to cold-dwell fatigue in Ti alloys', *International Journal of Plasticity* **23**(6), 1061–1083.

Fatemi, A. & Kurath, P. [1988], 'Multiaxial Fatigue Life Predictions Under the Influence of Mean-Stresses', *Journal of Engineering Materials and Technology* **110**(October 1988), 380–388.

Fatemi, A. & Shamsaei, N. [2011], 'Multiaxial fatigue: An overview and some approximation models for life estimation', *International Journal of Fatigue* **33**(8), 948–958.

Fatemi, A. & Socie, D. F. [1988], 'A CRITICAL PLANE APPROACH TO MULTIAXIAL FATIGUE DAMAGE INCLUDING OUT-OF-PHASE LOADING', *Fatigue & Fracture of Engineering Materials & Structures* **11**(3), 149–165.

Findley, W. N. [1958], *A theory for the effect of mean stress on fatigue of metals under combined torsion and axial load or bending*, 6, Engineering Materials Research Laboratory, Division of Engineering, Brown University.

Findley, W. N. [1959], 'A theory for the effect of mean stress on fatigue of metals under combined torsion and axial load or bending', *Journal of Engineering for Industry* **81**(4), 301–305.

Fleck, N. & Hutchinson, J. [1994], 'Strain gradient plasticity :theory and experiment, acta metal material'.

Found, M. S., Fernando, U. S. & Miller, K. J. [1985], Requirements of a new multiaxial fatigue testing facility, *in* 'Multiaxial fatigue', ASTM International.

Garud, Y. S. [1981*a*], 'A new approach to the evaluation of fatigue under multiaxial loadings', *Journal of Engineering Materials and Technology(Transactions of the ASME)* **103**(2), 118–125.

Garud, Y. S. [1981*b*], 'Multiaxial Fatigue: A Survey of the State of the Art', *Journal of Testing and Evaluation* **9**(3), 165–178.

Gates, N. R. [2016], Fatigue Behavior under Multiaxial Stress States Including Notch Effects and Variable Amplitude Loading, PhD thesis, The University of Toledo.

Gibbs, G. B. [1969], 'Thermodynamic Analysis of Dislocation Glide Controlled by Dispersed Local Obstacles', *Materials Science and Engineering* .

Gonçalves, C. A., Araújo, J. A. & Mamiya, E. N. [2005], 'Multiaxial fatigue: A stress based criterion for hard metals', *International Journal of Fatigue* **27**(2), 177–187.

Gough, H. J. [1949], Engineering steels under combined cyclic and static stresses, *in* 'Proceedings of the Institution of Mechanical Engineers', Vol. 160, pp. 417–440.

Gough, H. J. & Pollard, H. V. [1935], 'The Strength of Metals under Combined Alternating Stresses', *Proceedings of the Institution of Mechanical Engineers* **131**(1), 3–103.

Granato, A. V., Lücke, K., Schlipf, J. & Teutonico, L. J. [1964], 'Entropy Factors for Thermally Activated Unpinning of Dislocations', *Journal of Applied Physics* **35**(9), 2732–2745.

Groeber, M. A. & Jackson, M. A. [2014], 'DREAM.3D: A Digital Representation Environment for the Analysis of Microstructure in 3D', *Integrating Materials and Manufacturing Innovation* **3**(1), 56–72.

Guest, J. J. [1937], 'Combined Stress. A Criticism of the Gough and Pollard Law', *The Automobile Engineer* pp. 326–332.

Guest, J. J. [1940], 'Recent Research on Combined Stress', *Proceedings. Institution of Automobile Engineers* pp. 33—-72 and 146—-171.

Haigh, B. P. [1923], 'The thermodynamic theory of mechanical fatigue and hysteresis in metals', *Rep British Association for the Advancement of Science* pp. 358–368.

Hannon, A. & Tiernan, P. [2008], 'A review of planar biaxial tensile test systems for sheet metal', *Journal of materials processing technology* **198**(1), 1–13.

Hull, D. & Bacon, D. J. [2011], *Introduction to dislocations*, Vol. 37, Elsevier.

Ince, A. [2012], Development of Computational Multiaxial Fatigue Modelling For Notched Components, PhD thesis, University of Waterloo.

Ince, A. & Glinka, G. [2014], 'A generalized fatigue damage parameter for multiaxial fatigue life prediction under proportional and non-proportional loadings', *International Journal of Fatigue* **62**, 34–41.

Ince, A., Glinka, G. & Buczynski, A. [2014], 'Computational modeling of multiaxial elasto-plastic stress-strain response for notched components under non-proportional loading', *International Journal of Fatigue* **62**, 42–52.

ISO-4287 [1997], 'Geometrical Product Specifications (GPS) — Surface texture: Profile method — Terms, definitions and surface texture parameters'.

Itoh, T., Sakane, M. & Ohnami, M. [1994], 'High Temperature Multiaxial Low Cycle Fatigue of Cruciform Specimen', *Journal of Engineering Materials and Technology* **116**(1), 90.

Itoh, T., Sakane, M. & Ohsuga, K. [2013], 'Multiaxial low cycle fatigue life under non-proportional loading', *International Journal of Pressure Vessels and Piping* **110**, 50–56.

Jayaraman, N. & Ditmars, M. M. [1989], 'Torsional and biaxial (tension-torsion) fatigue damage mechanisms in Waspaloy at room temperature', *International Journal of Fatigue* **11**(5), 309–318.

Jiang, J., Yang, J., Zhang, T., Zou, J., Wang, Y., Dunne, F. & Britton, T. [2016], 'Microstructurally sensitive crack nucleation around inclusions in powder metallurgy nickel-based superalloys', *Acta Materialia* **117**, 333–344.

Jones, C. A. [2016], A micromechanical investigation of proton irradiated oxide dispersion strengthened steels, PhD thesis, University of Oxford.

Kalluri, S. & Bonacuse, P. J. [1993], In-phase and out-of-phase axial-torsional fatigue behavior of haynes 188 superalloy at 760 C, *in* 'Advances in multiaxial fatigue', ASTM International.

Kanazawa, K., Miller, K. J. & Brown, M. W. [1979], 'Cyclic deformation of 1% Cr-Mo-V steel under out-of-phase loads', *Fatigue & Fracture of Engineering Materials & Structures* **2**(2), 217–228.

Kandil, F. A., Brown, M. W. & Miller, K. J. [1982], Biaxial low-cycle fatigue failure of 316 stainless steel at elevated temperatures, *in* 'Mechanical behaviour and nuclear applications of stainless steel at elevated temperatures', Metals Society, United Kingdom.

Kang, G., Li, Y. & Gao, Q. [2005], 'Non-proportionally multiaxial ratcheting of cyclic hardening materials at elevated temperatures: Experiments and simulations', *Mechanics of Materials* **37**(11), 1101–1118.

Karolczuk, A. & Macha, E. [2005], 'A review of critical plane orientations in multiaxial fatigue failure criteria of metallic materials'.

Kiwanuka, R. [2013], Micro-deformation and texture in engineering materials, Ph.d thesis, University of Oxford.

Korsunsky, A. M., Dini, D., Dunne, F. P. & Walsh, M. J. [2007], 'Comparative assessment of dissipated energy and other fatigue criteria', *International Journal of Fatigue* **29**(9-11), 1990–1995.

Kumar, R. S., Wang, A. J. & McDowell, D. L. [2006], 'Effects of microstructure variability on intrinsic fatigue resistance of nickel-base superalloys - A computational micromechanics approach', *International Journal of Fracture* **137**(1-4), 173–210.

Lanza, G. [1886], 'Strength of shafting subjected to both twisting and bending', *Trans ASME* **8**, 121–196.

Lee, E. H. [1969], 'Elastic-Plastic Deformation at Finite Strains', *Journal of Applied Mechanics* **36**(1), 1–6.

Lerch, B. A., Jayaraman, N. & Antolovich, S. D. [1984], 'A study of fatigue damage mechanisms in Waspaloy from 25 to 800°C', *Materials Science and Engineering* **66**(2), 151–166.

Liu, K. [1993], A Method Based on Virtual Strain-Energy Parameters for Multiaxial Fatigue Life Prediction, *in* 'Advances in Multiaxial Fatigue', ASTM International, 100 Barr Harbor Drive, PO Box C700, West Conshohocken, PA 19428-2959, pp. 67–67–18.

Lopez-Crespo, P., Moreno, B., Lopez-Moreno, A. & Zapatero, J. [2015], 'Study of crack orientation and fatigue life prediction in biaxial fatigue with critical plane models', *Engineering Fracture Mechanics* **136**, 115–130.

Macha, E. & Sonsino, C. M. [1999], 'Energy criteria of multiaxial fatigue failure', *Fatigue and Fracture of Engineering Materials and Structures* **22**(12), 1053–1070.

Makinde, A., Thibodeau, L. & Neale, K. W. [1992], 'Development of an apparatus for biaxial testing using cruciform specimens', *Experimental mechanics* **32**(2), 138–144.

Mamiya, E. N., Araújo, J. A. & Castro, F. C. [2009], 'Prismatic hull: A new measure of shear stress amplitude in multiaxial high cycle fatigue', *International Journal of Fatigue* **31**(7), 1144–1153.

Manonukul, A. & Dunne, F. P. [2004], 'High- and low-cycle fatigue crack initiation using polycrystal plasticity', *Proceedings of the Royal Society A: Mathematical, Physical and Engineering Sciences* **460**(2047), 1881–1903.

Mason, W. [1917], 'Alternating stress experiments', *Proceedings of the Institution of Mechanical Engineers* **92**(1), 121–196.

Mason, W. [1923], 'The Distribution of Stress in Round Mild Steel Bars under Alternating Torsion or Bending', *Reports British Association for the Advancement of Science, London* pp. 386–409.

Mason, W. & Delaney, W. J. [1921], 'Alternating Combined Stress Experiments', *Reports British Association for the Advancement of Science, London* pp. 329–341.

Matake, T. [1977], 'An Explanation on Fatigue Limit under Combined Stress', *Bulletin of JSME* **20**(141), 257–263.

McDiarmid, D. L. [1991], 'A GENERAL CRITERION FOR HIGH CYCLE MULTIAXIAL FATIGUE FAILURE', *Fatigue & Fracture of Engineering Materials & Structures* **14**(4), 429–453.

McDowell, D. L. [2007], 'Simulation-based strategies for microstructure-sensitive fatigue modeling', *Materials Science and Engineering A* **468-470**(SPEC. ISS.), 4–14.

McDowell, D. L. & Dunne, F. P. [2010], 'Microstructure-sensitive computational modeling of fatigue crack formation', *International Journal of Fatigue* **32**(9), 1521–1542.

McEvily, A., Eifler, D. & Macherauch, E. [1991], 'An analysis of the growth of short fatigue cracks', *Engineering Fracture Mechanics* **40**(3), 571–584.

Miller, K. J. [1982], 'THE SHORT CRACK PROBLEM', *Fatigue & Fracture of Engineering Materials and Structures* **5**(3), 223–232.

Miller, K. J. [1991], 'Metal fatigue-past, current and future'.

Moosbrugger, J. & Morrison, D. [1997], 'Nonlinear kinematic hardening rule parameters—direct determination from completely reversed proportional cycling', *International journal of plasticity* **13**(6-7), 633–668.

Morel, F. & Huyen, N. [2008], 'Plasticity and damage heterogeneity in fatigue', *Theoretical and Applied Fracture Mechanics* **49**(1), 98–127.

Mousa, J. A. B. [2011], Multiaxial Fatigue Characterization and Modeling of AZ31B Magnesium Extrusion, PhD thesis, University of Waterloo.

Mughrabi, H. [2009], 'Cyclic slip irreversibilities and the evolution of fatigue damage', *Metallurgical and Materials Transactions B: Process Metallurgy and Materials Processing Science* **40**(4), 431–453.

Mughrabi, H., Ott, M. & Tetzlaff, U. [1997], 'New microstructural concepts to optimize the high-temperature strength of γ'-hardened monocrystalline nickel-based superalloys', *Materials Science and Engineering A* **234-236**(97), 434–437.

Nishihara, T. & Kawamoto, M. [1941], 'The strength of metals under combined alternating bending and torsion', *Trans. Japan Soc. Mech. Engrs* **7**, 185–194.

Nishihara, T. & Kawamoto, M. [1944], 'A new criterion for the strength of metals under combined alternating stresses', *Memoirs of College of Engineering, Kyoto Imperial University* **11**, 65–83.

Nishihara, T. & Kawamoto, M. [1945], 'The strength of metals under combined alternating bending and torsion with phase difference', *Memoirs of the College of Engineering, Kyoto Imperial University* **11**(5), 85–112.

Nye, J. F. [1953], 'Some geometrical relations in dislocated crystals', *Acta Metallurgica* **1**(2), 153–162.

Ott, M., Tetzlaff, U. & Mughrabi, H. [1999], 'Influence of directional coarsening on the isothermal high-temperature fatigue behaviour of the monocrystalline nickel-base superalloys CMSX-6 and CMSX-4', **272**, 24–30.

Papadopoulos, I. [1997], 'A comparative study of multiaxial high-cycle fatigue criteria for metals', *International Journal of Fatigue* **19**(3), 219–235.

Papadopoulos, I. V. [1995], 'A HIGH-CYCLE FATIGUE CRITERION APPLIED IN BIAXIAL AND TRIAXIAL OUT-OF-PHASE STRESS CONDITIONS', *Fatigue & Fracture of Engineering Materials & Structures* **18**(1), 79–91.

Papuga, J. [2011], 'A survey on evaluating the fatigue limit under multiaxial loading', *International Journal of Fatigue* **33**(2), 153–165.

Paris, P. & Erdogan, F. [1963], 'A critical analysis of crack propagation laws'.

Pattison, S. J. [2012], Multi-axial and thermo-mechanical loading effects in Nickel-based disc superalloys, D.eng thesis, Swansea University.

Polák, J. [2007], 'Mechanisms and kinetics of the early fatigue damage in crystalline materials', *Materials Science and Engineering A* **468-470**(SPEC. ISS.), 33–39.

Polák, J., Man, J. & Obrtlík, K. [2003], 'AFM evidence of surface relief formation and models of fatigue crack nucleation', *International Journal of Fatigue* **25**(9-11), 1027–1036.

Preuss, M., Withers, P. J. & Baxter, G. J. [2006], 'A comparison of inertia friction welds in three nickel base superalloys', **437**, 38–45.

Reed, R. C. [2006], *The Superalloys: Fundamentals and Applications*, Cambridge University Press, Cambridge.

Reis, L., Li, B. & de Freitas, M. [2009], 'Crack initiation and growth path under multiaxial fatigue loading in structural steels', *International Journal of Fatigue* **31**(11-12), 1660–1668.

Seeger, A. [1955], 'CXXXII. The generation of lattice defects by moving dislocations, and its application to the temperature dependence of the flow-stress of F.C.C. crystals', *The London, Edinburgh, and Dublin Philosophical Magazine and Journal of Science* **46**(382), 1194–1217.

Shamsaei, N. [2010], Multiaxial fatigue and deformation including nonproportional hardening and variable amplitude loading effects, PhD thesis, The University of Toledo.

Shamsaei, N. & Fatemi, A. [2010], 'Effect of microstructure and hardness on nonproportional cyclic hardening coefficient and predictions', *Materials Science and Engineering A* **527**(12), 3015–3024.

Shamsaei, N., Fatemi, A. & Socie, D. F. [2010], 'Multiaxial cyclic deformation and nonproportional hardening employing discriminating load paths', *International Journal of Plasticity* **26**(12), 1680–1701.

Shamsaei, N., Fatemi, A. & Socie, D. F. [2011], 'Multiaxial fatigue evaluation using discriminating strain paths', *International Journal of Fatigue* **33**(4), 597–609.

Shamsaei, N., Gladskyi, M., Panasovskyi, K., Shukaev, S. & Fatemi, A. [2010], 'Multiaxial fatigue of titanium including step loading and load path alteration and sequence effects', *International Journal of Fatigue* **32**(11), 1862–1874.

Sines, G. [1955], Failure of materials under combined repeated stresses with superimposed static stresses, Technical report, No. NACA-TN-3495, Los Angeles: California Univ.

Sines, G. [1959], 'Behavior of Metals under Complex Static and Alternating Stresses', *Met Fatigue* pp. 145–169.

Smith, K. N., Watson, P. & Topper, T. H. [1970], 'Stress- strain function for the fatigue of metals', *J Mater* **5**(4), 767–778.

Socie, D. [1987], 'Multiaxial Fatigue Damage Models', *Journal of Engineering Materials and Technology* **109**(October 1987), 293–298.

Socie, D. & Marquis, G. [1999], *Multiaxial Fatigue*, SAE International, Warrendale, PA.

Stephens, R. I., Fatemi, A., Stephens, R. R. & Fuchs, H. O. [2000], *Metal fatigue in engineering*, John Wiley & Sons.

Stroh, A. N. [1953], 'A theoretical calculation of the stored energy in a work-hardened material', *Proceedings of the Royal Society of London. Series A. Mathematical and Physical Sciences* **218**(1134), 391–400.

Stroh, A. N. [1954], 'The formation of cracks as a result of plastic flow', *Proceedings of the Royal Society of London. Series A. Mathematical and Physical Sciences* **223**, 404–414.

Suresh, S. [1998], *Fatigue of Materials*, Cambridge University Press, Cambridge.

Taylor, G. I. [1934*a*], 'The Mechanism of Plastic Deformation of Crystals. Part I. Theoretical', *Proceedings of the Royal Society A: Mathematical, Physical and Engineering Sciences* **145**(855), 362–387.

Taylor, G. I. [1934*b*], 'The Mechanism of Plastic Deformation of Crystals. Part II. Comparison with Observations', *Proceedings of the Royal Society A: Mathematical, Physical and Engineering Sciences* **145**(855), 388–404.

Tresca, H. [1868], 'Memoire sur l'ecoulement des corps solides.', *Mém. pres. par div. sav.* **18**, 733—-799.

von Mises, R. [1913], 'Göttinger nachrichten', *Math-Phys Klasse* p. 582.

Walker, K. [1970], The Effect of Stress Ratio During Crack Propagation and Fatigue for 2024-T3 and 7075-T6 Aluminum, *in* 'Effects of Environment and Complex Load History on Fatigue Life', ASTM International, 100 Barr Harbor Drive, PO Box C700, West Conshohocken, PA 19428-2959, pp. 1–1–14.

Wan, V. V. C., Maclachlan, D. W. & Dunne, F. P. E. [2014], 'A stored energy criterion for fatigue crack nucleation in polycrystals', *International Journal of Fatigue* **68**, 90–102.

Wan, V. V., Jiang, J., MacLachlan, D. W. & Dunne, F. P. [2016], 'Microstructure-sensitive fatigue crack nucleation in a polycrystalline Ni superalloy', *International Journal of Fatigue* **90**, 181–190.

Wang, C. H. & Brown, M. W. [1996*a*], 'Life Prediction Techniques for Variable Amplitude Multiaxial Fatigue—Part 1: Theories', *Journal of Engineering Materials and Technology* **118**(3), 367–370.

Wang, C. H. & Brown, M. W. [1996*b*], 'Life Prediction Techniques for Variable Amplitude Multiaxial Fatigue—Part 2: Comparison With Experimental Results', *Journal of Engineering Materials and Technology* **118**(3), 371.

Wang, J., Levkovitch, V., Reusch, F., Svendsen, B., Huétink, J. & van Riel, M. [2008], 'On the modeling of hardening in metals during non-proportional loading', *International Journal of Plasticity* **24**(6), 1039–1070.

Wang, Q. Y., Bathias, C., Kawagoishi, N. & Chen, Q. [2002], 'Effect of inclusion on subsurface crack initiation and gigacycle fatigue strength', *International Journal of Fatigue* **24**(12), 1269–1274.

Wang, Y.-y. [2004], 'Evaluation and comparison of several multiaxial fatigue criteria', *International Journal of Fatigue* **26**(1), 17–25.

Wilkinson, A. J. & Randman, D. [2010], 'Determination of elastic strain fields and geometrically necessary dislocation distributions near nanoindents using electron back scatter diffraction', *Philosophical Magazine* **90**(9), 1159–1177.

Xia, Z. [1993], 'A general fatigue theory and its application to out-of-phase cyclic loading', *Journal of engineering materials and technology* **18**(4), 411–416.

Xia, Z., Kujawski, D. & Ellyin, F. [1996], 'Effect of mean stress and ratcheting strain on fatigue life of steel', *International Journal of Fatigue* **18**(5), 335–341.

Xue, L. [2010], *Laser consolidation: A rapid manufacturing process for making net-shape functional components*, second edi edn, Elsevier Ltd.

You, B.-r. & Lee, S.-b. [1996], 'A critical review on multiaxial fatigue assessments of metals', **18**(4), 235–244.